



HAL
open science

Study of high-order vorticity confinement schemes

Ilias Petropoulos

► **To cite this version:**

Ilias Petropoulos. Study of high-order vorticity confinement schemes. Fluids mechanics [physics.class-ph]. Ecole nationale supérieure d'arts et métiers - ENSAM, 2018. English. NNT : 2018ENAM0001 . tel-01885220

HAL Id: tel-01885220

<https://pastel.hal.science/tel-01885220>

Submitted on 1 Oct 2018

HAL is a multi-disciplinary open access archive for the deposit and dissemination of scientific research documents, whether they are published or not. The documents may come from teaching and research institutions in France or abroad, or from public or private research centers.

L'archive ouverte pluridisciplinaire **HAL**, est destinée au dépôt et à la diffusion de documents scientifiques de niveau recherche, publiés ou non, émanant des établissements d'enseignement et de recherche français ou étrangers, des laboratoires publics ou privés.

École doctorale n° 432 : Sciences des Métiers de l'Ingénieur

Doctorat ParisTech

T H È S E

pour obtenir le grade de docteur délivré par

l'École Nationale Supérieure d'Arts et Métiers

Spécialité “ Énergétique ”

présentée et soutenue publiquement par

Ilias PETROPOULOS

le 22 janvier 2018

Study of high-order vorticity confinement schemes

Etude de schémas de confinement d'ordre élevé

Directeurs de thèse : **Paola CINNELLA, Michel COSTES**

Jury

M. Christophe CORRE, Professeur, Laboratoire MFAE/LMFA, École Centrale de Lyon
Mme. Héloïse BEAUGENDRE, Maître de Conférences, Inria Bordeaux - Sud-Ouest
M. John STEINHOFF, Professeur, University of Tennessee Space Institute
Mme. Paola CINNELLA, Professeur, Arts et Métiers ParisTech
M. Michel COSTES, Maître de Recherche, ONERA, Meudon
M. Éric LAMBALLAIS, Professeur, Institut Pprime, Université de Poitiers
Mme. Subhashini CHITTA, Research Scientist, Wave CPC, Inc., Tullahoma
M. Yann DOUTRELEAU, Responsable du domaine Fluides & Structures, DGA/MRIS, Paris

Président
Rapporteur
Rapporteur
Examineur
Examineur
Examineur
Invité
Invité

**T
H
È
S
E**

Acknowledgements

This thesis constitutes the main result of the research work of the past three years, which includes an important contribution of many others, direct and indirect.

First of all I would like to heartfully thank my thesis' directors, Michel Costes and Paola Cinnella, who I greatly appreciated working with and from whom I have learned a lot. In particular for their scientific advice, but also for their trust throughout periods of slow progress. I have also appreciated their good humour and our many discussions, not limited to work. Special thanks to Michel for his invaluable experience on confinement methods, his patience and for always being available. At the same time, I would like to thank Paola for her support and for her advice on numerical analyses. Their guidance has had a clear and invaluable contribution to the present work, both scientifically and on a personal, human level.

I would also like to express my gratitude to the members of my thesis' jury for being interested in this work. In particular for some interesting comments and suggestions which I will certainly keep in mind in my future works. Also, I would like to acknowledge ONERA and the DGA for the co-funding of the research work of this thesis.

Many thanks to Cédric Content and Bertrand Michel for introducing me to DynHoLab, as well as for their support regarding numerical implementations. I would also like to thank Luca Sciacovelli for the initialization and an important part of the post-processing routines for the HIT case, Bruno Maugars for his development version of k-exact schemes and also the members of the DynFluid Laboratory, with whom I had the chance to discuss on several occasions.

In addition, I would like to thank all my colleagues at the department of Aerodynamics, Aeroelasticity and Acoustics who, apart from sharing their knowledge and experience, make the working environment or the coffee breaks even more interesting and entertaining. I am grateful for having the chance to continue working with them. Besides the permanent researchers, I would like to thank the other PhD students, undergraduate students and other research members at Meudon and Châtillon, who also largely contribute to the quality of working life at ONERA: Andrea, Johnny, Nicolas R., Amaury, Loïc, Mickael, Alexandre S., Cédric, Benjamin, Alexandre M., Tito, Edoardo, Paul, Hélène, Anthony, Florent, Jérémy, Daniel, Frédéric, Matthieu, Alan, Maxime, Simon, Luis, Ye-Bonne, Damien, Nicolas B., Holly,... A special mention to my office colleagues over this period for the office adventures and for making work more pleasurable.

Finally, I would like to thank my friends, with whom I have had the chance to share a lot, and continue to do so. Many thanks as well to Dimitra, for her support and for the great time we have spent together. Last, I could never thank my family enough, and especially my parents, for always being a source of encouragement and inspiration.

Contents

1	Introduction	1
2	Review and state of the art of numerical methods for the calculation of vortical flows	7
2.1	Numerical calculation of vortical flows	7
2.2	Computational strategies	8
2.2.1	Lagrangian methods	8
2.2.2	Hybrid strategies	9
2.2.3	Adaptive mesh refinement	10
2.2.4	High-order methods	10
2.2.5	Vorticity-preserving schemes	14
2.2.6	Adaptive artificial dissipation techniques	14
2.2.7	The Vorticity Confinement (VC) method	15
2.3	Overview and thesis scope	17
3	Analysis of high-order scalar confinement schemes for the linear transport equation	19
3.1	The linear transport equation	20
3.2	Formulation of confinement	20
3.2.1	Lax-Wendroff family of schemes	21
3.2.2	Warming-Beam family of schemes	24
3.2.3	Directional Non-Compact family of schemes	24
3.2.4	Discussion of the coupled and uncoupled approaches	26
3.3	Analytical spectral analysis based on linear theory	27
3.3.1	Fourier analysis of numerical discretizations	27
3.3.2	Linear spectral analysis of schemes with confinement	29
3.4	Numerical quasi-linear spectral analysis	31
3.4.1	Description of the method	31
3.4.2	Validation and study of numerical precision	32
3.4.3	Spectral properties of schemes with confinement	32
3.4.4	Accuracy limit	36
3.4.5	Stability region and coupling with explicit Runge-Kutta algorithms	38
3.5	Application of the schemes to long-distance advection studies	39
3.5.1	Theoretical analysis of the asymptotic solution	40
3.5.2	Numerical results	41
3.5.2.1	Hyperbolic secant pulse	41
3.5.2.2	Wave packet	44
3.6	Chapter summary	47

4	Development of high-order Vorticity Confinement schemes for the Euler and Navier-Stokes equations	49
4.1	Navier-Stokes equations	50
4.2	Description of the solver and baseline numerical methods	52
4.2.1	Finite volume space discretization	52
4.2.1.1	Conservative approximation of convective fluxes	53
4.2.1.2	Approximation of viscous fluxes	56
4.2.1.3	Approximation of gradients	57
4.2.2	Time integration	57
4.3	Development of a high-order Vorticity Confinement method	58
4.3.1	Original VC2 formulation	58
4.3.2	Analogy with the scalar formulation	60
4.3.3	Extension of the Vorticity Confinement method to higher orders	62
4.3.4	Discussion of the confinement parameters	64
4.3.5	Equivalence with an anti-dissipative flux correction	65
4.4	Numerical implementation of the high-order Vorticity Confinement method	66
4.4.1	Recursive approximation of derivatives	66
4.4.1.1	Implementation of undivided differences	67
4.4.1.2	Conservativity of undivided differences in non-Cartesian meshes	68
4.4.1.3	Consistent evaluation of gradients on general meshes	69
4.4.1.4	Derivatives of the harmonic mean function	70
4.4.2	Boundary treatment	70
4.4.3	Identification of vortical flow regions and cut-off	72
4.4.3.1	Deactivation of VC correction	72
4.4.3.2	Identification of vortical flow regions	72
4.4.3.3	Application of the cut-off and conservativity	73
4.4.4	Laplacian schemes	74
4.4.4.1	5-point scheme	74
4.4.4.2	3-point scheme	74
4.5	Validation and numerical tests	74
4.5.1	Evaluation of the order of accuracy	74
4.5.2	Advection of an isentropic vortex	80
4.5.3	Discussion on computational cost	87
4.6	Chapter summary	88
5	Application to complex unsteady vortical flows	91
5.1	Viscous Taylor-Green vortex	91
5.1.1	Description of the test case and numerical strategy	91
5.1.2	Grid convergence study	93
5.1.3	Numerical results	94
5.1.4	Sensitivity to the velocity gradient calculation scheme	98
5.2	Decay of compressible Homogeneous Isotropic Turbulence	99
5.2.1	Description of the initial condition	99
5.2.2	Low-compressibility HIT at $M_{t0} = 0.2$ and $M_{t0} = 0.5$	100
5.2.3	Highly-compressible HIT at $M_{t0} = 1.0$	106
5.3	Chapter summary	110
6	Conclusions and perspectives	113
A	Treatments for the discontinuity of harmonic mean derivatives on the vortex boundary	119
B	Application to an airfoil-vortex interaction	125

C List of publications	133
D Résumé étendu	135
Bibliography	147

Chapter 1

Introduction

Context

During the last decades, numerical methods are gradually taking over the role of experimental studies in the design process of aerodynamic devices. Experiments remain of course indispensable, containing the complete physics of complex phenomena. They have shown remarkable progress over the past years, with the emergence of techniques [12, 62] being capable of detecting and measuring complex flow features even in realistic configurations (see Fig. 1.1). The setup of experiments is still however costly and time-demanding, making them prohibitive for broad explorative studies, often necessary in the concept and early industrial design phases.

At the same time, the significant progress in scientific computing capabilities has given a base for the extensive development of Computational Fluid Dynamics (CFD) methods. Although they were originally developed with the view to becoming an alternative to experiments, computational studies are presently far more than such a replacement. They have become mature enough in terms of precision, efficiency and robustness to be capable of providing both quantitative measures and valuable insight into flow physics. The latter is especially important for cases such as combustion chambers and turbomachine secondary flows where experimental measurements, and specifically flow field visualizations, are very difficult to obtain due to extreme thermodynamic conditions and geometry restrictions. Given the appropriate resolution in space and time, modern CFD methods are capable of accurately representing large and small scale flow mechanisms in a wide range of cases. However, the resources required to adequately resolve the flow field in space and time are prohibitive for many applications, especially concerning the resolution of fine turbulent structures associated to large values of the Reynolds number. The accurate calculation of steady transonic flows, which was the primary concern during the early development of CFD methods, is now achieved at a reasonable computational cost. However, the improvement in the efficiency of present aircraft and aerodynamic devices relies on the understanding and prediction of finer phenomena that occur at the limit of the flight envelope, often related to turbulent flow structures (turbulence-induced vibrations, transonic buffet, separated flows etc.) [187]. Such phenomena are usually inherently unsteady and require the use of more advanced wall-modeled and zonal Large Eddy Simulation (LES) simulation approaches [164, 175]. In terms of spatial and temporal resolution, these approaches are significantly more demanding than the Reynolds-averaged Navier-Stokes (RANS) methods which are more commonly applied in industry. As a result, the research community is constantly working on the development of accurate and efficient numerical methods for CFD.

A specific subject where the majority of standard CFD methods fail is to provide an accurate representation of flows containing vortical structures. This problem concerns both the research and industrial field, as vortices are flow features of primary interest in fluid dynamics and aerodynamics. Vortex motions are however particularly complex. They were concisely described by D. Küchemann as the *sinews and muscles of fluid motions* [115]. They are responsible for mass, momentum or energy transfer, as well as for the mixing of particles of passive or reactive scalars. Vorticity lies also at the heart of turbulence, as the chaotic three-dimensional fluctuations characteristic of tur-



Figure 1.1: Photograph of a BO105 light utility helicopter during a swinging maneuver and visualization of the blade-tip vortices by a background-oriented schlieren (BOS) technique. A. Bauknecht et al. [12].



Figure 1.2: Von Karman vortex street off Jeju-Do Island, South Korea, 2011. MODIS instrument on the Terra satellite, NASA.

bulent flows are maintained through the interaction between vorticity and velocity gradients [55]. Furthermore, they have an important role in the characterization of turbulent flows, in the form of coherent structures [168]. As a result, the interest in vortical structures spreads to numerous fluid dynamics applications, ranging from weather forecasting and atmospheric flows (Fig. 1.2) to aeronautics configurations (Fig. 1.3). Among many other engineering applications, vortical structures are important in the case of flow separation and dynamic stall conditions, as they produce increased lift but also induce vibrations and significantly augment structural loads. Additional challenging external aerodynamic simulations concern the accurate prediction of the generation and propagation of wakes generated from lifting surfaces (Fig. 1.3). In helicopter applications, blade-vortex interaction is a major source of aerodynamic noise, whereas the interaction of the main rotor wake with the tail and fuselage is an important factor for aerodynamic performance and flight stability. Wakes are also of particular interest for the acceleration of airport traffic, since the airflow perturbation following the take-off or landing of a transport aircraft poses strong restrictions on the minimum allowed aircraft separation distance.

The weakness of CFD methods to accurately predict vortical flows is partly related to the wide use of directional methods, based mostly on solvers and formulations developed for one space dimension [170]. The main problem however lies in the use of overly dissipative numerical schemes



Figure 1.3: Hydrodynamic tunnel visualization of a helicopter rotor wake (left) and the leading edge vortices formed due to the flow separation at the apex of a thin delta wing (right). H. Werlé, ONERA [60, 225].

in the discretization of the flow equations. The introduction of numerical dissipation itself in the discretization of the flow equations is necessary for stability, so as to ensure the damping of spurious oscillations. Nonetheless, the design of effectively stabilizing numerical dissipation which at the same time has minimal effect on flow features of interest – and in particular vortices – is an open subject of research. The dissipation of most numerical methods is thus inadequately tuned for the calculation of vortical flows, and results in the artificial spreading and diffusion of vortex structures in numerical simulations.

A common approach to this problem is the design of adaptive numerical dissipation, or the reduction of numerical dissipation in vortical flow regions. Among such approaches exists the Vorticity Confinement (VC) method proposed by J. Steinhoff in the '90s [189, 199]. This method was originally developed in the incompressible flow framework, as a model of thin vortical flow features at high Reynolds number flows. The idea of VC consists in adding a nonlinear negative dissipation source term in the flow equations to balance the excessive artificial dissipation of the baseline scheme in vortical regions. Rather than a model for thin vortical flow features, the VC method has also been applied as a purely numerical correction of the baseline scheme's dissipation [41]. The efficiency of this method has been demonstrated by its extensive application in the aeronautics field over the last two decades [149, 150, 194, 197, 198], including Large Eddy Simulations [195], turbulent flow calculations at high Reynolds numbers [196] and rotorcraft applications [48]. It has allowed the calculation of the main characteristics of vortical flows and the advection of thin vortical structures over long distances on coarse meshes, therefore at a greatly reduced computational cost compared to conventional methods.

Another more fundamental approach to treat the problem of spurious vortex diffusion is the use of high-order methods, being continuously more adopted for both research and industrial applications [114, 220]. These provide a more precise approximation of the fluid dynamics equations and yield improved wave propagation properties, but the numerical diffusion of vortices still cannot be completely prevented. This problem can eventually be mitigated by the use of VC alongside high-order methods. However, the original method of J. Steinhoff is at most first-order accurate, meaning that it results in a rapid domination of vortex profiles and a degradation of the global order of accuracy in vortical regions when applied to high-order simulations. The development of a VC method that is appropriate for high-order computations shows therefore great interest, especially since in the vast majority of cases VC can be applied independently of the choice of the underlying numerical scheme and is not restricted to a specific formulation.

The first step in this direction was taken in the study of M. Costes and F. Juliet [45]. They developed and analyzed VC corrections for high-order extensions of the Lax-Wendroff and Warming-Beam schemes in the case of the linear advection equation. Furthermore, they demonstrated an-

analytically and numerically that the asymptotic solution, i.e. the asymptotic balance between the baseline scheme's artificial dissipation and the nonlinear anti-dissipation of VC, is the same for all orders of accuracy. The rate of convergence towards this asymptotic solution was however shown to be slower for higher orders, as the magnitude of the VC correction is reduced. This is analogous to the reduction of numerical dissipation for higher-order accurate schemes. On this basis, a third-order extension of VC for the Euler equations on Cartesian grids was developed by M. Costes [43] based on the VC2 formulation of J. Steinhoff. Preliminary results were presented for helicopter-related applications, indicating that a higher-order VC scheme combines the confinement capability of the original VC method with the increased order of accuracy of the underlying high-order scheme. Nonetheless, a more rigorous analysis and understanding of the nonlinear properties of these schemes remains to be performed for complex flows.

This is the objective of the present thesis. Specifically, this study aims at developing extensions of the Vorticity Confinement method of J. Steinhoff to third- and fifth-order of accuracy for the Navier-Stokes equations. Moreover it aims at analyzing the intrinsically nonlinear properties of schemes with VC and evaluating their performance in the calculation of vortical aerodynamic flows.

Organization of the study

The first part of the present work, presented in chapter 2, consists in a literature study of numerical methods for the computation of vortical flows. In this chapter, a brief discussion is first given regarding common numerical difficulties and sources of error that arise in the case of vortical structures. A review is then presented on some major families of methods adopted for their calculation. This aims at identifying the principal axes and trends in modern approaches used within the research or industrial aerodynamics field. Additionally, the review presents the evolution and basic principles of the Vorticity Confinement method, which is the core subject of this thesis. Finally, a short overview is given and the scope of the present work is presented.

A fundamental step towards the extension of the VC method to higher orders of accuracy is subsequently made in the study of chapter 3. This consists in an analysis of high-order scalar confinement schemes for the linear transport equation, the simplicity of which makes it an appropriate basis for the analysis of numerical schemes. Confinement schemes are standard discretizations including a nonlinear anti-dissipative correction term in the scheme's numerical flux. Previously developed schemes of this type were based on coupled discretizations in space and time [45], in which case the effects of space and time discretization are often difficult to separate. To better isolate the effect the two discretizations, a new family of high-order scalar confinement schemes is developed based on decoupled schemes in space and time. Apart from decoupling the two discretizations, this approach is also interesting due to the wider use of space-time decoupled methods compared to coupled ones in numerical solvers. The schemes are then analyzed with respect to their spectral properties, i.e. their dispersive and dissipative error in the frequency space. The objectives of this study are to provide an improved understanding of their nonlinear numerical properties, give quantitative measures of their resolution and investigate the advantage of extending the confinement approach to higher orders of accuracy. Finally, the observations of this analysis are verified against results from the application of the schemes to numerical tests.

On the basis of this analysis, chapter 4 presents the extension of the VC method to higher orders of accuracy for the Navier-Stokes equations. This is the principal development of the present work. The extensions of the VC method are derived analytically, by making use of vector operators in the continuous framework. The derived VC term is thus naturally based on high-order derivatives, as standard high-order dissipation terms. Furthermore, the equivalence of the VC method with a nonlinear anti-dissipative correction of the scheme's dissipation in vortical flow regions is investigated. The discretization and implementation details of the method are also discussed. Then, the developed high-order VC corrections are validated in a series of numerical tests. Specifically, their order of convergence towards the exact solution is evaluated in the case of a two-dimensional

isentropic vortex. Next, their capacity to effectively balance the excess dissipation within vortical flow regions is evaluated in a series of long distance vortex advection studies.

In chapter 5, the developed VC schemes are applied to the calculation of complex vortical flows alongside standard high-order non-compact schemes. This study aims at evaluating their robustness and consistency in geometrically simple but physically complex cases, and turbulent flows in particular. The first case is the viscous Taylor-Green vortex flow, which involves multi-scale vortex dynamics and is a well-documented benchmark for high-order methods. A more detailed investigation of the schemes' dissipation is then performed in the case of decaying homogeneous isotropic turbulence. In this case, the performance of VC is evaluated at different turbulent Mach number initial conditions, including a turbulent flow with compressible effects.

Conclusions of the present work and some perspectives for subsequent investigations are given at the end of the thesis. Finally, a list of publications related to the work presented in this manuscript is given in Appendix C.

Chapter 2

Review and state of the art of numerical methods for the calculation of vortical flows

Contents

2.1	Numerical calculation of vortical flows	7
2.2	Computational strategies	8
2.2.1	Lagrangian methods	8
2.2.2	Hybrid strategies	9
2.2.3	Adaptive mesh refinement	10
2.2.4	High-order methods	10
2.2.5	Vorticity-preserving schemes	14
2.2.6	Adaptive artificial dissipation techniques	14
2.2.7	The Vorticity Confinement (VC) method	15
2.3	Overview and thesis scope	17

This chapter briefly discusses the difficulties that arise in the numerical calculation of vortical flows. It then reviews modern numerical approaches used in the research and industrial field for their calculation, and presents the historical development and current status of the Vorticity Confinement (VC) method, which is the main subject of this thesis. Last, it provides a short overview and presents the scope of the present work.

2.1 Numerical calculation of vortical flows

Vortices are generated primarily from shear layers, and are usually long-lived structures in fluid flows. Although their effect is important and useful in a large number of aeronautics applications, the longevity of vortices is not always beneficial (e.g. aircraft trailing wakes). At the same time, the evolution of vorticity within a fluid flow is characterized by complex dynamics involving transport, stretching, diffusion by fluid viscosity and baroclinic effects. Vorticity is also tightly related to drag generation and, on a more general level, it is important for the investigation and characterization of fluid flows, especially in the turbulent regime. On the other hand, vorticity dynamics mechanisms are delicate and make vortices particularly sensitive to numerical error. The accurate calculation of vortical flows thus remains a challenge, despite the significant progress and overall maturity of numerical methods for Computational Fluid Dynamics (CFD).

For this reason, the CFD community has been in a continuous search and development of numerical methods for the precise calculation of vortical flows. Lagrangian methods seem promising in that aspect, and have been efficiently applied to the calculation of wakes over several decades,

but are hindered by high computational requirements in treating complex flow configurations or no-slip boundaries. In the long-established Eulerian approach, the occurrence of numerical errors in vortical flow regions may have multiple origins. A fundamental issue concerns the use of “directional” methods, i.e. solvers and techniques formulated for one-dimensional problems [170], even though vortices are genuinely multidimensional structures. This deficiency concerns the calculation of both vortices and discontinuities, thus leading to a large body of recent research being devoted to the development of multidimensional numerical methods. Furthermore, the vast majority of CFD solvers use a primitive or conservative variable formulation. Numerical errors are thus further augmented as vorticity is not computed directly, but appears through the gradients of primitive variables. Another source of error can be the overprediction of turbulent eddy viscosity for Reynolds-averaged Navier-Stokes (RANS) models in vortices and wakes. This can be regulated by the introduction of rotational corrections in the RANS model production terms [51, 188] or by the use of a Large Eddy Simulation strategy, as this includes more accurate small scale dissipation modeling and a finer mesh resolution compared to RANS computations. The most important issues in the calculation of vortices however arise from numerical dissipation. More specifically, introducing an excess of numerical dissipation in vortical regions leads to a fast spreading and diffusion of vortical structures in numerical simulations. The use of artificial numerical dissipation itself for the capturing of discontinuities dates back to the early work of J. Von Neumann and R. Richtmyer [215]. To this day, it is a central component of most numerical methods, used to allow shock capturing and the damping of numerical oscillations in the treatment of realistic flows. Nonetheless, it naturally follows that the introduction of numerical dissipation in the discretized flow equations plays a significant role in the accuracy of results. At the same time, it drives the convergence of numerical schemes to steady-state solutions. Successful numerical dissipation should effectively remove numerical errors and spurious oscillations from the solution, but also have a negligible effect in the resolution of flow structures of interest. The fine balance between these two features is thus an essential ingredient in the design of numerical schemes, still being a core subject of computational fluid dynamics research. Due to a combination of the aforementioned reasons, standard CFD methods used in the research and industrial fields produce important errors in the simulation of vortices, related either to their generation or their transport.

The following section presents the historical development and state-of-the-art of computational strategies for the calculation of vortical flows. These range from very general categories of numerical methods, such as Lagrangian or Eulerian formulations, to families of numerical schemes and computational techniques. Rather than being exhaustive, this review aims at identifying the capabilities and limitations of these strategies and at providing a representative overview of modern computational fluid dynamics research for the calculation of vortices.

2.2 Computational strategies

2.2.1 Lagrangian methods

This general category contains numerical methods that resolve the flow equations in Lagrangian coordinates, i.e. the domain coordinates move as particles of the fluid. It contains the vortex lattice, or filament, methods, which are very cost effective for inviscid wake calculations and were especially used during the early development of CFD [81, 117]. Other Lagrangian methods, which have drawn more attention in the recent years, are vortex particle [49, 112, 119] and smoothed particle hydrodynamics methods [146, 147]. Smoothed particle hydrodynamics methods are primarily employed for the calculation of free-surface problems (e.g. wave simulation), moving bodies immersed in fluids, stellar collisions or hypervelocity impacts. On the other hand, vortex particle methods have been extensively applied to a wide number of aerodynamics applications ranging from fundamental flows [113, 129, 161] to engineering applications such as wind turbines, rotorcraft [216], and aircraft trailing wakes [34, 226].

Lagrangian methods are significantly different from the Eulerian methods widely adopted in the

CFD community, as they are mesh-less, can have an infinite far-field boundary and are theoretically non-dissipative. Vortex methods in particular are very accurate and efficient for the modeling of flows with localized vorticity such as vortex sheets. They are based on a discretization of the vorticity field by a number of discrete vortex particles, or blobs, and use the Biot-Savart law to calculate the induced velocities at each position of the domain. Viscous vortex particle algorithms usually consider the convective and diffusive effects in separate sub-steps (viscous splitting) [49]. Diffusive effects are then calculated with methods such as the random walk method [35] or the particle strength exchange scheme [59, 226]. Furthermore, re-meshing algorithms are often employed to avoid the appearance of distortions and accuracy loss due to non-uniform particle distribution [49].

The majority of vortex particle methods are developed for the modeling of inviscid or viscous flows in an incompressible framework. Extensions to compressible flows exist, by reformulating the dependent quantities carried by the independent vorticity particles. Except vorticity, these quantities can be divergence, temperature and density [152], dilatation, density, enthalpy and entropy [68] or mass, dilatation and energy [156].

A number of techniques have been developed to increase the efficiency of operations for very high resolution [82, 180], allowing simulations with large numbers of particles [34, 209]. The major drawback of vortex particle methods however concerns the handling of wall boundary conditions in viscous flow, which requires very costly operations on a large number of particles, especially on high Reynolds number flows [113]. This is a very restrictive constraint for realistic engineering applications and for this reason the use of purely Lagrangian methods remains limited to research for advanced vortical flow calculations.

2.2.2 Hybrid strategies

Hybrid strategies are based on the concept of domain decomposition, i.e. the separation of the computational domain in individual regions. Usually, domain decomposition is performed for the sake of reducing computational time by distributing the calculation into multiple processors. There exist however approaches where domain sub-regions are solved on a different formulation. These approaches, referred to as hybrid, aim at applying the most efficient simulation strategy in each flow region.

The first main category of hybrid methods consists of hybrid Eulerian-Lagrangian strategies. In such approaches, the difficulty of vortex particle methods to treat solid boundaries is overcome by using a Lagrangian representation of the field only away from solid boundaries and coupling it to a near-body Eulerian CFD method [49, 85]. This way, viscous boundary conditions are easily introduced on solid surfaces. Naturally, the subtlety lies with the coupling method of the two formulations. Some recent studies have worked on the coupling of Eulerian-Lagrangian approaches [6, 65, 200] based on incompressible vortex particle methods, but require an explicit treatment of density and pressure at the interface between the two formulations [200]. Other approaches are based on the development of compressible Lagrangian solvers particularly for the purpose of Eulerian-Lagrangian coupling [155–157]. In these, finite volume Eulerian and compressible Lagrangian zones are consistently coupled considering a domain decomposition with a complete overlap of the two regions. In [156, 157] however, the compressible Lagrangian formulation does not assume isentropic flow variations and is therefore applicable to a wider range of Mach number cases. Albeit the important increase in computational complexity, such approaches can have multiple advantages such as the ease of handling of multi-body geometries. Furthermore, the Lagrangian representation of the field away from solid boundaries allows the long-distance propagation of vortical structures and wakes with very low numerical diffusion and therefore hybrid Eulerian-Lagrangian approaches appear promising for vortical flow calculations.

Another possibility in a purely Eulerian formulation is the use of coupled structured-unstructured mesh solvers of the Navier-Stokes equations, usually taking advantage of near-body unstructured grids to facilitate the meshing of very complex geometries. Some of these were developed for the calculation of rotary wing flows [177, 227]. They couple unstructured grid regions for the rotating

bodies with background Cartesian meshes, using an overset grid approach [13, 183, 228]. Since the accurate calculation of vortical structures in the wakes is of high interest for rotorcraft applications, these methods are often combined with Adaptive Mesh Refinement techniques (see Section 2.2.3) in the background Cartesian region. Others were developed primarily for turbomachinery flows, even though their formulation is not restricted to these cases. They employ a coupling of near-body unstructured grids with structured curvilinear ones in the rest of the domain [56, 57, 233]. These methods avoid the communication via an overset grid technique to ensure the preservation of conservativity – and especially the conservation of mass – on the structured-unstructured mesh interface, which can be very important for turbomachinery and other compressible flow applications [230].

2.2.3 Adaptive mesh refinement

Mesh refinement, often referred to as h -adaptation in the finite element framework, consists in reducing solution error by increasing the density of the computational grid in regions of interest. Algorithms developed to automate the detection of increased error and the refinement of the mesh itself are collectively called Adaptive Mesh Refinement (AMR) approaches. They are especially interesting for cases where the region to be refined is usually only approximately known *a priori* (e.g. shock location, wake vortices), but also to mitigate computational cost by coarsening the mesh if the solution is already well approximated. AMR methods are different for the case of structured or unstructured meshes, mainly because of the ease in cell decomposition and refinement for the latter case, without requiring significant data structure modifications. Pioneered by the work of M. J. Berger et al. [16, 18] for Cartesian grids and then extended to curvilinear ones [17], AMR methods remain a very active research domain.

Mesh adaptation can be driven by flow features, i.e. based on physical criteria or flow quantities, [25, 158], solution error estimates [18, 76] or adjoint variables [74, 210]. The latter approach is more expensive as it generally requires the solution of an adjoint problem, but is very powerful since it allows mesh adaptation specifically to reduce the error in the calculation of an output variable (e.g. aerodynamic drag). The majority of AMR approaches are however feature-based, using a sensor to detect flow regions to refine or coarsen. Sensors can be based on variable gradients, physical criteria (e.g. vorticity magnitude, Q -criterion), or different forms of undivided differences of flow variables [26, 92, 201], often complemented by a smoothing process to prevent oversensitivity to numerical errors. It is however important that sensors are simple to compute, for the sake of parallelization, but also dimensionless and case-independent [108].

AMR methods have also been developed for curvilinear structured grids [92], but in this case very special care must be taken to ensure the preservation of the geometrical properties of the mesh [26, 201]. For structured grids, AMR methods are thus rather applied on Cartesian meshes due to their topological simplicity and due to the higher efficiency of Cartesian solvers compared to curvilinear ones (simplicity of high-order flux implementation, less operations and memory requirements) [25, 158, 179]. To treat realistic geometries, aerodynamic bodies are discretized by structured or unstructured near-body grids. These are then coupled to a background Cartesian mesh with AMR, using an overset grid approach [14, 31, 32, 158]. Such approaches can yield very detailed representation of wakes and blade-vortex interactions, albeit at a significantly increased computational cost due to the very high number of cells in the refined mesh [31, 32].

2.2.4 High-order methods

One could argue that the development of high-order methods has been most influenced historically by S. Godunov's theorem [80], demonstrating that linear monotonous schemes can be at most first-order accurate, and thus making nonlinearity an indispensable component of modern high-order shock-capturing schemes. The basis of modern high-order methods can be attributed to a series of works of B. Van Leer leading to the development of the MUSCL scheme [208] and later the Piecewise-Parabolic Method by P. Colella and P. Woodward [38]. B. Van Leer developed an extension of Godunov's method to second order of accuracy in space by considering linear variation

within computational cells and preserved monotonicity in the presence of flow discontinuities by introducing nonlinearity through slope limiters [208].

At present, the development of high-order methods forms an integral part of Computational Fluid Dynamics. They allow a more precise approximation of partial differential equations and possess improved wave propagation properties compared to lower-order ones. Regarding the calculation of vortical flows, this is translated to their capability of computing the propagation of vortices with less numerical dissipation and more accurate trajectory prediction. The notion of high order of accuracy nowadays refers to third or higher order, in contrast with the majority of methods used in the industry, which are first- or second-order accurate. In terms of computational cost, high-order methods are more complex and require more operations per degree of freedom (DOF). They are however overall less expensive than lower-order methods since they achieve a greater reduction of error for a given refinement of the mesh, or equivalently they achieve the same levels of error on coarser computational meshes [220]. Nonetheless, their development and industrialization is hindered by increased difficulties in terms of robustness, rate of convergence to steady-state solutions, parallelization and memory requirements, compared to low-order methods.

Due to significant progress in their development, references on the development of high-order methods in the scientific literature are so numerous and diverse that a detailed review lies far beyond the scope of the present study. The goal of this section is rather to provide a brief review of some major categories of modern high-order numerical methods for the solution of flow problems. More extensive reviews of high-order methods can be found in [67, 219], whereas comparisons on benchmark problems can be found at the results of the first and following workshops on high-order CFD methods [220].

Discontinuous Galerkin The discontinuous Galerkin (DG) method was introduced by W. H. Reed and T. R. Hill [163] and extended to fluid dynamics equations by numerous researchers. The DG formulation assumes continuity only within elements and is therefore especially appropriate for compressible flow problems, *hp*-adaptation and large parallelization (see [37] for a review of their properties and evolution). Since they originate from the finite element theory, DG methods naturally express the solution in terms of a polynomial expansion in each element and their accuracy can be increased to an arbitrary order on unstructured grids, by increasing the degree of the approximating polynomials. This is fundamentally different from finite volume methods, which only express the solution in the form of cell-averaged values. High-order DG methods have significantly evolved and have been applied to complex cases such as the calculation of turbulent flows [33, 78]. Their main drawback is the fast increase in degrees of freedom compared to continuous finite-element-like methods, whereas their use is currently mostly limited to the research field.

Spectral Volume/Spectral Difference Spectral Volume (SV) and Spectral Difference (SD) methods are based on a representation of the solution by discontinuous polynomials across elements, similarly to DG methods. Reviews of the SV/SD methods and results can be found in [67, 219, 221]. The SV method has been developed by Z. J. Wang, Y. Liu et al. [134, 202, 218] for conservation laws on unstructured grids, including the Navier-Stokes equations. It consists in a decomposition of each element into control volumes and a subsequent reconstruction of a, generally discontinuous across interfaces, high-order polynomial approximation in the spectral volume using cell-averaged data of its sub-volumes, rather than of its neighboring cells. Quadrature-free variants of the method have also been developed with the view to reducing the excessive cost of the original formulation in three space dimensions [89]. Their biggest drawback concerns the restrictive time step limitations imposed by the CFL condition, especially as the order of the method increases. The SD method has been developed as a simpler and improved formulation in terms of computational efficiency [133, 217]. It is based on the definition of two sets of points, the solution points and flux points, and does not require the numerical calculation of integrals. The method has since been extended to the Euler and Navier-Stokes equations and many other cases [221]. The development of SD methods is also linked to the Flux Reconstruction approach.

Flux Reconstruction The Flux Reconstruction (FR) approach towards high-order of accuracy, also referred to as Correction Procedure via Reconstruction (CPR), was recently proposed by H. T. Huynh using the differential form of the flow equations [99, 100]. It represents a unifying framework for some existing families of high-order methods, namely the nodal discontinuous Galerkin and the spectral difference approaches. The basis of the method lies in using the solution points to evaluate the derivative of a, generally piecewise discontinuous, flux. This discontinuous flux function is subsequently corrected to retrieve the continuous upwind flux at the cell interfaces. Schemes obtained via the FR approach are conservative and efficient, requiring a single set of points, i.e. the solution points, and evaluating fluxes only at cell interfaces [99]. Extensive research has led to the formulation of new schemes using the FR/CPR approach [7, 172, 212] and improved the insight on their numerical properties (see [101] for a review). Successful implementations have been presented in three-dimensions [24, 229] and the FR/CPR approach remains an active domain of research.

Residual Distribution The basis of Residual Distribution (RD) schemes, or fluctuation-splitting schemes, goes back to the work of R.-H. Ni [151] and P. Roe [171]. They were further developed by a number of researchers, R. Abgrall, H. Deconinck and M. Ricchiuto among others, combining a finite element basis with concepts of the finite volume formulation [1, 3, 58]. Standard, i.e. continuous, RD schemes use a continuous approximation of the solution based on the integral form of the flow equations. They consist in the computation of a cell-based residual and its conservative distribution to the cell nodes to update the nodal solutions. Their fundamental advantage is the incorporation of multidimensional upwinding due to their residual-based formulation, contrary to standard multidimensional finite volume schemes which rely on inherently one-dimensional Riemann solvers. RD schemes have been successfully applied to numerous steady and unsteady problems and have shown good accuracy and shock-capturing capabilities. More recently, various extensions of RD schemes have been developed, including extensions to higher orders of accuracy [4, 28, 166], discontinuous elements [2, 97] and local p -adaptation capabilities [5].

Residual-Based Compact Residual-Based Compact (RBC) schemes were developed by A. Lerat and C. Corre [124–126] for the calculation of compressible flows. Although they were originally developed for structured grids, they are related – in principle – to RD schemes. In the RBC formulation, both the consistent part of the flow equations and the numerical dissipation are based on compact approximations of the complete residual on the computational cell. RBC schemes have been extended to higher than third-order of accuracy [39, 40] and to unstructured grids [63], proving to be very effective for the resolution of steady and unsteady multidimensional problems with good accuracy and small effects of numerical dissipation, even on complex turbomachinery flows [123, 142]. More recent analyses have provided improved insight on their high-order residual-based dissipation for unsteady problems [128], but also their spectral properties [83] and steady discrete shock profiles [120]. Novel developments have also been presented in terms of formulation, including a third-order finite volume RBC scheme [84], an explicit high-order time formulation [121] and an efficient simplified compact scheme based on the RBC formulation [122].

ENO/WENO methods The concept of Essentially Non-Oscillatory (ENO) schemes was first introduced in a series of works by A. Harten et al. [90]. The basis of the method is the combination of high-order of accuracy and an *essentially* non-oscillatory property, respectively by considering high-order reconstruction polynomials and by using an adaptive stencil-choosing process. A significantly improved version was later proposed by X.-D. Liu, S. Osher and T. Chan [132], and further developed by G.-S. Jiang and C.-W. Shu as the Weighted Essentially Non-Oscillatory (WENO) schemes [107, 186]. The difference with respect to the ENO method is a very efficient analytical non-linear weighting process of all ENO candidate stencils, based on smoothness indicators. Through this process, WENO schemes can adaptively eliminate candidate stencils that contain discontinuities or combine them to achieve optimal reconstruction order in smooth regions. Numerous proposed variants of the original WENO method concern, among others, extensions to higher orders

of accuracy [9, 79], computational efficiency and order adaptivity [8], but more frequently address the choice of smoothness indicators [23, 91]. A survey of results obtained with WENO schemes can be found in [185]. They are very efficient and accurate for academic configurations, but remain mostly limited to a finite difference framework as they become significantly more expensive in a finite volume approach, when the number of dimensions increases.

High-order centered finite difference schemes with filtering The use of Finite Difference (FD) schemes on structured grids is one of the earliest approaches in CFD. FD schemes are not as robust and extendable to complex geometries as finite volume or finite element methods. They remain however interesting for moderately complex configurations, as they are significantly more efficient, algorithmically simple and straightforwardly extendable to higher orders of accuracy. The latter can be achieved on large stencils by means of Taylor expansions [93] or in compact form, using Padé fractions [118, 126, 213]. Compact FD schemes achieve high order of accuracy and very low approximation errors without increasing the stencil size, at the price of requiring implicit matrix operations. On the other hand, explicit large-stencil FD schemes can be of optimal order of accuracy on the given stencil size or use optimized coefficients to minimize dispersion and dissipation error in the wavenumber space, such as the Dispersion-Relation Preserving (DRP) schemes commonly applied in aeroacoustics simulations [20, 203]. To retain algorithmic simplicity and since their precision can be very dependent on mesh quality, high-order FD schemes are usually applied on Cartesian meshes, using an overset grid approach for the treatment of solid boundaries. On curvilinear meshes, they require a high-quality computational grid to preserve high order of accuracy. Alternatively, their application to low-quality, moving and deforming curvilinear grids is possible through appropriate techniques for spatial metric evaluation and preservation of the geometric conservation law [213]. High-order FD schemes are usually purely centered, i.e. they represent purely dispersive operators, and are thus often coupled with a filtering procedure to remove the appearance of spurious oscillations [70], specifically in the context of an LES or DNS approach. The objective of filter design is the development of efficient “sharp” low-pass filters, that is filters which effectively damp high-frequency amplitudes and have minimum effect on resolved structures. Such filters with sharp response functions can be obtained by the use of compact implicit approximations [118, 213]. Sharp response functions can also be obtained in the explicit filtering context, by the use of higher-order accurate operators [70], or optimization of coefficients in the wavenumber space [20]. The filtering strategy can also be adaptive, combining background high-order filtering with low-order filtering near discontinuities [22]. A recent review of explicit filters can be found in [71]. Centered FD schemes with filtering approaches have been successfully applied to the LES or DNS of compressible turbulent flows [21, 214].

k -exact finite volume methods The notion of k -exact methods refers to a class of high-order finite volume extensions of the Godunov method [80], originally developed by T. Barth and P. Fredrickson [10, 11]. These methods achieve high-order spatial accuracy on structured and unstructured grids by combining a high-order piecewise polynomial reconstruction of the solution with quadrature rules of appropriate order for flux integration on cell surfaces. By definition, a k -exact reconstruction operator provides an exact representation of solutions that are piecewise polynomials of degree k or lower [11]. The majority of k -exact schemes rely on a (weighted) Least Square (LS) [29, 103, 153] reconstruction, which becomes increasingly expensive for higher degrees of reconstruction polynomials, in terms of operations and memory required to evaluate and store the successive derivatives of the solution. Others rely on a recursive approximation of derivatives using a Green-Gauss-type approach. To mitigate the excessive requirements in terms of computational resources, more recent formulations of k -exact schemes have been developed using successive correction algorithms [29, 87, 140, 162, 232]. In these cases, derivatives are recursively approximated using compact stencils, i.e. involving only the close neighborhood of control volumes. High-order reconstructions are then obtained through recursive corrections of the truncation error of lower-order ones, based on a Taylor expansion. In addition to a successive correction algorithm, some of these approaches also introduce geometric corrections to account for mesh irregularities, allowing to compute consistent

approximations of gradients and preserve high-order of accuracy on arbitrary unstructured grids [87, 140, 162]. This can be important as gradient approximations, and especially LS methods, may result in high errors on highly stretched or curved meshes [141, 184]. The resulting schemes can be efficiently parallelized and provide accurate results on general meshes, their major drawback being the rapid increase of computational cost for higher than third order of accuracy.

2.2.5 Vorticity-preserving schemes

The development of specific numerical schemes for the accurate calculation of vortical flows represents a more fundamental approach to the problem of vortex diffusion by numerical dissipation. Such schemes were originally investigated by K. Morton and P. Roe [148] based on the Lax-Wendroff method [116]. The idea consists in the evaluation of the scheme's discrete operators in terms of conservation of local solution derivatives, and vorticity in particular. Numerical schemes are called "vorticity-preserving" if the approximation does not introduce any dissipation terms in the discrete vorticity transport equation. Such types of discretizations have been investigated in the more general framework of constraint-preserving schemes [105, 143, 144, 205], motivated either by the discrete preservation of vorticity or that of divergence-free fields in Magnetohydrodynamics (MHD). In the frame of aerodynamics, F. Falissard, A. Lerat and J. Sidès developed a second-order vorticity-preserving scheme for the compressible Euler equations based on the RBC family of schemes and extended it to structured curvilinear meshes [69, 72, 127].

A different approach to vorticity preservation has been proposed by F. Ismail and P. Roe [102]. Their method is based on the correction of numerical fluxes corresponding to the momentum equation to achieve the discrete preservation of pseudovorticity, i.e. the discrete curl of momentum. Flux corrections are calculated with respect to an independent vorticity estimate, but require the resolution of an elliptic problem at every time step of the calculation. An improved projection method has later been proposed by U. Fjordholm and S. Mishra for the system wave equation and the shallow water equations [75].

2.2.6 Adaptive artificial dissipation techniques

The majority of errors in the propagation of vortical structures arise from inadequately tuned numerical dissipation. AMR approaches or high-order schemes achieve an effective reduction of numerical dissipation in vortical flow regions respectively by locally increasing mesh resolution and by employing high-order dissipative operators. Alternatively, other approaches pursue the design of improved numerical dissipation, or the adaptive calibration of numerical dissipation within vortices. This is different from high-order schemes, as this calibration is performed by improved upwinding strategies or adaptation via flow sensors and not by increasing the order of the approximation. Such techniques are diverse, but in their majority are associated to a finite difference or finite volume formulation, due to their wider use in CFD. Naturally, the subtlety lies in scaling numerical dissipation without degrading the stability and convergence properties of the scheme.

The more fundamental approach consists in the development of flux vector splitting (FVS) or flux difference splitting (FDS) methods with reduced numerical dissipation. An example is the advection upstream splitting method (AUSM) developed by M.-S. Liou and C. Steffen [131]. The basis of the AUSM approach is the separation of convective and pressure terms in the inviscid flux treatment and the definition of appropriate upwinding splitting functions for Mach number and pressure. Several variants have since been presented and successfully applied to a wide range of cases [66, 130, 138, 139].

Another approach is the design of adaptive artificial dissipation, in the sense of combining low-order numerical dissipation near discontinuities with reduced, usually higher-order, numerical dissipation to damp spurious oscillations in the rest of the domain. The most popular of these approaches is probably the one proposed by A. Jameson, W. Schmidt and E. Turkel [104], where a centered second-order space discretization is used alongside a hybrid dissipation, switching from fourth- to second-order accurate depending on a pressure-based shock sensor. This approach has

been improved by F. Ducros et al. [64], by introducing an additional vorticity-based sensor. The Ducros sensor is a relative local weight measure between the velocity field divergence and its rotational, i.e. the vorticity. It provides an improved scaling of numerical dissipation in vortical regions and has been adopted alongside the original dissipation of Jameson et al. or high-order extensions (see e.g. [109]) for LES applications [36, 64].

A similar approach is the use of hybrid centered/upwind numerical schemes in the discretization of inviscid fluxes. The idea is the use of a centered, i.e. non-dissipative, version of the numerical scheme in smooth flow regions and its upwind version elsewhere, to ensure numerical stability and shock capturing. Such a hybrid even/odd order scheme has been proposed by A. Travin et al. [206] using an empirical blending function of the two versions in the context of Detached-Eddy Simulation (DES). Alternatively, I. Mary and P. Sagaut [138] have used a hybrid method that alternates between the central and upwind version of an AUSM+(P) scheme depending on the smoothness of the primitive flow variables. Last, G. Pont et al. [162] have proposed a partial recentering strategy using an analytical switch function that depends on the Ducros sensor and the grid Reynolds number.

Increased errors in the calculation of vortices can however also be induced from the use of flux limiting procedures. These errors arise from the local degeneration to first-order of accuracy at smooth extrema of primitive variables, occurring within vortical flow. To overcome the problem of vortex dissipation, R. Löhner [135] proposed a limiting procedure in a local rotational frame, specifically by suppressing the limiting in the direction normal to the vorticity vector and the direction of increasing vorticity gradient, and combined it with a vorticity confinement method. This approach was further developed by K. Mohamed et al. [145], who proposed the suppression of the limiting procedure and the reduction of numerical dissipation during the reconstruction of velocity in the vortex swirl plane.

2.2.7 The Vorticity Confinement (VC) method

An alternative to the previously reviewed approaches in a purely Eulerian coordinate framework is the Vorticity Confinement (VC) method proposed by J. Steinhoff et al. in the early '90s [189, 199]. The VC approach has been initially developed for the calculation of incompressible flows at high Reynolds numbers. In the original method, vortices are treated as concentrated structures, and therefore the accurate prediction of circulation, thickness and centroid position is prioritized over the prediction of their internal structure. In that sense, the resolution of vortices is similar to the treatment of discontinuities in shock capturing methods, satisfying the preservation of integral quantities without attempting to resolve their internal structure. The preservation of vortices is achieved by introducing a correction in the form of a negative dissipation source term in the flow equations. This negative dissipation, or anti-dissipation, balances the spreading of vortices due to numerical diffusion until an equilibrium is reached between the numerical dissipation and the VC correction, and the structure reaches an asymptotic shape that is propagated at the correct speed without diffusion. More extensive reviews of the formulation and physical insights can be found in [194–196]. The VC method has been proposed in two formulations, denoted as VC1 and VC2, which have been the basis for subsequent variants.

The first vorticity confinement method (VC1) is based on first derivatives of velocity [189, 199]. The VC term represents a convection of vorticity towards the direction of increasing gradient of vorticity magnitude, countering the spreading effect due to numerical dissipation. In an isolated vortex case, this corresponds to a convection of vorticity towards the vortex core. It is the most widely adopted of the two formulations due to its simplicity and efficiency in keeping vortex structures concentrated in few grid cells over very long advection distances. Over the past decades, the method has been successfully applied to a wide range of cases, such as helicopter rotor flows [199], interacting vortex rings [198], airfoil-vortex interactions [189] and even for the qualitative simulation of flows for computer graphics [73]. Despite its efficiency and algorithmic simplicity, the VC1 approach suffers from two main drawbacks. The first concerns a difficulty in the analytical

investigation of its properties, since its contribution to the vorticity transport equation is singular at the vortex core [41, 48]. The second is that the VC1 term does not have an equivalent conservative form. Therefore, it does not ensure the conservation of momentum, although errors in momentum conservation have been reported to remain limited for many cases by J. Steinhoff et al. [194].

An improved second formulation of the VC method (VC2) has been later presented, based on second derivatives of velocity and correcting the major disadvantages of the original VC1 [192, 193]. The VC correction in the VC2 formulation can be cast under conservative form and is regular at the vortex core, allowing more detailed analyses of its properties [42, 44, 193, 197]. In terms of vorticity preservation and easiness in the accommodation of complex topology changes, VC2 is very similar to the VC1 formulation, but may also permit more relaxation in the confinement of the advected structures and a more accurate trajectory prediction in long distance advection studies [195].

Besides the long-distance propagation of vortices, VC has also been employed in an immersed-boundary-like approach. This technique, also referred to as surface or body confinement, has been adopted to preserve a thin boundary layer thickness on a coarse background Cartesian grid, particularly in the calculation of massively separated flows [195, 223, 224]. Furthermore, the VC2 formulation, having been developed for the treatment of flow features as nonlinear solitary waves [193], has constituted the basis of the more recently proposed Wave Confinement (WC) method for the scalar wave equation. The WC method has been successfully applied to the calculation of thin pulses over long distances, including reflection from solid surfaces [190, 191].

Extensions of the VC method have also been developed for the compressible Euler and Navier-Stokes equations. The most commonly adopted approach is the one proposed by G. Hu et al. [95, 96], where the VC1 contribution is treated as a body-force term, and thus a VC correction is added to both the momentum and energy equations. The VC method has been widely applied to the calculation of compressible flows on structured and unstructured grids using this formulation, for cases such as wing-tip and delta-wing leading edge vortices [150], airfoil-vortex interactions [149], rotorcraft flows [27] and separated flows from blunt bodies [95]. It has been however identified that the contribution of VC in the energy equation may result in unphysical total temperature variations [52]. Additional studies regarding the pertinence of the body-force approach demonstrated that it also results in a diffusion of density at the vortex core and investigated the addition of a confinement term in the mass conservation equation to correct this problem [41, 42, 46]. Such negative effects are however not observed if the VC term contributions to the mass and energy equations are eliminated [41, 42, 52]. M. Costes thus recommended the interpretation of the VC method as a purely numerical correction, added only to the momentum equation, rather than a physical source term [41, 42]. On this spirit, extensions of the VC1 and VC2 formulations for compressible flow have been developed and applied to the calculation of rotorcraft flows [19, 42, 48].

Another ambiguity in the use of the VC method concerns the choice of the confinement parameters, and in particular the parameter commonly denoted as ε , which determines the magnitude of negative dissipation in the VC correction. To ensure consistency with the original partial differential equation and provide a means of scaling with mesh resolution, VC has often been applied with confinement parameters that are dependent on a characteristic mesh size [73, 136]. Based on dimensional analysis similarly to R. Löhner et al. [136], M. Robinson proposed a scaling for VC1 based on helicity [167]. N. Butsumtorn and A. Jameson combined the latter approach with a cell-volume scaling, based on a domain-averaged cell volume value [27]. In an attempt to completely remove the amount of empiricism that the choice of parameters entails, other studies have focused on the development of adaptive confinement parameter models. M. Costes and G. Kowani proposed an adaptive calculation of ε so that the VC1 or VC2 correction balances the truncation error in the approximation of the momentum equations [42, 46]. On a similar principle, S. Hahn and G. Iaccarino proposed an adaptive calculation of ε based on an estimation of numerical dissipation, calculated as the difference between the centered and upwind discretizations of the convective terms [86]. Nevertheless, even the VC2 formulation is no longer conservative if the values of the confinement parameters are varying in space. Conservativity can be preserved by the use of constant, i.e. averaged, parameter values within isolated vortical regions [42], but this cannot be straightforwardly

applied to complex flows.

In spite of the number of studies employing VC to treat the excessive diffusion of vortical structures, the vast majority use a VC formulation that is at most first-order accurate. Such an approach is not however consistent with high-order flux discretizations, although good results may be obtained on coarse grids [173], where the numerical error of high-order methods can be of comparable magnitude to the first-order VC correction. High-order extensions of the VC method were first thoroughly investigated for the linear transport equation by M. Costes and F. Juillet [45]. In that study, VC corrections were developed for high-order extensions of the Lax-Wendroff [116] and Warming-Beam [222] schemes by basing the VC correction on high-order dissipative terms. Analytical and numerical results demonstrated that the developed high-order extensions of VC have the same pulse-preserving property and asymptotic solution as the original one, albeit at a slower relaxation rate, as the magnitude of the correction is lower at higher-orders. Last, preliminary results of a third-order extension of VC2 for the Euler equations were presented by M. Costes for helicopter applications [43]. This extension was based on the high-order extensions previously developed for the linear transport equation and showed promising results, indicating that the developed scheme combines increased order of accuracy with the vorticity-preserving capability of the original VC2.

2.3 Overview and thesis scope

Despite the abundance of numerical formulations developed for the accurate calculation of vortical flows, a rather important portion remains limited to research. This is largely due to the difficulty of development and validation of new large-scale computational codes. Especially in the frame of industrial computational fluid dynamics, this validation and integration process is strenuous and time-demanding. As regards the numerical strategy, the vast majority of recent industrial CFD codes employ a finite volume approximation of the Navier-Stokes equations in a purely Eulerian formulation. This choice is usually made for reasons of robustness, generality and broad availability of numerical techniques due to its long-time use in the aeronautics field. In this framework, AMR approaches are also regularly used but require a significant increase of computational cost, to an extent which the numerical study itself cannot always justify. On the other hand, vorticity-preserving schemes are rarely preferred against shock-capturing methods, as the capturing of discontinuities is prioritized over the calculation of vorticity for the calculation of realistic aeronautic flows. An important amelioration regarding the calculation of vortical flows has been achieved by the development of high-order methods, but still errors often remain important for many aerodynamics applications. As a result, techniques to calibrate the numerical dissipation of the existing low- or high-order schemes in vortical flow regions are very often used to address the problem of spurious vortex diffusion.

Vorticity Confinement appears to be a promising technique in that matter. It combines generality, as it is formulated independently of the baseline scheme, with very efficient reduction of numerical dissipation in vortical regions at a reasonable computational cost. The original VC formulation of Steinhoff was developed as a cost-effective low-order method designed to model thin vortical flow features on coarse computational meshes. Its interpretation for compressible flows varies from a physical body-source term to a numerical correction of the baseline scheme's dissipation (see Section 2.2.7), although substantial evidence support the latter as a more pertinent approach. Still, the low-order formulation of VC is a prohibitive factor for its application alongside high-order methods.

The present thesis constitutes an investigation of high-order extensions of the Vorticity Confinement method, specifically the VC2 formulation, for the compressible Euler and Navier-Stokes equations. This problem is approached from a numerical point of view. First, the VC method is interpreted as a numerical correction of the baseline numerical dissipation, rather than a physical source term of the flow equations, following the work of M. Costes [41]. At higher order of accuracy, VC extensions

are developed as high-order nonlinear anti-dissipative corrections of the excess numerical dissipation in vortical regions. Second, the derivation of high-order extensions is analytical, but the present work also investigates their numerical discretization in the finite volume framework. The aim of the thesis can be divided into three principal axes:

- Providing an improved understanding of the nonlinear properties of vorticity confinement schemes using the basis of the linear transport equation. For this purpose, high-order extensions are developed for decoupled schemes in space and time, based on the work already performed for the Lax-Wendroff and Warming-Beam schemes [45]. These formulations are then analyzed in terms of their spectral properties in the wavenumber space.
- Development of high-order extensions of the Vorticity Confinement method for the compressible Euler and Navier-Stokes equations. These should be consistent with high-order flux discretizations and preserve the strong points of the original VC2 method. They should therefore remain conservative, rotationally invariant and be formulated independently of the baseline numerical scheme.
- Application of the developed schemes in vortical flow calculations and analysis of their order of accuracy, numerical error and vorticity-preservation capabilities. Moreover, these studies aim at evaluating their limitations but also their robustness and consistency in the calculation of complex turbulent flows.

Chapter 3

Analysis of high-order scalar confinement schemes for the linear transport equation

Contents

3.1	The linear transport equation	20
3.2	Formulation of confinement	20
3.2.1	Lax-Wendroff family of schemes	21
3.2.2	Warming-Beam family of schemes	24
3.2.3	Directional Non-Compact family of schemes	24
3.2.4	Discussion of the coupled and uncoupled approaches	26
3.3	Analytical spectral analysis based on linear theory	27
3.3.1	Fourier analysis of numerical discretizations	27
3.3.2	Linear spectral analysis of schemes with confinement	29
3.4	Numerical quasi-linear spectral analysis	31
3.4.1	Description of the method	31
3.4.2	Validation and study of numerical precision	32
3.4.3	Spectral properties of schemes with confinement	32
3.4.4	Accuracy limit	36
3.4.5	Stability region and coupling with explicit Runge-Kutta algorithms	38
3.5	Application of the schemes to long-distance advection studies	39
3.5.1	Theoretical analysis of the asymptotic solution	40
3.5.2	Numerical results	41
3.6	Chapter summary	47

This chapter consists in an analysis of high-order anti-dissipative confinement corrections for the linear scalar transport equation. First, previously developed high-order confinement corrections for the Lax-Wendroff and Warming-Beam schemes are reviewed. Then, a new formulation is presented for decoupled schemes in space and time. A quasi-linear spectral analysis is subsequently performed to provide an improved representation of the schemes' resolution and numerical errors. This allows the quantification of their resolvability and the decomposition of their numerical error in terms of dispersion and dissipation. More importantly though, this analysis allows to evaluate the interest of confinement corrections for higher-order accurate flux discretizations. The accuracy of the aforementioned nonlinear schemes with confinement is finally evaluated via application to scalar advection problems.

3.1 The linear transport equation

The present chapter investigates high-order vorticity confinement schemes for the discretization of the linear transport equation. In one space dimension x , this equation is written:

$$\frac{\partial u}{\partial t} + c \frac{\partial u}{\partial x} = 0 \quad (3.1)$$

where t denotes time and the spatial domain is considered infinite or periodic. Above, $u = u(x, t)$ is a scalar quantity and c is the advection speed, which is taken constant in space and time. Eq. (3.1) describes the passive advection of a scalar quantity u at speed c , without diffusion. For an arbitrary initial condition $u_0(x) = u(x, 0)$, the exact solution after time t is:

$$u(x, t) = u_0(x - ct) \quad (3.2)$$

The solution (3.2) is a simple shift of the initial condition u_0 by a distance ct . In the following, $c > 0$ is assumed for simplicity.

The linear transport equation (3.1) is the simplest hyperbolic partial differential equation that allows the evaluation of numerical schemes for spatial derivatives and time integration, in terms of their capability to approximate the exact solution (3.2). It is therefore regularly used as a simple model, where the analytical solution is known and the accuracy of numerical schemes can be analyzed easier than for more complex systems of equations.

3.2 Formulation of confinement

In the framework of the linear transport equation, which is the subject of the present chapter, the VC method will be simply referred to as ‘‘confinement’’ or ‘‘scalar confinement’’ since the transported variable does not specifically correspond to vorticity.

We consider discrete approximations of Eq. (3.1) on a uniform grid with spacing Δx ($x_j = j \Delta x$, $j \in \mathbb{Z}$) and a time step Δt ($t_n = n \Delta t$, $n \in \mathbb{Z}$). The discrete solution on the grid point x_j at time t_n is denoted as $u_j^n = u(x_j, t_n)$. For example, the first-order upwind scheme is written:

$$\frac{u_j^{n+1} - u_j^n}{\Delta t} + \frac{c}{\Delta x} (u_j^n - u_{j-1}^n) = 0 \quad (3.3)$$

Alternatively, Eq. (3.3) can be written:

$$u_j^{n+1} = u_j^n - \sigma (u_j^n - u_{j-1}^n) \quad (3.4)$$

where $\sigma = c\Delta t/\Delta x$ is the Courant–Friedrichs–Lewy (CFL) number.

A semi-discrete – continuous in time, discrete in space – approximation of equation (3.1) can be written in the generic form:

$$\frac{\partial u}{\partial t} + \mathcal{G}(u) = 0 \quad (3.5)$$

where $\mathcal{G}(\bullet)$ is a discretization operator of the spatial-derivative part of Eq. (3.1). The idea of confinement is to introduce a nonlinear anti-dissipative correction term to balance the excess dissipation of the baseline space discretization:

$$\frac{\partial u}{\partial t} + \mathcal{G}(u) - \mathcal{C}(\tilde{h}(u)) = 0 \quad (3.6)$$

Requirements for the design of the correction \mathcal{C} are discussed by J. Steinhoff [195]. It must be nonlinear, so that the negative dissipation does not lead to divergence of the solution. Since it represents an anti-dissipative correction, \mathcal{C} is based on a dissipative operator. As denoted in Eq. (3.6),

it is commonly formulated using the harmonic mean of the transported scalar variable at each grid position, instead of the variable itself. By introducing the space backshift operator:

$$Tu_j = u_{j-1} \quad (3.7)$$

the harmonic mean between two neighboring grid points can be defined as:

$$(\tilde{h}(\bullet))_j = \tilde{h}((\bullet)_j, T(\bullet)_j) = \tilde{h}((\bullet)_j, (\bullet)_{j-1}) = \begin{cases} \frac{2(\bullet)_j(\bullet)_{j-1}}{(\bullet)_j + (\bullet)_{j-1}} & , \text{if } (\bullet)_j(\bullet)_{j-1} > 0 \\ 0 & , \text{otherwise} \end{cases} \quad (3.8)$$

which is a nonlinear averaging function dominated by the smallest of its arguments. Other possibilities exist besides the harmonic mean for the formulation of the confinement correction, but such alternatives are not investigated in the present work.

At this point, a fundamental difference should be noted between the scalar confinement schemes of the present chapter and the vorticity confinement schemes for the Euler and Navier-Stokes equations. In the latter case, the confinement correction is based on vorticity and applied to the physical fluxes, whereas in the scalar transport case it is directly based on the advected scalar. The confinement correction in the scalar case can therefore be more straightforwardly adapted to the baseline scheme dissipation.

There exists however a discernible analogy between the two formulations. Specifically, the contribution of the vorticity confinement correction in the transport equation for vorticity results in a similar form to the equivalent differential equation in the scalar case. This is demonstrated in Section 4.3.2.

3.2.1 Lax-Wendroff family of schemes

The present section reviews the formulation of confinement for high-order extensions of the Lax-Wendroff scheme, developed by M. Costes and F. Juillet [45]. The classical second-order Lax-Wendroff scheme [116] is written on a uniform grid with spacing Δx ($x_j = j \Delta x$, $j \in \mathbb{Z}$) and a time step Δt ($t_n = n \Delta t$, $n \in \mathbb{Z}$) as:

$$u_j^{n+1} = u_j^n - \frac{\sigma}{2}(u_{j+1}^n - u_{j-1}^n) + \frac{\sigma^2}{2}(u_{j+1}^n - 2u_j^n + u_{j-1}^n) \quad (3.9)$$

One way of obtaining the above Lax-Wendroff scheme is by correcting the leading truncation error term of the first-order upwind scheme. Performing a Taylor expansion of the terms of Eq. (3.4) up to terms of second order and using the original partial differential equation (3.1) to convert the time derivatives of u as space derivatives, we obtain the equivalent differential equation:

$$\frac{\partial u}{\partial t} + c \frac{\partial u}{\partial x} = \frac{\Delta x^2}{\Delta t} \frac{\sigma(\sigma - 1)}{2!} \frac{\partial^2 u}{\partial x^2} \quad (3.10)$$

where the term on the right-hand side corresponds to the leading truncation error term of the scheme (3.4). By subtracting a centered discrete approximation of the leading error term in (3.10) from the scheme (3.3), we obtain:

$$u_j^{n+1} = u_j^n - \sigma(u_j^n - u_{j-1}^n) + \frac{\sigma(\sigma - 1)}{2}(u_{j+1}^n - 2u_j^n + u_{j-1}^n) \quad (3.11)$$

which is an equivalent form of Eq. (3.9), by rearrangement of the terms of the right-hand side. The Lax-Wendroff scheme can thus be expressed as a sum of a first-order upwind difference and a second-difference correction.

On a similar error correction principle, the original first-order VC2 is formulated to correct the highly diffusive error of the first-order upwind scheme (3.4). This approach leads to similar results

with the approach of J. Steinhoff, who developed the VC2 correction to model thin features as nonlinear solitary waves [197]. In the original VC2 method, the correction is based on a second difference of the harmonic mean as:

$$u_j^{n+1} = u_j^n - \sigma \left(u_j^n - u_{j-1}^n \right) + \varepsilon \frac{\sigma(\sigma - 1)}{2} \delta^2 \tilde{h}(u_j^n, Tu_j^n) \quad (3.12)$$

where $\delta(\bullet)_{j+\frac{1}{2}} \triangleq (\bullet)_{j+1} - (\bullet)_j$ is the difference operator, $\delta^2(\bullet) = \delta(\delta(\bullet))$, and ε is a real constant called the confinement parameter. A central evaluation of the second difference in the confinement correction gives:

$$u_j^{n+1} = u_j^n - \sigma \left(u_j^n - u_{j-1}^n \right) + \varepsilon \frac{\sigma(\sigma - 1)}{2} \left(\tilde{h}(u_{j+1}^n, Tu_{j+1}^n) - 2\tilde{h}(u_j^n, Tu_j^n) + \tilde{h}(u_{j-1}^n, Tu_{j-1}^n) \right) \quad (3.13)$$

The Lax-Wendroff scheme (3.11) is retrieved by taking $\varepsilon = 1$ and replacing the harmonic mean with the scalar variable u . However, since usually $\varepsilon \neq 1$ and $\tilde{h}(u_j^n, Tu_j^n) \neq u_j^n$ for non-trivial solutions, the scheme (3.13) is globally 1st-order accurate. In the following it will therefore be referred to as the LW1-C scheme. Despite the reduced order of accuracy, the nonlinear correction of the scheme (3.13) provides the capability to indefinitely conserve non-trivial asymptotic solutions, which are transported at the correct speed. The form of asymptotic solution, which occurs from the balance between the anti-dissipation of confinement and the dissipation of the baseline scheme, is further discussed in Section 3.5.1.

Linear extensions of the Lax-Wendroff (LW) scheme (3.11) to higher orders of accuracy can be obtained in a similar manner. A p th-order scheme of the LW family can be extended to $(p+1)$ th-order of accuracy as follows:

Algorithm 3.1 High-order extension of the Lax-Wendroff scheme

- 1: Perform Taylor series expansions for the p th-order scheme up to terms of $(p+1)$ th order
 - 2: Substitute time derivatives of u with space derivatives using Eq. (3.1)
 - 3: Retrieve the equivalent partial differential equation and the leading error term of the p th-order scheme
 - 4: Subtract a discrete approximation of this leading error term from the p th-order scheme. Use an upwind approximation stencil for odd derivatives and a centered stencil for even derivatives.
-

Schemes obtained through this process are high-order accurate both in space and in time. Furthermore, they are space-time coupled and stable under the CFL condition $\sigma \leq 1$. They correspond to the unlimited version of the one-step monotonicity-preserving (OSMP) schemes developed by V. Daru and C. Tenaud [54]. In the above algorithm, the last step corresponds to a correction of the dissipative error of the p th-order scheme if p is an odd order, and to a correction of its dispersive error if p is an even order. Equivalently, these schemes can be obtained by following the classical Lax-Wendroff approach of performing a Taylor expansion in time for u_j^{n+1} and introducing space derivatives by substituting the high-order time derivatives using Eq. (3.1).

Following this procedure, a 4th-order extension of the Lax-Wendroff scheme (LW4) is:

$$\begin{aligned} u_j^{n+1} = & u_j^n - \sigma \left(u_j^n - u_{j-1}^n \right) + \frac{\sigma(\sigma - 1)}{2!} \left(u_{j+1}^n - 2u_j^n + u_{j-1}^n \right) \\ & - \frac{(\sigma + 1)\sigma(\sigma - 1)}{3!} \left(u_{j+1}^n - 3u_j^n + 3u_{j-1}^n - u_{j-2}^n \right) \\ & + \frac{(\sigma + 1)\sigma(\sigma - 1)(\sigma - 2)}{4!} \left(u_{j+2}^n - 4u_{j+1}^n + 6u_j^n - 4u_{j-1}^n + u_{j-2}^n \right) \end{aligned} \quad (3.14)$$

High-order extensions of confinement were developed for these schemes using the same ideas underlying the first-order approach [45]. The high-order dissipative truncation error correction of an even-order LW scheme is replaced with a confinement correction. The confinement correction

has the same coefficients and is built on the same stencil, but using the harmonic mean instead of the scalar variable u and multiplied with ε . An additional point is thus included to the actual stencil of the scheme, due to the harmonic mean (3.8). For the LW4 scheme of Eq. (3.14), the confinement correction is formulated as:

$$\begin{aligned} u_j^{n+1} = & u_j^n - \sigma (u_j^n - u_{j-1}^n) + \frac{\sigma(\sigma-1)}{2!} (u_{j+1}^n - 2u_j^n + u_{j-1}^n) \\ & - \frac{(\sigma+1)\sigma(\sigma-1)}{3!} (u_{j+1}^n - 3u_j^n + 3u_{j-1}^n - u_{j-2}^n) \\ & + \varepsilon \frac{(\sigma+1)\sigma(\sigma-1)(\sigma-2)}{4!} (\tilde{h}(u_{j+2}^n, Tu_{j+2}^n) - 4\tilde{h}(u_{j+1}^n, Tu_{j+1}^n) + 6\tilde{h}(u_j^n, Tu_j^n) \\ & - 4\tilde{h}(u_{j-1}^n, Tu_{j-1}^n) + \tilde{h}(u_{j-2}^n, Tu_{j-2}^n)) \end{aligned} \quad (3.15)$$

which is third-order accurate. The scheme of Eq. (3.15) will be referred to as the third-order extension of the Lax-Wendroff scheme with confinement (LW3-C). Extensions to even higher odd orders of accuracy are obtained on the same principle.

These schemes can be written in conservative form as:

$$u_j^{n+1} = u_j^n - \frac{\Delta t}{\Delta x} \left(F_{j+\frac{1}{2}}^p - F_{j-\frac{1}{2}}^p \right) \quad (3.16)$$

where $F_{j+\frac{1}{2}}^p$ denotes the numerical flux of the explicit scheme. For the first-order upwind scheme of Eq. (3.4) this is:

$$F_{j+\frac{1}{2}}^1 = c u_j^n \quad (3.17)$$

The numerical flux of a linear p th-order scheme of the Lax-Wendroff family (LW p) can be expressed through the recurrence relation [53]:

$$F_{j+\frac{1}{2}}^p = F_{j+\frac{1}{2}}^1 + \sum_{r=1}^{p-1} \Lambda^r \quad (3.18)$$

for $p \geq 2$. Above, Λ^r denotes the negative (i.e. with opposite sign) discrete approximation of the leading error term of the r th-order scheme:

$$\Lambda^r = c \zeta_{r+1} \sum_{l=0}^r (-1)^l C_r^l u_{j+m-l}^n \quad (3.19)$$

with:

$$\zeta_l = \prod_{q=2}^l (-1)^q \frac{\lfloor \frac{q}{2} \rfloor - (-1)^q \sigma}{q} \quad (3.20)$$

In Eq. (3.19), C_r^l and m respectively denote the binomial coefficient and the integer division:

$$C_r^l = \frac{r!}{(r-l)! l!} \quad m = \left\lfloor \frac{r+1}{2} \right\rfloor \quad (3.21)$$

In turn, the numerical flux of a high-order extension of the Lax-Wendroff scheme with confinement (LW p -C) can be expressed through:

$$F_{j+\frac{1}{2}}^p = F_{j+\frac{1}{2}}^1 + \sum_{r=1}^{p-1} \Lambda^r + \varepsilon c \zeta_{p+1} \sum_{l=0}^p (-1)^l C_p^l \tilde{h} \left(u_{j+\lfloor \frac{p+1}{2} \rfloor - l}^n, Tu_{j+\lfloor \frac{p+1}{2} \rfloor - l}^n \right) \quad (3.22)$$

for p odd and $p \geq 1$. We also define sums with no summands to be equal to zero, i.e. $\sum_{\alpha}^{\beta} (\bullet) = 0$ for $\alpha > \beta$.

Eq. (3.22) shows that starting from any p th-order LW scheme with confinement (LW p -C), suppressing the nonlinear confinement term yields the baseline LW p scheme, whereas taking $\varepsilon = 1$ and replacing the harmonic mean with the scalar variable u cancels the leading error term and recovers the baseline LW($p+1$). For the same number of truncation error correction terms, confinement thus introduces a nonlinear negative dissipation at the price of reducing by one the scheme's order of accuracy.

The equivalent differential equation for the high-order Lax-Wendroff extensions with confinement to any odd order p takes the mixed continuous/discrete form:

$$\frac{\partial u}{\partial t} + c \frac{\partial u}{\partial x} = c \zeta_{p+1} \Delta x^p \left(\frac{\partial^{p+1} u}{\partial x^{p+1}} - \varepsilon \frac{\delta^{p+1} \tilde{h}(u_j^n, Tu_j^n)}{\Delta x^{p+1}} \right) \quad (3.23)$$

The above corresponds to the equivalent differential equation for linear LW p schemes at even orders p by suppressing the harmonic mean term. Eq. (3.23) shows that the numerical error of the scheme is defined by the balance between the confinement correction and the error of the baseline LW p scheme. This balance defines the asymptotic solution, as is further discussed in Section 3.5.1.

3.2.2 Warming-Beam family of schemes

Confinement corrections for high-order extensions of the explicit upwind Warming-Beam (WB) scheme [222] were also developed by M. Costes and F. Juliet using the same approach. The classical second-order Warming-Beam scheme is obtained on the same principle with the Lax-Wendroff scheme (3.11), but using an upwind approximation to correct the leading error term (3.10):

$$u_j^{n+1} = u_j^n - \sigma(u_j^n - u_{j-1}^n) + \frac{\sigma(\sigma - 1)}{2} (u_j^n - 2u_{j-1}^n + u_{j-2}^n) \quad (3.24)$$

This scheme can be extended to higher orders of accuracy by recursive application of the Algorithm 3.1, but using upwind approximation stencils for both odd and even derivatives in Step 4. Error terms, i.e. truncation error corrections at higher orders, are thus different than for Lax-Wendroff schemes. For odd differences this leads to a different real coefficient ζ_p , whereas for even differences it leads to the same real coefficient but a different approximation stencil. Confinement corrections for high-order extensions of the Warming-Beam scheme are as effective as the ones based on the Lax-Wendroff approach [45].

The construction principle of these schemes is reviewed here for the sake of completeness. However, the use of upwind stencils in the approximation of even derivatives results in an increased space approximation error compared to the Lax-Wendroff schemes of the previous section. As such, following analyses for coupled schemes in space and time with confinement will be performed with the high-order Lax-Wendroff schemes of Section 3.2.1 as a reference.

3.2.3 Directional Non-Compact family of schemes

Previous studies consisted in the investigation of confinement for high-order extensions of the Lax-Wendroff and Warming-Beam schemes. Despite their efficiency, an analysis of their space discretization is not straightforward since they are coupled in space and time. The present section is therefore focusing on the development of high-order confinement corrections for a decoupled family of schemes, based on high-order centered space discretizations.

Considering again a uniform grid with spacing Δx , the convective derivative of Eq. (3.1) can be approximated at m^{th} -order of accuracy using a linear flux discretization operator \mathcal{R}^m of the generic conservative form:

$$\begin{aligned} \left. \frac{\partial(\bullet)}{\partial x} \right|_{x=x_j} &= \frac{1}{\Delta x} \left(\mathcal{R}_{j+\frac{1}{2}}^m(\bullet) - \mathcal{R}_{j-\frac{1}{2}}^m(\bullet) \right) + \mathcal{O}(\Delta x^m) \\ &= \frac{1}{\Delta x} \sum_{l=-k}^r a_l (\bullet)_{j+l} + \mathcal{O}(\Delta x^m) \end{aligned} \quad (3.25)$$

where k, r define the stencil of the discrete operator and a_l are real constants. Space approximation operators can be written under a more compact form by introducing the averaging and differencing operators:

$$\mu(\bullet)_{j+\frac{1}{2}} \triangleq \frac{1}{2} ((\bullet)_{j+1} + (\bullet)_j) \quad \delta(\bullet)_{j+\frac{1}{2}} \triangleq (\bullet)_{j+1} - (\bullet)_j \quad (3.26)$$

For standard centered discretizations, that is for $r = k$ and $a_l = -a_{-l}$, and using the discretization operators (3.26), the space approximation operator of Eq. (3.25) can be written at 10th-order of accuracy under the more compact form [93, 126]:

$$\frac{\partial(\bullet)}{\partial x} = \frac{1}{\Delta x} \delta \mu \left(I - \frac{1}{6} \delta^2 + \frac{1}{30} \delta^4 - \frac{1}{140} \delta^6 + \frac{1}{630} \delta^8 \right) (\bullet) + \mathcal{O}(\Delta x^{10}) \quad (3.27)$$

with I being the identity operator. The above discretization uses an 11-point stencil and results from recursive corrections of the leading truncation error term of a low-order discretization. The corresponding 8th, 6th, 4th and 2nd-order approximations can be obtained by recursively suppressing the $\delta^8, \delta^6, \delta^4$ and δ^2 terms.

In conservative form, the semi-discrete – continuous in time, discrete in space – approximation of Eq. (3.1) can be written as:

$$\frac{\partial u}{\partial t} + \frac{1}{\Delta x} \left(F_{j+\frac{1}{2}}^p - F_{j-\frac{1}{2}}^p \right) = 0 \quad (3.28)$$

where the space discretization is expressed by the numerical flux $F_{j+\frac{1}{2}}^p$. Since the operator of Eq. (3.27) is purely dispersive, explicit artificial dissipation is introduced to the discretization for stability. High-order numerical dissipation terms are based on approximations of higher-order even derivatives. This numerical dissipation can be represented with a linear flux discretization operator \mathcal{D}^m :

$$\mathcal{D}_{j+\frac{1}{2}}^m(\bullet) = \delta \left(\delta^{m-2} \right) (\bullet)_j \quad (3.29)$$

so that the flux balance gives an approximation of an m th (even)-order derivative as:

$$\frac{1}{\Delta x} \left(\mathcal{D}_{j+\frac{1}{2}}^m(\bullet) - \mathcal{D}_{j-\frac{1}{2}}^m(\bullet) \right) = \Delta x^{m-1} \left. \frac{\partial^m(\bullet)}{\partial x^m} \right|_{x=x_j} \quad (3.30)$$

The coefficient Δx^{m-1} in the above equation ensures that the numerical flux is a consistent and high-order approximation of the convective derivative. An approximation of the space-associated part of Eq. (3.1) can then be expressed by the numerical flux:

$$\begin{aligned} F_{j+\frac{1}{2}}^p &= c \mathcal{R}_{j+\frac{1}{2}}^{p+1}(u) - |c| k_p \mathcal{D}_{j+\frac{1}{2}}^{p+1}(u) \\ &= c \mu \left(\sum_{l=0}^{(p-1)/2} b_l \delta^{2l} \right) u_j - |c| k_p \delta \left(\delta^{p-1} \right) u_j \end{aligned} \quad (3.31)$$

where p is an odd order of accuracy due to the introduction of the numerical dissipation term, as shown in Eq. (3.30). Above, b_l are the real coefficients of Eq. (3.27) and k_p is a real constant called the artificial dissipation coefficient. It is demonstrated in [126] that, for the specific choice $k_p = \frac{1}{2} b_{\frac{p-1}{2}}$, the numerical flux of Eq. (3.31) is equivalent to that of a non-compact upwind scheme. In that case, the discretization corresponds to the directional non-compact (DNC) family of schemes derived by A. Lerat and C. Corre in [126]. These are equivalent to high-order generalizations of the MUSCL reconstruction of B. Van Leer, based on Flux Extrapolation and without limiters (FE-MUSCL).

The idea of confinement is to introduce an additional nonlinear negative dissipation to balance the excess dissipation of the baseline numerical scheme. This nonlinear dissipation can be formulated as the operator:

$$\mathcal{C}_{j+\frac{1}{2}}^m(\bullet) = \mathcal{D}_{j+\frac{1}{2}}^m \left(\tilde{h}(\bullet) \right) = \delta \left(\delta^{m-2} \right) \tilde{h} \left((\bullet)_j, T(\bullet)_j \right) \quad (3.32)$$

which is referred to as the confinement term. Note that the operator of Eq. (3.32) is built on the same stencil as the operator \mathcal{D}^m of Eq. (3.29), using the harmonic mean \tilde{h} at each grid position, instead of the scalar variable u itself.

The numerical flux of the space discretization with confinement can be written as a sum of baseline convective flux discretization, artificial dissipation and the confinement correction. At p^{th} (odd)-order of accuracy this is:

$$\begin{aligned} F_{j+\frac{1}{2}}^p &= c \mathcal{R}_{j+\frac{1}{2}}^{p+1}(u) - |c| k_p \mathcal{D}_{j+\frac{1}{2}}^{p+1}(u) + |c| \varepsilon \mathcal{D}_{j+\frac{1}{2}}^{p+1}(\tilde{h}(u)) \\ &= c \mu \left(\sum_{l=0}^{(p-1)/2} b_l \delta^{2l} \right) u_j - |c| k_p \delta \left(\delta^{p-1} \right) u_j + |c| \varepsilon \delta \left(\delta^{p-1} \right) \tilde{h}(u_j, Tu_j) \end{aligned} \quad (3.33)$$

where the confinement term is multiplied by the confinement parameter ε . To ensure a scaling of the confinement correction at higher orders of accuracy, the confinement parameter can be taken $\varepsilon \propto k_p$. Since the operator \mathcal{D}^m is linear and the coefficients k_p , ε are constant in space, the numerical flux of Eq. (3.33) can also be written in the more compact form:

$$F_{j+\frac{1}{2}}^p = c \mathcal{R}_{j+\frac{1}{2}}^{p+1}(u) - |c| \mathcal{D}_{j+\frac{1}{2}}^{p+1} \left(k_p u - \varepsilon \tilde{h}(u) \right) \quad (3.34)$$

in which case the added computational cost of confinement is practically reduced to the cost of the calculation of the harmonic mean of Eq. (3.8).

For the linear flux discretization of Eq. (3.31) the scheme will be referred to as the baseline p^{th} -order FE-MUSCL scheme (FE-MUSCL $_p$) whereas for the nonlinear flux discretization of Eq. (3.33) it will be referred to as the p^{th} -order FE-MUSCL scheme with confinement (FE-MUSCL $_p$ -C).

The semi-discrete approximation of Eq. (3.28) can be equally represented by its equivalent partial differential equation, which is representative of the numerical error of the discretized problem. For the p^{th} (odd)-order flux discretization of Eq. (3.33) this is written:

$$\frac{\partial u}{\partial t} + c \frac{\partial u}{\partial x} = |c| \Delta x^p \left(k_p \frac{\partial^{p+1} u}{\partial x^{p+1}} - \varepsilon \frac{\delta^{p+1} \tilde{h}(u_j, Tu_j)}{\Delta x^{p+1}} \right) + c b_{\frac{p+1}{2}} \Delta x^{p+1} \frac{\partial^{p+2} u}{\partial x^{p+2}} \quad (3.35)$$

where the harmonic mean has been kept intact for simplicity. Above, the leading truncation error term is of dissipative nature since the FE-MUSCL discretizations (3.31), (3.33) are odd-order accurate. This leading dissipation term is driven by the nonlinear balance between the operators \mathcal{D}^m and \mathcal{C}^m . The second term of the right-hand side represents the leading dispersive error term, which comes from the discretization operator \mathcal{R}^m . Note however that the harmonic mean term is nonlinear and therefore its expansion yields mixed dispersive, dissipative and even singular error terms that cannot be straightforwardly analyzed [45]. This mixed nature of the harmonic mean will be further discussed in Sections 3.3 and 3.4.

The construction of confinement corrections has been presented here for standard centered space discretization operators, i.e. operators of optimal order of accuracy on the given stencil. The numerical flux formulation is not however restricted to this case. In principle, any dissipation operator \mathcal{D}^m can be used in the numerical flux (3.33), using the present approach. The confinement correction should be adapted to the baseline numerical dissipation as long as both are based on the same dissipation operator.

3.2.4 Discussion of the coupled and uncoupled approaches

At this point, some differences should be discussed between the design principle of confinement for FE-MUSCL and Lax-Wendroff/Warming-Beam schemes.

- Schemes of the LW and WB families involve coupled discretization in space and time. Since the confinement correction is based on the scheme's leading truncation error term, it inherits two characteristics:

- It is space-time coupled, introducing anti-dissipation adapted to both the space and time discretization.
- It is naturally adapted to the reduced dissipation error of the scheme at higher orders of accuracy.
- For decoupled FE-MUSCL schemes, the confinement correction is constructed based on a high-order centered dissipation operator. This operator is the same as for the baseline numerical dissipation. As a result:
 - The anti-dissipation of the confinement correction is related only to space discretization.
 - The confinement correction is adapted to the response function of the baseline scheme's dissipation operator. This will be further evaluated in Section 3.4, by means of a spectral analysis study. The scaling of the confinement correction at higher orders of accuracy is then ensured by taking $\varepsilon \propto k_p$.

Furthermore, the confinement correction requires the calculation of an additional term, that involves a large stencil at higher orders. For LW/WB schemes, confinement is introduced in the place of a truncation error correction (see Eq. (3.22)). The dissipation reduction should thus be comparable to increasing the scheme's order of accuracy by one. For decoupled FE-MUSCL schemes however, the increase of computational cost can be considerably reduced through the numerical flux form (3.34), for a linear dissipation operator and constant k_p , ε in space.

3.3 Analytical spectral analysis based on linear theory

A more detailed analysis of numerical error can be performed in terms of the scheme's resolvability in the wavenumber space, also referred to as its spectral properties. Such an analysis is very informative as it expresses the accuracy of the schemes in terms of spatial frequency, or equivalently depending on the mesh resolution of the advected wave. Furthermore, it permits a separation of numerical error in terms of dispersion (phase approximation) and dissipation. The present section consists in a spectral analysis of the schemes presented in Section 3.2, by application of linear theory.

3.3.1 Fourier analysis of numerical discretizations

We first consider the general form of sinusoidal wave solutions of the continuous Eq. (3.1):

$$u_{e,k}(x, t) = \hat{u}_k(0) e^{ik(x-ct)} \quad (3.36)$$

where k is the wavenumber and $\hat{u}_k(t)$ is the solution amplitude. The subscript e is used to denote the exact solution of the linear transport equation. On a discrete uniform grid with spacing Δx ($x_j = j \Delta x$, $j \in \mathbb{Z}$) this exact solution is written:

$$u_{e,k}(x_j, t) = \hat{u}_k(0) e^{i\xi(j - \frac{ct}{\Delta x})} = \hat{u}_k(0) e^{-i\frac{ct}{\Delta x}\xi} e^{ij\xi} \quad (3.37)$$

where $\xi = k \Delta x$ is the reduced wavenumber.

For decoupled schemes in space time, where the space and time discretizations are independent, the semi-discrete form of the linear transport equation can be written under a single space approximation operator $\mathcal{S}(\bullet)$ as:

$$\frac{\partial u}{\partial t} = \mathcal{S}(u_j) \iff \frac{\partial u}{\partial t} = -\frac{1}{\Delta x} \left(F_{j+\frac{1}{2}}^p - F_{j-\frac{1}{2}}^p \right) \quad (3.38)$$

A general discrete harmonic:

$$u_k(x_j, t) = \hat{u}_k(t) e^{ij\xi} \quad (3.39)$$

is a solution of the semi-discrete Eq. (3.38) when:

$$\frac{\partial \hat{u}_k(t)}{\partial t} = \Omega(\xi) \hat{u}_k(t) \iff \hat{u}_k(t) = \hat{u}_k(0) e^{\Omega(\xi)t} \quad (3.40)$$

where $\Omega(\xi)$ is the Fourier symbol (or equivalently the eigenvalues) of the space discretization. For an explicit space discretization operator $\mathcal{S}(\bullet)$, i.e. for an explicit flux discretization $F_{j+\frac{1}{2}}^p$, the Fourier symbol results from [93, 211]:

$$\Omega(\xi) e^{ij\xi} = \mathcal{S}(e^{ij\xi}) \quad (3.41)$$

Taking advantage of Eq. (3.41), Eq. (3.40) gives the complex amplitude for which the harmonic (3.39) is a solution of Eq. (3.38):

$$\hat{u}_k(t) = \hat{u}_k(0) e[\mathcal{S}(e^{ij\xi})/e^{ij\xi}]t \quad (3.42)$$

expressed through the space discretization operator. If the operator $\mathcal{S}(\bullet)$ is linear, the amplitude can be expressed as a function of the modified wavenumber $\xi^* = \xi^*(\xi)$ of the space discretization as:

$$\hat{u}_k(t) = \hat{u}_k(0) e^{-i \frac{ct}{\Delta x} \xi^*} \quad (3.43)$$

The semi-discrete solution (3.39) then writes:

$$u_k(x_j, t) = \hat{u}_k(0) e^{-i \frac{ct}{\Delta x} \xi^*} e^{ij\xi} \quad (3.44)$$

From a comparison with the exact solution (3.37) it is clear that the modified wavenumber ξ^* expresses the differencing error of the space discretization in the wavenumber space. The equivalent of Eq. (3.44) for the Fourier symbol Ω can be obtained if the amplitude $\hat{u}_k(t)$ is expressed directly using Eq. (3.40).

Since the exact solution corresponds to $\xi^* = \xi$, $|Re(\xi^*) - \xi|/\pi$ can be used as a measure of dispersion or phase approximation error and $Im(\xi^*)$ can be used as a measure of dissipation of the flux discretizations $F_{j+\frac{1}{2}}^p$ compared to the exact solution.

The analysis is similar for coupled schemes in space and time, such as the Lax-Wendroff and Warm-ing Beam schemes described in Sections 3.2.1 and 3.2.2. In this case, we are considering the complete numerical scheme, that is the discretization of Eq. (3.1) in both time and space.

Considering a general discrete harmonic (3.39), the error of the fully discrete numerical approximation of the form (3.16) can be expressed through the amplification factor $G = G(\xi)$:

$$G \triangleq \frac{\hat{u}_k(t + \Delta t)}{\hat{u}_k(t)} \quad (3.45)$$

which expresses the ratio between the complex amplitude of the solution between two subsequent time steps n and $n + 1$. Its relation to the modified wavenumber, i.e. the space discretization error, can be obtained by substituting the complex amplitude in the above equation using (3.43):

$$G = e^{-i\sigma\xi^*} \quad (3.46)$$

Since ξ^* is a complex function of ξ , the amplification factor is usually separated to amplitude and phase as:

$$G = |G| e^{-i\sigma\omega(\xi)} \quad (3.47)$$

where $\omega(\xi) = -(1/\sigma) \arg G$. For the exact solution, the amplification factor is $G_e = e^{-i\sigma\xi}$. Under the form (3.47), the phase approximation error can then be expressed as the difference $\xi - \omega(\xi)$ and the dissipation error can be expressed as $1 - |G|$.

3.3.2 Linear spectral analysis of schemes with confinement

The modified wavenumber for linear space discretization schemes can be derived by following the above procedure and writing the semi-discrete solution in the form of Eq. (3.44). For linear discretizations both in space and time, the amplification factor of the scheme can be written in the form of Eq. (3.46).

It is not straightforward though to do the same for schemes with confinement, because the confinement correction is intrinsically non-linear. Confinement schemes can however be linearized using exponent functions, which behave like eigenfunctions for the harmonic mean on a uniform grid. For a single harmonic on a uniform grid with spacing Δx ($x_j = j \Delta x$, $j \in \mathbb{Z}$) and a time step Δt ($t = n \Delta t$, $n \in \mathbb{Z}$) the harmonic mean simplifies to:

$$\left(\tilde{h}(u)\right)_j^n = \tilde{h}(u_j^n, T u_j^n) = \left[\frac{1}{2} \left(\frac{1}{u_j^n} + \frac{1}{u_{j-1}^n}\right)\right]^{-1} = \frac{2}{1 + e^{i\xi}} u_j^n \quad (3.48)$$

where $u_j^n = u_k(x_j, t) = \hat{u}_k(t) e^{ij\xi}$ and the factor $2/(1 + e^{i\xi})$ is independent of the position j on the computational grid. Taking advantage of Eq. (3.48), nonlinear discretizations with confinement can be now analyzed as described in Section 3.3.1.

For linear time-space coupled schemes of the Lax-Wendroff family (LW p), the amplification factor is [53]:

$$G_{LWp}(\xi) = 1 - \sigma \left(1 - e^{-i\xi}\right) \left[1 + \sum_{r=1}^{p-1} \zeta_{r+1} \sum_{l=0}^r (-1)^l C_r^l e^{i(m-l)\xi}\right] \quad (3.49)$$

with ζ and m given by (3.20)-(3.21). Eq. (3.49) yields the amplification factor for both odd- and even-order schemes. For schemes of the Lax-Wendroff family with confinement (LW p -C), as in the flux discretization of Eq. (3.22), the amplification factor becomes:

$$G_{LWp-C}(\xi) = 1 - \sigma \left(1 - e^{-i\xi}\right) \left[1 + \sum_{r=1}^{p-1} \zeta_{r+1} \sum_{l=0}^r (-1)^l C_r^l e^{i(m-l)\xi} + \varepsilon \frac{2}{1 + e^{i\xi}} \zeta_{p+1} \sum_{l=0}^p (-1)^l C_p^l e^{i(\lfloor \frac{p+1}{2} \rfloor - l)\xi}\right] \quad (3.50)$$

where p is an odd order. The amplification factor G_{LWp-C} includes an additional term corresponding to the confinement correction. This term is the same as for the linear truncation error correction used to increase the scheme order to $p + 1$, but with an additional factor due to the harmonic mean linearization.

The linearization (3.48) can also be used for the FE-MUSCL flux discretizations with confinement (FE-MUSCL p -C). In this case, the contribution of each term in Eq. (3.33) can be straightforwardly separated. The modified wavenumber of the space discretization at p th-(odd) order of accuracy is finally given by:

$$\begin{aligned} \xi_p^*(\xi) &= \sum_{l=0}^{(p-1)/2} b_l \left(\sum_{q=1}^{l+1} \eta_{l,q} \sin(q\xi)\right) - i 2^{\frac{p+1}{2}} (-1)^{\frac{p+1}{2}} k_p (\cos \xi - 1)^{\frac{p+1}{2}} \\ &+ 2^{\frac{p+1}{2}} (-1)^{\frac{p+1}{2}} \varepsilon \sin \xi \frac{(\cos \xi - 1)^{\frac{p+1}{2}}}{\cos \xi + 1} + i 2^{\frac{p+1}{2}} (-1)^{\frac{p+1}{2}} \varepsilon (\cos \xi - 1)^{\frac{p+1}{2}} \end{aligned} \quad (3.51)$$

where b_l are the coefficients of Eqs. (3.27), (3.31) and η are the real coefficients of the expanded centered difference operators of Eq. (3.27), given by:

$$\delta\mu(\delta^m(\bullet)_j) = \sum_{q=1}^{1+(m/2)} \eta_{m,q}(\bullet)_{j+q} - \eta_{m,q}(\bullet)_{j-q} \quad (3.52)$$

and presented in Table 3.1. Note that since the FE-MUSCL space discretization is decoupled from time integration, the modified wavenumber is independent of the time step or the CFL number. The first term in Eq. (3.51) is related to the centered space discretization operator \mathcal{R}^m , the second to the explicit artificial dissipation operator \mathcal{D}^m and the last two are related to the nonlinear confinement correction \mathcal{C}^m . By suppressing the terms associated with ε in Eq. (3.51), the expression of ξ^* for the baseline p th-order FE-MUSCL flux discretizations of Eq. (3.31) is recovered.

Table 3.1: Coefficients $\eta_{m,q}$ in Eq. (3.52)

m	$q = 1$	$q = 2$	$q = 3$	$q = 4$	$q = 5$
0	1				
2	-2	1			
4	5	-4	1		
6	-14	14	-6	1	
8	42	-48	27	-8	1

Eq. (3.51) demonstrates that dissipation derives only from the artificial dissipation and confinement terms. It also shows that the nonlinear character of the confinement term produces an additional effect on the dispersion error of the scheme, i.e. on $Re(\xi^*)$, even though the operator \mathcal{C}^m is originally based on an even difference. The same occurs for confinement corrections for coupled Lax-Wendroff schemes, as the factor $2/(1 + e^{i\xi})$ in (3.50) yields a contribution to both dispersion and dissipation.

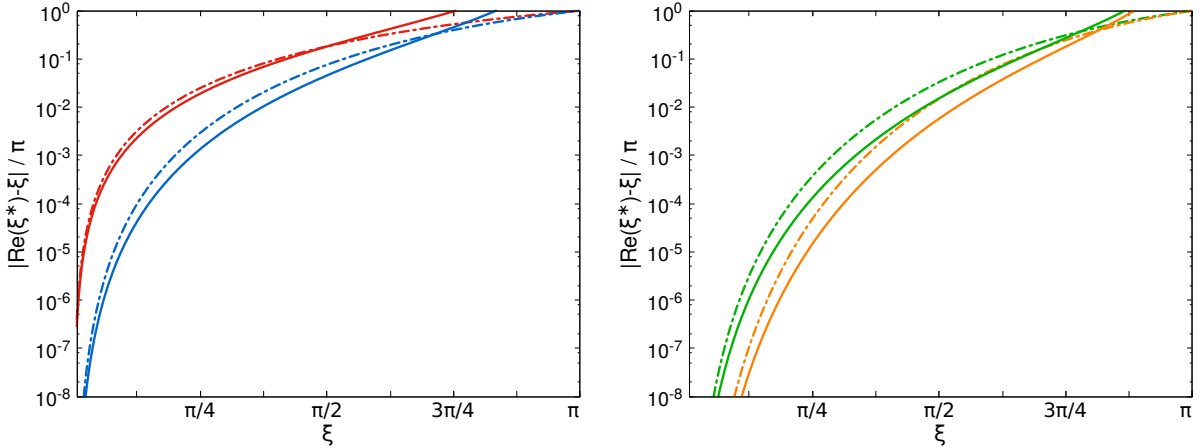


Figure 3.1: Relative dispersion error of FE-MUSCL schemes evaluated from linear spectral analysis. 1st-order: —, 3rd-order: —, 5th-order: —, 7th-order: —. Baseline version of the schemes (dash-dotted lines) and with confinement correction (solid lines), $\varepsilon = 1.14 k_p$.

Fig. 3.1 compares the dispersive properties of FE-MUSCL-C confinement schemes with the corresponding baseline FE-MUSCL schemes up to 7th-order of accuracy. The confinement parameter is taken $\varepsilon = 1.14 k_p$, but similar trends are obtained for values of ε at the same order of magnitude. FE-MUSCL schemes with confinement are shown to have decreased phase approximation error compared to their linear counterparts at least up to the grid resolvability limit $\xi = \pi/2$ for all orders of accuracy.

However, linear theory predicts a highly unstable behavior of both FE-MUSCL and Lax-Wendroff schemes, when an anti-dissipative confinement correction is added. This is more clearly seen analytically for the case of decoupled FE-MUSCL schemes. In Eq. (3.51), the effect of confinement on dissipation is depicted as equivalent to a linear artificial dissipation, its nonlinear effect appearing only in phase approximation. As a result, FE-MUSCL schemes with confinement are predicted as stable only for $\varepsilon \leq k_p$, where $Im(\xi^*) \leq 0$. For $\varepsilon > k_p$ they are predicted as unstable in the complete wavenumber range, though this is not in agreement with extensive numerical experiments which

have verified the stability of confinement schemes for such values [42, 44, 45]. This discrepancy might be a result of the linearization of Eq. (3.48), which permits the application of linear stability theory, but does not appear to accurately represent the nonlinear mechanism of the confinement correction.

3.4 Numerical quasi-linear spectral analysis

This section focuses on a quasi-linear spectral analysis approach, with the view to obtaining an improved representation of the properties of schemes with a nonlinear confinement correction. This approach was originally applied by S. Pirozzoli [160] for the study of non-linear shock capturing schemes. Its results were shown to be improved compared to conventional analyses and in general agreement with observations from the schemes' application in numerical experiments.

3.4.1 Description of the method

The numerical method of S. Pirozzoli can be used to evaluate the modified wavenumber of a space discretization scheme via application to the short-time advection of a series of monochromatic initial conditions. The basis of this approach is the relation of the scheme's modified wavenumber to the computed solution in the case of a sinusoidal monochromatic initial condition.

On a uniform grid with spacing Δx ($x_j = j \Delta x$, $j \in \mathbb{Z}$), sinusoidal monochromatic conditions can be written:

$$u_\xi(x_j, t) = \hat{u}_\xi(t) e^{ij\xi} \quad (3.53)$$

The Discrete Fourier Transform (DFT) $\bar{u} = \bar{u}(\xi, t)$ is defined as:

$$\bar{u}(\xi, t) \triangleq \frac{1}{N} \sum_{j=0}^{N-1} u_j(t) e^{-ij\xi} \quad (3.54)$$

where $u_j(t) = u_\xi(x_j, t)$.

We then consider only wavenumbers $\xi = 2\pi n/N$, $n = 0, \dots, N/2$, which result in periodic initial conditions of the type (3.53) on a grid with points $j = 0, \dots, N$. For a single harmonic of the type (3.53), the DFT \bar{u} is the complex amplitude (3.43) of the solution. For a numerical approximation of this solution after time τ , the DFT is thus equal to:

$$\begin{aligned} \bar{u}_\xi(\xi, \tau) &= \hat{u}_\xi(\tau) \\ &= \hat{u}_\xi(0) e^{-i \frac{c\tau}{\Delta x} \xi^*} \end{aligned} \quad (3.55)$$

provided that the time τ is sufficiently small to exclude time integration error and ensure that the solution at time τ remains monochromatic. Above, $\xi^* = \xi^*(\xi)$ is the modified wavenumber which expresses the error due to the space approximation (see Section 3.3.1). It follows from (3.55) that:

$$\bar{u}_\xi(\xi, 0) = \hat{u}_\xi(0) \quad (3.56)$$

Inserting (3.56) in (3.55) and for time τ corresponding to a single time step, the modified wavenumber can be expressed as:

$$\xi^*(\xi) = -\frac{1}{i\sigma} \ln \left(\frac{\bar{u}_\xi(\xi, \tau)}{\bar{u}_\xi(\xi, 0)} \right) \quad (3.57)$$

where σ is the CFL number.

The relation (3.57) can be used to numerically evaluate the modified wavenumber of a space discretization scheme in the calculation of a single harmonic. It can thus be recursively applied for a series of harmonics to evaluate the modified wavenumber of the scheme in the complete wavenumber range. This process is described in Algorithm 3.2. For an unlimited computational domain, or periodic boundary conditions, this approach includes the nonlinear characteristics of the space discretization. It should be however noted that it does not account for nonlinear mode interactions occurring at later times [160].

Algorithm 3.2 Numerical evaluation of modified wavenumber

- 1: **loop** $n \{n \in \mathbb{Z} : 0 \leq n \leq N/2\}$
- 2: Initialize a sinusoidal monochromatic condition with reduced wavenumber $\xi_n = 2\pi n/N$
- 3: Compute the DFT $\overline{u_{\xi_n}}(\xi_n, 0)$ of the initial condition from (3.54)
- 4: Apply the scheme to compute the solution $u_{\xi_n}(x_j, \tau)$ after one time step
- 5: Compute the DFT $\overline{u_{\xi_n}}(\xi_n, \tau)$ of the computed condition from (3.54)
- 6: Use (3.57) to derive the modified wavenumber $\xi^*(\xi_n)$

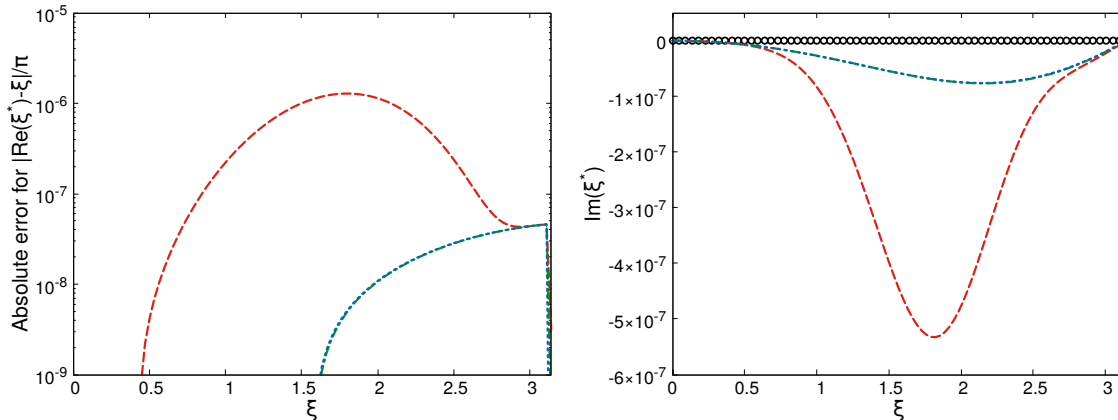


Figure 3.2: Convergence of the numerical spectral analysis method by the CFL number, in terms of prediction of dispersion (left) and dissipation (right). Exact/analytical: \circ , $\sigma = 1e-1$: $---$, $\sigma = 1e-2$: $- \cdot -$, $\sigma = 1e-5$: \dots . Purely centered linear fourth-order scheme and RK4 time integration.

3.4.2 Validation and study of numerical precision

First, the numerical method is validated on the analysis of the spectral properties of a linear space discretization scheme. The selected scheme is a purely centered fourth-order discretization operator of the form (3.27). It corresponds to the numerical flux of Eq. (3.31) for $p = 3$, without the dissipation operator ($k_3 = 0$). Since it includes no numerical dissipation or confinement terms, it has exactly zero dissipation in the complete wavenumber range. Furthermore, since the scheme is linear, its exact modified wavenumber is given analytically from Eq. (3.51).

The modified wavenumber of the scheme is then calculated numerically, as described in Algorithm 3.2. Time integration is performed with a 4-step Runge-Kutta algorithm (RK4). The prediction of the numerical method is compared to the scheme's analytical properties to quantify the effect of time integration and evaluate the precision of the numerical results.

The errors of the numerical method with respect to the exact spectral properties of the scheme are presented in Fig. 3.2. Results show that these errors remain low in the complete wavenumber range, both for dispersion and for dissipation. Furthermore, convergence is quickly achieved with a reduction of the CFL number. These low errors and fast convergence are respectively related to the precision and the fourth-order accuracy of the RK algorithm. Errors introduced by the time integration can however be important for time integration algorithms of lower precision. The rest of the studies of this section using the numerical method were performed at a CFL number $\sigma \leq 1e-4$. For the example of the purely centered fourth-order accurate scheme, this corresponds to a maximum error $E_{max} < 10^{-7}$ compared to the analytical solution, in the complete wavenumber range (Fig. 3.2).

3.4.3 Spectral properties of schemes with confinement

Following its validation, the numerical approach has been applied to the evaluation of the spectral properties of schemes with confinement. This evaluation has been performed for confinement schemes based on both the space-time coupled Lax-Wendroff and the decoupled FE-MUSCL

schemes. Interestingly, the numerically evaluated spectral properties are equivalent between the two families, both for their linear versions and with the confinement correction. This is due to the numerical method requiring a very small time step, in turn causing many time-coupled terms to vanish for schemes of the Lax-Wendroff family.

This can also be verified analytically. For a p th-order baseline scheme of the Lax-Wendroff family, the leading truncation error term is given by:

$$c \zeta_{p+1} \Delta x^p \frac{\partial^{p+1} u}{\partial x^{p+1}} \quad (3.58)$$

as shown by the equivalent differential equation (3.23). The products ζ , given by Eq. (3.20), are $\mathcal{O}(1)$ when $\sigma \propto \mathcal{O}(1)$. It is not however the same in the general case when $\sigma \propto \mathcal{O}(\Delta x^\alpha)$, or equivalently when the time step Δt is related to the mesh size as $\Delta t \propto \Delta x^{\alpha+1}$. The products ζ can be expanded as:

$$\zeta_{p+1} = \prod_{q=2}^{p+1} (-1)^q \frac{\lfloor \frac{q}{2} \rfloor - (-1)^q \sigma}{q} = \prod_{q=2}^{p+1} (-1)^q \frac{\lfloor q/2 \rfloor}{q} + \dots \quad (3.59)$$

with the omitted terms being $\mathcal{O}(\Delta x^\alpha)$ and higher, in turn giving error terms of order $\mathcal{O}(\Delta x^{p+\alpha})$ and higher in Eq. (3.58). For $\alpha \geq 1$, the leading truncation error term (3.58) can then be written:

$$c \prod_{q=2}^{p+1} (-1)^q \frac{\lfloor q/2 \rfloor}{q} \Delta x^p \frac{\partial^{p+1} u}{\partial x^{p+1}} + \dots = c \beta \Delta x^p \frac{\partial^{p+1} u}{\partial x^{p+1}} + \dots \quad (3.60)$$

where the coefficient β is introduced to simplify the form of the equation. Notice that $\beta = k_p = \frac{1}{2} b_{\frac{p-1}{2}}$ for an odd order p (where the leading error term is dissipative) and that $\beta = b_{\frac{p+1}{2}}$ for an even order p (where the leading error term is dispersive). The coefficients k_p , $b_{\frac{p+1}{2}}$ are respectively the artificial dissipation coefficient and the real coefficient of the leading dispersive error term, as in Eq. (3.35). For $\sigma \ll 1$, the leading error term (3.60) – both for a dispersive and dissipative nature – is thus the same as in the case of FE-MUSCL schemes. The same is true for Lax-Wendroff schemes with a confinement correction. Following results of the numerical spectral analysis are thus presented for the case of decoupled FE-MUSCL schemes.

A comparison of the numerical approach with linear analysis results is presented in Fig. 3.3 for the 3rd-order FE-MUSCL scheme. Again, the numerical method is in excellent agreement with the analytical prediction for the linear version of the scheme, without confinement. Results are however different for the nonlinear version of the scheme, which linear theory predicts as unstable in the complete wavenumber range (see Section 3.3.2). The numerical method shows that the scheme with confinement is stable and has reduced dissipation compared to the linear version. Furthermore, the confinement correction is shown to extend the well-resolved wavenumber range compared to the baseline version, in terms of both dissipation and phase approximation. The latter is not obvious, as the confinement correction in Eq. (3.33) is originally based on a dissipative operator. This mixed dispersive/dissipative effect of the confinement correction is related to the nonlinear harmonic mean, and is even depicted in the harmonic mean linearization (3.48) for the case of a single harmonic.

Fig. 3.3 also shows that results of the numerical spectral analysis for confinement schemes are not smooth in the complete wavenumber range. Specifically, the effect of confinement appears to be slightly reduced for an initial condition corresponding to certain distinct spatial frequencies. There exists however a specific set of wavenumbers $\mathbf{P} = \{\pi/2, 3\pi/4, 4\pi/5, 9\pi/10\}$ for which the effect of confinement is exactly zero. These are all equal or greater than the grid resolvability limit $\pi/2$ posed by the Nyquist-Shannon theorem, corresponding to a resolution of four points per wavelength. For wavenumbers of \mathbf{P} , the discrete initial condition is such that the harmonic mean (3.8) results to $\tilde{h}(u_j, Tu_j) = 0$, $\forall j \in \{0, 1, \dots, N\}$. In this case, the total contribution of confinement vanishes and the flux discretization of Eq. (3.33) degrades to the baseline FE-MUSCL of Eq. (3.31). As a

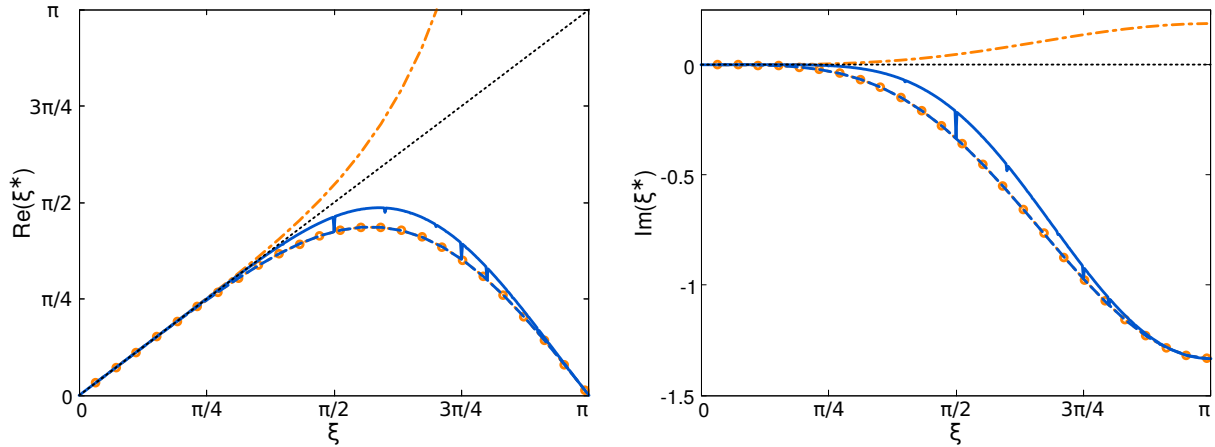


Figure 3.3: Comparison of the numerical method with linear analysis results for the 3rd-order FE-MUSCL scheme ($\varepsilon = 1.14 k_p$). Spectral accuracy: \cdots , analytical - linear scheme: $-\circ-$, analytical - confinement: $-\circ-$, numerical - linear scheme: $-\cdot-$, numerical - confinement: $-\bullet-$.

result, the spectral properties of the scheme with confinement are reduced to the ones of the linear version for $\xi \in \mathcal{P}$. This weakness of confinement however refers to single harmonics and has not been observed in general problems, since frequencies higher than $\pi/2$ are under-resolved and should in any case be damped by the numerical scheme's dissipation.

The phase approximation and relative dispersion error of FE-MUSCL schemes with and without confinement up to 9th-order of accuracy are presented in Fig. 3.4. Naturally, higher-order schemes are shown to provide a good approximation of the exact solution for a wider range of wavenumbers. Results also show that the effect of confinement is not restricted to a low-order discretization, but improves the phase approximation of the scheme even at higher order of accuracy. The difference introduced by the confinement correction is smaller as the order increases, in line with the reduced numerical error of the baseline scheme. Also, since for wavenumbers $\xi \in \mathcal{P}$ the scheme reduces to its linear version due to the harmonic mean, this effect is observed for the same wavenumbers at all orders of accuracy. It should also be noted that optimized schemes in the wavenumber space may achieve improved resolution of higher frequencies at the expense of higher dispersion error compared to standard schemes at very low wavenumbers [50]. Fig. 3.4 however shows that the confinement correction introduces a reduction of dispersion error in the complete wavenumber range.

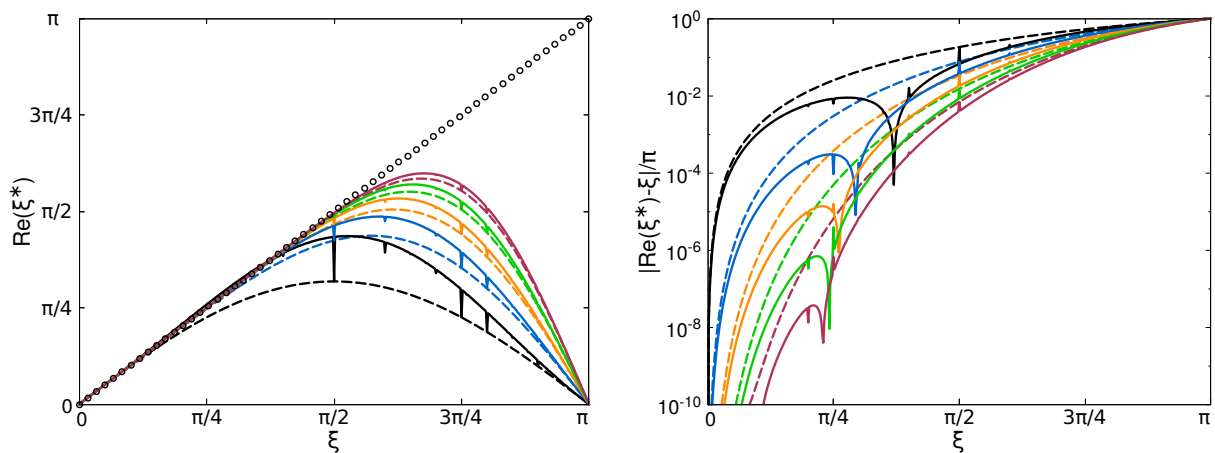


Figure 3.4: Phase approximation and relative dispersion error for FE-MUSCL schemes. Spectral accuracy: \circ , 1st-order: $-\bullet-$, 3rd-order: $-\bullet-$, 5th-order: $-\bullet-$, 7th-order: $-\bullet-$, 9th-order: $-\bullet-$. Baseline version of the schemes (dashed) and with confinement correction (solid), $\varepsilon = 1.14 k_p$.

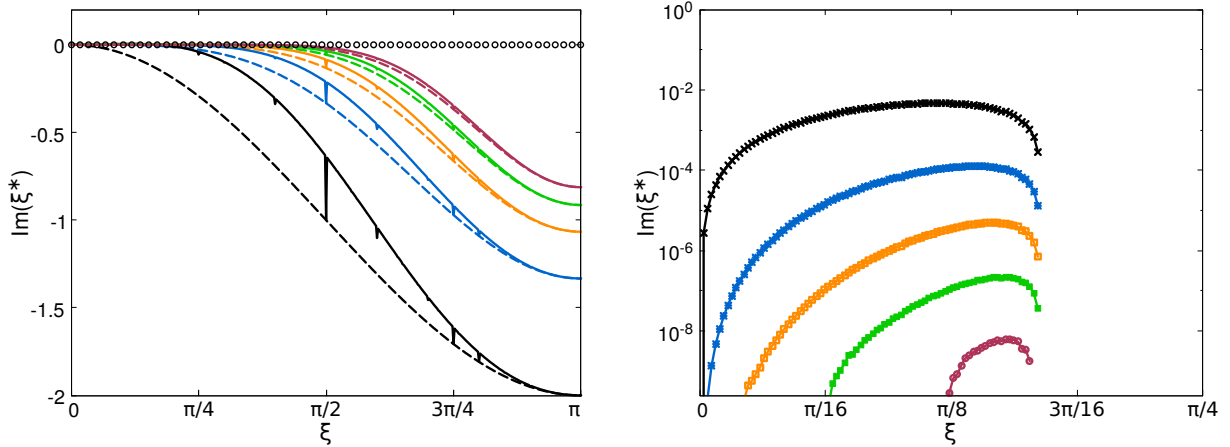


Figure 3.5: Dissipation of FE-MUSCL schemes and detail of slightly positive values in the low-wavenumber range. Spectral accuracy: \circ , 1st-order:—, 3rd-order:—, 5th-order:—, 7th-order:—, 9th-order:—, Baseline version of the schemes (dashed) and with confinement correction (solid), $\varepsilon = 1.14 k_p$.

The dissipation properties of the same schemes are shown in Fig. 3.5. Results show that schemes with confinement have effectively reduced dissipation at all orders of accuracy, similar to the improvement in terms of dispersive error. Again, the confinement correction introduces anti-dissipation adapted to the high-order numerical dissipation of the baseline scheme, as the two are based on the same operator (Eq. (3.33)). Its effect is thus smaller at higher orders of accuracy. Furthermore, confinement can also achieve the preservation of asymptotic solution over arbitrarily long distances [45, 47], a non-linear property which is not taken into account by the present analysis but cannot be achieved even for high-order baseline schemes (see also Section 3.5). Schemes with confinement also appear to be stable at all orders, contrary to the linear analysis results of the previous section. Finally, it is important to note that the negative dissipation introduced by the confinement correction is shown to decrease progressively at high frequencies and does not affect the damping of the shortest wavelength $\xi = \pi$, which is associated to grid-to-grid oscillations.

Fig. 3.5 however shows that schemes with confinement may display slightly positive values in the imaginary part of the modified wavenumber. Such positive values correspond to an augmentation of the signal amplitude, or equivalently to unstable behavior. They are observed in the low wavenumber range and do not occur for $\varepsilon \leq k_p$, whereas their magnitude is rapidly decreased for an increasing order of accuracy. Furthermore, Fig. 3.5 shows that these positive values are observed up to an upper frequency bound that is similar at all orders of accuracy. This bound has in fact been found to be driven by the value of the confinement parameter ε . It is interesting to consider this alongside the nonlinear mechanism of schemes with confinement, which are known to be able to propagate asymptotic pulse solutions over arbitrary distances. These solutions correspond to a signal shape that is defined by the value of ε (see Section 3.5.1). For a signal that is wider than the asymptotic shape, confinement introduces anti-dissipation and compresses the signal to counter the baseline dissipation, which corresponds to an increase in the solution amplitude. After the signal reaches the asymptotic shape, the confinement correction decreases in magnitude so as to allow numerical dissipation to relax the signal and avoid divergence. This mechanism and the asymptotic solution are likely related to the upper bound up to which positive $Im(\xi^*)$ values are obtained, as both depend on the value of the confinement parameter ε . Moreover, these slightly positive values are not necessarily translated to an instability of the numerical scheme. In fact, previous studies using Lax-Wendroff schemes with confinement were regularly performed using $\varepsilon > 1$, while showing no unstable behavior [42, 44, 45]. This subject is further investigated in Section 3.5, by application of the schemes to a series of long-distance advection studies.

The isolated contribution of the confinement correction to the dispersion and dissipation of

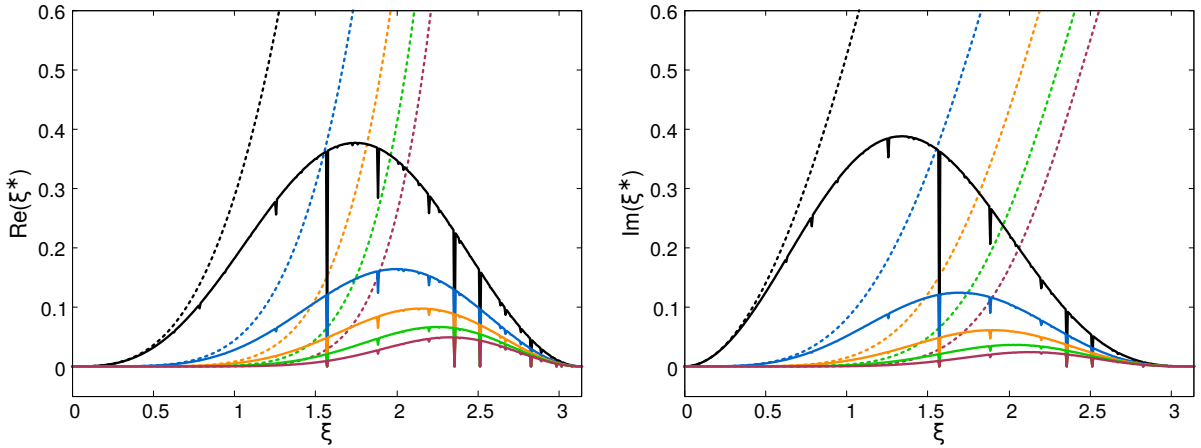


Figure 3.6: Confinement contribution to phase approximation (left) and dissipation (right) for the case of decoupled FE-MUSCL schemes. 1st-order:—, 3rd-order:—, 5th-order:—, 7th-order:—, 9th-order:—. Spectral properties predicted by the numerical method in solid lines and by a linear spectral analysis in dotted lines, $\varepsilon = 1.14 k_p$.

the schemes is shown in Fig. 3.6. Results are presented for both the linear spectral analysis and the numerical method at different orders of accuracy. It is clear that the linear analysis gives a significant overprediction of the effect of confinement compared to the numerical method. Since the linearization (3.48) is exact, the discrepancy is possibly related to the use of the discrete harmonic mean function (3.8), rather than its continuous version which is considered in the linear spectral analysis. More importantly however, the results of the numerical method show that as the order increases, the anti-dissipation of the confinement correction is transferred to higher frequencies, having a reduced effect on the well-resolved wavenumber range. This is a result of basing the confinement correction on a high-order dissipation operator. Moreover, the effect of confinement on dispersion is displaced towards higher wavenumbers compared to its effect on dissipation.

An additional remark should also be made on the dispersive effect of the nonlinear confinement correction. This effect is favorable (Fig. 3.4) because the confinement correction is constructed on a high-order dissipative operator. It would no longer be the case for a low-order standard operator or, more precisely, for an operator with reduced spectral resolution. The dissipative effect of confinement should still be positive, as long as the same operator is used for both the scheme's dissipation and the confinement correction. Its dispersive effect is however uncoupled from the baseline phase approximation for a flux discretization in the form of Eq. (3.33). As a result, the use of a low-resolution dissipative operator for the confinement correction alongside a high-resolution dispersive operator would lead to a degradation of the baseline scheme's phase approximation in the low-wavenumber range (Fig. 3.6).

Finally, the sensitivity of the spectral properties to the choice of the confinement parameter ε is assessed by means of a parametric analysis. The phase approximation and dissipation of the scheme are shown in Fig. 3.7 for six equidistant values of the confinement parameter, ranging from $\varepsilon = 0.4 k_p$ to $\varepsilon = 1.4 k_p$. Results are straightforward in the sense that a larger confinement parameter leads to a larger effect on the scheme's resolution. It is interesting however to note that the sensitivity of the spectral properties to the value of ε is smaller at higher orders of accuracy. This is related both to ε being taken proportionate to the artificial dissipation coefficient and to the use of a high-order dissipation operator for the confinement correction.

3.4.4 Accuracy limit

The accuracy of the numerical schemes can be quantified by comparing their resolvability limit in the wavenumber space, or equivalently by computing the maximum wavenumber ξ_n for which the

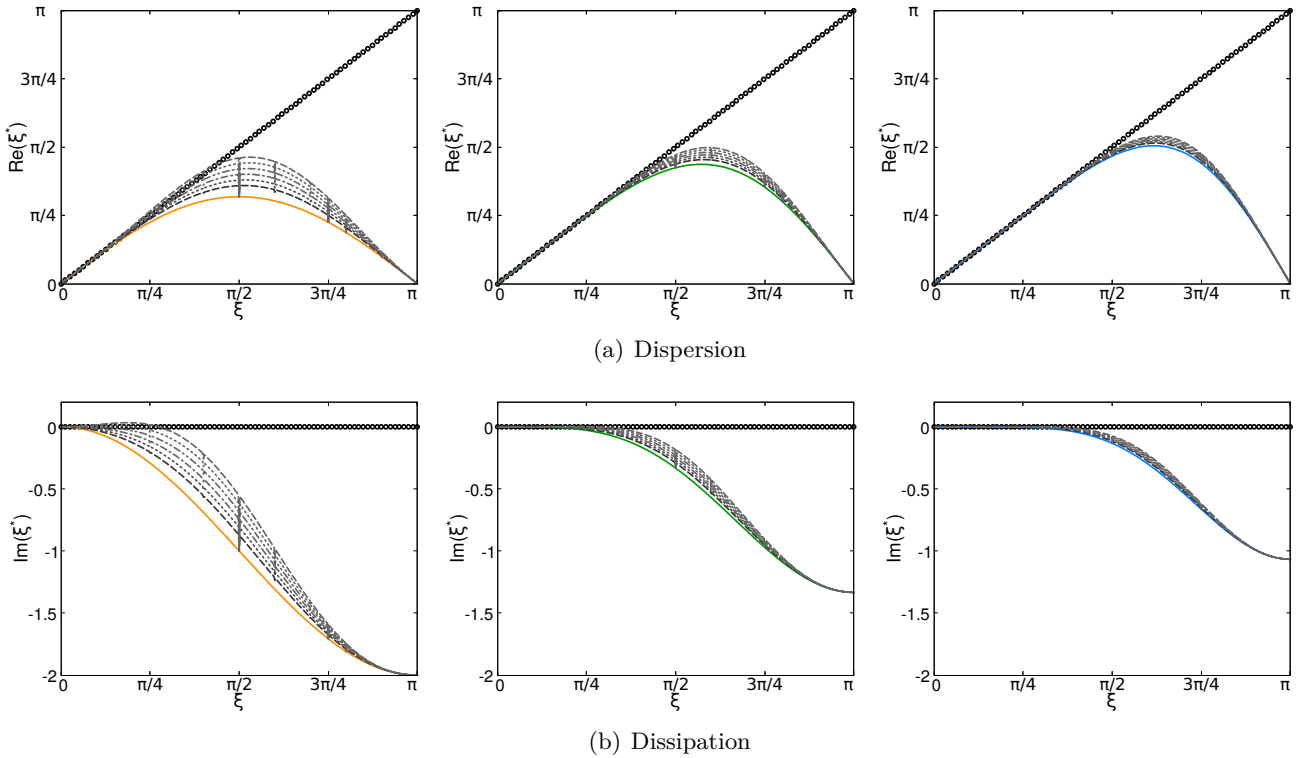


Figure 3.7: Sensitivity of spectral properties to the value of the confinement parameter ε . Spectral accuracy (\circ), baseline scheme (colored solid line), scheme with confinement (black dashed lines): six levels ranging from $\varepsilon = 0.4 k_p$ to $\varepsilon = 1.4 k_p$. From left to right, FE-MUSCL schemes at 1st-, 3rd- and 5th- order of accuracy.

scheme approximates the exact solution under a defined error threshold E . In turn, this reduced wavenumber is equivalent to a minimum number of grid points per wavelength $\lambda_n/\Delta x$ required to ensure the accurate approximation of Eq. (3.1).

Tables 3.2 and 3.3 show the effect of confinement on the resolvability limit of FE-MUSCL schemes due to dispersion and due to dissipation. These schemes are odd-order accurate and therefore have a leading truncation error term of dissipative nature, the accuracy limit being in turn defined by their dissipation error, rather than dispersion. Confinement is shown to achieve a considerable improvement of this limit due to dissipation, with the difference being lower as the order of accuracy increases. The confinement correction halves the minimum number of points per wavelength for the FE-MUSCL3 and extends the well-resolved wavenumber range even for the more precise higher-order schemes. Interestingly, the FE-MUSCL3-C scheme exhibits even better 1D resolvability properties than a third-order (residual-based) compact scheme [83]. The 5th- and 7th-order schemes with confinement tend toward the resolvability limits of the compact schemes of the same order. Furthermore, confinement is shown to improve phase approximation errors by an amount comparable to the improvement in terms of dissipation, even though the method had not been designed for this purpose.

It can be argued that, having a higher cut-off wavenumber both in terms of dispersion and dissipation, the FE-MUSCL3-C scheme is a preferable choice over the baseline FE-MUSCL5. This is true for $\xi < \xi_n$, but not representative of the complete wavenumber range, where the FE-MUSCL5 shows overall superior properties (Figs. 3.4-3.5). Furthermore, spectral analysis represents only wave propagation properties and not the improved approximation of the convective derivative provided by the FE-MUSCL5 scheme. Confinement is not equivalent to a correction of the leading truncation error term but represents a conservative correction to the baseline scheme allowing the accurate calculation of wave advection over very long distances. This makes confinement an

Table 3.2: Resolvability limit due to dispersion for FE-MUSCL schemes ($E = 10^{-3}$)

	baseline		confinement	
	ξ_n	$\lambda_n/\Delta x$	ξ_n	$\lambda_n/\Delta x$
FE-MUSCL1	0.176	35.71	0.201	31.25
FE-MUSCL3	0.496	12.66	0.974	6.45
FE-MUSCL5	0.767	8.20	1.024	6.13
FE-MUSCL7	0.974	6.45	1.144	5.49
FE-MUSCL9	1.144	5.49	1.250	5.03

Table 3.3: Resolvability limit due to dissipation for FE-MUSCL schemes ($E = 10^{-3}$)

	baseline		confinement	
	ξ_n	$\lambda_n/\Delta x$	ξ_n	$\lambda_n/\Delta x$
FE-MUSCL1	0.044	142.86	0.119	52.63
FE-MUSCL3	0.327	19.23	0.660	9.52
FE-MUSCL5	0.635	9.90	0.855	7.35
FE-MUSCL7	0.880	7.14	1.037	6.06
FE-MUSCL9	1.068	5.88	1.188	5.29

interesting method for approaching advection problems for which numerical schemes introduce too much diffusion. It is not however capable of preserving structures that are not captured by the baseline scheme.

3.4.5 Stability region and coupling with explicit Runge-Kutta algorithms

Decoupled FE-MUSCL flux discretizations with confinement were investigated by means of a quasi-linear numerical method, but this does not convey sufficient information on the stability and dispersive properties of the fully discrete equation. This section evaluates the stability of fully discrete schemes combining the flux discretizations of Eqs. (3.31), (3.33) with classical Runge-Kutta methods for time integration.

The stability of a complete numerical scheme is evaluated by investigating whether the Fourier symbol of the space discretization lies within the stability region of the time integration method. The Fourier symbol Ω results from Eq. (3.41). It is an equivalent expression of space discretization error to the modified wavenumber of Eq. (3.44). The two are related as:

$$\Omega\Delta t = -i\sigma\xi^* \quad (3.61)$$

The Fourier symbol of the space discretization can therefore be obtained from Eq. (3.61) using the modified wavenumber obtained by the numerical method presented in Section 3.4.1.

For the present analysis we consider the family of classical explicit low-storage Runge-Kutta (RK) algorithms:

$$\begin{aligned} u^{(0)} &= u^n \\ u^{(q)} &= u^{(0)} + d_q\Delta t \mathcal{L}\left(u^{(q-1)}\right) \\ u^{n+1} &= u^{(k)} \end{aligned} \quad (3.62)$$

for $q = 1, \dots, k$. Above, d_q are the RK scheme coefficients and \mathcal{L} is the discretization of the right hand side of the original differential equation $\frac{du}{dt} = \mathcal{L}(u)$. For linear partial differential equations, the amplification factor G of classical k -stage RK algorithms (RKK) is equal to the exact amplification

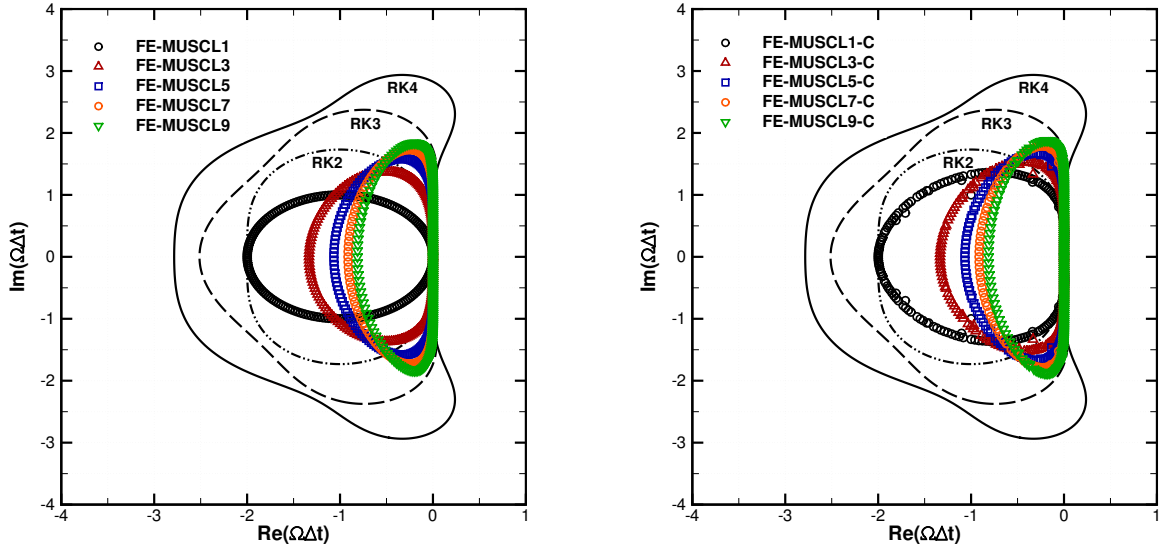


Figure 3.8: Fourier symbol of FE-MUSCL and FE-MUSCL-C space discretizations against the stability region of classical Runge-Kutta algorithms ($\sigma = 1.0$, $\varepsilon = 1.14 k_p$).

factor:

$$G_{exact} = 1 + \sum_{j=1}^{\infty} \frac{(\Omega\Delta t)^j}{j!} \quad (3.63)$$

up to the term of k th-order. In turn, this means that the scheme is k th-order accurate for linear problems. The stability region of the algorithm is finally defined by prescribing $|G| \leq 1$.

Fig. 3.8 shows the stability region of RK algorithms against the Fourier symbol of FE-MUSCL schemes with and without a confinement correction. Both FE-MUSCL and FE-MUSCL-C schemes remain within the stability region of RK3 and RK4 under the CFL condition. It should however be noted that for $\varepsilon > k_p$, the slightly positive $Im(\xi^*)$ values already discussed in Section 3.4.3 correspond to slightly positive values of $Re(\Omega\Delta t)$ through the transformation (3.61). Finally, the eigenvalues for the pure centered discretizations of Eq. (3.27) would be located on the imaginary axis, therefore the dissipative contribution is attributed only to the artificial dissipation and confinement term.

A sensitivity study to the values of the CFL number and the confinement parameter ε is presented in Fig. 3.9. The eigenvalues of the space discretization with confinement remain within the stability region of RK3/RK4 algorithms for a wide range of values of σ , and show small sensitivity to the choice of the confinement parameter.

3.5 Application of the schemes to long-distance advection studies

A characteristic feature of schemes with confinement is their capability to preserve thin pulses over arbitrary distances without dissipation. This is achieved by the confinement correction, which is based on the nonlinear harmonic mean. This allows it to adjust between introducing anti-dissipation, so as to concentrate the pulse over a few grid cells when it spreads due to numerical dissipation, and going to zero when the pulse is concentrated, so as to avoid divergence [194].

This section first presents an analysis of the asymptotic solution of schemes with confinement, i.e. the shape satisfying the balance between the scheme's dissipation and the confinement correction. The schemes with confinement are then applied to long-distance advection studies, to numerically evaluate their stability and capability to calculate the long-distance advection of disturbances. Such an evaluation has already been performed for the space-time coupled high-order schemes with confinement [44, 45]. The primary purpose of the present study is the validation of the space-time decoupled schemes and their comparison against coupled schemes of the Lax-Wendroff family.

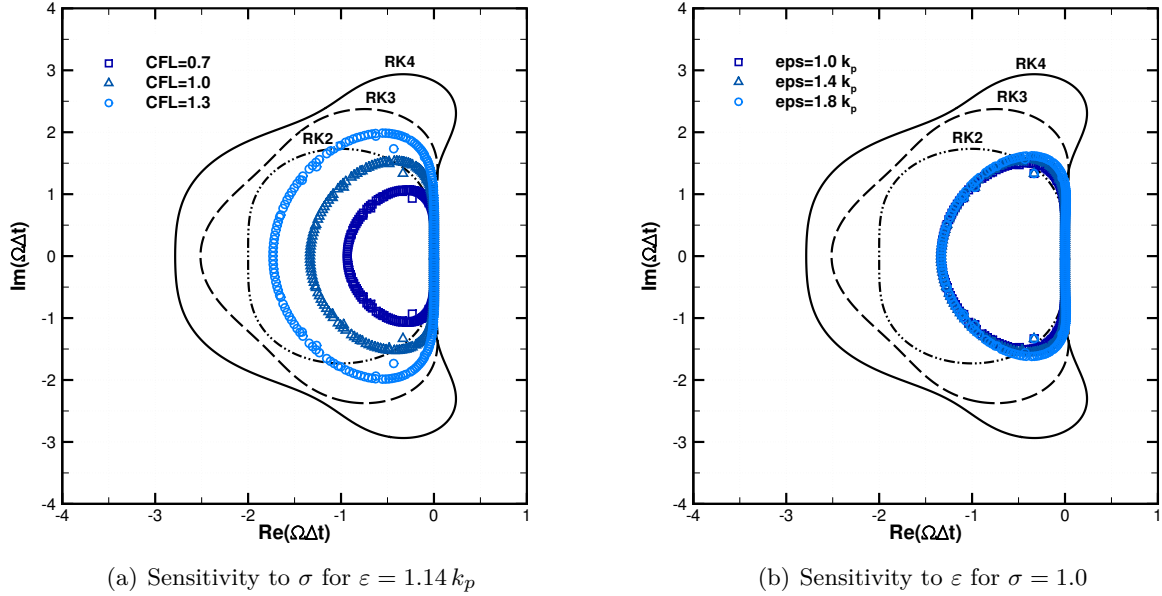


Figure 3.9: Sensitivity to the value of the CFL number and to the value of the confinement parameter for the Fourier symbol of the FE-MUSCL3-C scheme.

3.5.1 Theoretical analysis of the asymptotic solution

Asymptotic solutions are solutions of the numerical scheme’s equivalent partial differential equation, which is representative of the discretized form of Eq. (3.1). They are called “asymptotic” as they represent solutions of this equation for very long times.

These solutions result from the balance between the baseline numerical dissipation and the nonlinear anti-dissipation of confinement. They were thoroughly investigated in [45] for different formulations of the harmonic mean function in the confinement correction. For schemes of the Lax-Wendroff family, the aforementioned balance is obtained from Eq. (3.23) as:

$$\frac{\partial^{p+1}u}{\partial x^{p+1}} = \varepsilon \frac{\delta^{p+1}\tilde{h}(u_j^n, Tu_j^n)}{\Delta x^{p+1}} \quad (3.64)$$

A non-trivial and non-singular solution to Eq. (3.64) is given by J. Steinhoff [194] in the form of a hyperbolic secant function:

$$u_j = \operatorname{sech}(\kappa x_j) = \frac{1}{\cosh(\kappa x_j)} \quad (3.65)$$

which corresponds to a thin pulse shape. For a discrete condition of the type (3.65) and using trigonometric identities, the harmonic mean (3.8) simplifies to [45]:

$$\tilde{h}(u_j, Tu_j) = \frac{1}{\cosh(\kappa \Delta x/2)} u_{j-\frac{1}{2}} \quad (3.66)$$

In the above equation, the left- and right-hand sides can be based on the same stencil by an approximation $u_{j-\frac{1}{2}} = \mu(u)_{j-\frac{1}{2}} = \frac{1}{2}(u_j + Tu_j)$. A fully discrete version of Eq. (3.64) can then be written as:

$$\frac{\delta^{p+1}\mu(u)_{j-\frac{1}{2}}}{\Delta x^{p+1}} = \varepsilon \frac{\delta^{p+1}\tilde{h}(u_j^n, Tu_j^n)}{\Delta x^{p+1}} \quad (3.67)$$

which is representative of the asymptotic balance on the discrete level. For approximations of the left- and right-hand side on the same stencil, the above equation reduces to:

$$\mu(u)_{j-\frac{1}{2}} = \varepsilon \tilde{h}(u_j^n, Tu_j^n) \quad (3.68)$$

for any p th-order Lax-Wendroff scheme with confinement, since the discrete operator δ is linear. The asymptotic solution is therefore the same at any order of accuracy. Substituting (3.66) in the above equation, we get:

$$\begin{aligned} \varepsilon &= \cosh\left(\frac{\kappa \Delta x}{2}\right) \\ \Leftrightarrow \quad \kappa \Delta x &= 2 \ln\left(\varepsilon + \sqrt{\varepsilon^2 - 1}\right) \end{aligned} \quad (3.69)$$

Eq. (3.69) shows that the shape of the discrete asymptotic solution is defined by the mesh size and the value of the confinement parameter ε . For an initial condition that resembles the form (3.65), it is therefore theoretically possible to adjust the value of the confinement parameter so that the asymptotic shape remains close to the shape of the exact solution [47].

The analysis of the asymptotic solution is similar for the space-time decoupled schemes presented in Section 3.2.3. In this case, the asymptotic balance is obtained from the equivalent differential equation (3.35) as:

$$k_p \frac{\partial^{p+1} u}{\partial x^{p+1}} = \varepsilon \frac{\delta^{p+1} \tilde{h}(u_j, T u_j)}{\Delta x^{p+1}} \quad (3.70)$$

which results in the same asymptotic solution as for Lax-Wendroff schemes, because $\varepsilon \propto k_p$.

3.5.2 Numerical results

In the following, the schemes with confinement presented in Section 3.2 are applied to long-distance advection studies. These cases are the advection of a hyperbolic secant pulse and the advection of mixed-frequency wave packets.

3.5.2.1 Hyperbolic secant pulse

To evaluate the schemes' capability to preserve thin pulses, we are considering an initial condition corresponding to a hyperbolic secant:

$$u(x, 0) = \operatorname{sech}(\kappa x) \quad (3.71)$$

The shape parameter κ is obtained from Eq. (3.69), corresponding to the asymptotic solution for a confinement parameter $\varepsilon = 1.6$. The confinement parameter in the computations is however deliberately chosen $\varepsilon = 1.14$ for Lax-Wendroff schemes and $\varepsilon = 1.14 k_p$ for FE-MUSCL schemes, a value commonly used in the literature. Since $\varepsilon \neq 1.6$, the confinement parameter is not adapted to the initial pulse shape, in the sense of Eq. (3.69).

The case is solved on a uniform mesh with spacing $\Delta x = 0.5$ ($x_j = j \Delta x$, $j \in \mathbb{Z}$). Periodicity conditions with sufficient points are applied on domain boundaries, so that boundary fluxes are calculated on the same large stencils as on the domain interior. For the FE-MUSCL decoupled schemes, time integration is performed with a classical 4-step low-storage Runge-Kutta algorithm, which is fourth-order accurate for linear problems.

A series of numerical experiments has shown that lower order FE-MUSCL schemes exhibit an unstable behavior for $\varepsilon > k_p$. This behavior is closely related to the slightly positive $Im(\xi^*)$ values discussed in the spectral analysis of Section 3.4.3. Interestingly, even though the numerically evaluated spectral properties are identical for schemes of the Lax-Wendroff family, these do not show a similar instability. This suggests that the time-associated dissipation of Lax-Wendroff schemes has an indispensable damping behavior. Note also that in the case of Lax-Wendroff schemes, the anti-dissipative confinement correction is also space-time coupled (see Eq. (3.22)). The magnitude of the slightly positive $Im(\xi^*)$ values however decreases rapidly for higher-order of accuracy (see Fig. 3.5). In other words, the instability is slower and at higher-orders is not obtained within a realistic advection distance. This is demonstrated in the following.

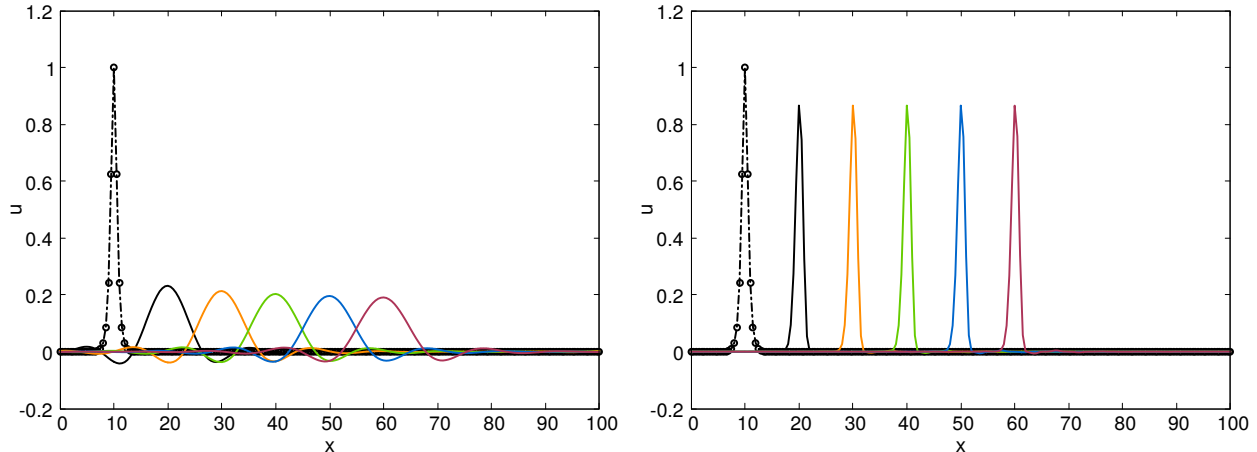


Figure 3.10: Computed hyperbolic secant pulse at different instants during a very long distance advection. FE-MUSCL7 scheme (left) and FE-MUSCL7-C with $\varepsilon = 1.14 k_p$ (right) at $\sigma = 0.02$. Exact: $-\bullet-$, $1.2 \cdot 10^7 \Delta x$: $—$, $2.4 \cdot 10^7 \Delta x$: $—$, $3.6 \cdot 10^7 \Delta x$: $—$, $4.8 \cdot 10^7 \Delta x$: $—$, $6 \cdot 10^7 \Delta x$: $—$. Subsequent curves are displaced by $+10$ on the x -axis for visibility.

The advection of the hyperbolic secant pulse (3.71) is computed over a very long distance $d = 6 \cdot 10^7 \Delta x$. A comparison of results with and without confinement are shown in Fig. 3.10 for the 7th-order FE-MUSCL scheme. The region of the thin pulse corresponds to a high-frequency disturbance and is thus rapidly diffused by the baseline scheme's dissipation, albeit the scheme's high-order of accuracy. This results in a smoothed solution with a reduced peak that is further propagated with less dissipation. On the other hand, the anti-dissipative confinement correction effectively balances the excess dissipation in the vicinity of the pulse. The computed solution shows a peak reduction, as the scheme's asymptotic solution is different from the initial shape. Nonetheless, the computed pulse is then propagated without observable effects of dissipation over a very long distance. Last, the confinement correction does not degrade the numerical advection speed, as the pulse position is exact even for a very long advection distance.

Another difference between space-time coupled and decoupled schemes concerns the sensitivity to the time discretization error. For small time step values, where the effect of time integration error remains small, high-order decoupled schemes with confinement result in the same asymptotic solution and similar pulse-preserving capabilities as Lax-Wendroff schemes. It is not however the case for a larger time step, or CFL number. For FE-MUSCL schemes, the confinement correction accounts only for space discretization error. As a result, for a larger time step, the dissipation of the time integration algorithm is accumulated over time and is not balanced by the confinement correction. To evaluate this effect, we are considering the evolution of the energy of the signal. At a specific time instant n the discrete energy is:

$$E^n = \Delta x \sum_{j=1}^N (u_j^n)^2 \quad (3.72)$$

The evolution of energy is shown in Fig. 3.11 for different CFL number values. For schemes with confinement, the energy displays a slight reduction during the first phases of the advection, but then relaxes to an asymptotic solution that is close to the initial value. Lax-Wendroff schemes have a time-coupled confinement correction, allowing it to inherently adapt to a different time step. On the other hand, FE-MUSCL schemes display a large sensitivity to the CFL number value, since in this case the confinement correction is only constructed to balance the spatial discretization error. As a result, the dissipation error of the time integration algorithm is accumulated and causes the pulse to diffuse over a long-enough advection distance. This dissipation is reduced by the use of a smaller time step, eventually allowing to retrieve an equivalent solution to the one obtained with Lax-Wendroff schemes.

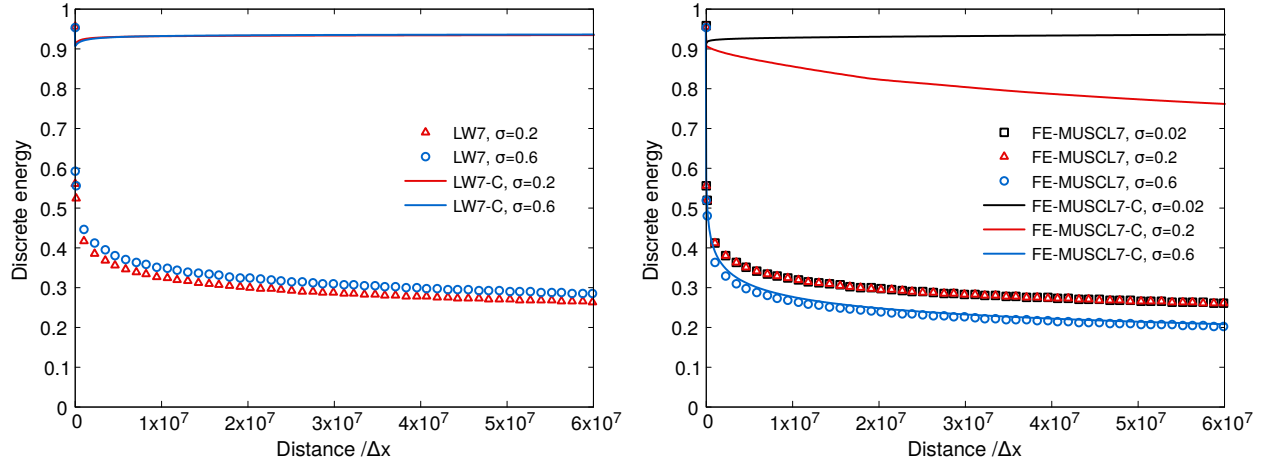


Figure 3.11: Evolution of the discrete energy of the solution over a very long distance advection for different values of the CFL number. Results with and without confinement for the Lax-Wendroff scheme (left) and FE-MUSCL scheme (right) at 7th-order of accuracy.

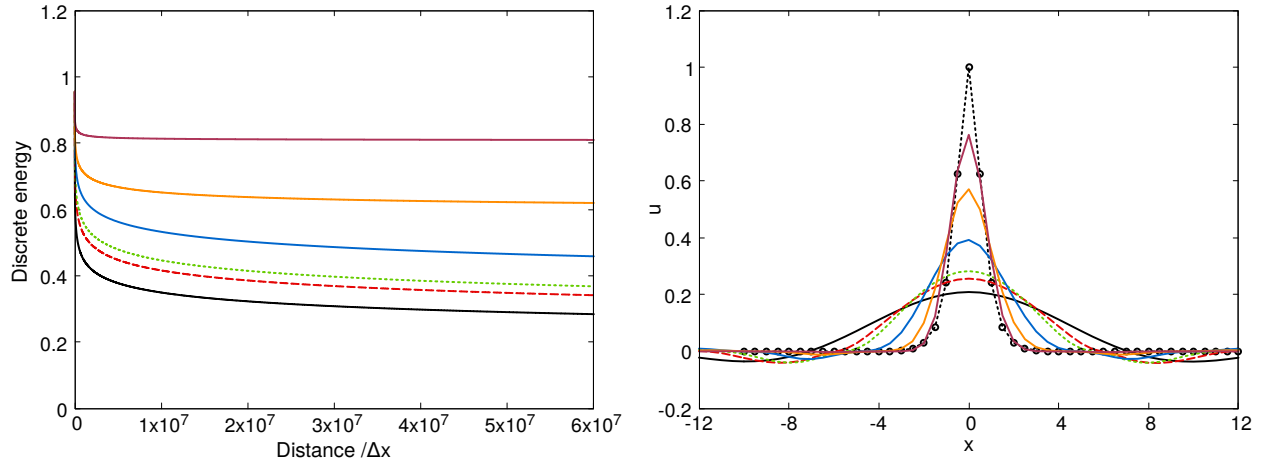


Figure 3.12: Preservation of a hyperbolic secant pulse for different values of the confinement parameter. Evolution of discrete energy (left) and pulse shape after a distance $d = 6 \cdot 10^7 \Delta x$ (right). Exact: $\cdots\circ\cdots$, $\varepsilon = 0$ (baseline LW7): — , $\varepsilon = 0.80$: -- -- , $\varepsilon = 0.90$: \cdots , $\varepsilon = 1.00$: — , $\varepsilon = 1.05$: — , $\varepsilon = 1.10$: — . Computed with the LW7-C scheme at $\sigma = 0.6$.

The influence of the value of the confinement parameter is then assessed by a parametric study on the same case. For both FE-MUSCL and Lax-Wendroff schemes, the confinement correction introduces anti-dissipation for any positive value of the confinement parameter. In particular, the objective of this study is thus to assess the capability of the confinement correction to overcome baseline dissipation for $\varepsilon \leq k_p$ (or $\varepsilon \leq 1$ for Lax-Wendroff schemes), in which case the schemes display no instability in the spectral analysis of Section 3.4.3. Results are shown in Fig. 3.12 for the 7th-order Lax-Wendroff scheme with confinement. For values of ε higher than 1, the confinement correction has the capability to overcome the effect of the baseline numerical dissipation and preserve the signal shape over an arbitrary distance. The asymptotic shape that is finally preserved, and therefore its discrete energy, depends on the value of the confinement parameter. The results of Fig. 3.13 for the 7th-order FE-MUSCL scheme are similar. Results for both families of schemes however show that for $\varepsilon \leq 1$ the magnitude of the confinement correction is not sufficient to completely balance the effect of baseline dissipation, and the signal is progressively dissipated over time. Still, for $\varepsilon \leq k_p$ (or $\varepsilon \leq 1$ for the Lax-Wendroff family), schemes with a confinement correction have effectively reduced numerical dissipation compared to the baseline version of the scheme. Furthermore, as

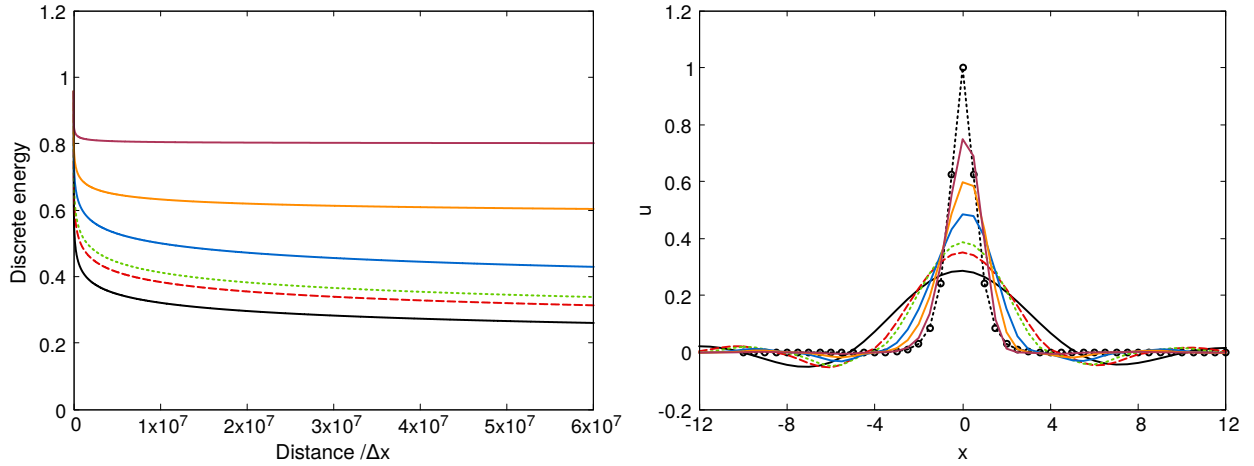


Figure 3.13: Preservation of a hyperbolic secant pulse for different values of the confinement parameter. Evolution of discrete energy (left) and pulse shape after a distance $d = 6 \cdot 10^7 \Delta x$ (right). Exact: $\cdots\circ\cdots$, $\varepsilon = 0$ (baseline FE-MUSCL7): --- , $\varepsilon = 0.80 k_p$: - - - , $\varepsilon = 0.90 k_p$: \cdots , $\varepsilon = 1.00 k_p$: --- , $\varepsilon = 1.05 k_p$: --- , $\varepsilon = 1.10 k_p$: --- . Computed with the FE-MUSCL7-C scheme at $\sigma = 0.02$.

confinement does not surpass baseline dissipation, it is possible that this reduction in dissipation is not accompanied by a strong compressive effect of confinement, which may be undesired in certain applications. This may be an interesting feature that can be further investigated in future studies.

3.5.2.2 Wave packet

The schemes can be further evaluated on the resolution of mixed-frequency signals, or wave packets. These are similar to cases encountered in aeroacoustics problems. We are considering here the case proposed in [20], corresponding to a disturbance of the form:

$$u(x, 0) = \sin\left(\frac{2\pi x}{\alpha\Delta x}\right) \exp\left(-\ln(2) \left(\frac{x}{\beta\Delta x}\right)^2\right) \quad (3.73)$$

where α , β are real coefficients. These respectively define the dominant wavelength of the wave packet and the half-width of the Gaussian. The disturbance of Eq. (3.73) is a common benchmark case for high-resolution schemes. It allows to evaluate their capability both in preserving disturbances discretized by few points and in propagating groups of frequencies at the correct speed. We are considering two different wave packet forms, corresponding to a medium- and a high-frequency signal. For FE-MUSCL schemes, time integration is performed with a classical 4-step low-storage Runge-Kutta algorithm, as for the case of the previous section.

The first wave packet form, referred to as Packet I, is given for $\alpha = 8$, $\beta = 3$. In that case, the disturbance has a spatial frequency content in the range $0 < \xi < \pi/2$ with a peak at $\xi_p = \pi/4$, where $\xi = k \Delta x$ is the reduced wavenumber. The advection of the signal is computed for a distance $800 \Delta x = 100 \lambda_p$ (with $\lambda_p = 2\pi\Delta x/\xi_p$). Fig. 3.14 shows the signal computed using high-order FE-MUSCL schemes at different values of the CFL number. Results show an important effect of dissipation, even at higher orders of accuracy. Schemes with confinement however produce an improved resolution of the disturbance peaks for all cases, compared to their linear counterparts. The anti-dissipation of confinement gives a slightly sharper signal, but does not result in an over-compression of the pulse, even though the computed distance is typically considered large for aeroacoustics problems. The effect of time integration error appears mostly at higher-orders of accuracy. As observed in the previous application, time integration error becomes important over time for decoupled FE-MUSCL schemes at a larger CFL number. Results for schemes of the Lax-Wendroff family are shown in Fig. 3.15. The effect of the choice of time step is opposite compared to the decoupled

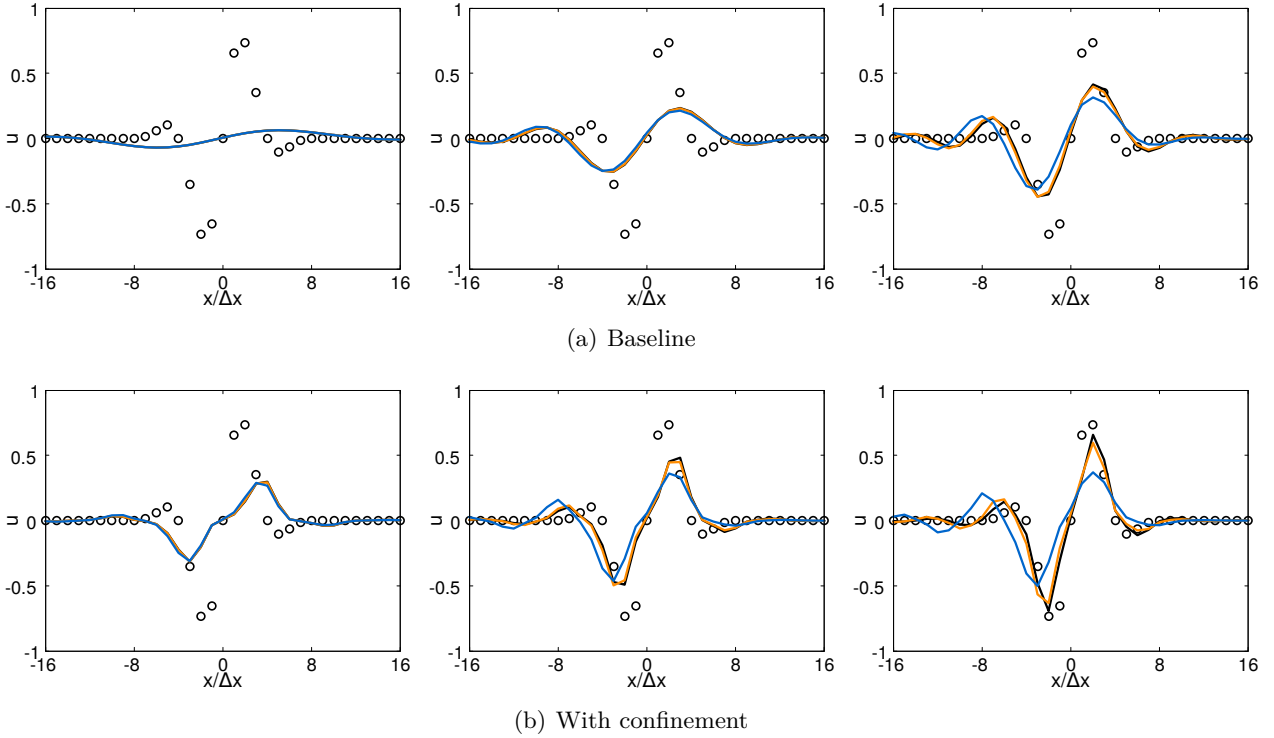


Figure 3.14: Results for Packet I after an advection distance $800 \Delta x$ at different values of the CFL number. Exact solution: \circ , $\sigma = 0.2$:—, $\sigma = 0.5$:—, $\sigma = 0.8$:— . From left to right, FE-MUSCL schemes at 3^{rd} , 5^{th} and 7^{th} order of accuracy ($\varepsilon = 1.14 k_p$).

schemes of Fig. 3.14. For this linear case, Lax-Wendroff schemes give more accurate results at a larger CFL number, in general agreement with results presented in [53].

Packet II is given for $\alpha = 6$, $\beta = 9$. It corresponds to a thinner spatial frequency bandwidth with a peak at $\xi_p = \pi/3$, or equivalently a dominant wavelength $\lambda_p = 6 \Delta x$. Its propagation is computed over a distance $200 \Delta x$. Results computed with high-order FE-MUSCL schemes are shown in Fig. 3.16. Again, the confinement correction greatly improves the preservation of the packet amplitude. The improvement appears as early as at 5th-order of accuracy, where the result of the baseline scheme is almost completely dissipated. At 9th-order of accuracy, the scheme with confinement gives a result close to the exact solution for $\sigma = 0.5$ and $\sigma = 0.2$. Dissipation is however increased at $\sigma = 0.8$ both for the baseline and confinement version of the scheme. Results computed with the Lax-Wendroff schemes are shown in Fig. 3.17. As for the case of Packet I, these schemes give a more accurate result at $\sigma = 0.8$, especially at lower orders of accuracy. Higher-order Lax-Wendroff schemes however display reduced sensitivity to the CFL number. This is possibly related to the temporal order of accuracy being the same as the order of the space discretization, whereas for the decoupled FE-MUSCL schemes the time discretization remains 4th-order accurate. In any case, Lax-Wendroff schemes give more accurate results than FE-MUSCL schemes at the same order, both with and without confinement.

The preceding results show that schemes with confinement consistently improve the preservation of mixed-frequency signals over long distances, both for Lax-Wendroff and FE-MUSCL schemes. The confinement corrections are shown to give consistent results with high-order schemes. Specifically for the higher-frequency wave packet, a p th-order scheme with confinement gives similar results to a baseline scheme of order $p+2$, for both families of schemes. Last, these results do not show any negative effect of the confinement correction on numerical group velocity.

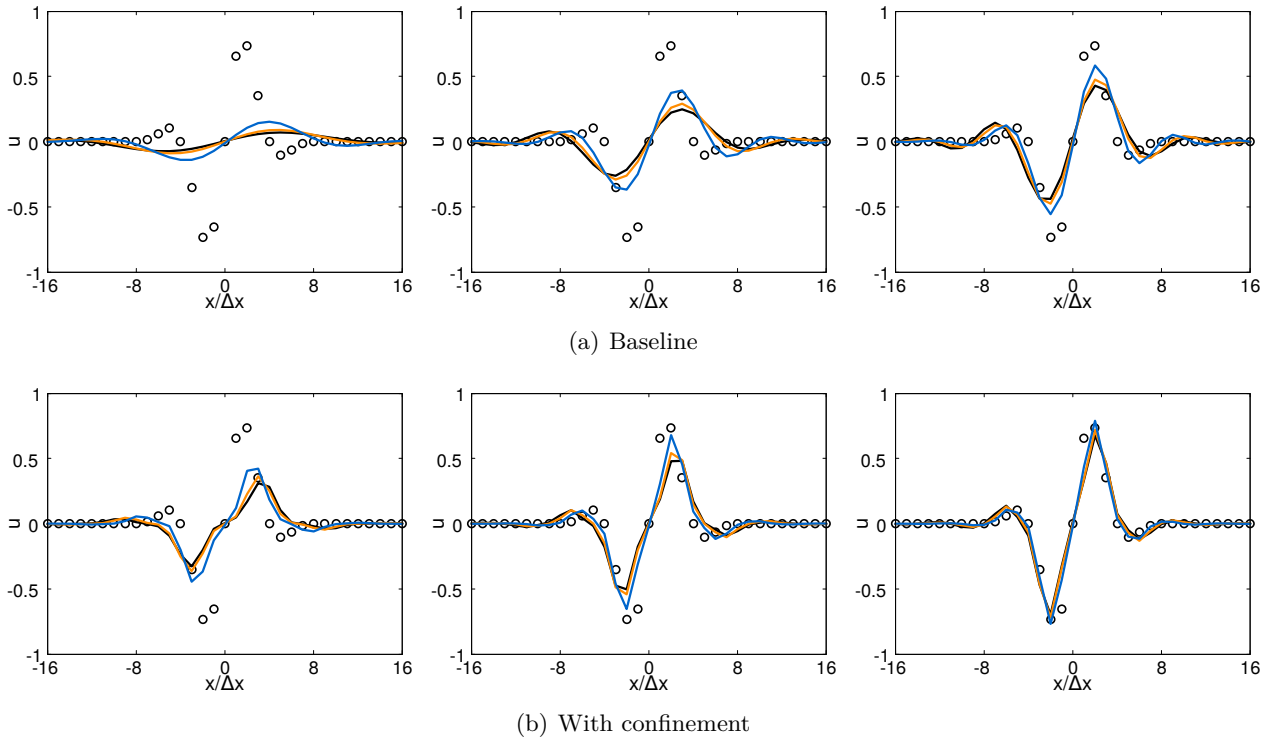


Figure 3.15: Results for Packet I after an advection distance $800 \Delta x$ at different values of the CFL number. Exact solution: \circ , $\sigma = 0.2$:—, $\sigma = 0.5$:—, $\sigma = 0.8$:— . From left to right, Lax-Wendroff schemes at 3^{rd} , 5^{th} and 7^{th} order of accuracy ($\varepsilon = 1.14$).

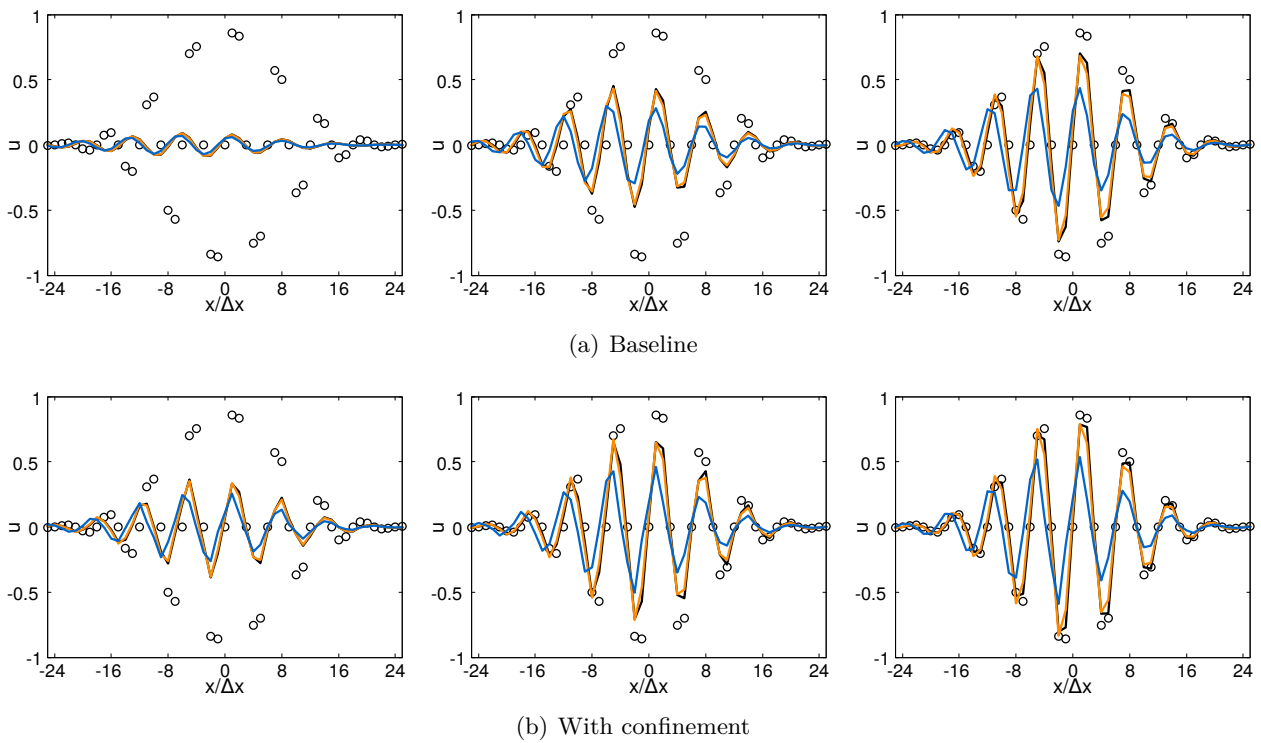


Figure 3.16: Results for Packet II after an advection distance $200 \Delta x$ at different values of the CFL number. Exact solution: \circ , $\sigma = 0.2$:—, $\sigma = 0.5$:—, $\sigma = 0.8$:— . From left to right, FE-MUSCL schemes at 5^{th} , 7^{th} and 9^{th} order of accuracy ($\varepsilon = 1.14 k_p$).

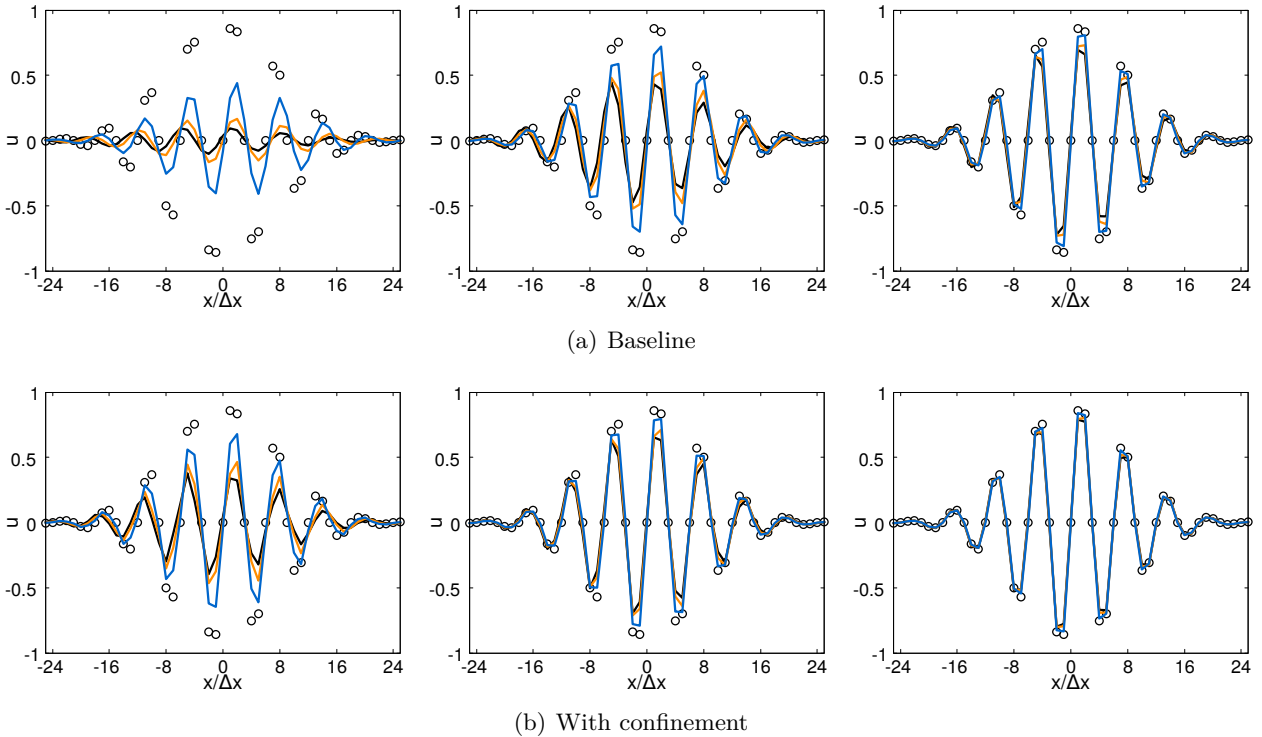


Figure 3.17: Results for Packet II after an advection distance $200 \Delta x$ at different values of the CFL number. Exact solution: \circ , $\sigma = 0.2$:—, $\sigma = 0.5$:—, $\sigma = 0.8$:— . From left to right, Lax-Wendroff schemes at 5^{th} , 7^{th} and 9^{th} order of accuracy ($\varepsilon = 1.14$).

3.6 Chapter summary

This chapter has presented a comprehensive analysis of confinement corrections for high-order schemes, in the case of the linear transport equation. These are nonlinear anti-dissipative corrections of the baseline scheme's numerical flux. First, previously developed formulations of confinement for coupled schemes in space and time have been reviewed. A new formulation of high-order confinement corrections has then been developed, for decoupled schemes in space and time. This formulation has been tested alongside standard linear non-compact schemes, which achieve the optimal order of accuracy on the given stencil. Nonetheless, the developed approach should be also applicable to other types of numerical dissipation, as long as the same dissipation operator is used for both the baseline dissipation and the confinement correction.

As a following step, the developed schemes with nonlinear confinement corrections have been analyzed with respect to their resolvability in the wavenumber space. This analysis has shown that schemes with a confinement correction have improved dispersive and dissipative properties compared to their linear counterparts. The improvement in terms of resolvability limit has been found particularly favorable at third- and fifth-order of accuracy, but is also maintained at even higher orders. More importantly, this analysis has demonstrated the advantage of building the confinement correction on a high-order dissipation operator. In a sense, the confinement correction inherits the form of the transfer function of the dissipation operator, and thus has a minimal contribution within the well-resolved wavenumber range. Another important property is that the anti-dissipative corrections do not modify the damping of grid-to-grid oscillations. Additionally, schemes with confinement corrections have been shown to be mildly unstable within the low-wavenumber range. This instability appears beyond a specific threshold of the confinement parameter, i.e. greater than the coefficient of the baseline numerical dissipation. For Lax-Wendroff schemes however, this instability is naturally balanced by the time-coupled dissipation. As for decoupled standard schemes, the instability is smaller for increasing order of accuracy. At higher orders, it is therefore observed only

if a very long distance advection is considered.

The above observations were confirmed by application of the schemes to scalar advection problems over long distances. In the case of Lax-Wendroff schemes, the confinement correction is space-time coupled and thus allows the preservation of signals over long distances, even at a large CFL number. On the other hand, standard decoupled schemes are more sensitive to time-associated dissipation, especially in a very long distance advection. For both families of schemes however, confinement corrections were shown to effectively reduce the excess numerical dissipation, even at high orders of accuracy. At the same time, the presented results show that they do not have a negative effect on numerical group velocity, even beyond realistic advection distances.

These applications have shown that confinement corrections in the case of space-time coupled Lax-Wendroff schemes are superior in many aspects. They allow accurate long-distance computations at a larger CFL number and have an inherently well-adapted numerical dissipation which balances the mild instability of confinement corrections. On the other hand, the confinement formulation for decoupled schemes is more limited due to the mild instability at low wavenumbers and the accumulation of time-associated dissipation over very long distances. This formulation remains however interesting, as decoupled schemes are more often applied in computational solvers due to the ease of implementation and offered freedom in terms of choice of space or time discretization schemes. Even more so, since for a confinement parameter smaller or equal to the coefficient of the baseline numerical dissipation, these schemes show no instability while at the same time being always less dissipative than the baseline scheme. Moreover, in the case of linear decoupled schemes, confinement corrections can be integrated at a very small computational cost.

On this basis, the following chapter is devoted to the development of high-order confinement corrections for the Navier-Stokes equations, specifically formulated to balance the excess numerical dissipation in vortical flow regions.

Chapter 4

Development of high-order Vorticity Confinement schemes for the Euler and Navier-Stokes equations

Contents

4.1	Navier-Stokes equations	50
4.2	Description of the solver and baseline numerical methods	52
4.2.1	Finite volume space discretization	52
4.2.2	Time integration	57
4.3	Development of a high-order Vorticity Confinement method	58
4.3.1	Original VC2 formulation	58
4.3.2	Analogy with the scalar formulation	60
4.3.3	Extension of the Vorticity Confinement method to higher orders	62
4.3.4	Discussion of the confinement parameters	64
4.3.5	Equivalence with an anti-dissipative flux correction	65
4.4	Numerical implementation of the high-order Vorticity Confinement method	66
4.4.1	Recursive approximation of derivatives	66
4.4.2	Boundary treatment	70
4.4.3	Identification of vortical flow regions and cut-off	72
4.4.4	Laplacian schemes	74
4.5	Validation and numerical tests	74
4.5.1	Evaluation of the order of accuracy	74
4.5.2	Advection of an isentropic vortex	80
4.5.3	Discussion on computational cost	87
4.6	Chapter summary	88

This chapter is dedicated to the development of high-order Vorticity Confinement corrections for the Euler and Navier-Stokes equations. The first part of the chapter presents the general numerical framework and the formulation of baseline methods that will be used in the rest of the thesis. Then, high-order Vorticity Confinement corrections are derived analytically, as extensions of the original first-order VC2 formulation. Theoretical analyses of these corrections are also presented. These address the analogy of Vorticity Confinement corrections with the scalar confinement approach of the previous chapter and their equivalence to anti-dissipative nonlinear corrections of the baseline scheme in regions of vortical flow. The discretization of these schemes in a finite volume formulation is then discussed in detail, and several numerical strategies are presented. This chapter

finally presents the validation of the developed schemes, by application to simple but representative academic test cases. The schemes are evaluated with respect to their order of accuracy, but also their consistency and improvement in the calculation of vortical flows alongside classical directional non-compact discretization schemes.

4.1 Navier-Stokes equations

The calculation of aerodynamic flows in the present work is performed based on the systems of the Euler and Navier-Stokes equations. The latter is the most complete system of the two, based on the assumption of continuum and the decomposition of the stress tensor in a pressure and viscous part. Both systems consist of three equations describing the conservation of mass, the conservation of momentum and the conservation of energy. The second one is a vector conservation equation, whereas the other two are conservation equations of scalar quantities. With respect to a Cartesian reference frame, the Navier-Stokes equations can be written in conservative vector form as:

$$\frac{\partial W}{\partial t} + \frac{\partial f}{\partial x} + \frac{\partial g}{\partial y} + \frac{\partial h}{\partial z} = Q_S \quad (4.1)$$

where t denotes time, $x_d = (x, y, z)$ is the vector of space coordinates, $d=1, 2, 3$ denoting the space direction, and Q_S denotes the vector of volume source terms. In the above, W is the state vector of conservative variables:

$$W = \left[\rho, \quad \rho u, \quad \rho v, \quad \rho w, \quad \rho E \right]^T \quad (4.2)$$

where ρ denotes the density, (u, v, w) denote the components of the velocity vector \vec{v} in the three space directions, and E the total energy. The physical flux vectors f, g, h in each space direction are separated into a convective, i.e. inviscid, and a viscous part as:

$$f = f^c - f^v \quad g = g^c - g^v \quad h = h^c - h^v \quad (4.3)$$

The convective fluxes are:

$$f^c = \begin{bmatrix} \rho u \\ \rho u^2 + p \\ \rho uv \\ \rho uw \\ \rho u H \end{bmatrix} \quad g^c = \begin{bmatrix} \rho v \\ \rho vu \\ \rho v^2 + p \\ \rho vw \\ \rho v H \end{bmatrix} \quad h^c = \begin{bmatrix} \rho w \\ \rho wu \\ \rho wv \\ \rho w^2 + p \\ \rho w H \end{bmatrix} \quad (4.4)$$

where p is the pressure. In Eqs. (4.2), (4.4), E denotes the specific total energy and H denotes the specific total enthalpy given by:

$$E = e + \frac{1}{2} \|\vec{v}\|^2 \quad H = h + \frac{1}{2} \|\vec{v}\|^2 \quad (4.5)$$

with e and h respectively being the specific internal energy and enthalpy. The viscous fluxes are:

$$f^v = \begin{bmatrix} 0 \\ \tau_{xx} \\ \tau_{xy} \\ \tau_{xz} \\ u\tau_{xx} + v\tau_{xy} + w\tau_{xz} + \kappa \frac{\partial T}{\partial x} \end{bmatrix} \quad g^v = \begin{bmatrix} 0 \\ \tau_{yx} \\ \tau_{yy} \\ \tau_{yz} \\ u\tau_{yx} + v\tau_{yy} + w\tau_{yz} + \kappa \frac{\partial T}{\partial y} \end{bmatrix} \quad (4.6)$$

$$h^v = \begin{bmatrix} 0 \\ \tau_{zx} \\ \tau_{zy} \\ \tau_{zz} \\ u\tau_{zx} + v\tau_{zy} + w\tau_{zz} + \kappa \frac{\partial T}{\partial z} \end{bmatrix}$$

where τ_{ij} ($i, j = x, y, z$) are the components of the viscous stress tensor $\bar{\bar{\tau}}$, T is the temperature and κ is the thermal conductivity of the fluid.

A reduced version of the above system can be derived under the assumption of inviscid and adiabatic flow, and corresponds to the system of Euler equations. This is obtained by neglecting heat exchange and the viscous fluxes of Eq. (4.6), thus considering only the convective part of physical fluxes as:

$$f = f^c \quad g = g^c \quad h = h^c \quad (4.7)$$

The system of Euler equations may be solved for the computation of convection-dominated problems. Additionally, it is very useful for the evaluation of numerical methods, since viscous effects are generally confined in the boundary layers and wakes. An efficient numerical method must therefore first of all give an accurate representation of the convection-dominated part of the flow.

Equation of state

Following investigations will be performed considering that the fluid is an ideal gas. The system (4.1) is therefore complemented with the equation of state:

$$p = \rho R_g T \quad (4.8)$$

where R_g is the gas constant. The internal energy and enthalpy are functions of temperature as:

$$e = c_v T \quad h = c_p T \quad (4.9)$$

where c_v , c_p denote the heat capacity respectively under constant volume and constant pressure, in turn defining the ratio $\gamma = c_p/c_v$. These are related to the gas constant via $c_p = [\gamma/(\gamma - 1)] R_g$.

Internal stresses

For the numerical investigations of the present thesis, fluids are assumed to be Newtonian. The total internal stress tensor $\bar{\bar{\sigma}}$ is thus considered to be a sum of an isotropic and a anisotropic part:

$$\bar{\bar{\sigma}} = -p\bar{\bar{I}} + \bar{\bar{\tau}} \quad (4.10)$$

where the former is related to pressure and the latter is related to viscous shear stresses. The viscous stress tensor is related to velocity gradients via:

$$\bar{\bar{\tau}} = \mu \left[\overline{\nabla v} + (\overline{\nabla v})^T - \frac{2}{3} \text{tr}(\overline{\nabla v}) \bar{\bar{I}} \right] \quad (4.11)$$

where the tensor $\overline{\nabla v}$ is the gradient of the velocity vector \vec{v} , μ is the dynamic viscosity of the fluid and $\text{tr}(\bullet)$ denotes the trace operator. Eq. (4.11) is obtained under the assumption that the second viscosity coefficient λ is related to μ under the Stokes relation $2\mu + 3\lambda = 0$. The dependence of dynamic viscosity on temperature is expressed either by the power law:

$$\mu = \mu_{ref} \left(\frac{T}{T_{ref}} \right)^{3/2} \quad (4.12)$$

or by Sutherland's law:

$$\mu = \mu_{ref} \left(\frac{T}{T_{ref}} \right)^{3/2} \frac{T_{ref} + S_{suth}}{T + S_{suth}} \quad (4.13)$$

where T_{ref} is the reference temperature, μ_{ref} the dynamic viscosity at reference temperature, and $S_{suth} = 110.4 K$ is the Sutherland temperature. The kinematic viscosity coefficient is finally defined as $\nu \triangleq \mu/\rho$.

4.2 Description of the solver and baseline numerical methods

The numerical methods presented in the main part of the present thesis were implemented within the DynHoLab code [154], which is an in-house research code of the DynFluid laboratory. DynHoLab is a solver of the Navier-Stokes equations on structured grids, using a Finite Volume approach.

Its architecture is dynamic and based on the combination of two programming languages, Fortran and Python. The first is selected for its high efficiency for scientific calculations and the second for its flexibility in terms of development, coupling with scientific libraries and pre-/post-processing. Parallel computations are performed using a multi-block approach based on an MPI implementation. Finally, the data structure is hierarchical, based on a CGNS tree (CFD General Notation System). The following description of baseline numerical methods is not exhaustive, but remains restricted to the methods that will be used in the frame of the thesis.

A large part of the pre- and post-processing of the presented numerical calculations was performed using functions of scientific libraries. Specifically, the Cassiopée partially open-source library of functions for CFD developed at ONERA [15] and the *NumPy* library [207].

4.2.1 Finite volume space discretization

This section introduces the Finite Volume (FV) approximation of the continuous Navier-Stokes equations. The FV approximation is presented for the space-associated terms of the flow equations: the convective fluxes, the viscous (or diffusive) fluxes and the approximation of gradients.

Finite Volume approximations are based on the integral form of the Navier-Stokes equations presented in Section. 4.1. The FV approach has two distinct advantages. First, it is very robust and straightforwardly generalized to any type of computational grid, and unstructured ones in particular. Second, it naturally expresses the conservative property of the numerical approximation within the control volumes (or cells).

The integral form of the Navier-Stokes equations is obtained by integrating Eq. (4.1) over a control volume Ω , bounded by a surface $S = \partial\Omega$:

$$\int_{\Omega} \frac{\partial W}{\partial t} d\Omega + \int_{\Omega} \nabla \cdot (\mathbf{F}^c - \mathbf{F}^v) d\Omega = \int_{\Omega} Q_S d\Omega \quad (4.14)$$

where $\mathbf{F}^c = \mathbf{F}^c(W)$, $\mathbf{F}^v = \mathbf{F}^v(W)$ collectively denote the convective and viscous fluxes. By application of the divergence theorem, the second term of the left-hand side can be expressed with respect to the boundary of the volume Ω :

$$\int_{\Omega} \frac{\partial W}{\partial t} d\Omega + \oint_{\partial\Omega} (\mathbf{F}^c - \mathbf{F}^v) \cdot \vec{n} dS = \int_{\Omega} Q_S d\Omega \quad (4.15)$$

where \vec{n} is the outwards-pointing normal vector. The vector of source terms Q_S is from here onwards neglected for simplicity.

In the following, we are adopting a structured grid notation. More precisely, we are considering the discretization of Eq. (4.15) on a grid composed of control volumes with indices i, j, k . It is also assumed that variables of the state vector W are stored at the centers of control volumes. Specifically, we are considering a control volume (cell) $\Omega_J \equiv \Omega_{i,j,k}$ of this grid, with volume $|\Omega_J|$ and its cell center positioned at $x_J \equiv x_{i,j,k}$. The unique subscript J is adopted to simplify the following directional approximation formulas. For quantities referring to neighbors or faces of the cell Ω_J , the superscript d is used to denote the corresponding direction on the structured grid. As such, the subscripts $J+\frac{1}{2}$ and $J-\frac{1}{2}$ are used to denote quantities on the cell interfaces (faces) $x_{J+\frac{1}{2}}^d$, $x_{J-\frac{1}{2}}^d$, in mesh direction d (see Fig. 4.1).

The averaged values of the state vector W within the volume Ω_J are:

$$\bar{W}_J = \frac{1}{|\Omega_J|} \int_{\Omega_J} W d\Omega \quad (4.16)$$

where $|\Omega_J| = \int_{\Omega_J} d\Omega$. Within the control volume Ω_J , an exact equivalent of Eq. (4.15) can then be written:

$$\frac{d\bar{W}_J}{dt} + \frac{1}{|\Omega_J|} \sum_{f=1}^{N_{\text{faces}}} (\mathbf{F}_f^c - \mathbf{F}_f^v) \cdot \vec{n}_f |S_f| = 0 \quad (4.17)$$

where no approximation error is included, apart from the one-point integration formula for the surface integrals. Above, F_f^c , F_f^v denote the convective and viscous fluxes crossing the face $x_f \equiv x_{J+\frac{1}{2}}^d$. From here onwards, unless explicitly specified, the notation $F_f \equiv F_{J+\frac{1}{2}}^d$ will be used to denote the convective part of the fluxes in space direction d .

Last, a Taylor series expansion of the state vector W around the center x_J in the integral of the cell average definition (4.16) gives:

$$\bar{W}_J = W_J + \mathcal{O}(\tilde{\Delta x}^2) \quad (4.18)$$

where $\tilde{\Delta x}$ denotes a characteristic mesh size. This is easily proven for one space dimension. In other words, Eq. (4.18) shows that cell-averaged values are second-order approximations of point values at the center of the cells.

4.2.1.1 Conservative approximation of convective fluxes

A numerical scheme for the discretization of the convective fluxes is uniquely defined by the way it approximates the exact convective flux $F_{J+\frac{1}{2}}^d$. This approximation is referred to as the scheme's numerical flux, and denoted here as $\mathcal{F}_{J+\frac{1}{2}}^d$.

Furthermore, if the scheme is conservative, then there exists a unique expression of the numerical flux $\mathcal{F}_{J+\frac{1}{2}}^d$ on both sides of the interface $x_{J+\frac{1}{2}}^d$. Equivalently, conservativity implies:

$$\begin{aligned} \mathcal{F}_{J+\frac{1}{2}}^d \Big|_{\Omega_J} &= \mathcal{F}_{J-\frac{1}{2}}^d \Big|_{\Omega_{J+1}^d} \\ \iff \mathcal{F}_{J+\frac{1}{2}}^d \Big|_{\Omega_J} \cdot \vec{n}_{J+\frac{1}{2}}^d \Big|_{\Omega_J} &= -\mathcal{F}_{J-\frac{1}{2}}^d \Big|_{\Omega_{J+1}^d} \cdot \vec{n}_{J-\frac{1}{2}}^d \Big|_{\Omega_{J+1}^d} \end{aligned} \quad (4.19)$$

The sign change in Eq. (4.19) is due to the outwards-pointing normal vector \vec{n} on the common interface $x_{J+\frac{1}{2}}^d$ having an opposite direction between the cells Ω_J and Ω_{J+1}^d .

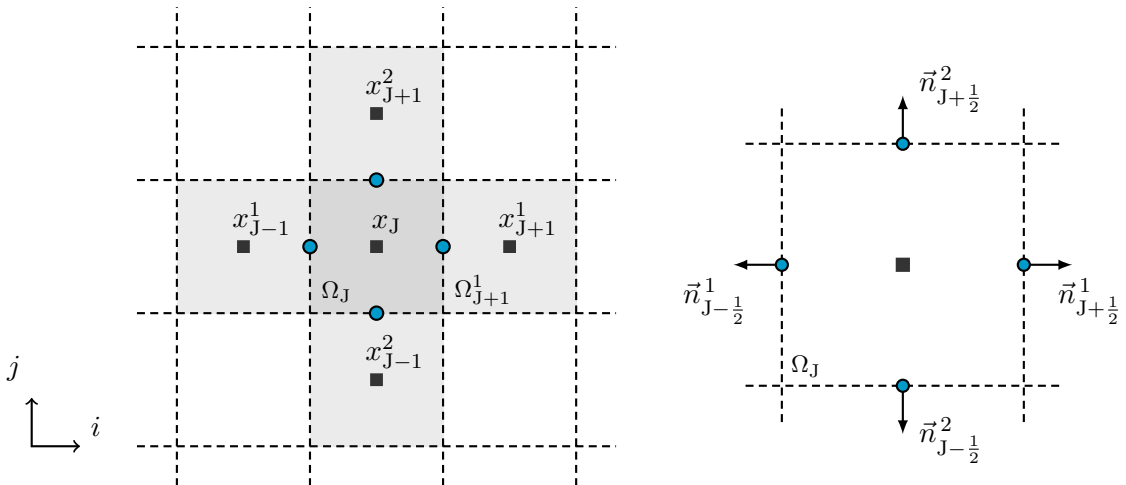


Figure 4.1: Finite volume discretization on a structured grid in two space dimensions. Notations for the close neighborhood of a cell $\Omega_J \equiv \Omega_{i,j}$ and notations for the faces of Ω_J .

The preservation of conservativity is indispensable. First of all, it ensures that the conservation law (4.15) is satisfied at the discrete level. Specifically, Eq. (4.19) dictates that the numerical fluxes on a common interface between two cells cancel. This ensures that mass, momentum and energy are conserved, and not artificially created or destroyed due to the discretization of the physical flux [93]. Furthermore, the use of a conservative scheme is essential in compressible flows to ensure the preservation of jump relations across discontinuities. More importantly however, conservativity is a necessary condition of the Lax-Wendroff theorem [116], which states that if a conservative discretization converges boundedly almost everywhere when the time step and mesh size tend to zero, then it converges towards a weak solution of the conservation law (here Eq. (4.1)). The latter is a fundamental requirement of the numerical discretization.

Moreover, data display a discontinuity on the interface between neighboring cells, known as a Riemann problem. This happens because the FV formulation is based on a cell-volume averaged representation of the data, and these cell-averages are generally different between neighboring cells. The numerical flux is finally a function:

$$\mathcal{F}_{J+\frac{1}{2}}^d = \mathcal{F} \left(W_{J+\frac{1}{2}}^d \Big|_L, W_{J+\frac{1}{2}}^d \Big|_R \right) \quad (4.20)$$

where $(\bullet)|^L, (\bullet)|^R$ respectively denote values associated to the left and right side of the face $x_{J+\frac{1}{2}}^d$. For the state vector and the fluxes, this notation means that their values on the face are approximated using data from the left or right side of the interface. Eq. (4.20) indicates that the Riemann problem on the cell interface is resolved by defining an appropriate reconstruction of variables. This is an essential feature of numerical schemes which is also related to the direction of upwinding, depending on the local characteristic speeds. This reconstruction must in any case be the same on each face to ensure conservation, as shown in Eq. (4.19).

Directional Non-Compact approximations

In most numerical approaches for structured grids, convective fluxes are discretized separately in each direction d . Again, we consider a discretization of the flow equations on a regular Cartesian grid. The averaging and differencing linear operators in direction d can then be introduced as:

$$\begin{aligned} (\mu_1(\bullet))_{i+\frac{1}{2},j,k} &\triangleq \frac{1}{2} ((\bullet)_{i+1,j,k} + (\bullet)_{i,j,k}) & (\delta_1(\bullet))_{i+\frac{1}{2},j,k} &\triangleq (\bullet)_{i+1,j,k} - (\bullet)_{i,j,k} \\ (\mu_2(\bullet))_{i,j+\frac{1}{2},k} &\triangleq \frac{1}{2} ((\bullet)_{i,j+1,k} + (\bullet)_{i,j,k}) & (\delta_2(\bullet))_{i,j+\frac{1}{2},k} &\triangleq (\bullet)_{i,j+1,k} - (\bullet)_{i,j,k} \\ (\mu_3(\bullet))_{i,j,k+\frac{1}{2}} &\triangleq \frac{1}{2} ((\bullet)_{i,j,k+1} + (\bullet)_{i,j,k}) & (\delta_3(\bullet))_{i,j,k+\frac{1}{2}} &\triangleq (\bullet)_{i,j,k+1} - (\bullet)_{i,j,k} \end{aligned} \quad (4.21)$$

since they can greatly simplify the non-compact approximation formulas. These operators are the analogue of (3.26) for more than one space dimensions.

We are considering here the space-time decoupled Directional Non-Compact family of schemes derived by A. Lerat and C. Corre in [126]. Their numerical flux is split in two parts: the consistent part (non-dissipative) which represents the approximation of the convective fluxes and the numerical dissipation part which is introduced to ensure the damping of spurious oscillations. Each is built on a purely centered stencil, but their mutual contribution is equivalent to an upwind scheme.

The schemes are derived starting from a straightforward approximation of the physical flux on the interface:

$$\mathcal{F}_{J+\frac{1}{2}}^d = \mu_d \mathbb{F}^d \quad (4.22)$$

Through the flux balance within the cell Ω_J , this approximation results in a second-order approximation of a convective derivative, as:

$$\frac{1}{\delta_d x_d} (\delta_d \mathcal{F}^d)_J = \frac{1}{\delta_d x_d} \left(\mathcal{F}_{J+\frac{1}{2}}^d - \mathcal{F}_{J-\frac{1}{2}}^d \right) = \frac{\partial \mathbb{F}^d}{\partial x_d} + \mathcal{O}(\tilde{\Delta x}^2) \quad (4.23)$$

where $\tilde{\Delta}x$ denotes a characteristic mesh size. The above approximation is centered and thus purely dispersive, meaning that the introduction of numerical dissipation is necessary for stability. Since (4.22) is centered, it has been easily written in conservative form. It is not however the case for the scheme's numerical dissipation, which should provide upwinding depending on the local direction of wave propagation.

Among the approaches that allow to overcome this difficulty there is the efficient and widely-adopted method proposed by P. Roe [169]. It belongs to the class of flux difference splitting (FDS) schemes, and leads to the conservative numerical flux:

$$\mathcal{F}_{J+\frac{1}{2}}^d = \mu_d F^d - \frac{1}{2} |A_R^d| \delta_d \bar{W} \quad (4.24)$$

where it is implied that the right-hand side is evaluated on the interface $x_{J+\frac{1}{2}}^d$. In the above, A_R is a dissipation matrix, called the Roe average matrix in direction d . The construction of such a matrix is detailed in [169]. One of its basic properties is that $|A_R^d| \delta_d \bar{W} = \delta_d F^d$. The second term in the numerical flux (4.24) is thus equivalent to an artificial dissipation based on the convective flux vector. Furthermore, this dissipation term is first-order accurate to ensure that the numerical flux is a consistent approximation of the convective flux $F_{J+\frac{1}{2}}^d$. The above numerical flux is therefore also first-order accurate.

The Roe scheme has been generalized to higher orders of accuracy in [126]. The consistent part (4.22) can be extended to higher orders by successive corrections of its leading truncation error terms. This results in an approximation of the form (3.27). In turn, high-order numerical dissipation can be introduced through higher-order differences in the dissipative second term of the numerical flux. These differences correspond to high-order even derivative approximations, as shown in Eq. (3.30).

Following this construction principle, the numerical fluxes at third- and fifth-order of accuracy are respectively:

$$\begin{aligned} \mathcal{F}_{J+\frac{1}{2}}^d &= \left(I - \frac{1}{6} \delta_d^2 \right) \mu_d F^d + \frac{1}{12} |A_R^d| \delta_d^3 \bar{W} \\ \mathcal{F}_{J+\frac{1}{2}}^d &= \left(I - \frac{1}{6} \delta_d^2 + \frac{1}{30} \delta_d^4 \right) \mu_d F^d - \frac{1}{60} |A_R^d| \delta_d^5 \bar{W} \end{aligned} \quad (4.25)$$

where I is the identity operator. The above numerical dissipation coefficients were derived by A. Lerat and C. Corre in [126]. In the same work, it was demonstrated that at all orders of accuracy of these upwind schemes, the dissipation coefficient is half the coefficient of the highest-order term in the consistent (non-dissipative) part of the numerical flux. As such, the numerical flux of these schemes at p th-order of accuracy can be written in the general form:

$$\mathcal{F}_{J+\frac{1}{2}}^d = \left(\sum_{\ell=0}^{(p-1)/2} b_\ell \delta_d^{2\ell} \right) \mu_d F^d - \frac{1}{2} b_{\frac{p-1}{2}} |A_R^d| \delta_d^p \bar{W} \quad (4.26)$$

where the real coefficients b are the coefficients of the truncation error terms of the non-dissipative part of the scheme, and are the same as in Eq. (3.27).

These schemes can be equivalently derived by a high-order MUSCL extrapolation [208] on the physical fluxes. In the following, they are thus referred to as FE-MUSCL schemes. Their numerical error, spectral properties and resolvability limits are detailed in the analysis of Chapter 3.

Contrary to the original first-order Roe scheme of Eq. (4.24), the above higher-order extensions are not monotone. For problems containing flow discontinuities, their shock-capturing properties can be improved by replacing the matrix dissipation in Eq. (4.26) with a hybrid low-/high-order numerical dissipation. This type of high-order dissipation was used for instance by J. W. Kim and

D. J. Lee [109], and is a higher-order generalization of the dissipation of A. Jameson et al. [104]. Following this approach, the numerical flux (4.26) at p th-order of accuracy is written:

$$\mathcal{F}_{J+\frac{1}{2}}^d = \left(\sum_{\ell=0}^{(p-1)/2} b_\ell \delta_d^{2\ell} \right) \mu_d \mathbf{F}^d - \lambda_{J+\frac{1}{2}}^d \left[\epsilon^{(2)} \delta_d \overline{W} + \epsilon^{(p+1)} \delta_d^p \overline{W} \right] \quad (4.27)$$

where it is implied that the right-hand side terms are evaluated at the interface $x_{J+\frac{1}{2}}^d$. Above, $\lambda_{J+\frac{1}{2}}^d$ denotes an approximation of the spectral radius of the inviscid flux Jacobian matrix $\frac{\partial F}{\partial W}$ on the interface. The dissipation coefficients $\epsilon^{(2)}$ and $\epsilon^{(p+1)}$ on the faces are given as:

$$\epsilon^{(2)}|_{J+\frac{1}{2}}^d = k_2 \max \left(\nu_J, \nu_{J+1}^d \right) \quad (4.28)$$

and:

$$\epsilon^{(p+1)}|_{J+\frac{1}{2}}^d = \max \left(0, k_{p+1} - \epsilon^{(2)}|_{J+\frac{1}{2}}^d \right) \quad (4.29)$$

where ν_J is the pressure-based shock sensor of A. Jameson et al. [104]:

$$\nu_J = \left| \frac{p_{J+1}^d - 2p_J + p_{J-1}^d}{p_{J+1}^d + 2p_J + p_{J-1}^d} \right| \quad (4.30)$$

Above, k_2 and k_{p+1} are real coefficients that adjust the magnitude of the dissipation term. These are usually chosen $k_2 \in [0, 1]$ and $k_{p+1} \approx \frac{1}{2} b_{\frac{p-1}{2}}$.

The numerical flux (4.27) may be overly dissipative for small scale simulations [77]. In that case, the scaling of numerical dissipation may be improved by multiplying the pressure-based sensor ν in the dissipation coefficient $\epsilon^{(2)}$ of Eq. (4.28) with an additional sensor proposed by F. Ducros et al. [64]. The continuous form of this vorticity-based sensor is given as:

$$\Phi_J = \frac{(\vec{\nabla} \cdot \vec{v}_J)^2}{(\vec{\nabla} \cdot \vec{v}_J)^2 + \|\vec{\nabla} \times \vec{v}_J\|^2 + r_o} \quad (4.31)$$

and provides an additional scaling of the low-order numerical dissipation in (4.27) within vortical flow regions. Above, r_o is a small real constant to prevent the denominator from becoming zero.

4.2.1.2 Approximation of viscous fluxes

Viscous (or diffusive) fluxes are approximated in a FV formulation. They require the calculation of temperature and velocity gradients, as shown in Eq. (4.6). There exist multiple methods to approximate these gradients, and therefore the viscous fluxes, on the center of cell faces. They involve the use of centered schemes, as these fluxes involve purely dissipative effects.

The most straightforward approach consists in calculating gradients at cell centers by the Green-Gauss theorem (described in Section 4.2.1.3). The gradient values at the center of cell faces can then be obtained by simple averaging of the values at the centers of adjacent cells:

$$\left(\vec{\nabla} \psi \right)_{J+\frac{1}{2}}^d = \mu_d \vec{\nabla} \psi = \frac{1}{2} \left(\left(\vec{\nabla} \psi \right)_{J+1}^d + \left(\vec{\nabla} \psi \right)_J \right) \quad (4.32)$$

where ψ denotes a scalar that can be temperature or a component of the velocity vector. It is implied that above gradients represent cell-averaged values. This formula is often referred to as a $5p$ (5-point) scheme.

Alternatively, the calculation of viscous fluxes can be performed on a compact formula. In this approach, gradients are calculated directly on cell face centers by applying the Green-Gauss theorem on shifted cells [93]. Since this stencil involves only direct neighbors of the cell Ω_J , it is often referred to as a $3p$ (3-point) scheme.

Both aforementioned schemes are second-order accurate on regular Cartesian grids. The $3p$ scheme is more computationally expensive, as it requires the calculation of normals and surfaces on the shifted cells, but is more accurate and thus has been preferred over the $5p$ scheme. The two schemes are discussed in greater detail in Section 4.4.4, for the calculation of the high-order VC corrections. After the approximation of velocity and temperature gradients on cell face centers, the calculation of the viscous fluxes of Eq. (4.6) is straightforward.

4.2.1.3 Approximation of gradients

Gradients are calculated in the FV framework based on the Green-Gauss theorem. For a scalar ψ within a control volume Ω , bounded by a surface $S = \partial\Omega$ this theorem gives:

$$\int_{\Omega} \vec{\nabla}\psi d\Omega = \oint_{\partial\Omega} \psi \vec{n} dS \quad (4.33)$$

where \vec{n} denotes the outwards-pointing normal vector on the boundary $\partial\Omega$. The volume-averaged gradient within Ω can then be obtained as:

$$\overline{\vec{\nabla}\psi} = \frac{1}{|\Omega|} \oint_{\partial\Omega} \psi \vec{n} dS \quad (4.34)$$

In a FV formulation, Eq. (4.34) is approximated by:

$$\overline{\vec{\nabla}\psi} = \frac{1}{|\Omega|} \sum_{f=1}^{N_{\text{faces}}} \overline{\psi}_f \vec{n}_f |S_f| \quad (4.35)$$

where $\overline{\psi}_f$ denotes the face-averaged value of ψ and $|S_f|$ the surface area of the face S_f . On regular Cartesian grids, the face-averaged values $\overline{\psi}_f = \overline{\psi}_{J+\frac{1}{2}}^d$ can be consistently approximated by a simple average of neighboring cell-averaged values as:

$$\overline{\psi}_{J+\frac{1}{2}}^d = \left(\mu_d \overline{\psi}\right)_{J+\frac{1}{2}} = \frac{1}{2} \left(\overline{\psi}_{J+1}^d + \overline{\psi}_J\right) \quad (4.36)$$

The approximation (4.35) is then second-order accurate on regular Cartesian grids.

However, the Green-Gauss method does not always provide sufficient accuracy in the calculation of gradients in complex flows, and turbulent flows in particular. For calculations on structured Cartesian grids, velocity gradients can also be calculated in a finite difference approach, using large stencils. This can be written:

$$\left. \frac{\partial(\bullet)}{\partial x_d} \right|_{x_J} = \frac{1}{\delta_d x_d} \sum_{\ell=-k}^r a_{\ell} (\bullet)_{J+\ell}^d \quad (4.37)$$

where r, k determine the computational stencil and a_{ℓ} are the stencil coefficients.

One possibility is the use of centered finite difference schemes that achieve maximum order of accuracy for a given stencil size, as in Eq. (3.27). Alternatively, the schemes may use optimized coefficients a_{ℓ} , such as the Dispersion-Relation Preserving (DRP) schemes proposed by C. K. W. Tam and J. C. Webb [203], which were further extended by C. Bogey and C. Bailly [20]. These sacrifice optimal order of accuracy for the sake of minimized phase approximation error in the wavenumber space, especially in the medium- to higher-frequency range.

4.2.2 Time integration

The present work investigates the numerical calculation of unsteady flows, although the developments are not restricted to the unsteady case. Computations were performed using explicit

algorithms of the Runge-Kutta (RK) family, already discussed in Section 3.4.5. These are used to integrate differential equations in the form:

$$\frac{\partial W}{\partial t} = \mathcal{L}(W) \quad (4.38)$$

For the case of the Navier-Stokes equations, \mathcal{L} collectively denotes the space-associated terms. Due to the form (4.38), these may also be referred to as the right-hand side terms. In a low-storage formulation, explicit RK algorithms are of the general form:

$$\begin{aligned} W^{(0)} &= W^n \\ W^{(q)} &= W^{(0)} + d_q \Delta t \mathcal{L}(W^{(q-1)}), \quad \text{for } q = 1, \dots, k \\ W^{n+1} &= W^{(k)} \end{aligned} \quad (4.39)$$

where k denotes the number of stages and d_q are the RK scheme coefficients.

The following computations were performed using two different schemes of the RK family. The first is the classical 4-stage RK scheme (RK4), which is fourth-order accurate for linear problems and second-order accurate in the general case. The other one is the formally second-order accurate 6-stage RK scheme developed by C. Bogey and C. Bailly in [20], following the work of F. Q. Hu et al. [94]. This was derived through an optimization of the coefficients d_q , with respect to the scheme's dispersion and dissipation error in the frequency space.

4.3 Development of a high-order Vorticity Confinement method

This section presents the development of high-order Vorticity Confinement corrections, based on the VC2 formulation of J. Steinhoff. First, the original first-order accurate VC2 formulation is presented in the compressible flow framework. Extensions of the method are then developed to third- and fifth-order of accuracy, based on high-order differences. Finally, the original VC2 method and its high-order extensions are analyzed, and their analogy with the scalar formulation of Chapter 3 is discussed. The developments of this section concern the continuous problem and its theoretical analysis. The numerical implementation of the method is discussed separately in Section 4.4.

4.3.1 Original VC2 formulation

The VC2 formulation was presented by J. Steinhoff et al. [192, 193] to model thin flow features as nonlinear solitary waves. It represents an improvement of the original VC1 in two primary aspects: it has an equivalent conservative form and presents no singularity at the vortex core. A more detailed review of the historical development of the VC method can be found in Section 2.2.7. Due to the aforementioned reasons, the high-order extensions developed in this thesis are restricted to the VC2 formulation.

The original first-order VC2 formulation was developed by J. Steinhoff et al. for incompressible flows, where the Vorticity Confinement term was added in the flow equations as a source term. Nonetheless, its interpretation in a compressible flow framework is ambiguous. A rather popular approach has been proposed by G. Hu et al. [95, 96], where the VC term has been considered to be a body force term and thus included in the energy equation. Results have however demonstrated that the VC contribution to the energy equation may lead to unphysical density and temperature variations [41, 52]. The latter is of particular importance at high Mach number flows. Moreover, there is no objective reason for the interpretation of VC as a body force term with a physical counterpart in the compressible Navier-Stokes equations. Consequently, the approach adopted here is that of M. Costes [41], where VC is interpreted as a purely numerical correction.

This interpretation has the following two implications. First, the VC contribution is only included in the momentum equation. Second, it should be consistent with the original Navier-Stokes equations. In other words, the VC correction should tend to zero when the continuous equations are

recovered, i.e. when the mesh is sufficiently refined, similarly to baseline artificial dissipation terms. This is achieved through the use of undivided differences in the numerical discretization of the VC correction, which is discussed in detail within Section 4.4. Nonetheless, in the frame of Section 4.3, both the original VC term and its high-order extensions will be written as terms of the continuous momentum conservation equation. This is done to facilitate the theoretical analyses of the present chapter, as well as the extension of the VC method to higher orders of accuracy, which is performed by introducing higher-order derivatives in the continuous framework.

The integration of the VC method in the flow equations is straightforward. The integral form of the Navier-Stokes momentum equation, including the VC2 term, is written:

$$\frac{\partial}{\partial t} \int_{\Omega} \rho \vec{v} d\Omega + \oint_S \rho \vec{v} (\vec{v} \cdot \vec{n}) dS + \oint_S p \cdot \vec{n} dS - \oint_S \bar{\tau} \cdot \vec{n} dS = \int_{\Omega} \vec{f} d\Omega \quad (4.40)$$

In turn, the conservative differential form of the momentum conservation equation is:

$$\frac{\partial \rho \vec{v}}{\partial t} + \vec{\nabla} \cdot (\rho \vec{v} \otimes \vec{v} + p \vec{I} - \bar{\tau}) = \vec{f} \quad (4.41)$$

In both cases, \vec{f} is the Vorticity Confinement source term in the VC2 formulation:

$$\vec{f} = -\vec{\nabla} \times (\mu \vec{\omega} - \varepsilon \vec{w}) \quad (4.42)$$

The above VC term is composed of two parts. The first is a linear artificial dissipation term with coefficient μ ¹. Unlike the baseline numerical dissipation, this is aligned with the vorticity vector $\vec{\omega} = \vec{\nabla} \times \vec{v}$. The most interesting is the second part of the term (4.42), which represents a nonlinear negative dissipation with coefficient ε . This part is the analogue of the confinement correction in the scalar case (Eq. (3.33)). It is based on a vector \vec{w} aligned with vorticity:

$$\vec{w} = \frac{\vec{\omega}}{\|\vec{\omega}\|} \tilde{h}(\omega_{\ell}) \quad (4.43)$$

where $\omega_{\ell} = \|\vec{\omega}_{\ell}\|$. The magnitude of \vec{w} is equal to the harmonic mean of the modulus of vorticity around the neighboring cells:

$$\tilde{h}(\omega_{\ell}) = N_c \left(\sum_{\ell=1}^{N_c} \|\vec{\omega}_{\ell}\|^{-1} \right)^{-1} \quad (4.44)$$

which represents a nonlinear spatial average. The above harmonic mean at a cell Ω_J is calculated using data from cells in its complete neighborhood, i.e. cells which share at least one node with the cell Ω_J and the cell itself. On a structured mesh, this corresponds to $N_c = 9$ in two space dimensions, and $N_c = 27$ in three space dimensions.

With respect to the conservative vector formulation (4.1) of the Navier-Stokes equations, the above VC2 formulation is equivalent to a source term vector:

$$Q_S = \begin{bmatrix} 0 \\ -\vec{\nabla} \times (\mu \vec{\omega} - \varepsilon \vec{w}) \cdot \vec{e}_i \\ -\vec{\nabla} \times (\mu \vec{\omega} - \varepsilon \vec{w}) \cdot \vec{e}_j \\ -\vec{\nabla} \times (\mu \vec{\omega} - \varepsilon \vec{w}) \cdot \vec{e}_k \\ 0 \end{bmatrix} \quad (4.45)$$

where $\vec{e}_i, \vec{e}_j, \vec{e}_k$ are the unit vectors in each space direction.

As the VC term is added to reduce the numerical dissipation of vortices, the introduction of an additional positive dissipation term in Eq. (4.42) may appear counterintuitive. This is especially the case due to the absence of an equivalent term in the scalar formulation of Section 3.2. The two formulations cannot however be directly compared, as the notion of vorticity does not exist in scalar conservation laws. Specifically:

¹not to be confused with the dynamic viscosity μ of the fluid.

- for the scalar transport equation, the confinement correction is applied directly to the physical flux. As a result, the role of the artificial dissipation term in Eq. (4.42) can be taken by the numerical dissipation of the baseline numerical scheme.
- for the Navier-Stokes equations, the confinement correction is computed based on vorticity, and not on the physical flux. The numerical dissipation of the baseline scheme (4.26) is thus fundamentally different from the positive dissipation part of the VC term (4.42). The numerical dissipation in Eq. (4.42) is both explicitly based on vorticity and independent of the baseline dissipation.

In cases where the baseline scheme's dissipation is low or not explicitly known, the numerical dissipation in Eq. (4.42) can thus be augmented to dominate the baseline dissipation and give more freedom in the adjustment of the strength of the VC term. The influence of this choice is discussed in Section 4.3.4 and further investigated in later sections, via application to numerical experiments.

The real coefficients μ, ε in Eq. (4.42) or Eq. (4.45) are usually taken proportionate to a characteristic mesh size, i.e. $\mu, \varepsilon \propto \tilde{\Delta}x$. This choice renders the VC term formally first-order accurate. More importantly though, as discussed previously, it ensures that the VC correction tends to zero with mesh refinement. On Cartesian grids, this is equivalent to using undivided differences in the calculation of the curl in Eq. (4.42), which in turn is similar to the formulation of numerical dissipation terms.

4.3.2 Analogy with the scalar formulation

The VC term of Eq. (4.42) is not a direct analogue of the confinement formulation (3.33) in the case of the linear transport equation. The analogy can be revealed by considering the transport equation for vorticity.

The vorticity transport equation is obtained starting from the momentum conservation equation (4.41). In non-conservative form, this is written:

$$\rho \frac{\partial \vec{v}}{\partial t} + \rho(\vec{v} \cdot \vec{\nabla})\vec{v} = -\vec{\nabla}p + \vec{\nabla} \cdot \vec{\tau} + \vec{f} \quad (4.46)$$

Considering now the vector identity

$$(\vec{v} \cdot \vec{\nabla})\vec{v} = \vec{\nabla} \left(\frac{\vec{v}^2}{2} \right) - \vec{v} \times (\vec{\nabla} \times \vec{v}) \quad (4.47)$$

an equivalent form of Eq. (4.46) is:

$$\frac{\partial \vec{v}}{\partial t} + \vec{\nabla} \left(\frac{\vec{v}^2}{2} \right) + \vec{\omega} \times \vec{v} = \frac{1}{\rho} \left(-\vec{\nabla}p + \vec{\nabla} \cdot \vec{\tau} + \vec{f} \right) \quad (4.48)$$

Taking the curl of the momentum equation (4.48) gives the vorticity transport equation:

$$\frac{\partial \vec{\omega}}{\partial t} + (\vec{v} \cdot \vec{\nabla})\vec{\omega} = (\vec{\omega} \cdot \vec{\nabla})\vec{v} - \vec{\omega}(\vec{\nabla} \cdot \vec{v}) - \vec{\nabla} \frac{1}{\rho} \times \vec{\nabla}p + \vec{\nabla} \times \left(\frac{1}{\rho} \vec{\nabla} \cdot \vec{\tau} \right) + \vec{\nabla} \times \frac{\vec{f}}{\rho} \quad (4.49)$$

where the left-hand side represents the material derivative of vorticity.

A transport equation for specific vorticity can then be derived by dividing Eq. (4.49) with density. The second term in the right-hand side of Eq. (4.49) represents the stretching of vorticity due to effects of compressibility. Its contribution can be substituted using the Navier-Stokes mass conservation equation as:

$$-\frac{\vec{\omega}}{\rho}(\vec{\nabla} \cdot \vec{v}) = \frac{\vec{\omega}}{\rho^2} \left(\frac{\partial \rho}{\partial t} + \vec{v} \cdot \vec{\nabla} \rho \right) \quad (4.50)$$

Taking advantage of the product rule, the following relations can also be obtained for the contribution of the left-hand side terms of Eq. (4.49):

$$\frac{1}{\rho} \frac{\partial \vec{\omega}}{\partial t} = \frac{\partial(\vec{\omega}/\rho)}{\partial t} + \frac{\vec{\omega}}{\rho^2} \frac{\partial \rho}{\partial t} \quad (4.51)$$

$$\frac{1}{\rho} (\vec{v} \cdot \vec{\nabla}) \vec{\omega} = \vec{v} \cdot \vec{\nabla}(\vec{\omega}/\rho) + \frac{\vec{\omega}}{\rho^2} (\vec{v} \cdot \vec{\nabla} \rho) \quad (4.52)$$

The specific vorticity transport equation is finally written:

$$\frac{\partial(\vec{\omega}/\rho)}{\partial t} + \vec{v} \cdot \vec{\nabla}(\vec{\omega}/\rho) = (\vec{\omega}/\rho) \cdot \vec{\nabla} \vec{v} + \frac{1}{\rho^3} (\vec{\nabla} \rho \times \vec{\nabla} p) + \frac{1}{\rho} \vec{\nabla} \times \left(\frac{1}{\rho} \vec{\nabla} \cdot \vec{\tau} \right) + \frac{1}{\rho} \vec{\nabla} \times \frac{\vec{f}}{\rho} \quad (4.53)$$

Note that Eqs. (4.51)-(4.52) allow to eliminate the effects of vortex stretching due to compressibility, that is the terms in Eq. (4.50). The direct analysis of Eq. (4.53) is complex as it represents the complete dynamics of specific vorticity in the Navier-Stokes equations.

A more informative analysis can however be performed by considering the case of a 2D isolated vortex in inviscid adiabatic flow. In that case, the first two terms on the right-hand side of Eq. (4.53) vanish respectively because the velocity vector lies in a plane perpendicular to vorticity and because the gradients of pressure and density are aligned. The third term on the right-hand side also vanishes in inviscid adiabatic flow. The VC term contribution can be simplified in the case of low Mach number flow, for which density variations can be neglected:

$$\vec{\nabla} \times \frac{\vec{f}}{\rho} = \frac{1}{\rho} (\vec{\nabla} \times \vec{f}) + \left(\vec{\nabla} \frac{1}{\rho} \right) \times \vec{f} \quad (4.54)$$

$$\cong \frac{1}{\rho} (\vec{\nabla} \times \vec{f}) \quad (4.55)$$

The contribution of the VC term can then be developed as:

$$\begin{aligned} \vec{\nabla} \times \vec{f} &= \vec{\nabla}^2 (\mu \vec{\omega} - \varepsilon \vec{w}) - \vec{\nabla} \left(\vec{\nabla} \cdot (\mu \vec{\omega} - \varepsilon \vec{w}) \right) \\ &= \vec{\nabla}^2 (\mu \vec{\omega} - \varepsilon \vec{w}) \end{aligned} \quad (4.56)$$

because:

$$\vec{\nabla} \cdot (\mu \vec{\omega}) = \mu \vec{\nabla} \cdot (\vec{\nabla} \times \vec{v}) = 0 \quad (4.57)$$

$$\vec{\nabla} \cdot (\varepsilon \vec{w}) = \varepsilon \vec{\nabla} \cdot \left(\frac{\vec{\omega}}{\|\vec{\omega}\|} \tilde{h}(\omega_\ell) \right) = \varepsilon \vec{\omega} \cdot \vec{\nabla} \left(\frac{\tilde{h}(\omega_\ell)}{\|\vec{\omega}\|} \right) + \varepsilon \frac{\tilde{h}(\omega_\ell)}{\|\vec{\omega}\|} \vec{\nabla} \cdot \vec{\omega} = 0 \quad (4.58)$$

where the first term in Eq. (4.58) is zero because vorticity is perpendicular to the gradient of $\tilde{h}(\omega_\ell)/\|\vec{\omega}\|$ in two space dimensions. Finally, the specific vorticity transport equation (4.53) reduces to:

$$\frac{\partial(\vec{\omega}/\rho)}{\partial t} + \vec{v} \cdot \vec{\nabla}(\vec{\omega}/\rho) - \frac{1}{\rho^2} \vec{\nabla}^2 (\mu \vec{\omega} - \varepsilon \vec{w}) = 0 \quad (4.59)$$

$$\text{or} \quad \frac{\partial(\omega/\rho)}{\partial t} + \vec{v} \cdot \vec{\nabla}(\omega/\rho) - \frac{1}{\rho^2} \vec{\nabla}^2 (\mu \omega - \varepsilon \tilde{h}(\omega_\ell)) = 0 \quad (4.60)$$

The above equation displays certain analogies with the equivalent differential equation of Eqs. (3.23), (3.35) for schemes with confinement in the scalar case. First, the contribution of the linear dissipation part of the VC term \vec{f} to the vorticity transport equation is similar to that of the linear artificial dissipation \mathcal{D}^m in the scalar case (see Eqs. (3.29) and (3.31)). Second, the balance between the positive (linear) dissipation and negative (nonlinear) dissipation part of the VC term \vec{f} is similar to the balance between baseline dissipation and confinement in the scalar case. In Eq. (4.60), the ratio

ε/μ is the equivalent of the value of ε in Eqs. (3.23), (3.35). Note also that under the assumption of quasi-incompressible flow, a similar form to Eq. (4.60) can also be obtained directly from the vorticity transport equation (4.49).

Furthermore, it is reminded that the contributions of the VC term are numerical (anti-) dissipation terms that tend to zero with mesh refinement and not consistent terms of the specific vorticity transport equation (see Section 4.3.1). By ignoring the baseline scheme's dissipation, the asymptotic solutions of Eq. (4.60) are thus driven by the VC term. In that case, it has been shown that these asymptotic solutions depend on the mesh size for given values of the confinement parameters [47], similarly to what is known for the asymptotic solutions of confinement for the linear transport equation (see Section 3.5.1).

4.3.3 Extension of the Vorticity Confinement method to higher orders

The first-order VC2 formulation of Section 4.3.1 has some specific advantages. First, it is rotationally invariant, an essential property since it is consistent with the physics of isolated vorticity. Second, it is independent of the baseline numerical scheme. The VC2 term can thus be applied independently of the baseline numerical method, although different values of the confinement parameters μ , ε might be necessary to adapt the magnitude of the VC term to the baseline scheme's dissipation. In the discretized problem, it is also reasonable that the derivatives of the VC term are evaluated similarly to the gradients of the baseline method. Last, it has an equivalent conservative form, a subject which will be discussed separately in Section 4.3.5. It is thus natural that the preservation of these properties is advantageous also for high-order extensions of the method.

As they represent (globally negative) numerical dissipation, high-order VC corrections should be based on higher-order differences. These in turn represent approximations of high-order derivatives, similarly to the design of the numerical dissipation of baseline schemes (as shown in Eq. (3.30)). A straightforward way to introduce higher-order derivatives while maintaining the rotational invariance property of the original VC is through vector operators.

As such, the curl operator can be recursively applied on the VC term of Eq. (4.42) to increase the order of differencing, by analogy with the $\delta_d(\bullet)$ operator in directional sense. By introducing the vector $\vec{\alpha} = -(\mu\vec{\omega} - \varepsilon\vec{w})$ to simplify the equations, the curl of the VC term \vec{f} is written:

$$\vec{\nabla} \times \vec{f} = \vec{\nabla} \times \vec{\nabla} \times \vec{\alpha} = \vec{\nabla} (\vec{\nabla} \cdot \vec{\alpha}) - \vec{\nabla}^2 \vec{\alpha} \quad (4.61)$$

Subsequently, by re-applying the curl operator we obtain:

$$\begin{aligned} \vec{f}_3 &= \vec{\nabla} \times \vec{\nabla} \times \vec{f} \\ &= \vec{\nabla} \times (\vec{\nabla} (\vec{\nabla} \cdot \vec{\alpha}) - \vec{\nabla}^2 \vec{\alpha}) \\ &= \vec{\nabla} \times (\vec{\nabla}^2 (\mu\vec{\omega} - \varepsilon\vec{w})) \end{aligned} \quad (4.62)$$

which is composed of fourth-order derivatives of velocity components, as opposed to the term of Eq. (4.42) which is built on second derivatives of velocity. A higher-order derivative extension of VC can therefore be obtained by taking the Laplacian of the vector $\vec{\alpha}$. Furthermore, the alternate sign of higher-order derivative terms is naturally introduced by the recursive applications of the curl operator.

The same process can be applied to further increase the order of differencing. A fifth-order VC term is then obtained by taking the bi-Laplacian of the VC term of Eq. (4.42), as:

$$\vec{f}_5 = \vec{\nabla} \times \vec{\nabla} \times \vec{f}_3 = \vec{\nabla} \times (\vec{\nabla}^4 \vec{\alpha}) = -\vec{\nabla} \times (\vec{\nabla}^4 (\mu\vec{\omega} - \varepsilon\vec{w})) \quad (4.63)$$

Since the higher difference alone does not suffice, the use of undivided differences in the computation of the Laplace operator will ensure consistency with the original partial differential equation and naturally provide the increased order of accuracy for both Eqs (4.62) and (4.63). Again, this is equivalent to the design of directional high-order numerical dissipation.

Note also that the higher-order VC extensions remain independent from the choice of space discretization or time integration scheme. Furthermore, they remain rotationally invariant, as they are based on the Laplace operator.

The analogy of the high-order VC extensions (4.62) and (4.63) with the original term (4.42), should be investigated with respect to their contribution to the vorticity transport equation (4.60). In the case of an isolated 2D vortex in inviscid quasi-incompressible flow, the curl of the third-order VC term is equal to:

$$\begin{aligned}
\vec{\nabla} \times \vec{f}_3 &= -\vec{\nabla} \times (\vec{\nabla} \times \vec{\nabla}^2 \vec{\alpha}) \\
&= -\vec{\nabla} \vec{\nabla} \cdot (\vec{\nabla}^2 (\mu \vec{\omega} - \varepsilon \vec{w})) + \vec{\nabla}^2 (\vec{\nabla}^2 (\mu \vec{\omega} - \varepsilon \vec{w})) \\
&= -\vec{\nabla} \vec{\nabla} \cdot (\vec{\nabla} (\vec{\nabla} \cdot \mu \vec{\omega} - \vec{\nabla} \cdot \varepsilon \vec{w}) - \vec{\nabla} \times \vec{\nabla} \times (\mu \vec{\omega} - \varepsilon \vec{w})) + \vec{\nabla}^2 (\vec{\nabla}^2 (\mu \vec{\omega} - \varepsilon \vec{w})) \\
&= -\vec{\nabla} \vec{\nabla} \cdot (\vec{\nabla} (\vec{\nabla} \cdot \mu \vec{\omega} - \vec{\nabla} \cdot \varepsilon \vec{w})) + \vec{\nabla} \vec{\nabla} \cdot (\vec{\nabla} \times \vec{\nabla} \times (\mu \vec{\omega} - \varepsilon \vec{w})) + \vec{\nabla}^2 (\vec{\nabla}^2 (\mu \vec{\omega} - \varepsilon \vec{w})) \\
&= \vec{\nabla}^2 (\vec{\nabla}^2 (\mu \vec{\omega} - \varepsilon \vec{w}))
\end{aligned} \tag{4.64}$$

due to Eq. (4.57) and because vorticity is perpendicular to the gradient of the harmonic mean of vorticity modulus in two space dimensions (see Eq. (4.58)). The new term has therefore an analogous contribution to the original VC term in Eq. (4.59), expressed as the sum of a high-order (linear) positive dissipation and a high-order (nonlinear) negative dissipation term. The analysis is equivalent for the fifth-order VC term.

In three space dimensions, the vector Laplacian of Eq. (4.62) is developed as:

$$\vec{\nabla}^2 \vec{\alpha} = \vec{\nabla} (\vec{\nabla} \cdot \vec{\alpha}) - \vec{\nabla} \times \vec{\nabla} \times \vec{\alpha} \tag{4.65}$$

Provided that $\vec{\alpha}$ is a continuous function in space and for a Cartesian coordinate system, cross derivatives cancel and the vector Laplacian (4.65) degrades to the scalar Laplacian of each component:

$$\vec{\nabla}^2 \vec{\alpha} = (\Delta \alpha_x, \Delta \alpha_y, \Delta \alpha_z) \tag{4.66}$$

This simplification is important for high-order VC extensions, as the numerical calculation of the term of Eq. (4.66) is less complex than the one of Eq. (4.65). With respect to the conservative vector formulation of the system (4.1), the third-order VC term can be written as the contribution of a source term vector:

$$Q_S = \begin{bmatrix} 0 \\ -(\vec{\nabla} \times \vec{\nabla}^2 \vec{\alpha}) \cdot \vec{e}_i \\ -(\vec{\nabla} \times \vec{\nabla}^2 \vec{\alpha}) \cdot \vec{e}_j \\ -(\vec{\nabla} \times \vec{\nabla}^2 \vec{\alpha}) \cdot \vec{e}_k \\ 0 \end{bmatrix} \tag{4.67}$$

where again derivatives should be calculated in an undivided difference form, so that the above term tends to zero with mesh refinement at third-order of accuracy. This is detailed in Section 4.4.

As already discussed above, the VC term introduces anti-dissipation based on high-order even derivatives of velocity components. Contrary to the baseline numerical dissipation however, in the case of VC these derivatives are mixed and not purely one-dimensional (see e.g. Eq. (4.67)). This can be revealed by developing the curl and the vorticity vector in Eq. (4.42) in terms of velocity components. The development is more straightforward if, for the sake of illustration, the nonlinear part of the VC term is neglected (i.e. by taking $\varepsilon=0$). The same can be done for the higher-order VC terms of Eqs. (4.62), (4.63).

Finally, it has already been remarked by J. Steinhoff that other nonlinear functions could be used to formulate the anti-dissipative part of the VC term, instead of the harmonic mean of Eq. (4.44). The requirements for such functions are discussed in [195]. It should be noted that although such alternatives are not investigated in the present thesis, the above high-order extension methodology is not limited to the harmonic mean. Therefore, it should be directly applicable for the case of any other nonlinear function.

4.3.4 Discussion of the confinement parameters

The magnitude of both the original VC method (4.42) and its high-order extensions (4.62), (4.63) is defined by the two confinement parameters μ and ε . These parameters must be constant in space to ensure the preservation of conservativity, at least if the VC term is integrated in the Navier-Stokes equations as a source term. This can be seen by the numerical flux contribution of the VC term, discussed separately in Section 4.3.5.

The confinement parameters are here taken constant both in space and in time. Apart from being advantageous in terms of preservation of conservativity and reduced computational complexity, this strategy is also analogous to the numerical dissipation of the baseline numerical flux (4.26). In both cases, the dissipation coefficient is constant in space and time, and the scaling of (anti-) dissipation is obtained through the high-order derivatives.

The selection of the confinement parameters is done on a trial-and-error basis but their role is quite straightforward:

- Being the coefficient of an artificial dissipation that is added to that of the baseline scheme in vortical regions, the value of μ should be kept to a minimum, and even set to zero, when possible. It might however be the case that the dissipation of some baseline schemes is not enough to balance the nonlinear negative dissipation part of VC, or that the numerical dissipation of the baseline scheme is not explicitly known. In such cases a small nonzero value of μ can be used to introduce some stabilizing rotational dissipation in vortical regions. For the dissipative FE-MUSCL schemes used in the present work on Cartesian grids, we have found that the value of μ can generally be set to zero without sacrificing the scheme's robustness, and further reducing dissipation for the same values of ε .
- On the other hand, the confinement parameter ε plays the primary role in adjusting the magnitude of VC to the dissipation error of the baseline flux discretization. For schemes with explicitly known artificial dissipation, the value of ε is usually chosen to be of the order of magnitude of the artificial dissipation coefficient. This is similar to the strategy used for the scalar confinement corrections of Chapter 3.

The choice of the confinement parameters and the influence of their values is further discussed in Section 4.5.2, by means of a parametric study.

In the presentation of results it has been chosen to express the values of the confinement parameters as ε and μ/ε . The first is then a measure of the intensity of the anti-dissipative nonlinear confinement part and the second represents the ratio between explicit artificial dissipation and confinement within the VC term. Note also that under this notation, it is the value of ε that defines the magnitude of the VC correction.

Dimensional analysis

Similarly to the VC1 formulation, the confinement parameters μ , ε in Eq. (4.42) are dimensional. Their dimensions can be retrieved from the Navier-Stokes momentum equation, the terms of which represent body forces and have dimensions of density times acceleration: $\text{kg} \cdot \text{m}^{-2} \cdot \text{s}^{-2}$. Since consistency dictates that either the coefficients μ , ε should be multiplied with the mesh size or undivided differences should be used in the calculation of the curl, the dimensions of the VC source term of Eq. (4.42) are:

$$[\mathbf{f}] = [\varepsilon] [\boldsymbol{\omega}] = [\varepsilon] [v] [L]^{-1} \quad (4.68)$$

where $[\bullet]$ is used to denote the SI units of a physical quantity. Also, it has been assumed that $\mu = 0$ to simplify the equations, as μ and ε have the same dimensions. By prescribing the dimensions of the VC source term, the dimensions of the confinement parameter ε are found to be:

$$[\varepsilon] = \text{kg} \cdot \text{m}^{-2} \cdot \text{s}^{-1} \quad (4.69)$$

which are equal to the dimensions of density times velocity. They are also equivalent to the dimensions of dynamic fluid viscosity divided by a characteristic length scale. For dimensional calculations, a possible dimensionalization of the confinement parameter ε is then:

$$\varepsilon^* = \rho_{\text{ref}} v_{\text{ref}} \varepsilon \quad (4.70)$$

where ε^* denotes the dimensional confinement parameter and ρ_{ref} , v_{ref} respectively denote a characteristic density and velocity scale. The analysis for the confinement parameter μ is identical to the case of ε . Note also that since high-order VC corrections are computed on undivided differences, the dimensions of the confinement parameters μ and ε remain unchanged at higher orders.

4.3.5 Equivalence with an anti-dissipative flux correction

The VC2 formulation of Steinhoff represents an amelioration of the original VC1 since it displays no singularity at the vortex core and has an equivalent conservative form. The latter is an essential property of the discretization, particularly for the calculation of compressible flows.

The equivalent conservative form of the VC term in Eq. (4.40) can be revealed by first establishing an integral relationship for the curl. For this purpose, we are considering two sample real vector fields \vec{q} , \vec{b} , smooth in the neighborhood of a volume Ω bounded by a surface $S = \partial\Omega$. An application of the divergence theorem for the cross product of these two vectors within Ω gives:

$$\int_{\Omega} \vec{\nabla} \cdot (\vec{q} \times \vec{b}) \, d\Omega = \oint_{\partial\Omega} (\vec{q} \times \vec{b}) \cdot \vec{n} \, dS \quad (4.71)$$

where \vec{n} is the unit vector normal to the boundary $\partial\Omega$. By expanding the left-hand side and performing a circular shift of the operands on the right-hand side we get:

$$\int_{\Omega} \vec{b} \cdot (\vec{\nabla} \times \vec{q}) - \vec{q} \cdot (\vec{\nabla} \times \vec{b}) \, d\Omega = \oint_{\partial\Omega} \vec{b} \cdot (\vec{n} \times \vec{q}) \, dS \quad (4.72)$$

If then, without loss of generality, we assume that the vector field \vec{b} remains constant within the volume Ω we obtain that:

$$\int_{\Omega} \vec{\nabla} \times \vec{q} \, d\Omega = \oint_S \vec{n} \times \vec{q} \, dS \quad (4.73)$$

which is a three-dimensional variation of the classical Kelvin-Stokes theorem. A more rigorous statement of this proof is given by S. Markvorsen [137].

Applied to the volume integral of the VC source term of Eq. (4.42), Eq. (4.73) gives:

$$-\int_{\Omega} \vec{\nabla} \times (\mu\vec{\omega} - \varepsilon\vec{w}) \, d\Omega = -\oint_S \vec{n} \times (\mu\vec{\omega} - \varepsilon\vec{w}) \, dS \quad (4.74)$$

Finally, the integral form (4.40) of the Navier-Stokes momentum equation writes:

$$\frac{\partial}{\partial t} \int_{\Omega} \rho \vec{v} \, d\Omega + \oint_S \rho \vec{v} (\vec{v} \cdot \vec{n}) \, dS + \oint_S p \cdot \vec{n} \, dS - \oint_S \bar{\tau} \cdot \vec{n} \, dS = -\oint_S \vec{n} \times (\mu\vec{\omega} - \varepsilon\vec{w}) \, dS \quad (4.75)$$

in which case the VC correction can be assimilated within the surface integral alongside physical fluxes as:

$$\frac{\partial}{\partial t} \int_{\Omega} \rho \vec{v} \, d\Omega + \oint_S \left[(\rho \vec{v} \otimes \vec{v} + p \bar{I} - \bar{\tau}) \cdot \vec{n} - (\mu\vec{\omega} - \varepsilon\vec{w}) \times \vec{n} \right] \, dS = 0 \quad (4.76)$$

Eq. (4.76) demonstrates that the VC2 formulation is equivalent to a nonlinear anti-dissipative flux correction applied in vortical regions. In principle, this is not so different from the idea of limited downwind fluxes or anti-dissipative flux corrections applied for the sharpening of contact discontinuities [61, 231]. For the case of VC however, the correction is explicitly formulated for vorticity rather than the approximation of convective terms. It naturally follows from Eqs. (4.62) and (4.63) that the same property stands for the high-order VC extensions.

4.4 Numerical implementation of the high-order Vorticity Confinement method

This section discusses the numerical implementation of the first-order VC2 method and its high-order extensions, developed in Section 4.3. Specifically, it addresses the approximation of high-order derivatives, the calculation of the VC correction on zone boundaries and the selection of vortical flow regions to apply the VC correction.

The Vorticity Confinement method can be implemented in two formulations: as a source term in the form of Eq. (4.42) or as a numerical flux correction in the form of Eq. (4.76). The same possibilities exist for the high-order extensions of the method. The two formulations are equivalent, except on the vortex boundary due to the different deactivation of the VC corrections. This is detailed in Section 4.4.3. The numerical calculations presented in this manuscript have been performed using a source term implementation of the VC method.

4.4.1 Recursive approximation of derivatives

The calculation of high-order derivatives is an essential part of the VC method. Already the original VC2 correction of Eq. 4.42 involves second derivatives of the velocity vector. Respectively the third-order and fifth-order terms of Eqs. (4.62) and (4.63) involve fourth- and sixth-order derivatives. These are of the same order as the high-order numerical dissipation terms in the case of the FE-MUSCL schemes of Section 4.2.1.1.

As the VC correction is formulated independently of the baseline scheme, the calculation of derivatives in this case is treated also separately. These derivatives can be calculated either by the recursive application of a derivation operator, or directly using larger stencils in a finite difference formulation. The latter can be very efficient on Cartesian grids, but else it is sensitive to the mesh quality if mesh curvature corrections are not applied. It is especially the case because high-order derivatives are calculated. We have thus chosen here the approximation of derivatives by the first approach, that is by recursive application of a compact operator for the approximation of first-order derivatives (i.e. the gradient). This approach has certain advantages:

- The derivation operator is explicit and computationally compact, meaning that only the close neighborhood of a control volume Ω_j is involved in the derivative calculation. It should however be stressed that the final stencil, occurring after recursive application of the derivation operator, is not compact.
- The derivation operator can be formulated in the finite-volume framework. It can thus be more accurate on curvilinear grids, than in a direct application of a finite-difference formulation.
- The recursive derivation is also applicable to the case of unstructured grids.

Furthermore, the storage of the intermediate derivatives in the calculation of a high-order VC correction is not necessary, allowing an implementation with reasonable memory requirements.

The calculation of gradients in a finite volume formulation is usually performed either by a Green-Gauss theorem, or by a (weighted) Least-Square method. In the present work, we are considering only the former method, also described in Section 4.2.1.3. Let $\mathcal{D}^{(\ell)}$ denote a differentiation operator for the approximation of the ℓ th continuous derivative $D^{(\ell)}$. By application of Eq. (4.33), the Green-Gauss derivation operator can then written:

$$\mathcal{D}^{(1)}(\bullet) \Big|_{\Omega_j} = \frac{1}{|\Omega_j|} \sum_{f=1}^{N_{\text{faces}}} (\bullet)_f \vec{n}_f |S_f| \quad (4.77)$$

where \vec{n} is the outwards-pointing normal vector and $|S_f|$ is the surface area of the face S_f . The face-center values $(\bullet)_f$ can be approximated (i.e. reconstructed) by the simple average formula:

$$(\bullet)_{J+\frac{1}{2}}^d = (\mu_d(\bullet))_{J+\frac{1}{2}}^d = \frac{1}{2} \left((\bullet)_{J+1}^d + (\bullet)_J^d \right) \quad (4.78)$$

where it is implied that values of the function are averages within the control volume.

The above Green-Gauss calculation of derivatives is second-order accurate on regular Cartesian grids. However, it degrades to first-order of accuracy on curvilinear ones and may even become inconsistent (i.e. zeroth-order) for highly stretched and perturbed grids. This is primarily due to the reconstruction formula (4.78), which no longer represents a consistent face center reconstruction if the mesh is largely deformed from the Cartesian case. Mesh stretching is commonly accounted for by the use of a distance-weighted reconstruction, which includes the simple average as a special case. Alternatively, the derivative calculation can be *a posteriori* corrected by appropriate mesh-deformation corrections [87, 140, 162]. Such an approach is investigated later in this section.

On Cartesian grids, the calculation of derivatives by a Green-Gauss method is accurate to second order. In such grids, the reconstruction by simple average is consistent and the recursive approximation of high-order derivatives can be written:

$$\mathcal{D}^{(1)}\left(\mathcal{D}^{(\ell-1)}(\bullet)\right)\Big|_{\Omega_J} \approx \mathcal{D}^{(\ell)}(\bullet)\Big|_{\Omega_J} \quad (4.79)$$

The above approximation leads to an error that increases for an increasing order of the derivative $\mathcal{D}^{(\ell)}(\bullet)$. However, the VC correction is a numerical dissipation term, and should rather be an approximation of $(\tilde{\Delta}x)^{\ell-1} \mathcal{D}^{(\ell)}(\bullet)$. This is explained in the following.

4.4.1.1 Implementation of undivided differences

A high-order VC term is not a physical term of the flow equations, but a high-order anti-dissipative correction of the excess numerical dissipation. It should therefore: introduce nonlinear anti-dissipation similarly to a high-order artificial dissipation, and tend to zero with mesh refinement according to the order of accuracy. As a result, its calculation should be overall less sensitive to numerical error than the consistent part of the numerical flux, which should approximate the continuous convective flux up to high-order terms in a Taylor series expansion.

In a finite difference formulation, an approximation of a high-order even derivative would be written:

$$\frac{\delta_d^m(\bullet)_j}{\delta_d x_d^m} \approx \frac{\partial^m(\bullet)_j}{\partial x_d^m} \Big|_{x=x_j} \quad (4.80)$$

A standard high-order artificial dissipation would thus be formulated so that the flux difference gives an approximation of an even derivative as:

$$\frac{\delta_d^m(\bullet)_j}{\delta_d x_d} \approx \tilde{\Delta}x^{m-1} \frac{\partial^m(\bullet)_j}{\partial x_d^m} \Big|_{x=x_j} \quad (4.81)$$

hence the term ‘‘undivided difference’’. An approximation of the convective flux usually includes an additional numerical dissipation of the form (4.81) to damp numerical oscillations. This dissipation is consistent in the sense that it goes to zero and thus allows the approximation to retrieve the convective flux, as the mesh is refined. This is similar to the design of the dissipation of the FE-MUSCL numerical fluxes (4.26). The design of the nonlinear anti-dissipative (vorticity) confinement corrections is built on the same consistency principle.

The above is not directly applicable to a finite volume framework. For the first-order VC method, it has already been mentioned in Section 4.3.1 that consistency can be ensured by multiplying the confinement parameters by the mesh size. Alternatively, this can be integrated in the Green-Gauss derivation operator (4.77). This can be achieved in two ways. The first would be to reformulate the derivation operator as:

$$\mathcal{D}_{\text{ud}}^{(1)}(\bullet)\Big|_{\Omega_J} = \left(\frac{1}{|\Omega_J|}\right)^{\frac{n-1}{n}} \sum_{f=1}^{N_{\text{faces}}} (\bullet)_f \vec{n}_f |S_f| \quad (4.82)$$

where n is the problem dimension. The second would be to use the derivation operator (4.77) as is, and integrate the undivided difference in the arithmetic average reconstruction of $(\bullet)_f$:

$$\mathcal{D}_{\text{ud}}^{(1)}(\bullet) \Big|_{\Omega_J} = \frac{1}{|\Omega_J|} \sum_{f=1}^{N_{\text{faces}}} (\bullet)_{f,\text{ud}} \vec{n}_f |S_f| \quad , \text{ with: } (\bullet)_{J+\frac{1}{2},\text{ud}}^d = q_{J+\frac{1}{2}}^d (\bullet)_{J+\frac{1}{2}}^d \quad (4.83)$$

where q is the mesh size, i.e. $q \approx \tilde{\Delta}x$. On Cartesian grids, $q_{J+\frac{1}{2}}^d = q_J = |\Omega_J|^{1/n}$. Furthermore, on Cartesian meshes, Eqs. (4.82) and (4.83) are equivalent. In other terms:

$$\mathcal{D}_{\text{ud}}^{(1)}(\bullet) \Big|_{\Omega_J} \approx \tilde{\Delta}x \, D^{(1)}(\bullet) \Big|_{\Omega_J} \quad (4.84)$$

A recursive approximation of derivatives with the above assimilation of undivided differences results in a VC correction that is both based on high-order even derivatives and high-order accurate.

Of course, a formally high-order accurate VC term could have also been obtained by simply multiplying the confinement parameters in Eq. (4.42) with an appropriate power of a characteristic mesh size, i.e. taking $\mu, \varepsilon \propto \tilde{\Delta}x^a$. In that case however, the nonlinear anti-dissipation is still based on a low-order difference, which is not consistent for schemes with a high-order numerical dissipation. The importance of basing the confinement correction on a high-order difference operator has been demonstrated in Section 3.4 for the linear transport case.

4.4.1.2 Conservativity of undivided differences in non-Cartesian meshes

The undivided difference implementations of Eqs. (4.82) and (4.83) are equivalent only in the case of regular Cartesian grids. The derivation operator (4.82) employs a cell-based undivided difference and therefore is not conservative on non-Cartesian grids. A conservative VC correction can be calculated with the operator (4.83), by using a characteristic mesh size q that is calculated on the faces. A straightforward choice is:

$$q_{J+\frac{1}{2}}^d = (\mu_d q)_{J+\frac{1}{2}}^d = \frac{1}{2} (q_{J+1}^d + q_J^d) \quad (4.85)$$

where $q_J = |\Omega_J|^{1/n}$, n denoting the number of space dimensions. Another possibility would be to compute the mesh size directly on the face surface, e.g. as $q_{J+\frac{1}{2}}^d = |S_{J+\frac{1}{2}}^d|^{1/2}$ in three dimensions. The two are equivalent in most cases, except on highly skewed grids where Eq. (4.85) was found to give more consistent results.

On non-Cartesian meshes, the introduction of a conservative undivided difference in the form of the operator (4.83) introduces an additional gradient due to cell-volume variation. This can be decomposed by an application of the product rule:

$$\begin{aligned} \mathcal{D}_{\text{ud}}^{(1)}(\bullet) \Big|_{\Omega_J} &= \mathcal{D}^{(1)}(q(\bullet)) \Big|_{\Omega_J} \\ &= q_J D^{(1)}(\bullet) \Big|_{\Omega_J} + (\bullet)_J D^{(1)}q \Big|_{\Omega_J} \end{aligned} \quad (4.86)$$

where the magnitude of the second term decreases for smaller variation of cell volume between neighboring cells. It has thus been preferred over an undivided difference in the form of the operator (4.82), which is free from a gradient induced by cell-volume variation, but is also non-conservative.

4.4.1.3 Consistent evaluation of gradients on general meshes

It has already been mentioned that the standard Green-Gauss operator (4.77) is consistent and second-order accurate only on Cartesian grids. Consistency can however be ensured even on highly irregular meshes by appropriate geometric corrections. These were developed in the frame of k -exact finite volume methods based on successive correction (see Section 2.2.4). Specifically, the mathematical foundation of this approach was established by F. Haider [87], whereas the incorporation of this approach alongside k -exact schemes can also be found in G. Pont et al. [162]. For the sake of brevity, only necessary equations and parts of the method will be reviewed here.

The first step is the replacement of the simple average reconstruction (4.78) with a weighted average:

$$(\bullet)_{J+\frac{1}{2},w}^d = \gamma_{J+1}^d (\bullet)_{J+1}^d + (1 - \gamma_{J+1}^d) (\bullet)_J \quad (4.87)$$

The above weights γ are based on the distance of the cell centers $\vec{x}_J, \vec{x}_{J+1}^d$ from the face:

$$\gamma_{J+1}^d = \frac{(\vec{x}_f - \vec{x}_J) \cdot \vec{n}_f}{(\vec{x}_{J+1}^d - \vec{x}_J) \cdot \vec{n}_f} \quad (4.88)$$

where $\vec{x}_f = \vec{x}_{J+\frac{1}{2}}^d$ is the center of the interface S_f , and \vec{n}_f is the normal vector on face S_f pointing outwards with respect to cell Ω_J . The above reconstruction satisfies the zero-exactness condition of the derivation operator.

It is then shown in [87, 162] that the 1-exactness condition of the derivation operator on general meshes can be represented by a matrix:

$$\overline{\overline{\mathbf{M}}_1} = \sum_{N_{\text{faces}}} |S_{J+\frac{1}{2}}^d| \gamma_{J+1}^d (\vec{x}_{J+1}^d - \vec{x}_J) \otimes \vec{n}_{J+\frac{1}{2}}^d \quad (4.89)$$

The above matrix depends only on mesh topology, and can therefore be calculated once and for all at the beginning of the computation for non-deforming grids. More importantly, the matrix $\overline{\overline{\mathbf{M}}_1}$ can be used for the *a posteriori* correction of the weighted derivation to ensure consistency even on highly irregular grids. This is accumulated in an operator:

$$\mathcal{D}_1^{(1)}(\bullet) \Big|_{\Omega_J} = \overline{\overline{\mathbf{M}}_1}^{-1} \sum_{f=1}^{N_{\text{faces}}} (\bullet)_{f,w} \vec{n}_f |S_f| \quad (4.90)$$

which is consistent (at least first-order accurate) on any grid and often referred to as a quasi-Green differentiation operator. Above, $(\bullet)_{f,w}$ is obtained by the reconstruction (4.87) and the correction matrix reduces to $\overline{\overline{\mathbf{M}}_1}^{-1} = |\Omega_J|^{-1}$ on Cartesian grids.

The calculation of the first-order VC correction (4.42) requires two successive derivations. On general meshes however, a direct consecutive application of the 1-exact operator $\mathcal{D}_1^{(1)}$ gives an inconsistent approximation of a second derivative:

$$\mathcal{D}_1^{(1)}(\mathcal{D}_1^{(1)}(\bullet)) \Big|_{\Omega_J} = \mathbf{D}^{(2)}(\bullet) \Big|_{\Omega_J} + \mathcal{O}(\tilde{\Delta}x^0) \quad (4.91)$$

The above operation can be corrected by the construction of a matrix similar to (4.89). This is written as a 1-exact operator for the second derivative:

$$\begin{aligned} \mathcal{D}_1^{(2)}(\bullet) &= \overline{\overline{\mathbf{M}}_2}^{-1} \mathcal{D}_1^{(1)}(\mathcal{D}_1^{(1)}(\bullet)) \Big|_{\Omega_J} \\ &= \mathbf{D}^{(2)}(\bullet) \Big|_{\Omega_J} + \mathcal{O}(\tilde{\Delta}x) \end{aligned} \quad (4.92)$$

where $\overline{\overline{\mathbf{M}}_2} = \mathcal{D}_1^{(1)} \mathcal{D}_1^{(1)} (\vec{x} \otimes \vec{x} |_{\Omega_J})$. However, since VC is nonlinear and the term (4.42) is not a direct second derivative of the state variables, the aforementioned correction is not directly applicable. It

has been proven by F. Haider [87] that a consistent (1-exact) second derivative approximation can be equivalently obtained by applying twice a 2-exact derivation operator:

$$\mathcal{D}_2^{(1)}\left(\mathcal{D}_2^{(1)}(\bullet)\right)\Big|_{\Omega_J} = \mathcal{D}^{(2)}(\bullet)\Big|_{\Omega_J} + \mathcal{O}(\tilde{\Delta}x) \quad (4.93)$$

Such a 2-exact derivation operator can be constructed by correcting the leading truncation error of (4.90). This is written:

$$\mathcal{D}_2^{(1)}(\bullet)\Big|_{\Omega_J} = \mathcal{D}_1^{(1)}(\bullet)\Big|_{\Omega_J} - \frac{1}{2}\mathcal{H}_2\mathcal{D}_1^{(2)}(\bullet)\Big|_{\Omega_J} \quad (4.94)$$

where $\mathcal{H}_2 = \mathcal{D}_1^{(1)}\left(\overline{\vec{x} \otimes \vec{x}}\Big|_{\Omega_J}\right)$ and $\mathcal{D}_1^{(2)}$ is given by (4.92). The derivation of the correction matrices can be found in [87].

A consistent first-order accurate VC correction can then be obtained by calculating the derivatives in Eq. (4.42) with a 2-exact derivation operator (4.94). A conservative undivided difference can also be introduced in the form (4.83). This approach has been implemented only for first-order VC, as the computational cost becomes excessive when higher-order derivatives are required for the VC correction.

4.4.1.4 Derivatives of the harmonic mean function

At this point, a particularity of the harmonic mean function should be discussed, with respect to the calculation of high-order derivatives. The function (4.44) is smooth within clearly identified vortical regions, where the direction of the vorticity vector does not change abruptly on successive mesh cells. This is more intuitive in two space dimensions. In this case, the harmonic mean is smooth when vorticity does not change sign among the cells N_c . It is not however the case in the close neighborhood of points where vorticity, and therefore the harmonic mean, is zero. At those points, the harmonic mean remains a continuous function, but displays a derivative discontinuity. Naturally, the latter becomes critical at higher-orders of accuracy, where higher-order derivatives are involved.

The VC correction is only applied within clearly defined vortical regions, as detailed in Section 4.4.3. However, the high-order derivative calculation involves a globally large stencil, which may cross the aforementioned discontinuity at high-orders of accuracy. This results in the production of oscillations which perturb the calculation of high-order derivatives on cells near the vortex boundary, i.e. near to the points of zero vorticity. These oscillations can be removed by identifying these cells and disabling the VC correction, or by appropriate adaptive stencil reconstruction. Such strategies are discussed in Appendix A.

It has however been found that the most robust approach is the use of an algebraically smooth formula, as the simple average of Eq. (4.78). This is not surprising, as high-order VC corrections involve the calculation of high-order derivatives. The calculation of such derivatives can be problematic for adaptive stencil methods, as changes of stencil result in a discontinuous reconstruction in space. It is especially the case for complex flows, where stencil modifications are more frequent. On the other hand, even without special treatment, the simple average reconstruction (4.78) has been found to provide accurate results and to be very robust, for all cases investigated in the present thesis.

4.4.2 Boundary treatment

Matching joins and periodicity condition

The boundaries of matching zones or of the computational domain in the case of a periodic boundary condition are treated in a similar manner. They are both implemented by introducing layers of ghost

cells to expand the computational domain in each mesh direction. This way boundary fluxes can be approximated using the same large-stencil centered schemes as in the domain interior.

The calculation of the VC term on boundaries is based on the same approach. Conservative variables \vec{W} are known in the extended computational domain. They are obtained from the periodicity condition or, in the case of zone boundaries, from an MPI exchange. Derivatives of state variables are then calculated successively in the extended computational domain, starting from the outer ghost cells and towards the domain interior, so that the VC term is accurately computed on the domain boundary. The harmonic mean stencil is reduced in the outmost ghost cell layer, as shown in Fig. 4.2, where velocity gradients (and therefore the vorticity) are not available in the complete compact stencil. This reduction is considered to have a negligible effect in the precision of the harmonic mean value. For high-order VC corrections, an additional number of ghost cell layers needs to be introduced, depending on the stencil of the Laplacian scheme. Specifically, a $5p$ Laplacian scheme requires two additional layers and a $3p$ Laplacian scheme requires one additional layer.

Albeit being straightforward, this approach requires a high number of ghost cells to accurately compute the VC correction on the boundary, particularly for the fifth-order VC correction computed with a $5p$ Laplacian scheme, which requires a minimum number of 6 ghost cell layers. This is even larger than for the baseline FE-MUSCL scheme at fifth-order, which is computed on a 7-point stencil and therefore requires a minimum number of 3 layers. The reduction of this requirement is important for industrial computations and should be improved in the future. It can be achieved by replacing the simple average reconstruction (4.78) with a two-point extrapolation formula on the boundary faces.

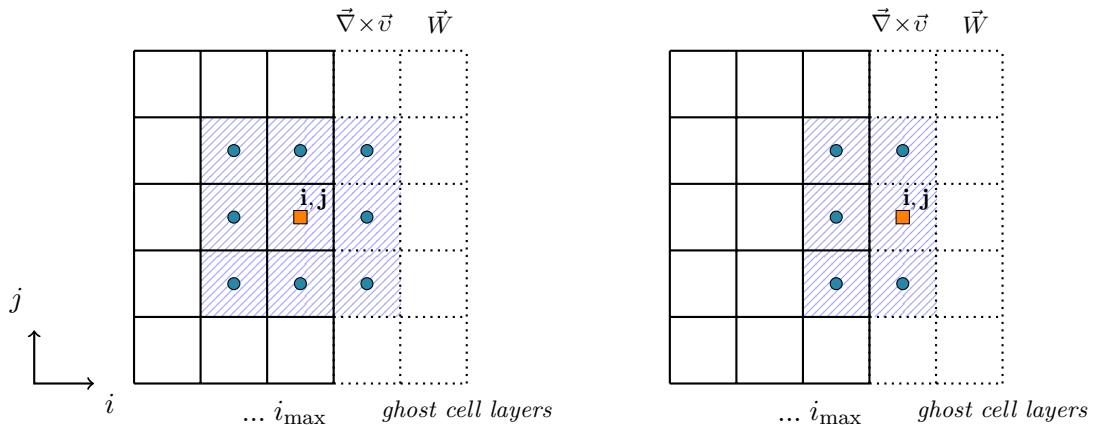


Figure 4.2: Complete stencil (left) and reduced stencil (right) of cells N_c for the harmonic mean calculation on cell i, j . Velocity gradients are calculated in the extended computational domain, starting from the second to last ghost cell.

Solid boundaries

The calculation of the VC correction near solid boundaries is less straightforward. A simple approach would be to deactivate the VC correction on the first computational cells, near the solid surface. This is not expected to degrade the vorticity-preserving capability of the method, as the numerical dissipation of vortices created on solid surfaces can generally be considered small during their advection over the first few cells. Furthermore, this strategy can be implemented in an efficient manner, as the deactivation mechanism of the VC corrections (discussed in the following section) is already an integral part of the method. Alternatively, values on boundary faces can be reconstructed using an extrapolation formula.

4.4.3 Identification of vortical flow regions and cut-off

Although the introduction of VC corrections in vortical regions is robust, it would not necessarily be the case if these corrections were to be applied in the complete flow field. By construction, the magnitude of the VC correction is very small in regions of low vorticity, but its effect may be accumulated over time. The introduction of nonlinear negative dissipation may thus result in the creation of unphysical vorticity concentration in irrotational flow regions. This can be easily avoided by setting the VC correction to zero outside vortices.

4.4.3.1 Deactivation of VC correction

The deactivation of the VC correction is managed by identifying and flagging cells that lie within clearly defined vortical regions. This identification is composed of two parts. The first is based on a classical vortex identification criterion. The second is based on the orientation of the vorticity vector. Specifically, the VC correction is deactivated on a cell Ω_J if the vorticity vector between the cell Ω_J and any cell in its close neighborhood $N(J)$ form a right or obtuse angle. This angle can be evaluated from the dot product of the two vorticity vectors, whereas the close neighborhood is defined as for the harmonic mean stencil (see Fig. 4.2). This deactivation is analogous to the definition of the harmonic mean function (3.8) in the scalar case. The two criteria can finally be assimilated in a cell-assigned variable:

$$\beta_J = \begin{cases} 1 & , \text{ if } \Psi_{\Omega_J} > \Psi_o \text{ and } \vec{\omega}_J \cdot \vec{\omega}_{N(J)} \geq \epsilon \\ 0 & , \text{ otherwise} \end{cases} \quad (4.95)$$

where $\beta_J = \beta_{\Omega_J}$ and ϵ denotes a small value, here taken 10^{-9} . Also, Ψ_o denotes a preset cut-off value of a vortex identification criterion Ψ . The VC correction can then simply be multiplied with β_J .

4.4.3.2 Identification of vortical flow regions

A strict definition and identification of vortices in fluid flows is far from a simple task [88]. The identification criteria (and therefore the definition of a vortex) should be case-independent and Galilean invariant. There exist multiple such criteria, many of which are based on the identification of local pressure minima.

For the identification of vortices in this work, we are employing the Q -criterion, originally proposed by J. C. R. Hunt et al. [98]. It is based on the decomposition of the velocity gradient tensor to a symmetric and anti-symmetric part as:

$$\overline{\overline{\nabla v}} = \overline{\overline{S}} + \overline{\overline{\Omega}} \quad (4.96)$$

where $\overline{\overline{S}}$ is the strain rate (symmetric) tensor and $\overline{\overline{\Omega}}$ is the vorticity (anti-symmetric) tensor:

$$\overline{\overline{S}} = \frac{1}{2} \left(\overline{\overline{\nabla v}} + \overline{\overline{\nabla v}}^T \right) \quad \overline{\overline{\Omega}} = \frac{1}{2} \left(\overline{\overline{\nabla v}} - \overline{\overline{\nabla v}}^T \right) \quad (4.97)$$

The Q -criterion is then defined as:

$$Q \triangleq \frac{1}{2} \left(\|\overline{\overline{\Omega}}\|^2 - \|\overline{\overline{S}}\|^2 \right) \quad (4.98)$$

In turn, vortical regions are defined as those for which $Q > 0$, that is where the norm of the vorticity tensor is larger than the norm of the strain rate tensor. A non-dimensional form can be obtained by dividing with the norm of the strain rate tensor:

$$Q' \triangleq \frac{1}{2} \left(\frac{\|\overline{\overline{\Omega}}\|^2}{\|\overline{\overline{S}}\|^2} - 1 \right) \quad (4.99)$$

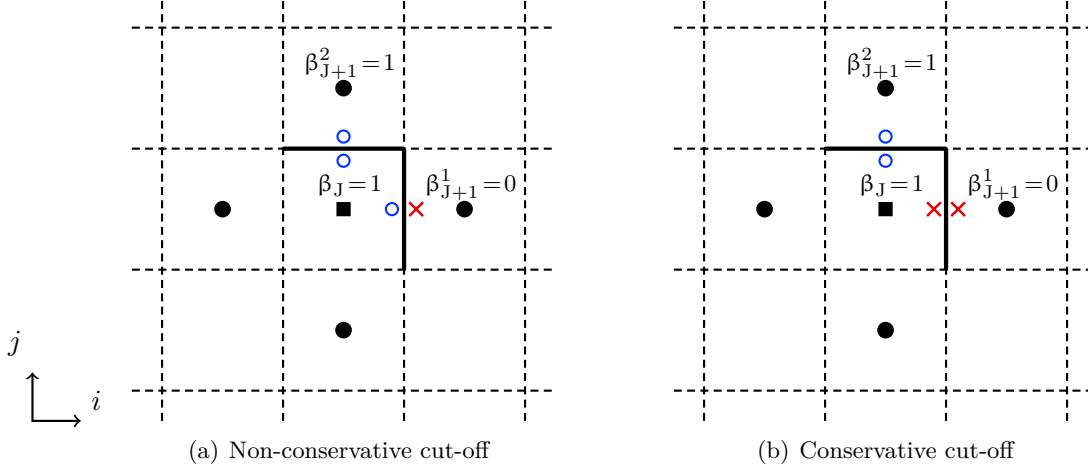


Figure 4.3: Application of the VC correction cut-off on the faces of a cell Ω_J .

where vortical regions are again characterized by a threshold $Q' > 0$. The form (4.99) can however be more representative than (4.98) for cases where a finer selection of vortical regions is required, e.g. by setting a threshold $Q' > 1$ [108].

Other identification criteria can also be used, such as the λ_2 -criterion of J. Jeong and F. Hussain [106]. However, the Q -criterion is computationally efficient and was found to be adequate for the cases investigated in the present thesis. Its dimensional cut-off value was set to $Q_o = 0.1$ for all presented computations. As already mentioned above, the aim of this cut-off value is to avoid introducing negative dissipation in irrotational flow regions. Therefore, it has not been used for the fine selection of vortical regions to apply VC, as this is not simple for realistic flows.

4.4.3.3 Application of the cut-off and conservativity

The deactivation of the VC correction is straightforward through the variable β_J of Eq. (4.95). The VC2 method and its high-order extensions are conservative, as demonstrated in Section 4.3.5. Furthermore, the source term formulation is equivalent to a numerical flux correction in the continuous framework. The two are not however equivalent with respect to the discrete application of the cut-off, i.e. the deactivation of the VC correction outside vortices.

For a source term formulation, the cut-off is applied on the VC source term, which is calculated on cell centers. That can be written:

$$[\vec{f}]_J = -\beta_J [\vec{\nabla} \times (\mu \vec{\omega} - \varepsilon \vec{w})]_J \quad (4.100)$$

where $[(\bullet)]_J$ denotes a discrete approximation of (\bullet) on the center of the cell Ω_J , using undivided differences in the calculation of derivatives. The above is not explicitly conservative in terms of numerical flux contribution, as it results in a different treatment of a face $x_{J+\frac{1}{2}}^d$ for the two adjacent cells Ω_J, Ω_{J+1}^d (Fig. 4.3). The loss of conservativity will occur only on the vortex boundary, on faces around which the value of β_J changes from zero to one, or opposite. On the other hand, the implementation of the cut-off in a flux formulation can be written:

$$\begin{aligned} \mathcal{F}_{vc}|_{J+\frac{1}{2}}^d &= \beta_J \beta_{J+1}^d [F_{vc}]_{J+\frac{1}{2}}^d \\ &= \beta_J \beta_{J+1}^d [(\mu \vec{\omega} - \varepsilon \vec{w}) \times \vec{n}]_{J+\frac{1}{2}}^d \end{aligned} \quad (4.101)$$

where F_{vc} is the VC flux contribution in the momentum equation (4.76). The application of the cut-off on the fluxes, as in Eq. (4.101), is explicitly conservative.

4.4.4 Laplacian schemes

High-order VC corrections require the calculation of a Laplace operator. This can be approximated either on a 5-point stencil or a compact 3-point stencil similar to the one used in the calculation of viscous fluxes. The two schemes were already discussed briefly in Section 4.2.1.2.

4.4.4.1 5-point scheme

The 5-point scheme presents the most straightforward and algorithmically simple approach for the calculation of the Laplace operator in a FV framework. It is composed of two steps, each involving the application of the Green-Gauss derivation operator on the cell volumes Ω_J . First, the values of a scalar ψ are reconstructed on the cell faces, and gradients are calculated at the cell centers. At the next step, gradients are reconstructed on cell faces, and the second derivatives are calculated at the cell centers (Fig. 4.4). The Laplacian is then directly calculated from the second derivatives. It should be noted that both applications of the derivation operator include the undivided difference (as described in Section 4.4.1), so as to obtain a consistent high-order VC correction.

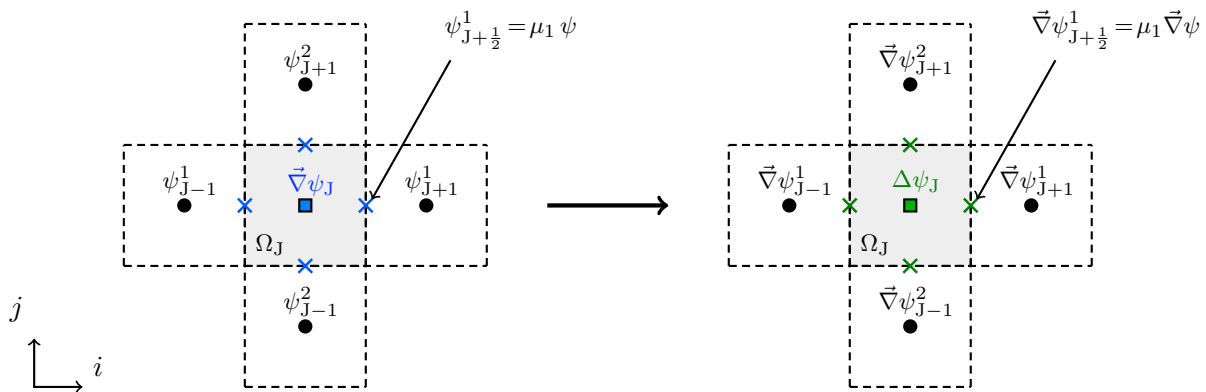


Figure 4.4: Finite volume calculation of Laplacian on a 5-point stencil. Derivatives are approximated by application of the Green-Gauss theorem on the shaded volume. Calculation of $\vec{\nabla}\psi$ on cell centers (left), followed by reconstruction of gradients and calculation of $\Delta\psi$ on cell centers (right).

4.4.4.2 3-point scheme

The 3-point scheme is also based on the application of the Green-Gauss theorem. It allows the approximation of the Laplacian on a compact stencil by calculating gradients directly on the center of cell faces. This is achieved by the application of the Green-Gauss derivation operator on a shifted control volume (Fig. 4.5). Face values for the shifted control volume are obtained either as the cell-centered values of adjacent cells, or as the arithmetic average of the four adjacent cell centers. The derivation operator can then be applied directly on the control volumes Ω_J to calculate the second derivatives. As discussed previously (see Section 4.4.1), the Green-Gauss operator is rearranged in the form of undivided differences.

The 3-point scheme results in a smaller stencil than that of the 5-point scheme (Fig. 4.6). Nonetheless, it is costly because it requires the calculation of the surface areas and normal vectors on the faces of the shifted control volume.

4.5 Validation and numerical tests

4.5.1 Evaluation of the order of accuracy

The first validation case is the evaluation of the order of accuracy in a grid convergence study of a 2D vortex. The flow field is static ($M_{\text{inf}} = 0$), the unsteady evolution thus arising only from the vortex rotation in the Lagrangian coordinate sense. The evolution of the flow is computed based on the Euler equations, meaning that any spreading and diffusion originate from the dissipation of

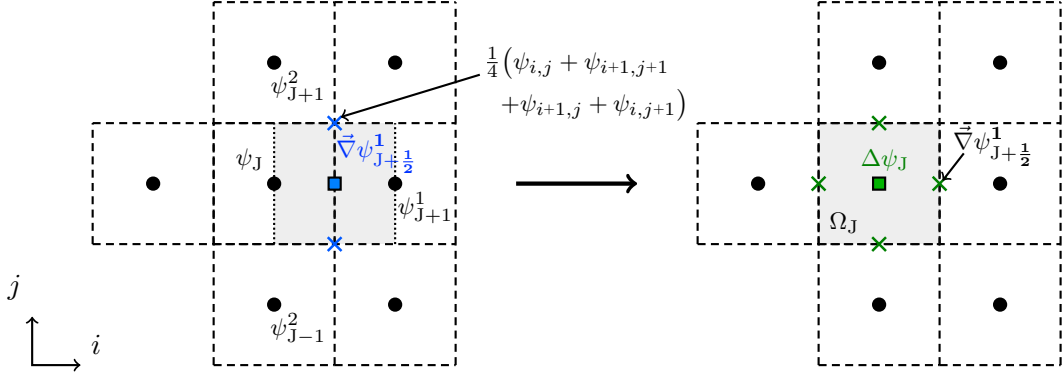


Figure 4.5: Finite volume calculation of Laplacian at cell $\Omega_J \equiv \Omega_{i,j}$ on a 3-point stencil. Gradients are approximated directly on the center of faces by application of the Green-Gauss theorem on shifted cells.

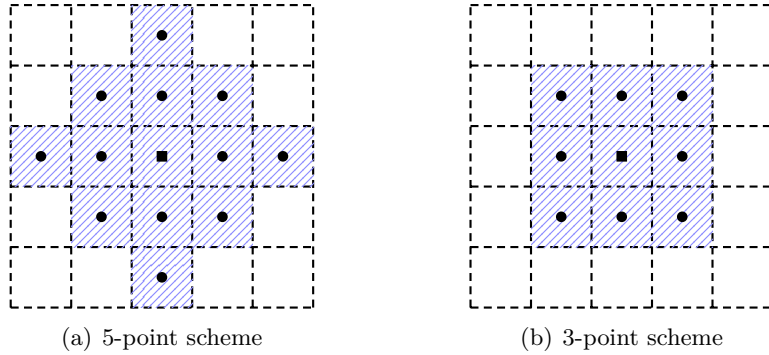


Figure 4.6: Final computational stencil in two dimensions for the finite volume Laplacian schemes.

the numerical discretization. The vortex is initialized on a flow at rest using the isentropic model proposed by H. C. Yee et al. [234]. The perturbations of the infinite state are given by:

$$\begin{aligned} (u', v') &= \frac{\Gamma}{2\pi} \exp\left(\frac{1-r^2}{2}\right) (-\bar{y}, \bar{x}) \\ T' &= -\frac{\gamma-1}{\gamma} \frac{\Gamma^2}{8\pi^2} \exp(1-r^2) \end{aligned} \quad (4.102)$$

where $r^2 = \bar{x}^2 + \bar{y}^2$, with $\bar{x} = x - x_o$, $\bar{y} = y - y_o$ and (x_o, y_o) being the initial position of the vortex core. The vortex intensity Γ is taken equal to 5. The fluid is considered a perfect gas with $\gamma = 1.4$ and $T = p/\rho$. The infinite state is here taken $p_{\text{inf}} = 1/\gamma$, $\rho_{\text{inf}} = 1$. Furthermore, the flow is considered isentropic meaning that $p/\rho^\gamma = p_{\text{inf}}/\rho_{\text{inf}}^\gamma = s_{\text{inf}}$, where s denotes the entropy. The conservative variables at the initial state are therefore given by:

$$\begin{aligned} \rho &= \left(\frac{T}{s_{\text{inf}}}\right)^{\frac{1}{\gamma-1}} = \left(\frac{1}{s_{\text{inf}}}\right)^{\frac{1}{\gamma-1}} \left[T_{\text{inf}} - \frac{\gamma-1}{\gamma} \frac{\Gamma^2}{8\pi^2} \exp(1-r^2)\right]^{\frac{1}{\gamma-1}} \\ \rho u &= \rho \left[u_{\text{inf}} - \frac{\Gamma}{2\pi} \exp\left(\frac{1-r^2}{2}\right) \bar{y}\right] \\ \rho v &= \rho \left[v_{\text{inf}} + \frac{\Gamma}{2\pi} \exp\left(\frac{1-r^2}{2}\right) \bar{x}\right] \\ p &= s_{\text{inf}} \rho^\gamma \\ \rho E &= \frac{p}{\gamma-1} + \frac{1}{2} \rho (u^2 + v^2) \end{aligned} \quad (4.103)$$

where internal energy has been calculated by Eq. (4.9) using the equation of state for a perfect gas. The above isentropic vortex model, defined from the perturbations (4.102), is an exact steady solution of the Euler equations.

The case is discretized on a square computational domain $(x, y) \in [-5, 5] \times [-5, 5]$, and the vortex is initialized at its center $(x_o, y_o) = (0, 0)$. The domain is discretized by a series of five different Cartesian meshes of varying density, ranging from $\Delta x = 0.4$ (625 cells) for the coarsest mesh to $\Delta x = 0.025$ (160 000 cells) for the finest mesh with the mesh size Δx being halved between two successive cases. Periodicity conditions were imposed on each side of the computational domain. Space discretization is performed using the FE-MUSCL schemes presented in Section 4.2.1.1, ranging from 1st- to 5th-order of accuracy. Time integration is performed using a classical 4-step Runge-Kutta algorithm. Computations were run from $t=0$ to $t=1$ using a fixed ratio of $\Delta t/\Delta x = 2 \cdot 10^{-4}$ for all cases, to minimize the numerical error introduced by the time integration algorithm.

For schemes with VC corrections, the absolute error is driven by the values of the confinement parameters, i.e. the magnitude of the VC correction. The order of accuracy has however been found to show very little sensitivity to these values. For the following analyses of the order of accuracy, no effort has been made to adjust the confinement parameters so as to achieve specific error values. The values of these parameters were taken $\mu/\varepsilon = 0.4$ and $\varepsilon = 0.02$ for all cases.

The analytical solution of this problem is the exact preservation of the initial condition. A measure of the numerical error of the discretization can thus be obtained by comparing the computed solution to the initial isentropic one. The L^2 -norm of entropy error is here defined as:

$$\text{Error}_{L^2}(\phi) = \left[\frac{\sum_{i=1}^n (\phi_i - \phi_{i,\text{exact}})^2 |\Omega_i|}{\sum_{i=1}^n |\Omega_i|} \right]^{1/2} \quad (4.104)$$

where ϕ is a solution variable. Errors are computed based on the cell-centered values of the solution.

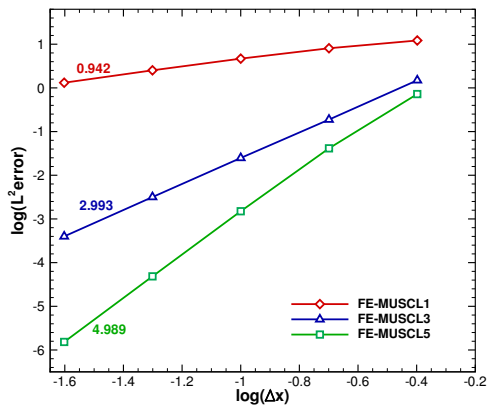
4.5.1.1 Order of accuracy on Cartesian grids

Fig. 4.7 shows the convergence of entropy error with mesh refinement for FE-MUSCL schemes with and without VC. For the cases with high-order VC corrections, the Laplacian was computed with the 5-point scheme. Fig. 4.7(a) shows the convergence of the L^2 norm of the error for baseline FE-MUSCL schemes of 1st-, 3rd- and 5th-order of accuracy. The error decreases according to the nominal convergence slope for all baseline schemes. Fig. 4.7(b) underlines the incompatibility of the original VC method with higher-order underlying methods. The lower-order VC term dominates the global error of the discretization, resulting in a 1st-order convergence slope regardless of the order of the baseline FE-MUSCL scheme.

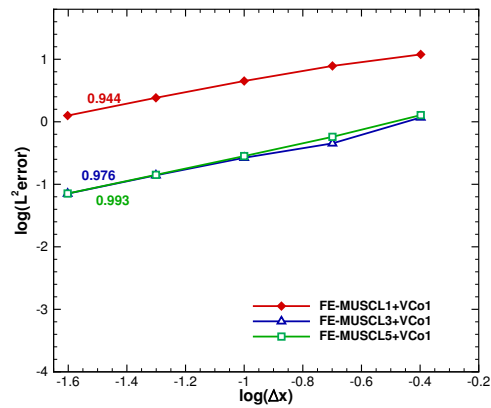
Figs. 4.7(c) and 4.7(d) however show that high-order VC extensions allow to recover the nominal order of accuracy. Details of the error convergence are presented in Table 4.1 for VC corrections of the same order as the baseline scheme. The application of VC is shown to reduce the absolute error values up to 3rd-order of accuracy. At 5th-order of accuracy, the scheme with VC gives a slightly higher error than its baseline version. However, these absolute errors depend on the balance between the anti-dissipation of VC and the baseline scheme's dissipation. Therefore, they cannot be straightforwardly used to evaluate the values of the confinement parameters for general cases, as the dissipation of the baseline scheme is also varying between different cases. In the vortex advection study of the following section, where the baseline dissipation is more important compared to the present static case, it is shown that the same values of confinement parameters allow the preservation of the vortex with considerably reduced effects of dissipation than the baseline scheme. Nonetheless, the order of accuracy of the scheme with VC at 5th-order of accuracy is always comparable to the baseline 5th-order scheme.

Table 4.1: Entropy error and order of accuracy for the isentropic vortex case on Cartesian grids.

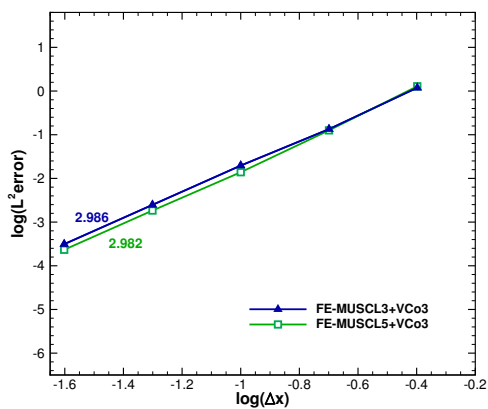
Scheme	Grid	Baseline		With VC	
		$\log(L^2 \text{ error})$	$L^2 \text{ order}$	$\log(L^2 \text{ error})$	$L^2 \text{ order}$
FE-MUSCL1	25 × 25	1.0850	-	1.0774	-
	50 × 50	0.9073	0.590	0.8933	0.612
	100 × 100	0.6697	0.789	0.6523	0.801
	200 × 200	0.4022	0.888	0.3836	0.893
	400 × 400	0.1186	0.942	0.0994	0.944
FE-MUSCL3	25 × 25	0.1740	-	0.0764	-
	50 × 50	-0.7258	2.989	-0.8729	3.153
	100 × 100	-1.6046	2.919	-1.7063	2.769
	200 × 200	-2.4991	2.971	-2.6061	2.989
	400 × 400	-3.4001	2.993	-3.5051	2.986
FE-MUSCL5	25 × 25	-0.1413	-	0.1429	-
	50 × 50	-1.3837	4.127	-1.1282	4.223
	100 × 100	-2.8237	4.783	-2.5886	4.852
	200 × 200	-4.3142	4.951	-4.2111	5.390
	400 × 400	-5.8159	4.989	-5.7172	5.003



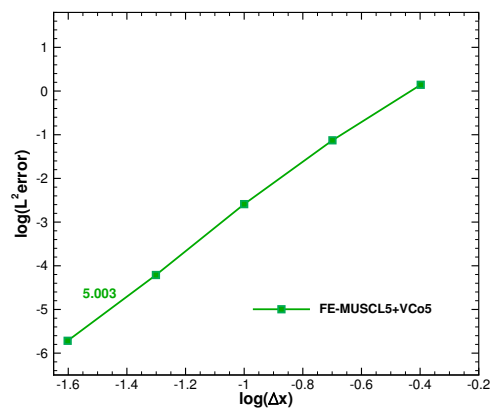
(a) Baseline FE-MUSCL



(b) FE-MUSCL and 1st-order VC



(c) FE-MUSCL and 3rd-order VC



(d) FE-MUSCL and 5th-order VC

Figure 4.7: Convergence of the computed error on entropy using FE-MUSCL schemes with and without VC.

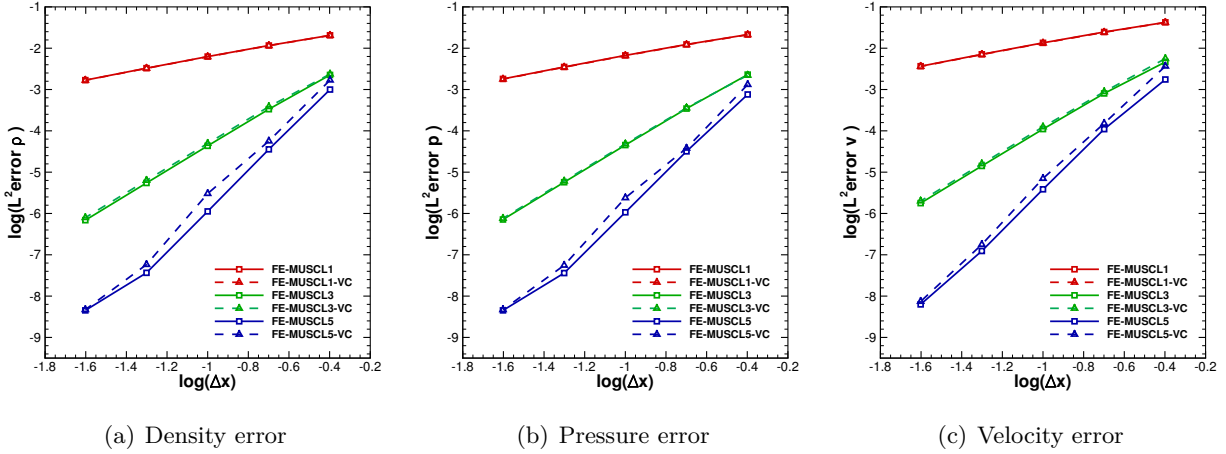


Figure 4.8: Convergence of the computed error on density, pressure and velocity. Computed with FE-MUSCL schemes with and without VC of the same order of accuracy.

Fig. 4.8 shows the error in the computation of the primitive flow variables, i.e. density, velocity and pressure. For cases with VC, the baseline scheme and the VC correction are of the same order of accuracy. The 5th-order schemes (both baseline and with VC) exhibit a decrease of convergence slope on the finest meshes, which is likely related to the precision of the calculation. The errors computed with VC display an overall similar convergence to the case of entropy, indicating no particular negative effect of VC on the calculation of primitive variables.

4.5.1.2 Evaluation of Laplacian schemes

Fig. 4.9 shows a comparison of error convergence for the two Laplacian schemes presented in Section 4.4.4. The high-order VC correction is applied alongside FE-MUSCL baseline schemes of the same order. At third-order of accuracy the two Laplacian schemes produce similar results, although the 5-point scheme results in a lower error on coarser meshes. The difference is however more important at fifth-order of accuracy. In this case, the 3-point scheme results in a significantly larger error than the 5-point scheme on coarser meshes. Not surprisingly, the two Laplacian schemes converge to the same error values on fine meshes both at third- and fifth-order of accuracy. Due to its lower error on coarser meshes and its reduced computational cost, the high-order VC corrections in the following calculations are computed using the 5-point scheme.

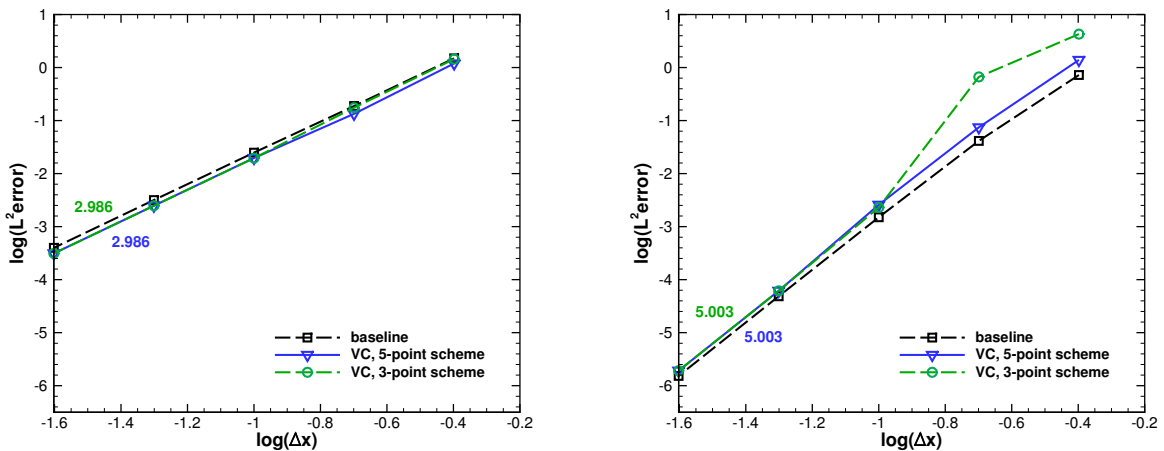


Figure 4.9: Comparison of error convergence for the 5-point and 3-point Laplacian schemes. FE-MUSCL baseline schemes with VC of the same order. Results at third-order (left) and fifth-order of accuracy (right).

Table 4.2: Entropy error and order of accuracy for the isentropic vortex case on curvilinear grids.

Scheme	Grid	Baseline		With VC-GG		With VC-qG	
		$\log(L^2 \text{ error})$	$L^2 \text{ order}$	$\log(L^2 \text{ error})$	$L^2 \text{ order}$	$\log(L^2 \text{ error})$	$L^2 \text{ order}$
FE-MUSCL1	25×25	1.3292	-	1.3271	-	1.3273	-
	50×50	1.0938	0.782	1.0884	0.793	1.0885	0.793
	100×100	0.7582	1.115	0.7457	1.138	0.7457	1.139
	200×200	0.4391	1.060	0.4223	1.074	0.4223	1.074
	400×400	0.1346	1.011	0.1162	1.017	0.1162	1.017
FE-MUSCL3	25×25	0.9886	-	0.9752	-		
	50×50	-0.3016	4.286	-0.3621	4.442		
	100×100	-1.4614	3.853	-1.5682	4.007		
	200×200	-2.4477	3.276	-2.5592	3.292		
	400×400	-3.3798	3.096	-3.4861	3.079		
FE-MUSCL5	25×25	0.8253	-	0.8087	-		
	50×50	-1.0077	6.089	-0.8833	5.621		
	100×100	-2.6428	5.432	-2.4724	5.279		
	200×200	-3.9941	4.489	-3.9520	4.915		
	400×400	-5.2300	4.106	-5.2175	4.204		

4.5.1.3 Order of accuracy on curvilinear grids

The order of accuracy is here evaluated on a series of curvilinear grids, generated by an analytical coordinate perturbation of the Cartesian grids of the previous study. The coordinate perturbations are of the form:

$$\begin{cases} x' = A_x \Delta x \sin [2\pi n_x (y - y_{\min}) / L_y] \\ y' = A_y \Delta y \sin [2\pi n_y (x - x_{\min}) / L_x] \end{cases} \quad (4.105)$$

where L_x, L_y denote the domain length in each dimension, $n_x = n_y = 3$ define the wavelength of the perturbation and the amplitudes are taken $A_x = A_y = 1$. Calculations are performed from $t = 0$ to $t = 1$ using a time step to mesh size ratio $\Delta t / \Delta x = 4 \cdot 10^{-4}$.

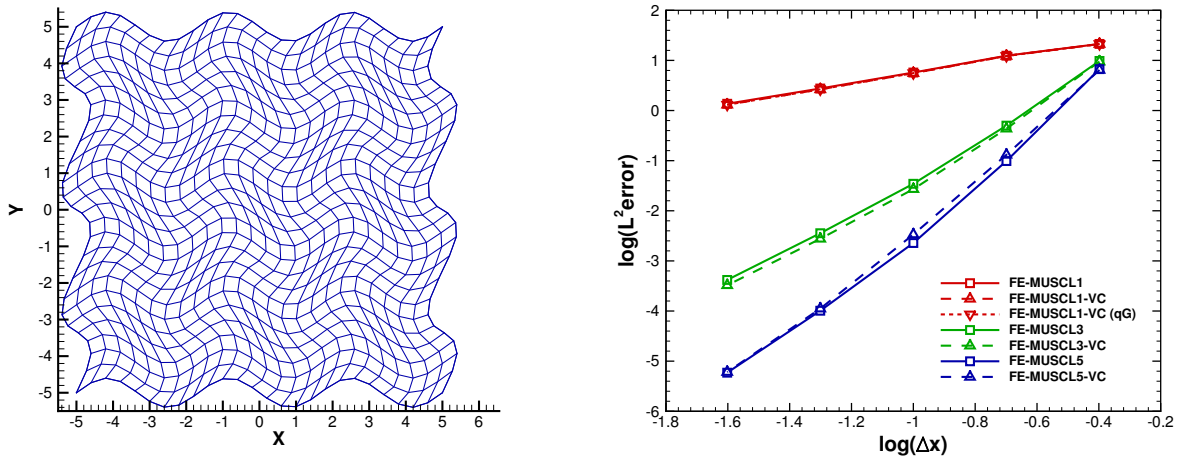


Figure 4.10: Order of accuracy on curvilinear grids. View of the coarser 25^2 mesh (left) and convergence of entropy error for FE-MUSCL schemes and VC (right).

Fig. 4.10 shows a view of the coarser grid and the convergence of entropy error, whereas detailed error values are given in Table 4.2. Naturally, the absolute error of the numerical schemes is larger compared to the calculation of the case on a Cartesian grid. The perturbations of Eq. (4.105) result in highly skewed cells for the coarsest resolution (see Fig. 4.10), therefore the convergence slope

is larger over the first refinement steps. Furthermore, the convergence slope of fifth-order schemes is slightly reduced on very fine grids, since the baseline FE-MUSCL schemes are applied without explicit metric corrections. The overall convergence for schemes with VC corrections is however similar to baseline FE-MUSCL schemes at all orders of accuracy.

Finally, the calculation of the derivatives of the VC term with the operator (qG) of Eq. (4.94) is shown to give equivalent results to the standard Green-Gauss operator at first-order of accuracy. This is partly because the baseline schemes of this study themselves are applied without metric corrections, and therefore have higher error on non-Cartesian grids. Moreover, as shown on the preceding results, the qG operator is similar to the standard Green-Gauss operator on moderately distorted meshes. The influence of a consistent k -exact operator is expected to be more important on highly irregular grids and especially alongside k -exact finite volume schemes, which are consistent and preserve high-order of accuracy on any grid.

4.5.2 Advection of an isentropic vortex

The following test case is the advection of a 2D vortex in an inviscid uniform flow. The FE-MUSCL schemes used in the present work, as well as the majority of numerical schemes in general, are directional, meaning that numerical error is increased when the grid is not aligned with the direction of advection. Computational meshes for simple applications can be appropriately constructed to follow the propagation direction of primary structures, but the same cannot be done for the majority of turbulent flows, which are naturally irregular. It is therefore necessary that numerical schemes are pertinently evaluated for such scenarios. In this case, the flow is thus inclined by 45° with respect to the grid direction, so as to underline the effect of numerical error of both the baseline schemes and with the VC corrections.

The advection is studied on a square computational domain $(x, y) \in [-15, 15] \times [-15, 15]$. The nondimensional flow velocity components are $u_{\text{inf}} = v_{\text{inf}} = 1$ so that $\|\vec{v}_{\text{inf}}\| = \sqrt{2}$ in the diagonal direction. The fluid variables are $\gamma = 1.4$, $p_{\text{inf}} = 1/\gamma$, $\rho_{\text{inf}} = 1$. The isentropic vortex is initialized at $(x_o, y_o) = (-10, -10)$ using the model of Eq. (4.102) as for the previous case. Time integration is performed with a classical 4-step explicit Runge-Kutta algorithm and a time step $\Delta t = 0.025$ for all cases, meaning an approximate $CFL \approx 0.083$. Note that a full advection is completed in time $T_p = 30$.

Table 4.3: Confinement parameters for the isentropic vortex advection case

Baseline scheme	Mesh	VC order	μ/ε	ε
FE-MUSCL3	100×100	1st	0.20	0.16
		3rd	0.20	0.16
		3rd	0.20	0.06
FE-MUSCL5	100×100	1st	0.40	0.02
		3rd	0.40	0.02
		5th	0.40	0.02

Space discretization is performed using third- and fifth-order FE-MUSCL baseline schemes. The problem is solved on a coarse 100×100 and a medium 200×200 Cartesian grid with approximately 4 and 8 cells respectively across the vortex core radius and periodicity conditions are imposed at each side of the domain. It should be noted that the coarse 100^2 mesh case is not expected to display significant difference between VC schemes of different order. This is because the difference in the error convergence of high-order VC for such a coarse mesh ($\Delta x = 0.3$) is not significant with respect to the first-order one (see Fig. 4.7). The purpose of this study is therefore to demonstrate the vorticity preserving capability of all orders of VC at very coarse meshes. In turn, the more refined 200^2 mesh is selected to demonstrate the increased compatibility of high-order VC with high-order baseline flux discretizations. For the FE-MUSCL3 scheme we are solving the case on both meshes, whereas for the more precise FE-MUSCL5 we are only calculating the case on the

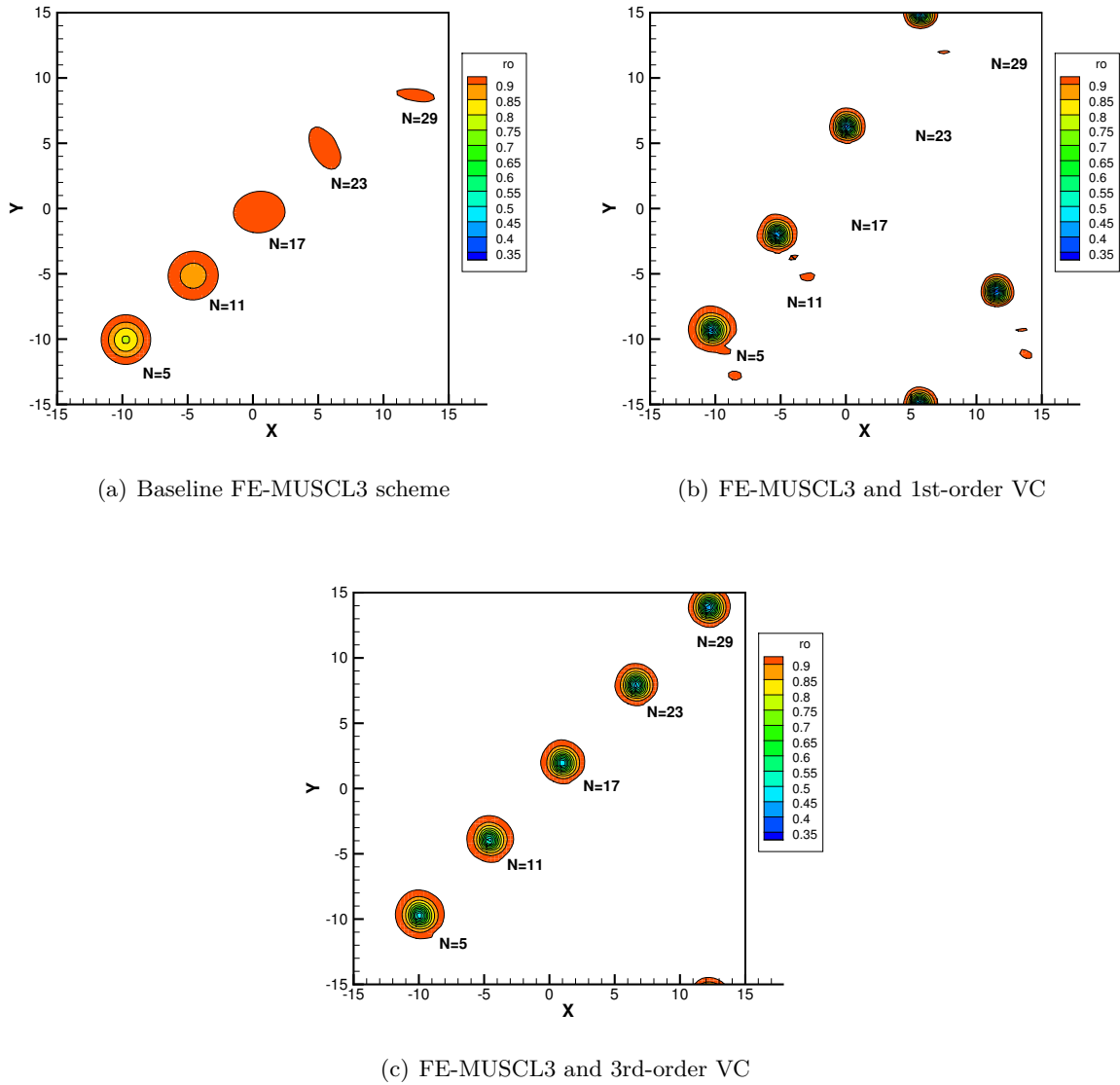


Figure 4.11: Iso-density snapshots during the diagonal vortex advection. Computed with the 3rd-order FE-MUSCL scheme with and without VC on the 100^2 mesh. The approximate number of completed passages at each snapshot is indicated next to the corresponding contour.

coarse mesh. The advection is computed over a distance of 30 passages across the computational domain (time $30 T_p$) for the FE-MUSCL3 and 300 passages (time $300 T_p$) for FE-MUSCL5. For the cases where VC was applied, the value of the confinement parameters is defined empirically depending on the numerical error of the baseline scheme, corresponding to stronger VC for a case with important effect of dissipation, that is for a lower-order baseline scheme or a coarser mesh resolution. The coefficients used for the study are shown in Table 4.3.

4.5.2.1 Results at third-order of accuracy

Fig. 4.11 shows iso-density contours during the advection of the vortex for the FE-MUSCL3 case on the 100^2 mesh. The effect of dissipative error is severe for the baseline scheme leading to a complete diffusion of the vortex after 30 passages across the computational domain. The 1st-order VC method achieves a good preservation of vortex intensity, but introduces significant dispersion error along the vertical direction. The 3rd-order VC scheme has similar vorticity preserving capabilities with a more accurate trajectory prediction than the 1st-order one. Fig. 4.12 shows a more quantitative

measure of preservation of vortex intensity through the evolution of minimum density, extracted at every passage across the computational domain. The effect of dissipation is apparent for the baseline scheme. For the more refined 200^2 mesh, the negative dissipation of the 1st-order VC term does not decrease according to the order of the baseline scheme, resulting in a rapid amplification of the advected structure. For this reason, results on the fine mesh are presented for the 3rd-order VC only.

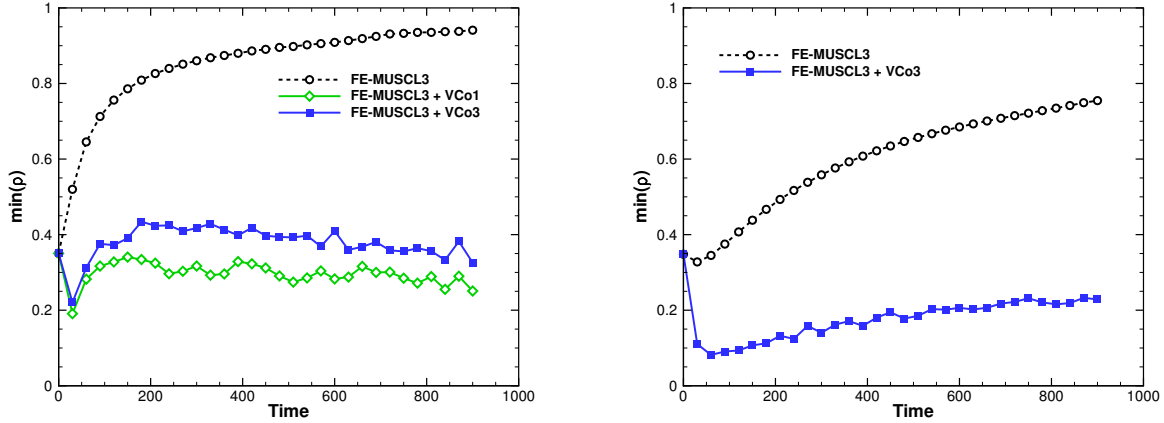


Figure 4.12: Time evolution of core density using FE-MUSCL3 and VC. Results computed on the 100^2 mesh (left) and on the 200^2 mesh (right).

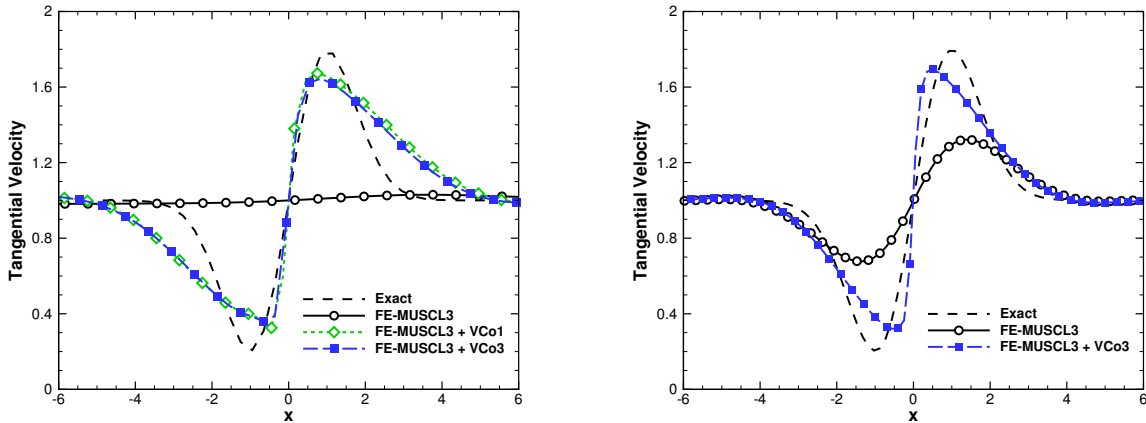


Figure 4.13: Comparison of tangential velocity profiles after 30 passages across the computational domain, i.e. after time $t = 30 T_p$. Computed with the FE-MUSCL3 scheme with and without VC on the 100^2 mesh (left) and on the 200^2 mesh (right).

The evolution of core density also shows an initial amplification of the vortex intensity, which then quickly relaxes to a shape that satisfies the balance between the joint linear dissipation of VC term and the baseline scheme against the nonlinear anti-dissipation of the VC correction. The initial stage of this mechanism might be related to the slightly positive values of the imaginary part of the modified wavenumber of confinement schemes already discussed in Section 3.4, since the spectral analysis portrays the characteristics of the numerical scheme for the calculation of a single time step and does not convey information on subsequent nonlinear mode interaction. The vortex will eventually relax to an asymptotic shape that is advected without diffusion over arbitrarily long distances. However, this relaxation is significantly slower for VC of higher-order [45, 47] and usually

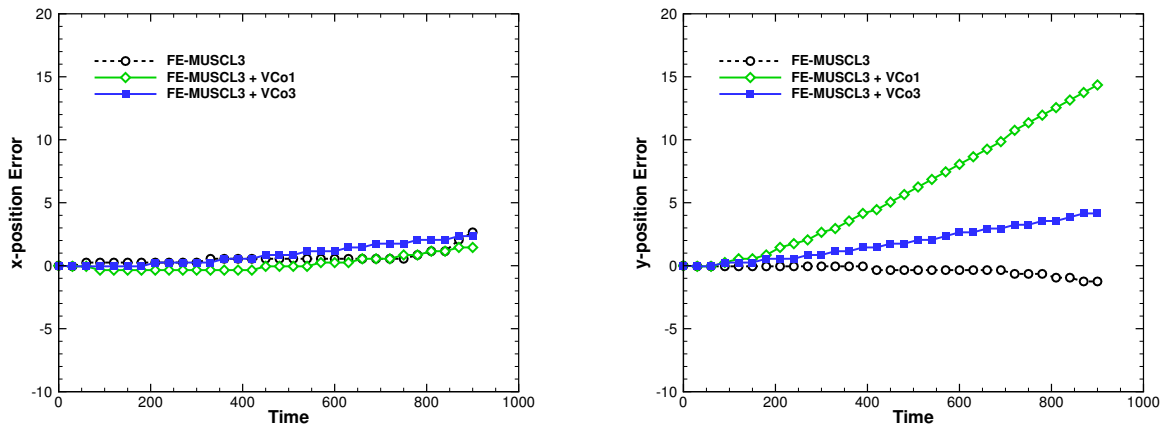


Figure 4.14: Error in trajectory calculation for the FE-MUSCL3 scheme and VC on the 100^2 mesh.

unreachable in realistic applications, meaning that results should remain closer to the exact solution for VC of higher-order.

Horizontal extractions of tangential velocity profiles at the end of the computation are shown in Fig. 4.13 and are representative of the schemes' capability of preserving the shape of advected vortical structures. All curves have been centered at $x=0$ for the sake of comparison. Computed profiles for schemes with and without VC show some spreading with respect to the exact solution, especially for the coarser mesh. However, VC clearly improves vorticity preservation for both meshes and produces satisfactory results especially in comparison to the baseline scheme and considering the length of the computed distance. The trajectory error with respect to the exact solution, which is the passive advection of the vortex along the diagonal, is shown in Fig. 4.14 as a measure of the schemes' phase approximation. Results are presented only for the coarser 100^2 mesh as trajectory errors are in the order of a few cells for the 200^2 case. The scheme with the 1st-order VC correction exhibits an increased dispersion error in the vertical direction since the early stages of the advection. For the 3rd-order VC, the difference with respect to the exact solution is equivalent to the baseline scheme.

4.5.2.2 On the influence of the confinement parameters

The present test case is an interesting basis to investigate the influence of the choice of confinement parameters, and particularly that of the linear dissipation of the VC term (μ term in Eq. (4.42)). There usually exist multiple pairs of parameters $(\mu/\varepsilon, \varepsilon)$ that produce equivalent results in terms of vortex preservation, but it is not straightforward to identify whether the nonlinear dynamics of VC are similar depending on the absolute value of the parameters. To investigate this, we are evaluating four different pairs of values $(\mu/\varepsilon, \varepsilon) = \{(0.0, 0.10), (0.2, 0.16), (0.4, 0.40), (0.6, 1.80)\}$, for the FE-MUSCL3 and 3rd-order VC case on the coarser 100^2 mesh. These were obtained by prescribing μ/ε and identifying the value of ε which gives roughly equivalent preservation of the vortex. For such a case with significant effect of numerical dissipation (see Fig. 4.12), a VC correction of relatively high magnitude (i.e. higher value of ε) is needed to preserve the vortex in the computation. Especially for high values of μ/ε , where numerical dissipation is further increased, the values of ε needed to preserve the vortex are necessarily even larger than what is usually applied in computations, but differences in dynamics should be easier observed in such a scenario. Results of the comparison are presented in Fig. 4.15, showing that significantly higher values of the confinement parameters lead to a more irregular evolution of the vortex core density and to larger trajectory errors. The dispersion error however remains acceptable for reasonable values of ε , in the order of the scheme's artificial dissipation coefficient.

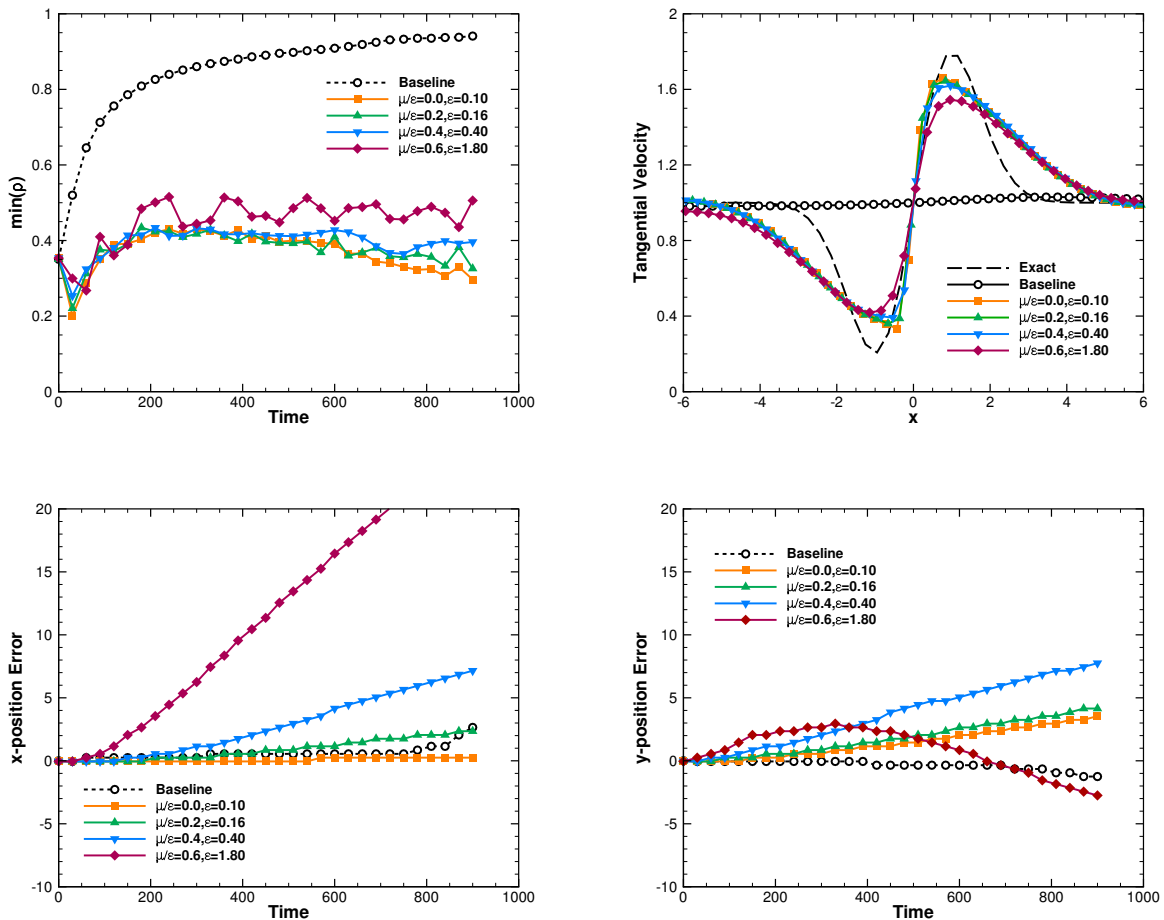


Figure 4.15: Effect of different sets of confinement parameters $(\mu/\varepsilon, \varepsilon)$. Computed with the FE-MUSCL3 baseline scheme and 3rd-order VC on the 100^2 mesh. The velocity profiles are plotted at time $t = 30 T_p = 900$.

It is interesting to consider these results in analogy with the spectral analysis of Section 3.4, where it was demonstrated that the nonlinear negative dissipation of the VC term of Eq. (4.42) affects both the dispersive and dissipative properties of the discretization. For the Euler equations, that is in the absence of fluid viscosity, the dissipation of the complete space discretization is defined from the balance between the linear artificial dissipation of the numerical flux (4.25) and both the linear and nonlinear part of the VC term (4.42). This means that an increased value of ε can easily be balanced by a reciprocally increased value of μ . The case is however different for dispersion. The dispersive properties of the space discretization are defined from the convective flux approximation of Eq. (4.25) and the dispersive effect of the nonlinear part of the VC term. In terms of confinement parameters, this means that the dissipation of the scheme is driven mainly by the balance between μ and ε , whereas its dispersive properties are driven by ε .

4.5.2.3 Results at fifth-order of accuracy

Fig. 4.16 demonstrates that VC corrections effectively balance the dissipation of the baseline scheme even at fifth-order of accuracy. Even though the fifth-order FE-MUSCL scheme has greatly reduced dissipation compared to the third-order version (see Fig. 4.12), the effect of dissipation becomes important over time. The VC flux corrections however allow the overall steady preservation of the intensity of the vortex over the very long distance advection. More importantly, Fig. 4.16 shows that the profiles for the cases with VC show little spreading and are considerably closer to the exact

profile than the baseline FE-MUSCL5. The trajectory error with respect to the exact solution is presented in Fig. 4.17. Again, the original 1st-order VC shows increased error in the vertical direction even at early times of the advection. Higher-order VC schemes show overall decreased error compared to the baseline FE-MUSCL5, even though no clear conclusion can be made regarding the order of VC in this case.

It is also interesting to consider the accuracy of these results against the error measured in the grid convergence study of Section 4.5.2. At fifth-order of accuracy, both the static case and the present vortex advection study were computed using the same confinement parameters μ/ε and ε . As already mentioned in the study of the previous section, the computed absolute error values depend on the values of the confinement parameters. In that study, the fifth-order scheme with VC produced a solution with higher error than its baseline version. In an advection case however, the baseline numerical dissipation is larger than in the static vortex case. It is even more so the case in the present study, since the direction of advection is misaligned with the computational grid. As a result, for the same confinement parameters as in the static case, the scheme with VC gives a result that is significantly closer to the exact solution than the baseline version.

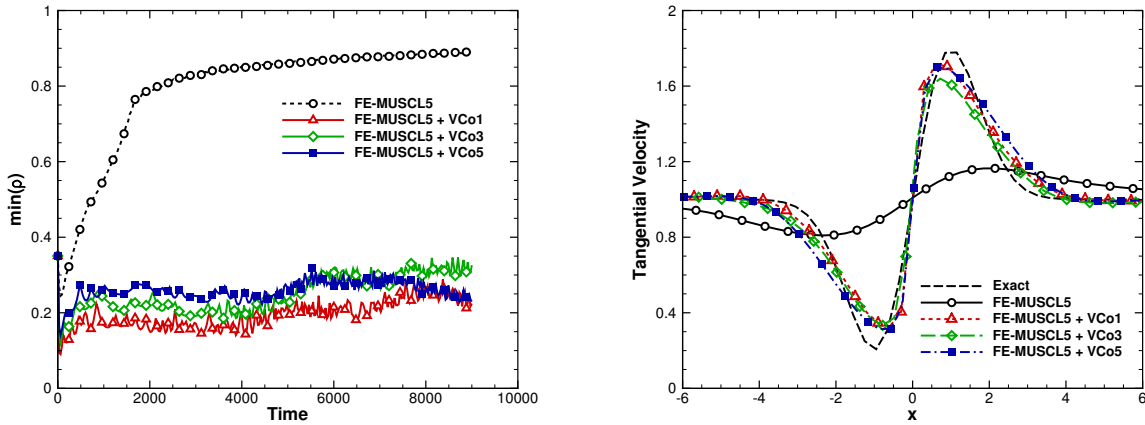


Figure 4.16: Time evolution of core density (left) and comparison of tangential velocity profiles after 300 passages across the computational domain, i.e. at time $t = 300 T_p = 9000$ (right). Computed with the FE-MUSCL5 scheme and VC on the 100^2 mesh.

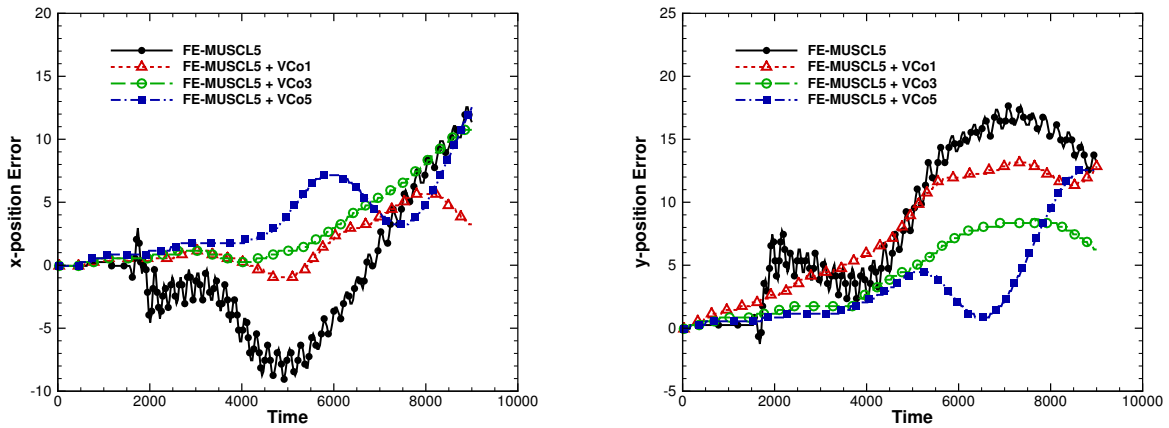


Figure 4.17: Error in trajectory calculation for the FE-MUSCL5 scheme and VC on the 100^2 mesh.

4.5.2.4 Results on non-Cartesian grids

The vorticity-preserving capability of the developed VC schemes is finally assessed on the same diagonal vortex advection case, considering a discretization on non-Cartesian grids. Specifically, we are considering two computational grids generated on the base of a 100^2 square Cartesian mesh covering the domain $(x, y) \in [-15, 15] \times [-15, 15]$. The coordinate perturbations for the two grids are given by:

$$\begin{cases} x'_1 = -A_x \Delta x \sin [2\pi n_x (y - y_{\min}) / L_y] \\ y'_1 = A_y \Delta y \sin [2\pi n_y (x - x_{\min}) / L_x] \end{cases} \quad \begin{cases} x'_2 = A_x \Delta x \sin [2\pi n_x (x - x_{\min}) / L_x] \\ y'_2 = A_y \Delta y \sin [2\pi n_y (y - y_{\min}) / L_y] \end{cases}$$

where L_x, L_y denote the domain length in each direction, the perturbation amplitudes are taken $A_x = A_y = 2$ and their wavelengths are defined by $n_x = n_y = 3$. The perturbations (x'_1, y'_1) result in a regular curvilinear grid and the perturbations (x'_2, y'_2) result in a stretched Cartesian grid. A view of the two grids is shown in Fig. 4.18.

The test case parameters are taken the same as for the previous calculations on Cartesian grids. As for the VC corrections, it was found that the method was less robust on the stretched grid, for very low values of μ/ε . This behavior is likely related to the larger volume variations between neighboring cells, which induce increased gradients in the VC term calculation (see Eq. (4.86)). These are more difficultly balanced by the baseline numerical dissipation than on a grid without significant cell-volume variations. However, an increased value of μ/ε introduces some additional dissipation that effectively allows to overcome this difficulty.

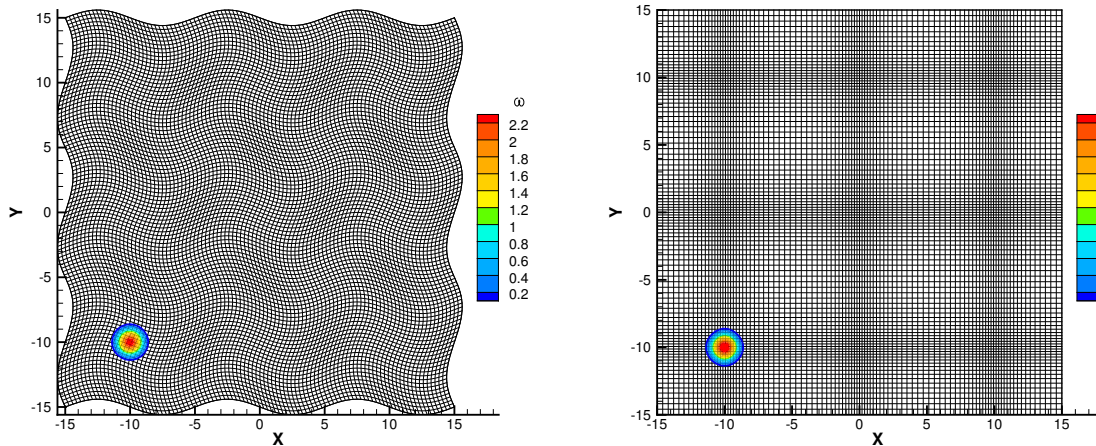


Figure 4.18: View of the initial vorticity field on the regular curvilinear and the stretched Cartesian grid composed of 100^2 cells.

A comparison of results is presented for the third-order FE-MUSCL scheme and third-order VC on the different meshes. In any case, the preservation of higher than third-order of accuracy in a finite volume formulation is not easily achieved on general curvilinear grids, especially under a reasonable computational cost. The confinement parameters are taken $\mu/\varepsilon = 0.4$ and $\varepsilon = 0.40$, which correspond to one of the parameter pairs evaluated in the parametric study of Fig. 4.15. The rest of the numerical parameters are the same as for previous computations. Results of the baseline scheme are shown only for the Cartesian mesh, as it is very dissipative and gives very similar results on all three meshes. Fig. 4.19 shows that the VC correction balances the excess dissipation and gives a roughly similar evolution of core density between the three cases, with larger density fluctuations being observed on the stretched grid. These might be related to the higher gradients in the VC correction induced by cell-volume variations, or to the sampling of minimum density on the grid at the moments of extraction. The error in trajectory prediction has been found to be fortuitously

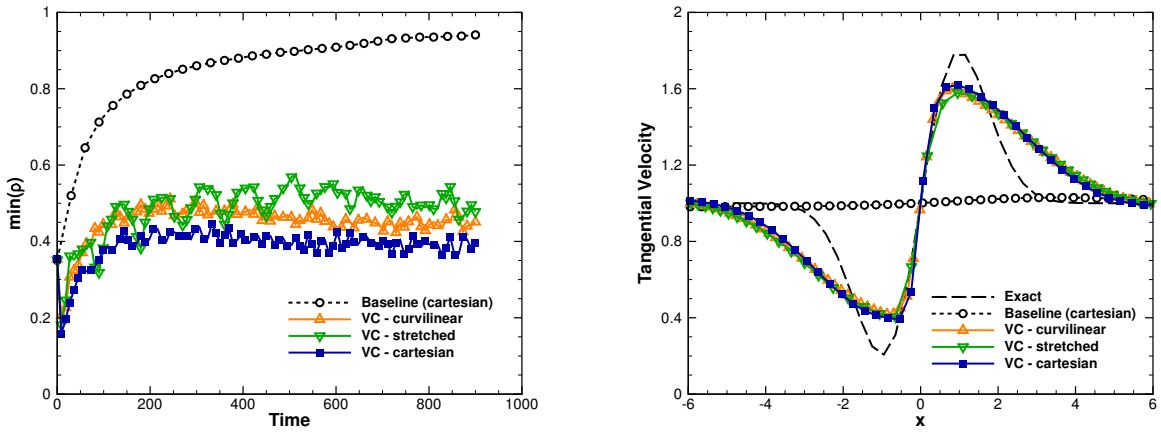


Figure 4.19: Effect of the VC correction on different types of computational meshes. Results computed with the FE-MUSCL3 scheme and 3rd-order VC on the 100^2 mesh, $\mu/\varepsilon = 0.4$, $\varepsilon = 0.40$. The velocity profiles are plotted at the end of the advection, at time $t = 30 T_p$.

lower on curvilinear grids, compared to the Cartesian case. The tangential velocity profiles at the end of the calculation however show that the computed vortex profile is almost equivalent for all three meshes.

As successive derivations are required for the calculation of high-order VC, the calculation of derivatives in a finite difference formulation would be very sensitive to numerical error on non-Cartesian meshes. The present results show that the calculation of derivatives in a finite volume approach gives consistent results on curvilinear grids, at least for the cases investigated in this study.

Case summary

It is clear in this study that schemes with VC have significantly improved vorticity preservation properties compared to baseline ones for all orders of the VC term. On very coarse meshes, high-order VC is not significantly closer to the exact solution compared to the original 1st-order one, the difference appearing mostly in terms of dispersion error. However, for finer meshes, the use of VC of the same order as the baseline scheme is important to guarantee consistency in terms of convergence towards the exact solution and to ensure that VC acts at a rate that matches the dissipation of the baseline scheme.

4.5.3 Discussion on computational cost

Table 4.4 shows measured computation times for the baseline FE-MUSCL schemes with and without VC corrections. Calculations were performed on an Intel Xeon E5-1620 v4 processor for the vortex advection study of the previous section over a total advection time $t = 30 T_p$ on a 100^2 Cartesian mesh. Derivatives for the VC correction are calculated in a finite volume formulation and the Laplacian for high-order VC is computed with the 5-point scheme presented in Section 4.4.4. For computations on Cartesian grids, derivatives for VC can be calculated in finite differences instead, which naturally requires less operations. On the other hand, baseline schemes are applied without metric corrections.

On this case, the cost of the VC correction is found to be reasonable compared to that of the baseline method. This cost is particularly justified by the effective reduction of excess numerical dissipation within the vortex (see study of Section 4.5.2). Note also that the cost of the Laplacian for higher-order VC is moderate compared to the cost of the first-order VC method itself in two space dimensions. Computations of three-dimensional problems require more operations, both for the baseline scheme and with VC. The actual computational cost is of course dependent on the

method's implementation. Considering the present development version of the method, important efficiency improvements can be achieved by reducing the required number of ghost cells for high-order VC (see Section 4.4.2) and also by re-using the velocity gradients calculated in other parts of the solver (e.g. viscous fluxes).

Table 4.4: Computation time per grid cell, per sub-iteration for FE-MUSCL schemes and VC.

	Baseline	1st-order VC	3rd-order VC	5th-order VC
1st-order (Roe)	0.32 μ s	0.44 μ s	-	-
3rd-order	0.36 μ s	0.47 μ s	0.50 μ s	-
5th-order	0.37 μ s	0.48 μ s	0.52 μ s	0.55 μ s

Nonetheless, it is difficult to reach a general conclusion regarding the computational cost introduced by VC, as it represents a correction added to the baseline scheme and not a complete numerical method. The relative cost increase with VC in the present case is more important, because of the low cost of standard linear FE-MUSCL schemes. The improvement in results is however also more important in this case. On the other hand, the relative cost increase with VC will be less for more complex baseline schemes, but the relative improvement in results is also likely to be less. A cost analysis will thus be always dependent on the baseline numerical method of choice. The use of VC corrections should however be cost-efficient for cases where the advection of vortical structures is of interest (e.g. wakes), as VC is particularly appropriate for such problems.

4.6 Chapter summary

In this chapter, high-order extensions of the Vorticity Confinement method have been developed for the compressible Navier-Stokes equations, based on the conservative VC2 formulation of J. Steinhoff. Both the original VC2 method and its high-order extensions are interpreted as a numerical correction of the baseline dissipation in vortical flow regions, and thus added only to the discretized momentum conservation equation.

The derivation of high-order VC corrections is analytical, based on the Laplacian of the original first-order VC term. In this way, the nonlinear anti-dissipation of VC is based on high-order derivatives, similarly to baseline high-order dissipation terms. At the same time, the developed high-order extensions remain rotationally invariant and independent of the baseline scheme. Additionally, it has been shown that both the first-order VC2 source term and its high-order extensions are analytically equivalent to a nonlinear anti-dissipative correction of the numerical flux in vortical flow regions. Then, the numerical discretization of the developed schemes has been discussed in detail, specifically regarding the calculation of high-order derivatives. On Cartesian grids, these can be calculated using large stencils in a finite difference formulation. On general grids, high-order derivatives can be calculated recursively in a finite volume formulation. This approach is applicable to both structured and unstructured grids. The implementation of boundary conditions and the deactivation of the VC correction outside vortices are also discussed.

The developed schemes have then been applied to a series of numerical tests. First, the actual order of accuracy of schemes with VC has been evaluated in the case of a static isentropic vortex. This study has shown that the original first-order method degrades the order of accuracy in vortical regions when applied to high-order simulations. On the other hand, high-order VC extensions have been shown to preserve high-order of accuracy and be consistent with high-order flux discretizations. In a following step, the developed schemes have been applied to long-distance vortex advection studies. These have demonstrated that schemes with VC provide results considerably closer to the exact solution than the baseline scheme, both at third- and at fifth-order of accuracy. They are thus capable of propagating vortices over very long distances with low effects of dissipation, even when the propagation direction is misaligned with the computational grid. Furthermore, it has been shown that there exists a wide range of pairs of confinement parameters yielding similar vorticity preserva-

tion, but too large values of these parameters tend to introduce additional dispersive errors in the calculation. In practice however, dispersion errors were found to be low for values of confinement parameters in the order of magnitude of the baseline artificial dissipation coefficient.

So far, the order of accuracy of high-order VC extensions and their capability to balance dissipation within vortices has been demonstrated in simple cases. Their applicability to the calculation of complex flows remains to be evaluated. In the following chapter, the robustness and resolvability of schemes with high-order VC are investigated in more detail by application to a series of scale-resolving simulations.

Chapter 5

Application to complex unsteady vortical flows

Contents

5.1	Viscous Taylor-Green vortex	91
5.1.1	Description of the test case and numerical strategy	91
5.1.2	Grid convergence study	93
5.1.3	Numerical results	94
5.1.4	Sensitivity to the velocity gradient calculation scheme	98
5.2	Decay of compressible Homogeneous Isotropic Turbulence	99
5.2.1	Description of the initial condition	99
5.2.2	Low-compressibility HIT at $M_{t0} = 0.2$ and $M_{t0} = 0.5$	100
5.2.3	Highly-compressible HIT at $M_{t0} = 1.0$	106
5.3	Chapter summary	110

In this chapter, the developed high-order Vorticity Confinement corrections are applied to the numerical calculation of complex vortical flows. The objective of these applications is to evaluate the robustness of high-order VC corrections and their consistency with multi-scale vortical flow dynamics. At the same time, these studies aim at evaluating the applicability of VC to turbulent flow simulations.

5.1 Viscous Taylor-Green vortex

5.1.1 Description of the test case and numerical strategy

The present section consists in a numerical study of the Taylor-Green Vortex (TGV) flow at $Re=1600$. The TGV flow, originally investigated by G. I. Taylor and A. E. Green [204], presents an excellent test case for the resolution and numerical dissipation properties of numerical methods. It is an unsteady problem solved in a periodic box $[2\pi]^3$. The two-dimensional initial condition for velocity $\vec{v}(x, y, z, t)$ is analytical and corresponds to large-scale vortices:

$$\begin{cases} u(x, y, z, 0) &= \sin x \cos y \cos z \\ v(x, y, z, 0) &= -\cos x \sin y \cos z \\ w(x, y, z, 0) &= 0 \end{cases} \quad (5.1)$$

The initial condition for pressure is given by:

$$p(x, y, z, 0) = p_0 + \frac{\rho}{16} (\cos(2x) + \cos(2y)) (\cos(2z) + 2) \quad (5.2)$$

where $p_0 = 100$. The initial density field is considered constant $\rho(x, y, z, 0) = \rho_0 = 1$. The fluid is considered a perfect gas with zero bulk viscosity μ_v , heat capacity ratio $\gamma = 1.4$, and the Prandtl number is $Pr = 0.71$. Computations are performed at a low Mach number $M_0 = 0.10$. In this condition, comparisons are possible with reference solutions of the incompressible Navier-Stokes equations. All quantities have been adimensionalized with the reference velocity, density and length of the periodic box.

Despite the simplicity of the above initial condition, the time evolution of the TGV flow is characterized by complex energy transfer from large to smaller scales through viscous, stretching and tilting mechanisms. For the viscous TGV case, kinetic energy cascade occurs due to fluid viscosity and numerical dissipation, as well as interaction and decay mechanisms that are characteristic of homogeneous turbulence. Due to the simplicity of the configuration and the complexity of the represented phenomena, the TGV is a common benchmark case for high-order CFD workshops [220] and high-accurate numerical methods [24, 30, 122, 209].

It is therefore chosen as a test case to assess the robustness and performance of high-order Vorticity Confinement. This assessment has multiple objectives. Having already proved the capability of VC to balance numerical dissipation in vortical flow regions and allow the advection of vortical structures over long distances, the primary objective is the investigation of the effect of VC in the dynamics of a complex and multi-scale flow, representative of a broad range of Large Eddy Simulation (LES) applications. Specifically, it is an important step to evaluate the applicability of high-order VC to the calculation of turbulent flows, where the improvement in the preservation of vortical structures is of crucial importance. The secondary objective is the evaluation of the improvement introduced by VC in the prediction of the TGV flow, compared to baseline upwind FE-MUSCL schemes.

The compressible Navier-Stokes equations are solved on a series of Cartesian meshes of varying density with total numbers of cells: 32^3 , 64^3 , 128^3 , 256^3 . Convective fluxes are discretized using the 5th-order accurate FE-MUSCL scheme described in Section 4.2.1.1. The discretization of viscous fluxes is second-order accurate and described in Section 4.2.1.2. Time integration is performed using an explicit 6-stage Runge-Kutta algorithm, formally accurate to 2nd-order with coefficients that are optimized in the wavenumber space to ensure minimal dispersive and dissipative error [20]. The time step is set equal to $\Delta t = 0.01/0.005/0.0025/0.00125$ for the coarser to the finer mesh respectively, so that the CFL number is kept approximately constant for all cases. The presented results have been found to be sufficiently converged for these time step values. For the cases with VC, the source term is always 5th-order accurate, as the baseline FE-MUSCL scheme. Presented results are compared against the reference calculation of the International Workshop of High-Order CFD Methods. This is the result of a converged direct numerical simulation (DNS) using a dealiased pseudo-spectral method on a 512^3 mesh.

In the TGV flow, a measure of the resolution of numerical methods is the prediction of the rate of dissipation of kinetic energy K . The integrated kinetic energy over the complete computational domain $\Omega = [0, 2\pi]^3$ is given as:

$$K = \frac{1}{\rho_0 \Omega} \int_{\Omega} \frac{1}{2} \rho_0 \|\vec{v}\|^2 d\Omega \quad (5.3)$$

The dissipation rate is then computed directly from the kinetic energy as $-\frac{dK}{dt}$. The decay of kinetic energy in the computational domain can be derived from the compressible Navier-Stokes equations as the sum of the three components [30]:

$$-\frac{dK}{dt} = 2 \frac{\mu}{\rho_0 \Omega} \int_{\Omega} \overline{\overline{S_d}} : \overline{\overline{S_d}} d\Omega + \frac{\mu_v}{\rho_0 \Omega} \int_{\Omega} (\overline{\overline{\nabla}} \cdot \overline{\overline{v}})^2 d\Omega - \frac{1}{\rho_0 \Omega} \int_{\Omega} p (\overline{\overline{\nabla}} \cdot \overline{\overline{v}}) d\Omega \quad (5.4)$$

where $\overline{\overline{S_d}}$ is the deviatoric part of the strain tensor. Above, the second component is zero since the fluid is considered to have zero bulk viscosity. Furthermore, the contribution of the third component is small for low effects of compressibility. The main contribution thus comes from the

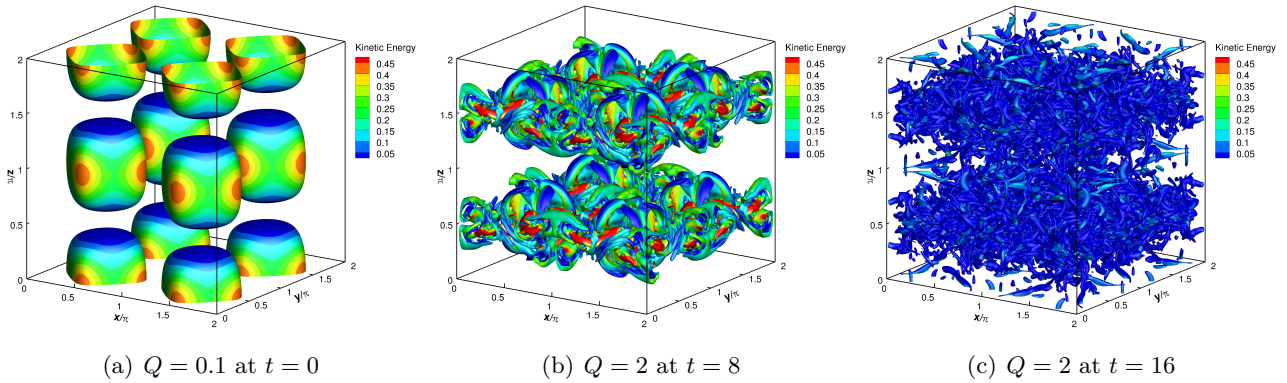


Figure 5.1: Iso-surfaces of the Q -criterion colored by kinetic energy at different time instants of the TGV flow evolution. Results computed with FE-MUSCL5 and 5th-order Vorticity Confinement on the 256^3 mesh.

first component. Under small compressibility effects, this can be approximated by the integral of enstrophy over the computational domain:

$$\mathcal{E} = \frac{1}{\rho_0 \Omega} \int_{\Omega} \frac{1}{2} \rho \|\vec{\omega}\|^2 d\Omega \quad (5.5)$$

where $\vec{\omega} = \vec{\nabla} \times \vec{v}$ is the vorticity. For incompressible flow without numerical dissipation, Eq. (5.4) gives the relation between kinetic energy dissipation rate and enstrophy:

$$-\frac{dK}{dt} = 2 \frac{\mu}{\rho_0} \mathcal{E} \quad (5.6)$$

In principle, the evolution of kinetic energy dissipation rate and enstrophy should be thus proportional, and related via Eq. (5.6). It is not however the case in practice. This is partly due to the appearance of compressibility effects, but primarily due to the numerical error of the discretization. The discrepancy between these two measures is thus often used as a criterion for the convergence of high-fidelity direct numerical simulations.

The calculation of enstrophy is particularly sensitive to numerical error. This is because enstrophy contains the integrated error in the computational domain both in the approximation of velocity and its gradients. For the following computations, enstrophy has been calculated through Eq. (5.5), using the 7-point Dispersion-Relation-Preserving (DRP) scheme of C. K. W. Tam and J. C. Webb [203] to approximate the velocity gradients.

5.1.2 Grid convergence study

The TGV problem is initially dominated by vortex stretching and tilting mechanisms, progressively generating smaller and smaller vortical structures. This continues up to non-dimensional time $t \approx 9$, at which the dissipation rate peaks. The flow then transitions to fully developed non-isotropic turbulence and finally decays due to the dissipation acting at the smaller scales. Snapshots of the flow computed with VC are shown in Fig. 5.1.

Fig. 5.2 presents a grid convergence study for the baseline FE-MUSCL5 scheme. It is apparent that the 32^3 mesh is too coarse to accurately represent the underlying physics and vortex interactions. As the mesh is refined however, the dissipation rate converges fast towards the reference DNS results. These are well matched already on the 256^3 mesh, except at later times during the end of the turbulence decay phase. As already discussed, the evolution of integrated enstrophy \mathcal{E} over the domain is more sensitive to numerical error and is not sufficiently converged towards the reference, even on the 256^3 mesh.

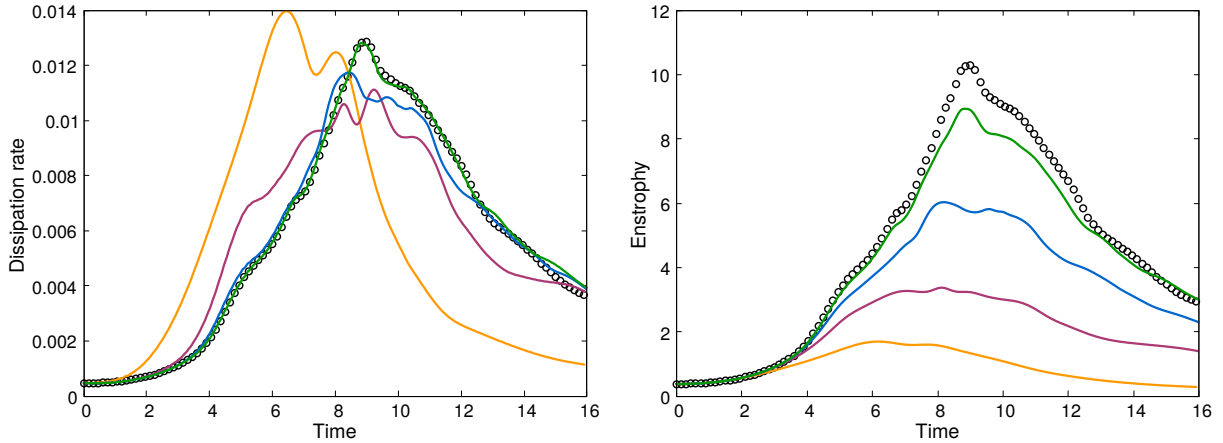


Figure 5.2: Grid convergence study for the baseline 5th-order FE-MUSCL scheme. Spectral– 512^3 : \circ , 32^3 mesh: —, 64^3 mesh: —, 128^3 mesh: —, 256^3 mesh: —. Time evolution of kinetic energy dissipation rate (left) and time evolution of enstrophy (right).

5.1.3 Numerical results

The evaluation of schemes with high-order VC is at first performed for two sets of confinement parameters, $(\mu/\varepsilon, \varepsilon) = (0.4, 0.02)$ and $(\mu/\varepsilon, \varepsilon) = (0.4, 0.04)$. The first set corresponds to standard values used in applications, such as for the diagonal vortex advection case of Section 4.5.2. The other corresponds to doubling ε , or equivalently the magnitude of VC, to test the robustness of the high-order VC correction. Note that the two values of $\varepsilon = \{0.02, 0.04\}$ correspond to $\varepsilon = \{1.2 k_5, 2.4 k_5\}$, where k_5 is the numerical dissipation coefficient of the 5th-order baseline numerical flux (4.25).

The left column of Fig. 5.3 shows the difference of the time evolution of the kinetic energy dissipation rate between the baseline case and the FE-MUSCL5 scheme with VC. On the 64^3 and 256^3 meshes, the dynamics of the scheme with VC are consistent with the vorticity dynamics of the flow, reducing dissipation during the vortex stretching phase and later on increasing the dissipation peak since it improves the preservation of small structures that largely contribute to this dissipation. For the 128^3 case however, VC is constantly reducing dissipation but does not increase the dissipation peak. For a large increase of the confinement parameter ε , or equivalently a large increase of the magnitude of the VC correction, the dissipation rate shows sharper changes during the flow evolution. Out of the two sets of parameters, the case $\varepsilon = 0.02$ gives results that are closer to the reference solution, especially for the 128^3 mesh during the vortex stretching phase. Furthermore, the effect of VC is smaller when the mesh is refined, or equivalently when numerical dissipation is reduced, displaying consistent behavior with the reduction of numerical dissipation for the baseline 5th-order FE-MUSCL scheme. This is true for the vortex stretching phase and up to the development of turbulence. During this last stage, VC increases the resolved dissipation compared to the baseline scheme due to the improved preservation of eddies in the inertial range, even when the baseline case is quite well-converged towards the reference results. A similar behavior can however also be observed for the baseline FE-MUSCL5 scheme, compared to the reference solution (see Fig. 5.2).

The time evolution of enstrophy is shown in the right column of Fig. 5.3 for the same cases. Results are straightforward meaning that VC introduces negative dissipation in the vorticity transport equation and therefore increases the integral value of enstrophy. In a sense, the introduction of VC thus accelerates the convergence towards the DNS solution. In the calculation of the kinetic energy dissipation rate, the effect of VC was shown to decrease with mesh refinement. Interestingly, it is not the case for enstrophy, where the influence of VC is more important as the mesh is refined. On the other hand, the magnitude of the negative dissipation of VC should decrease with mesh refinement according to the order of accuracy, similarly to the baseline high-order numerical dissipation. This is indeed observed for the kinetic energy dissipation rate. Regarding the calculation of enstrophy,

the efficiency of VC on the finer meshes is then possibly related to the better alignment of the term with local vorticity.

The consistency of high-order VC extensions is further demonstrated by the iso-contours of the dimensionless vorticity norm on a periodic face of the computational domain at time $t=8$. These are presented in Fig. 5.4. Results of the VC and baseline FE-MUSCL5 scheme are compared to the reference spectral computation and provide a good approximation of the main flow structures. The calculation with VC, corresponding to confinement parameters $(\mu/\varepsilon, \varepsilon) = (0.4, 0.02)$, shows improved preservation of vortices compared to the baseline scheme, without any introduction of spurious structures.

Another interesting evaluation of the schemes can also be performed independently of the ref-

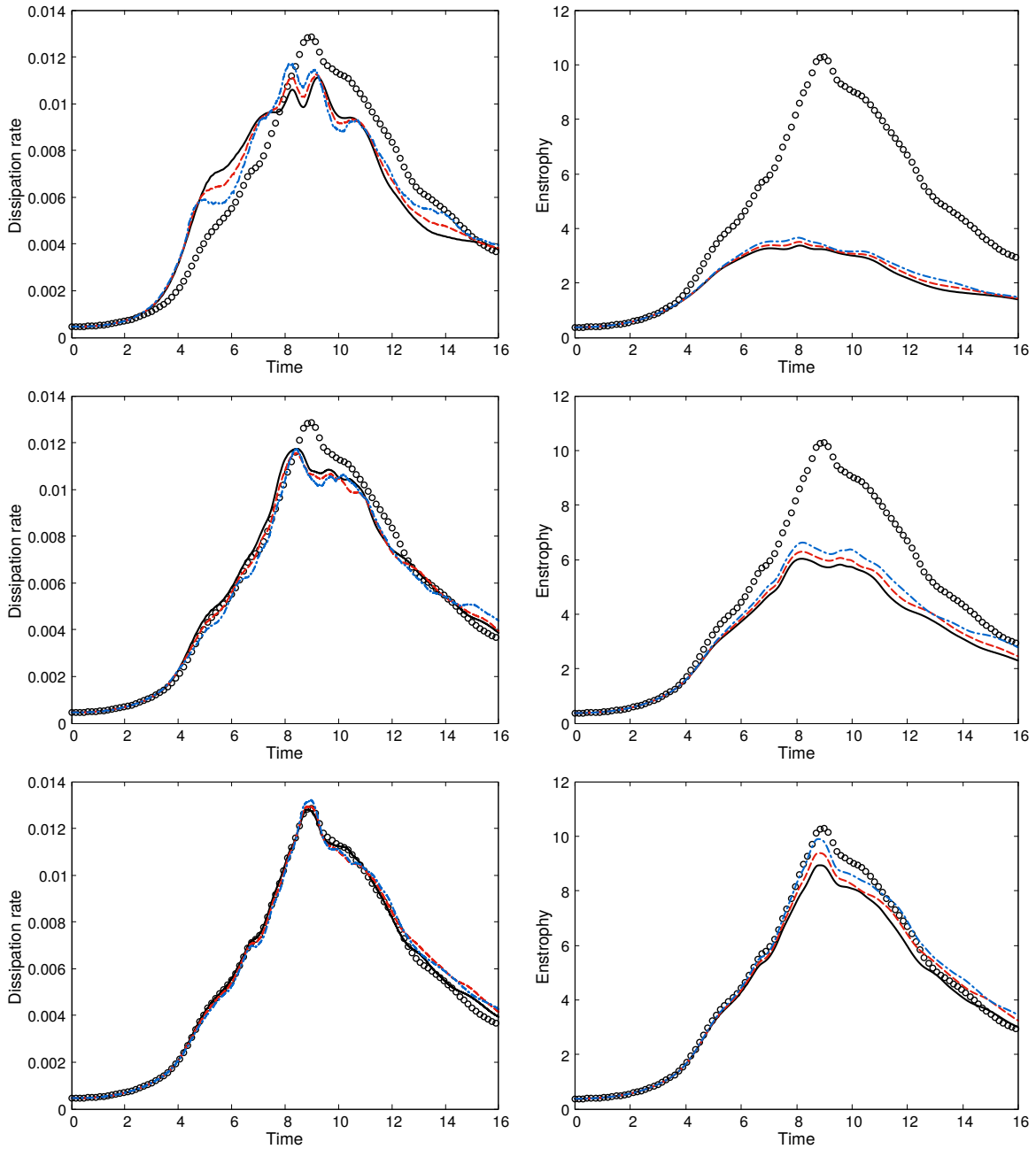


Figure 5.3: Effect of VC on the kinetic energy dissipation rate $-\frac{dK}{dt}$ and the evolution of enstrophy for $\mu/\varepsilon = 0.4$ and different values of ε . Spectral – 512^3 : \circ , baseline scheme:—, $\varepsilon = 0.02$:- - -, $\varepsilon = 0.04$:- · - ·. From top to bottom, 64^3 , 128^3 and 256^3 mesh. FE-MUSCL5 and 5th-order Vorticity Confinement.

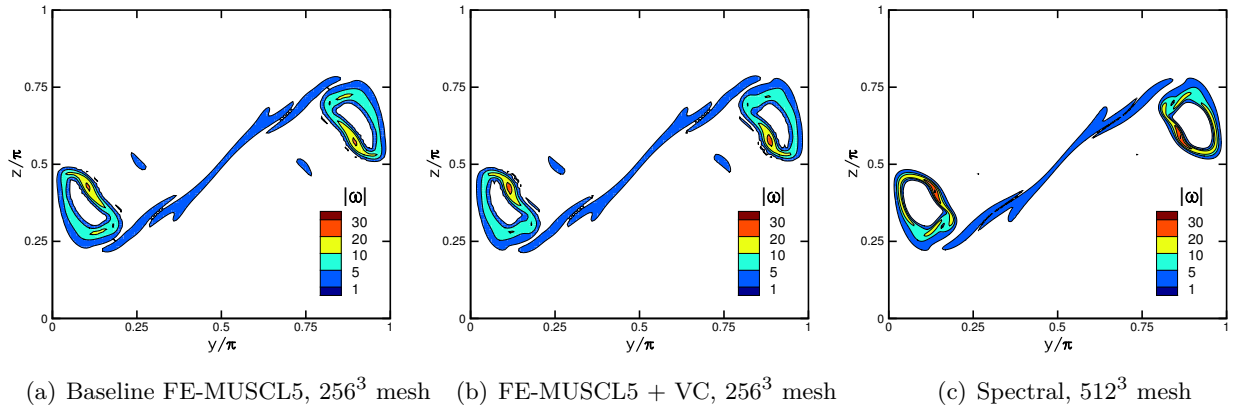


Figure 5.4: Iso-contours of the dimensionless vorticity norm $\|\vec{\omega}\|$ on the periodic face $x = 0$ at nondimensional time $t = 8$.

erence solution. Specifically, an error norm for each method can be defined by comparing the calculated enstrophy to the kinetic energy dissipation rate via Eq. (5.6):

$$e = \left| 2 \frac{\mu}{\rho_0} \mathcal{E} + \frac{dK}{dt} \right| \quad (5.7)$$

which is a measure of effects of compressibility and numerical dissipation, as per Eq. (5.4). The evolution of this error norm over time is shown in Fig. 5.5. The plotted errors are normalized with the peak value of the kinetic energy dissipation rate of the reference solution. Schemes with a VC correction are shown to have a lower error than the baseline scheme in the approximation of Eq. (5.6). However, doubling the value of ε does not further reduce the error during the vortex stretching phase on the 256^3 mesh.

The previous investigations have shown that good results can be obtained for ε in the order of the baseline high-order artificial dissipation coefficient. As a next step, the sensitivity of the solution to the value of μ/ε in a complex flow is assessed by means of a parametric study. At the same time, this study is performed to evaluate the stability of schemes with VC, if the internal dissipation of VC is reduced, or even set to zero. For this purpose, calculations with high-order VC are performed for $\mu/\varepsilon = \{0.0, 0.2, 0.4\}$. The confinement parameter ε is taken equal to $\varepsilon = 1.2 k_5 = 0.02$ and constant for all cases, for clearer comparison of the absolute values of μ .

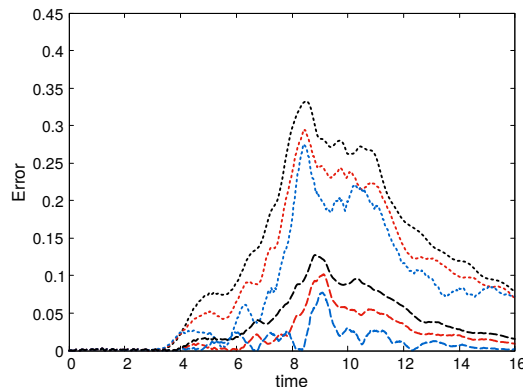


Figure 5.5: Relative error norm corresponding to compressibility and numerical dissipation effects. Baseline scheme: —, $\varepsilon = 0.02$: —, $\varepsilon = 0.04$: —. Error on the 128^3 mesh (dotted lines) and the 256^3 mesh (dashed lines). FE-MUSCL5 and 5th-order Vorticity Confinement, $\mu/\varepsilon = 0.4$.

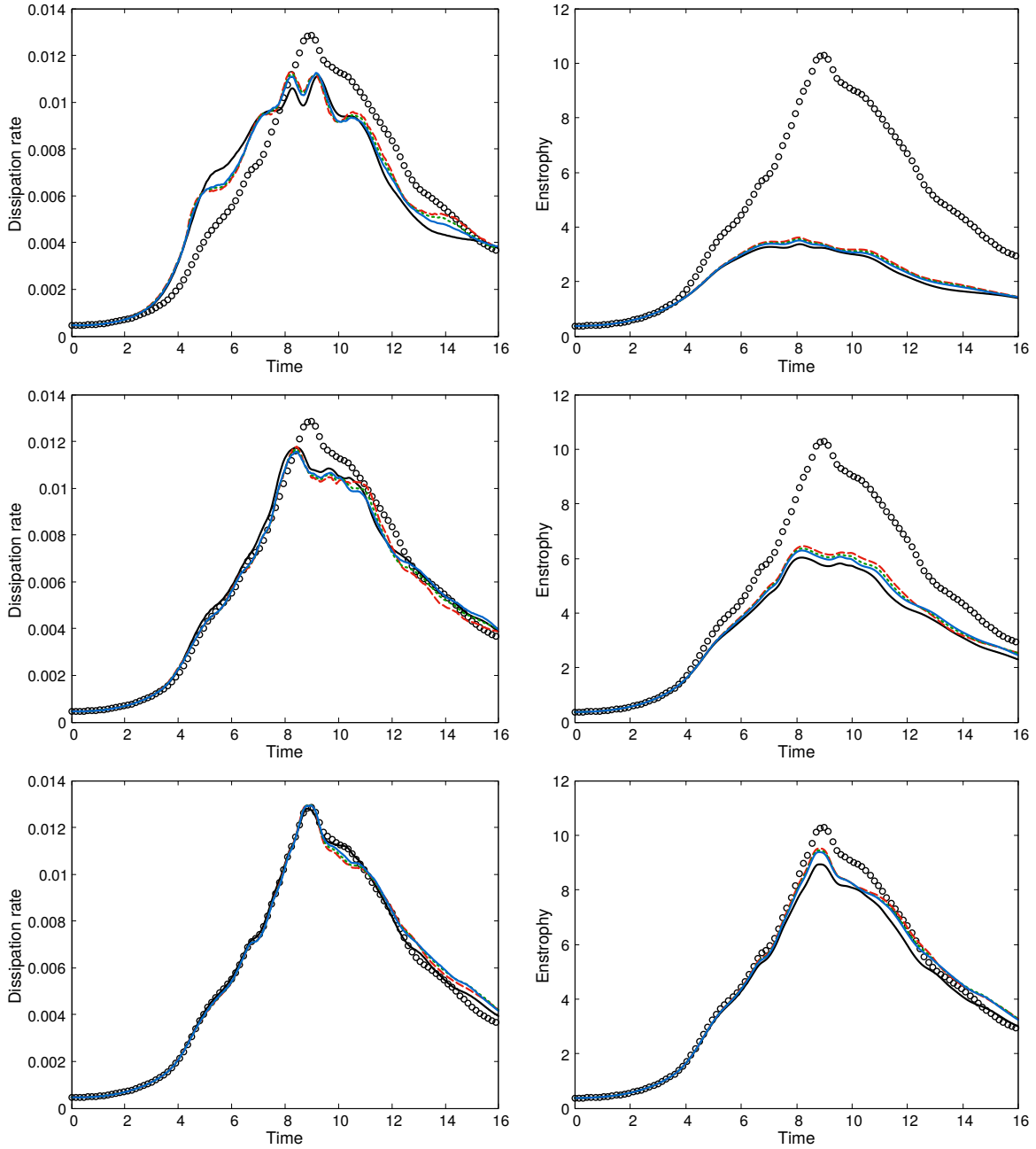


Figure 5.6: Effect of VC on the kinetic energy dissipation rate $-\frac{dK}{dt}$ and the evolution of enstrophy for $\varepsilon = 0.02$ and different values of μ/ε . Spectral -512^3 : \circ , baseline scheme: — , $\mu/\varepsilon = 0.0$: $-\cdot-\cdot-$, $\mu/\varepsilon = 0.2$: \cdots , $\mu/\varepsilon = 0.4$: — . From top to bottom, 64^3 , 128^3 and 256^3 mesh. FE-MUSCL5 and 5th-order Vorticity Confinement.

Fig. 5.6 shows the effect of VC on the rate of dissipation of kinetic energy and on enstrophy for different values of μ/ε . As already mentioned, the peak value of the dissipation rate is largely dependent on the preservation of intermediate scales during the vortex stretching phase, and is therefore increased for a larger magnitude of the VC correction. As expected, this peak value is then reduced for higher values of μ/ε , where the internal numerical dissipation of the VC correction is increased. The influence of the solution to the choice of μ/ε is overall small during the vortex stretching phase, especially for the finer 128^3 and 256^3 grids. Differences appear mostly at later times, as small variations in the preservation of vortices in the early decay phase ($t \approx 9-11$) lead to variations of their subsequent interaction. Observations are similar with respect to the calculation of enstrophy. The sensitivity to the choice of μ/ε remains very small during the vortex stretching

phase, but higher values of μ/ε slightly decrease the enstrophy peak. Last, the value of μ/ε seems to affect the evolution of enstrophy in the late stages of turbulent decay. This influence is not observed on the 64^3 grid due to the very coarse mesh size, but appears to be diminishing on the more refined 256^3 case compared to the intermediate 128^3 .

5.1.4 Sensitivity to the velocity gradient calculation scheme

It can be argued that the efficiency of VC and its high-order extensions may be dependent on the precision of the vorticity field, or equivalently the velocity gradient calculation scheme, since the VC term is calculated based on vorticity (see Section 4.3). To assess this dependence, different velocity gradient calculation schemes are compared for the 128^3 mesh using the FE-MUSCL5 with VC and confinement parameters $\mu/\varepsilon = 0.4$, $\varepsilon = 0.02$. The evaluated schemes are the standard 2nd-order compact scheme which is equivalent to the Green-Gauss theorem and is the scheme used for the previous results, two large-stencil standard schemes which achieve the maximum order of accuracy on the given stencil and the formally 4th-order accurate 13-point DRP scheme of C. Bogey & C. Bailly with optimized coefficients in the wavenumber space [20]. The two standard schemes are 6th- and 10th-order accurate on a 7- and 11-point stencil respectively. All aforementioned orders of accuracy refer to Cartesian grids. A comparison of the results is presented in Fig. 5.7. Results of the baseline case without VC are also plotted, for comparison. The evolution of the kinetic energy dissipation rate shows that the scheme's influence is small up to time $t=9$ where dissipation peaks and vortical structures are well resolved by all schemes. The 13-point DRP and the optimal order standard schemes produce very similar results for the complete time evolution of the flow. The Green-Gauss scheme is in very good agreement with high-resolution schemes up to the dissipation peak. It does however display a small difference with respect to high-accuracy schemes during the turbulence decay phase, since the quality of the solution is largely-dependent on the resolution of small structures. The calculated enstrophy is similar for all schemes, with a smaller difference between Green-Gauss and high-precision schemes at the turbulence decay phase than for the kinetic energy dissipation rate.

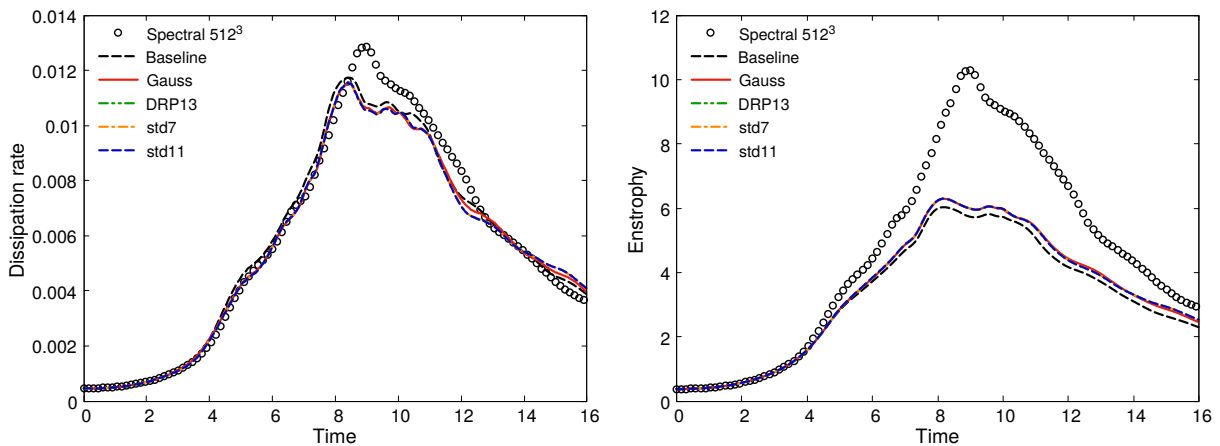


Figure 5.7: Influence of the velocity gradient calculation scheme. FE-MUSCL5 and 5th-order Vorticity Confinement, $\mu/\varepsilon = 0.4$, $\varepsilon = 0.02$, 128^3 mesh.

Case summary

This study shows that schemes with VC can give results that are consistent with the dynamics of the TGV flow, without the need for a special treatment or a more sophisticated choice of confinement parameters compared to standard applications. For reasonable values of the confinement parameters, VC introduces an improvement to the baseline scheme over the vortex stretching phase, where the treatment of large structures is involved. It has also been found that results show small sensitivity to the value of the parameter μ/ε , defining the magnitude of the internal numerical dissipation

of the VC term. However, results indicate that VC increases the life-span of vortices during the turbulence decay phase, especially for higher values of the confinement parameter ε . This eventually produces more dissipation at the smallest scales compared to the reference results, a behavior which is also observed for the baseline flux discretization. To obtain an improved understanding of the effect of VC in scale-resolving simulations, the following case consists in the application of VC to the simulation of pure turbulence decay.

5.2 Decay of compressible Homogeneous Isotropic Turbulence

The present case is the numerical simulation of the decay of compressible Homogeneous Isotropic Turbulence (HIT). This is a fundamental and well-monitored academic case which will allow a closer and more detailed investigation of the effect of high-order VC corrections in the resolution of smaller scales.

5.2.1 Description of the initial condition

The HIT decay problem is solved in a periodic box of dimensions $[0, 2\pi]^3$. There exist multiple methods for the numerical initialization of a turbulent flow field. These may be compressible or incompressible, and may differ with respect to the flow quantities on which fluctuations will be imposed.

For the following calculations, the turbulent flow initialization consists in a divergence-free velocity field with no fluctuations of thermodynamic quantities. Velocity component fluctuations are initialized following a prescribed turbulent kinetic energy spectrum. This is a Passot-Pouquet spectrum of the form:

$$E(\kappa) = A_0 \kappa^4 \exp\left(-2\kappa^2/\kappa_0^2\right) \quad (5.8)$$

where κ_0 is the wavenumber corresponding to the energy spectrum peak and A_0 is a real coefficient that defines the initial volume averaged kinetic energy K_0 .

For this type of initial condition, the volume averaged kinetic energy K_0 , volume averaged enstrophy Ω_0 , integral length scale L_I and large-eddy turnover time τ_e can be analytically derived from Eq. (5.8) [176]:

$$K_0 = \frac{3 A_0}{64} \sqrt{2\pi} \kappa_0^5 \quad \Omega_0 = \frac{15 A_0}{256} \sqrt{2\pi} \kappa_0^7 \quad L_I = \frac{\sqrt{2\pi}}{\kappa_0} \quad \tau_e = \sqrt{\frac{32}{A_0}} (2\pi)^{1/4} \kappa_0^{-7/2} \quad (5.9)$$

The fluid is considered a perfect gas and the dependence of viscosity on temperature is assumed to follow a power-law $\mu = T^{0.76}$. Finally, the compressibility ratio in the initial condition was set to zero. Both the initialization procedure and the numerical strategy have been thoroughly validated in [181]. Following simulations were performed for Reynolds number $Re_\lambda = 175$ – based on the Taylor microscale – and the energy spectrum peak was chosen at $\kappa_0 = 4$.

Since the initial turbulent field is purely solenoidal, the flow evolution displays a rapid initial transient phase until dilatational fluctuations develop (see [181] and references therein). During this phase, correlations are developed in the random initial velocity field, and turbulent fluctuations are developed for the thermodynamic quantities.

Numerical discretization

The HIT decay has been computed for different values of the initial turbulent Mach number, or equivalently for different values of the initial averaged kinetic energy K_0 . The turbulent Mach number is defined as:

$$M_t = \frac{\langle u'^2 + v'^2 + w'^2 \rangle^{1/2}}{\langle a \rangle} \quad (5.10)$$

where u', v', w' denote the components of the turbulent fluctuating velocity, $\langle \bullet \rangle$ denotes an average over the domain and a is the speed of sound. First, two conditions $M_{t0} = 0.2$ and $M_{t0} = 0.5$

are investigated, up to which compressibility effects are moderate, allowing calculation using the FE-MUSCL schemes with matrix dissipation, i.e. the numerical flux (4.26). These studies aim at investigating the effect of high-order VC alongside the same baseline scheme used for the previous test cases. It should also be noted that up to $M_{t0} = 0.5$, the influence of thermodynamic fluctuations in the initial condition has been found to be small by R. Samtaney et al. [176]. Next, the HIT decay is computed at $M_{t0} = 1.0$. The primary difference with respect to the previous initial conditions is the appearance of random shocklets during the main part of the HIT decay. At this initial condition, calculations were performed using FE-MUSCL schemes with a scalar dissipation based on the spectral radius of the inviscid flux Jacobian, i.e. the numerical flux (4.27). The introduction of VC is expected to introduce negligible modifications of the scheme's shock-capturing properties, as dissipation near shocks (including the high-order negative dissipation of VC) is dominated by the low-order dissipation term in Eq. (4.27).

The computational domain $[2\pi]^3$ is discretized by a regular Cartesian grid composed of 128^3 cells. This spatial resolution corresponds to an Implicit Large-Eddy Simulation (ILES) strategy, since the grid does not suffice for the adequate resolution of the Kolmogorov microscale, and the role of small-scale turbulent dissipation is taken up by the scheme's high-order numerical dissipation, rather than by an explicit subgrid scale model [36, 77]. Even though it may not be always appropriate for physical analyses, this approach is particularly fitting for the evaluation of the schemes' numerical dissipation.

Computations are performed up to time $t = 10\tau_e$, where τ_e is the large-eddy turnover time given by Eq. (5.9). Time integration is performed by an explicit 6-stage Runge-Kutta algorithm with optimized coefficients [20], as in Section 5.1. The time step is chosen depending on the initial turbulent Mach number M_{t0} . The maximal acoustic CFL number ranges between $CFL_{0,\max} \approx 0.27 - 0.31$ in the initial condition of the presented cases, where $CFL = \Delta t \left(a + \sqrt{u'^2 + v'^2 + w'^2} \right) / \Delta x$ since the mean velocity field is zero. Calculations with VC are performed at 5th-order of accuracy and for different values of the confinement parameters. The effect of VC is evaluated against the baseline 5th-order scheme without confinement. A reference solution is also computed with a 9th-order accurate upwind FE-MUSCL scheme on the same grid. For the calculation of quantities that require the velocity gradients in post-processing, these have been computed with the 7-point Dispersion-Relation-Preserving (DRP) scheme of C. K. W. Tam and J. C. Webb [203].

Last, the computations presented in this section were performed on dimensional quantities. The values of the confinement parameters given below are non-dimensional. Their dimensional values were calculated as $\varepsilon^* = \rho_0 M_{t0} a_0 \varepsilon$, where a is the speed of sound (see Eq. (4.70)).

5.2.2 Low-compressibility HIT at $M_{t0} = 0.2$ and $M_{t0} = 0.5$

First, the HIT decay is investigated at initial turbulent Mach number $M_{t0} = 0.2$ and $M_{t0} = 0.5$. FE-MUSCL schemes with VC are compared to their baseline version and a reference computation using a 9th-order accurate linear scheme. The numerical schemes and confinement parameters investigated in this study are summed up in Table 5.1. For all these cases, the numerical flux of the baseline scheme is given by Eq. (4.26) and uses a matrix form of dissipation.

Table 5.1: Summary of numerical schemes and VC parameters

	FE-MUSCL flux	VC order	ε	μ/ε
Reference	9th-order	-	-	-
Baseline	5th-order	-	-	-
VC-Case 1	"	5th	$1.2 k_5$	0.00
VC-Case 2	"	5th	$1.2 k_5$	0.20
VC-Case 3	"	5th	$2.4 k_5$	0.00

The HIT evolution consists of a vortex stretching phase, where viscous effects are negligible and enstrophy increases up to a peak value, and a subsequent decay phase characterized by viscous

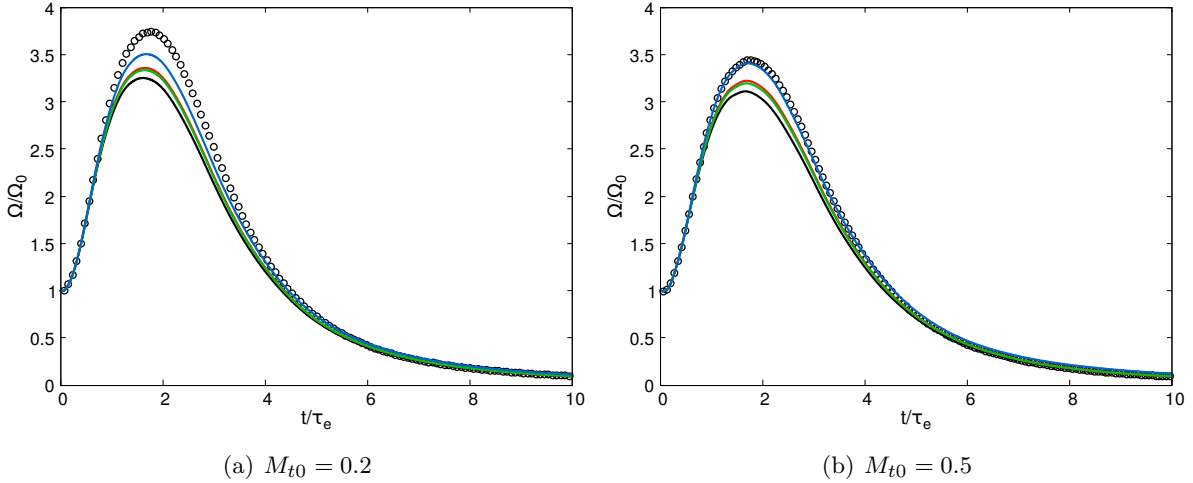


Figure 5.8: Comparison of the time evolution of enstrophy obtained with FE-MUSCL schemes with and without VC. Reference: \circ , Baseline FE-MUSCL5:—, $(\mu/\varepsilon, \varepsilon) = (0.0, 1.2k_5)$:—, $(\mu/\varepsilon, \varepsilon) = (0.2, 1.2k_5)$:—, $(\mu/\varepsilon, \varepsilon) = (0.0, 2.4k_5)$:—.

dissipation at the Kolmogorov microscales. The resolvability of the enstrophy peak is often used as measure of the resolution of numerical schemes. Fig. 5.8 shows the evolution of enstrophy obtained with FE-MUSCL schemes with and without VC for the two different initial turbulent Mach number cases. Schemes with VC manage to predict an increased enstrophy peak compared to the baseline 5th-order FE-MUSCL scheme for all cases. Furthermore, the instant where the enstrophy peak occurs is slightly delayed for schemes with less effects of numerical dissipation. The effect of VC is primarily driven by the value of ε as this parameter defines the magnitude of the VC term. Good results are obtained for ε close to the value of the 5th-order artificial dissipation coefficient, in consistency with the previous studies. An augmented value of this parameter gives a further increased dissipation peak, which at $M_{t0} = 0.5$ is comparable to the reference 9th-order solution, but results in slightly higher enstrophy values compared to the reference during the late time instants (Case 3).

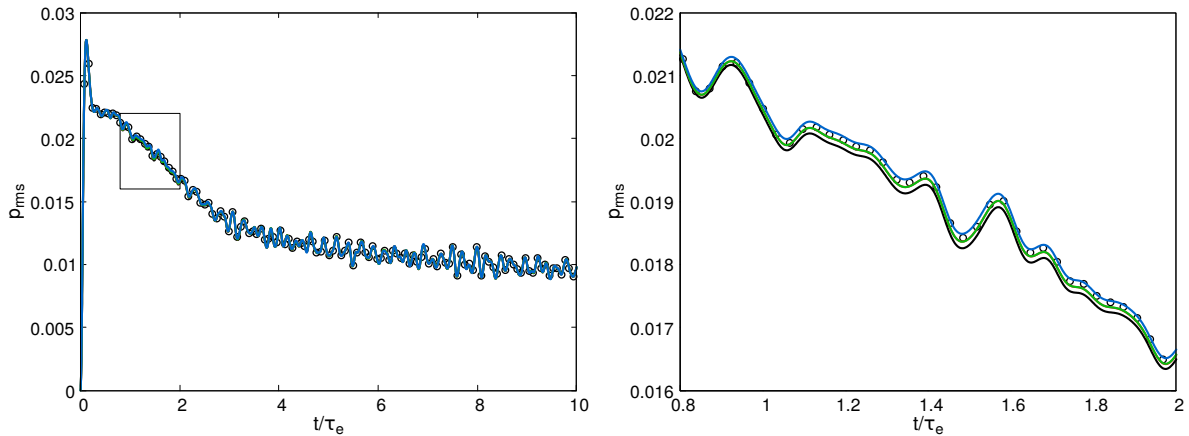


Figure 5.9: Time evolution of r.m.s. pressure obtained with FE-MUSCL schemes with and without VC at $M_{t0} = 0.2$. Reference: \circ , Baseline FE-MUSCL5:—, $(\mu/\varepsilon, \varepsilon) = (0.0, 1.2k_5)$:—, $(\mu/\varepsilon, \varepsilon) = (0.2, 1.2k_5)$:—, $(\mu/\varepsilon, \varepsilon) = (0.0, 2.4k_5)$:—. Evolution during the complete computed time (left) and detail at $t = 0.8\tau_e - 2\tau_e$ (right).

The influence of VC on the evolution of thermodynamic quantities is monitored through the time evolution of the root-mean-square (r.m.s.) of pressure fluctuations, presented in Figs. 5.9-5.10. These results show little sensitivity to the space discretization scheme, with differences appearing

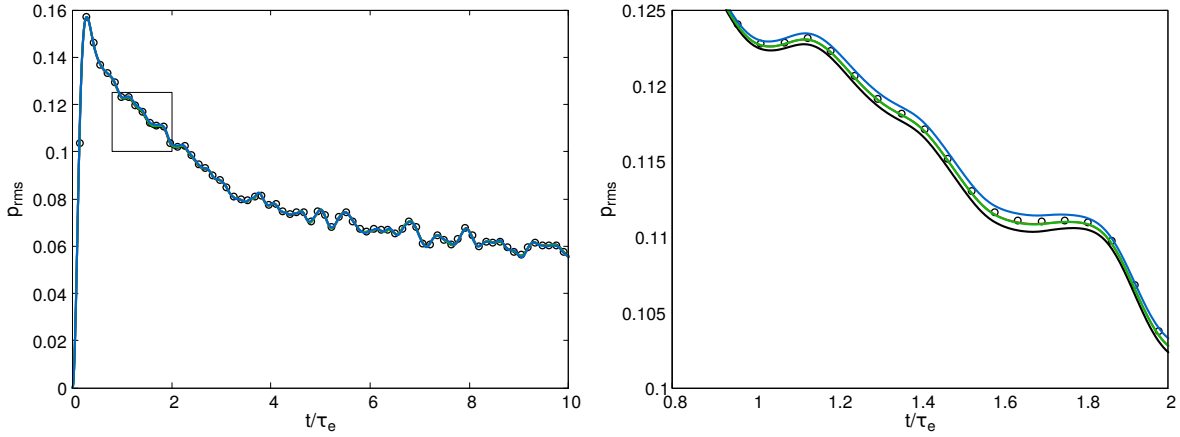
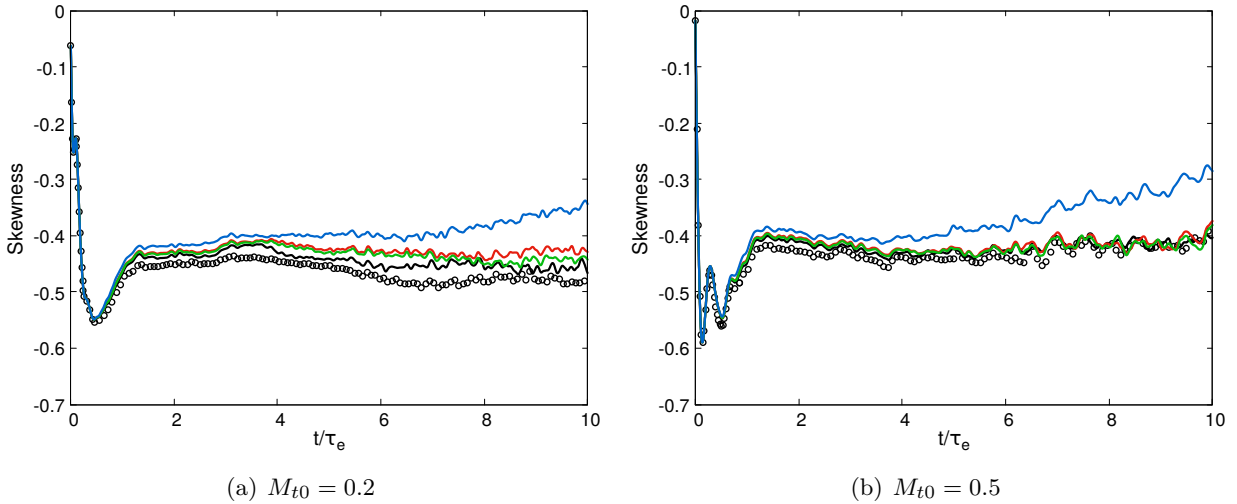


Figure 5.10: Time evolution of r.m.s. pressure obtained with FE-MUSCL schemes with and without VC at $M_{t0} = 0.5$. Reference: \circ , Baseline FE-MUSCL5:—, $(\mu/\varepsilon, \varepsilon) = (0.0, 1.2k_5)$:—, $(\mu/\varepsilon, \varepsilon) = (0.2, 1.2k_5)$:—, $(\mu/\varepsilon, \varepsilon) = (0.0, 2.4k_5)$:— (left) and detail at $t = 0.8\tau_e - 2\tau_e$ (right).



(a) $M_{t0} = 0.2$

(b) $M_{t0} = 0.5$

Figure 5.11: Time evolution of the skewness factor of the fluctuating velocity gradient distribution obtained with FE-MUSCL schemes with and without VC. Reference: \circ , Baseline FE-MUSCL5:—, $(\mu/\varepsilon, \varepsilon) = (0.0, 1.2k_5)$:—, $(\mu/\varepsilon, \varepsilon) = (0.2, 1.2k_5)$:—, $(\mu/\varepsilon, \varepsilon) = (0.0, 2.4k_5)$:—.

mainly close to the time of the enstrophy peak (before $t = 2\tau_e$). The effect of VC on the evolution of p_{rms} is found to be small for all cases. Close-up views show that results with VC are very close to the reference 9th-order computation, at least for Cases 1-2. The influence of the choice of μ/ε between the two latter Cases is found to be small, the results being superimposed within plotting accuracy. Similar trends are observed for the time evolution of the r.m.s. values of density and temperature fluctuations.

An interesting comparison can be made by considering the time evolution of high-order statistical moments of the turbulent flow. Comparisons are presented for the skewness and flatness factor:

$$S(\bullet) \triangleq \frac{\langle(\bullet)^3\rangle}{\langle(\bullet)^2\rangle^{3/2}} \quad F(\bullet) \triangleq \frac{\langle(\bullet)^4\rangle}{\langle(\bullet)^2\rangle^2} \quad (5.11)$$

of the fluctuating velocity gradient distribution, where $\langle\bullet\rangle$ denotes a volume average over the computational domain at a fixed time instant. These quantities represent measures of the difference of the velocity fluctuation field from a Gaussian distribution and are generally more sensitive to the space discretization scheme. For a Gaussian distribution, the skewness factor is equal to zero and

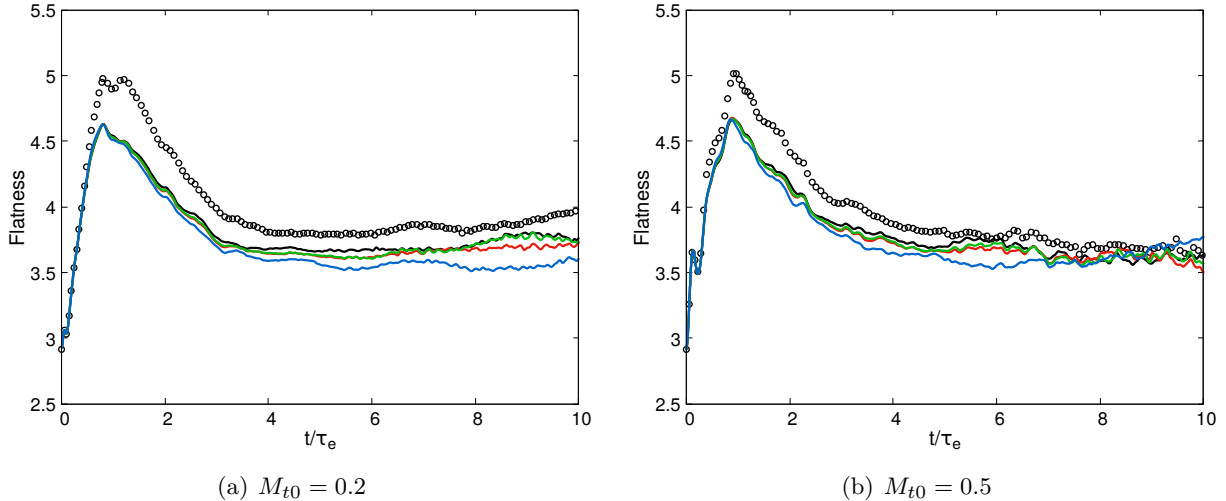


Figure 5.12: Time evolution of the flatness factor of the fluctuating velocity gradient distribution obtained with FE-MUSCL schemes with and without VC. Reference: \circ , Baseline FE-MUSCL5: — , $(\mu/\varepsilon, \varepsilon) = (0.0, 1.2k_5)$: — (red), $(\mu/\varepsilon, \varepsilon) = (0.2, 1.2k_5)$: — (green), $(\mu/\varepsilon, \varepsilon) = (0.0, 2.4k_5)$: — (blue).

the flatness factor is equal to 3. Typical values of the skewness factor for incompressible HIT are $S = -0.4 \pm 0.1$ [174]. The value of the flatness factor depends on the Reynolds number.

The time evolution of the skewness factor is presented in Fig. 5.11 for the two turbulent Mach number cases. Cases with VC do not provide results closer to the reference than the baseline 5th-order scheme. Specifically, the skewness factor for Case 3 seems to diverge over long times, especially for the $M_{t0} = 0.5$ case. Cases 1-2 however give consistent results, very close to those of the baseline schemes. The time evolution of the flatness factor is presented in Fig. 5.12. Schemes with VC give consistent results with smaller differences from the baseline than for the time evolution of the skewness factor (Fig. 5.11). An exception is again observed for Case 3, which displays a larger difference from the baseline than Cases 1-2, and also follows a different trend at late times for $M_{t0} = 0.5$.

The resolvability of numerical schemes is further depicted on the turbulent kinetic energy spectrum, presented in Fig. 5.13 for different time instants during the HIT decay. An inertial range following the $-5/3$ law has not been fully developed for the low Reynolds number Re_λ of this study, but differences in the energy spectrum are observed due to the schemes' numerical dissipation, even at times as early as $t = 2\tau_e$. The application of VC extends the cut-off wavenumber of the baseline 5th-order FE-MUSCL scheme for all cases, the differences being naturally more important at later times, due to the accumulation of numerical dissipation for the baseline scheme. As discussed previously, high-values of the confinement parameter ε lead to the negative dissipation of VC being very large compared to the dissipation of the baseline scheme, thus causing reduced dissipation and accumulation of energy at high wavenumbers during the late stages of the decay (Case 3). This is probably related to the increased enstrophy at late times, observed previously in the results of Fig. 5.8 for the same Case. Such values are possibly more suitable for an explicit Large-Eddy Simulation approach, so that the dissipation of the baseline scheme is efficiently balanced by VC and small-scale dissipation is introduced in the form of an explicit subgrid scale (SGS) model. Reasonable and consistent results are however obtained for ε closer to the value of the high-order artificial dissipation coefficient (Cases 1-2).

Fig. 5.14 shows iso-surfaces of constant vorticity magnitude at $t = 10\tau_e$, colored by the local Mach number. Results are in agreement with previous observations. Specifically, high values of the parameter ε (Case 3) lead to overly reduced dissipation at smaller scales and accumulation of small structures in the domain at late times. However, for values of ε closer to the high-order artificial dissipation coefficient (Case 1), the solution is consistent with the reference and the preservation of turbulent structures is noticeably improved compared to the baseline 5th-order FE-MUSCL scheme.

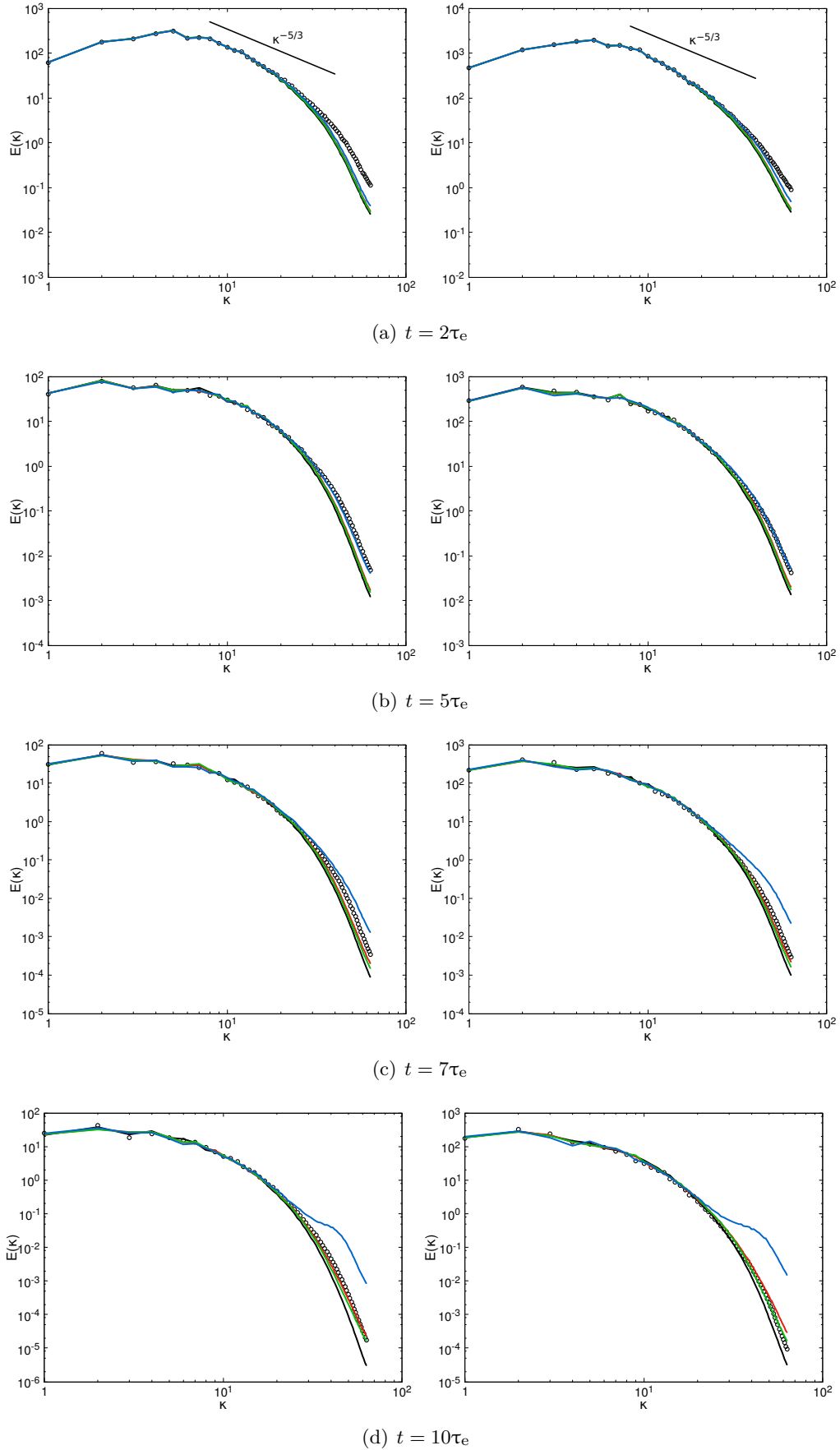


Figure 5.13: Comparison of the turbulent kinetic energy spectrum at different time instants during the HIT decay. Reference: \circ , Baseline FE-MUSCL5:—, $(\mu/\varepsilon, \varepsilon) = (0.0, 1.2k_5)$:—, $(\mu/\varepsilon, \varepsilon) = (0.2, 1.2k_5)$:—, $(\mu/\varepsilon, \varepsilon) = (0.0, 2.4k_5)$:—. FE-MUSCL schemes with and without VC for initial turbulent Mach number $M_{t0} = 0.2$ (left) and $M_{t0} = 0.5$ (right).

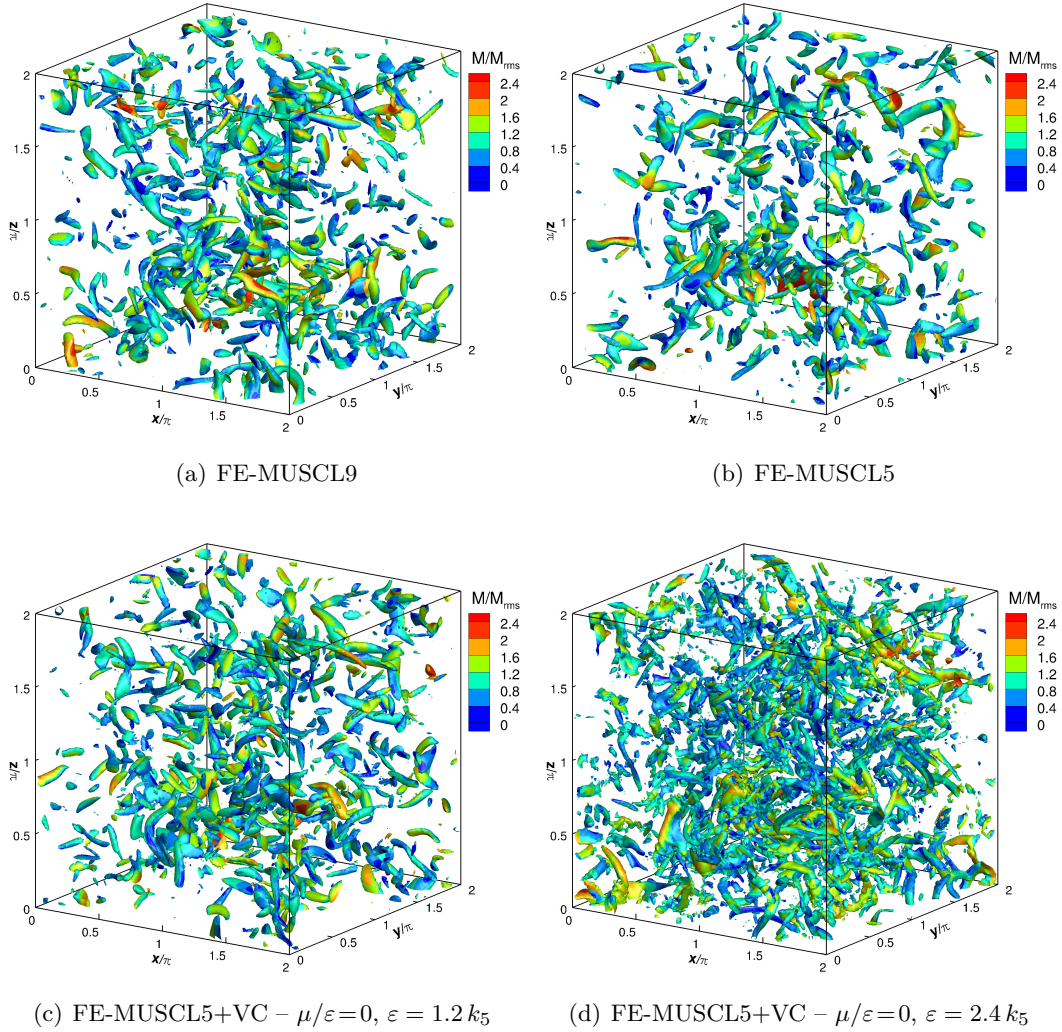


Figure 5.14: Iso-surfaces of constant vorticity magnitude at $t = 10\tau_e$ colored by the local Mach number. FE-MUSCL schemes with and without VC on a 128^3 grid for initial turbulent Mach number $M_{t0}=0.2$.

As a next step, we are investigating whether the overly reduced dissipation for higher values of ε can be balanced by augmenting the magnitude of the numerical dissipation of VC. For this purpose, we are considering different values for the parameter μ , which determines the magnitude of the internal dissipation of the VC term. The investigated values correspond to $\mu/\varepsilon = \{0.0, 0.2, 0.4, 0.6\}$. The parameter ε is taken $\varepsilon = 2.4 k_5$ for all cases. It is reminded that for $\mu/\varepsilon = 0.0$, the confinement parameters correspond to the Case 3 of the previous study. Fig. 5.15 shows the time evolution of enstrophy at $M_{t0} = 0.5$. As expected, the effect of the VC correction is reduced for an increased value of μ/ε . For all values of μ/ε however, the prediction of the enstrophy peak is still improved compared to the baseline FE-MUSCL5. The same figure shows also the turbulent kinetic energy spectrum at time $t = 10\tau_e$. An increase of the VC term's internal dissipation is shown to mitigate the accumulation of energy at the smallest scales. It is however unlikely that, for an increased value of ε , the problem of overly reduced small-scale dissipation can be completely corrected by increasing the dissipation of VC alone. A careful choice of ε is more important, as this parameter adjusts the magnitude of the nonlinear anti-dissipation of VC. Last, Fig. 5.16 shows the evolution of high-order statistics for the same cases. Here, an increased value of μ/ε is shown to quickly reduce the effect of VC on the skewness and flatness factor. For $\mu/\varepsilon = 0.4$ and $\mu/\varepsilon = 0.6$, the result is very close to that of the baseline scheme. Observations for the $M_{t0} = 0.2$ case are similar.

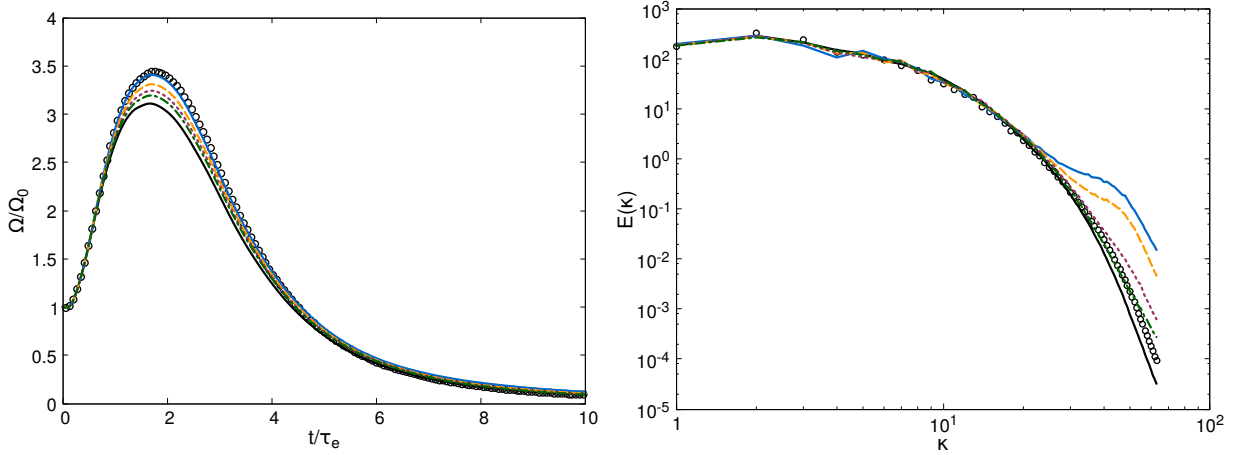


Figure 5.15: Effect of μ/ε in the time evolution of enstrophy and the turbulent kinetic energy spectrum at $t = 10 \tau_e$. FE-MUSCL schemes and VC, $\varepsilon = 2.4 k_5$ at $M_{t0} = 0.5$. Reference: \circ , Baseline FE-MUSCL5: —, $\mu/\varepsilon = 0.0$: —, $\mu/\varepsilon = 0.2$: - - - , $\mu/\varepsilon = 0.4$: ····, $\mu/\varepsilon = 0.6$: - · - ·.

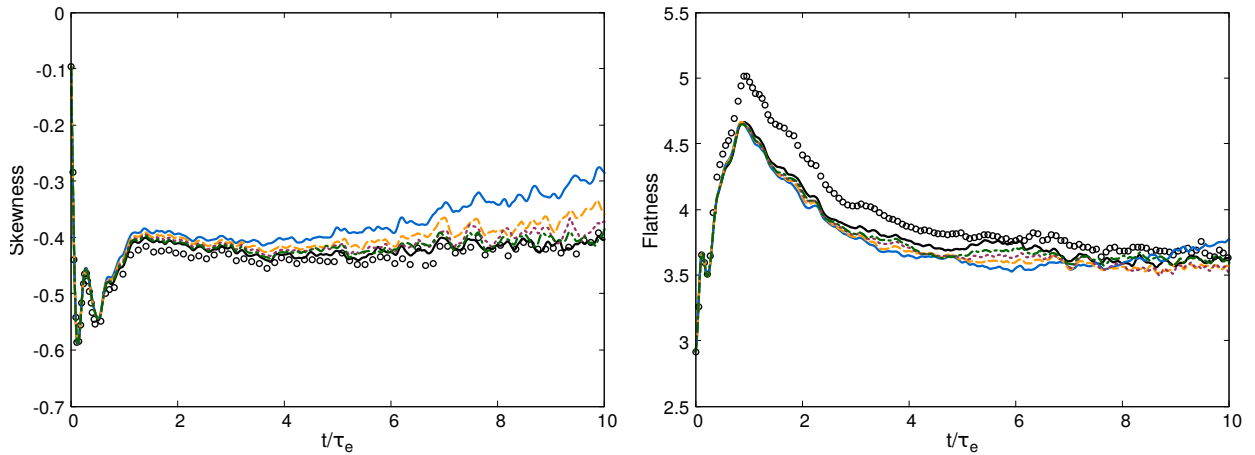


Figure 5.16: Effect of μ/ε in the time evolution of the skewness and flatness factor of the fluctuating velocity gradient distribution. FE-MUSCL schemes and VC, $\varepsilon = 2.4 k_5$ at $M_{t0} = 0.5$. Reference: \circ , Baseline FE-MUSCL5: —, $\mu/\varepsilon = 0.0$: —, $\mu/\varepsilon = 0.2$: - - - , $\mu/\varepsilon = 0.4$: ····, $\mu/\varepsilon = 0.6$: - · - ·.

5.2.3 Highly-compressible HIT at $M_{t0} = 1.0$

The consistency of high-order VC in compressible flow simulations is assessed in the case of the HIT decay at $M_{t0} = 1.0$. As already discussed previously, eddy shocklets appear during the main part of the HIT decay at a sufficiently high initial turbulent Mach number [176, 181]. The FE-MUSCL schemes used in the previous studies employ a purely high-order matrix-form of dissipation, which cannot efficiently damp oscillations near discontinuities. The scheme's shock-capturing properties are improved by replacing the dissipative part of the numerical flux with a hybrid low-/high-order numerical dissipation. This is based on the spectral radius of the inviscid flux Jacobian matrix, with the resulting numerical flux given by Eq. (4.27). In all following studies, the second-order dissipation parameter is taken $k_2 = 1.0$. The high-order dissipation coefficients at 5th- and 9th-order of accuracy are taken $k_5 = 1/60$ and $k_9 = 1/1260$ respectively to maintain consistency with the previous computations at a lower M_{t0} . Although efficient for the capturing of flow discontinuities, the use of this type of dissipation is however inferior to a matrix-form of dissipation in smooth flow regions, as shown in the following.

Before investigating the $M_{t0} = 1.0$ case, a comparison of the two types of numerical dissipation is performed at an intermediate initial turbulent Mach number $M_{t0} = 0.5$. Results of this study

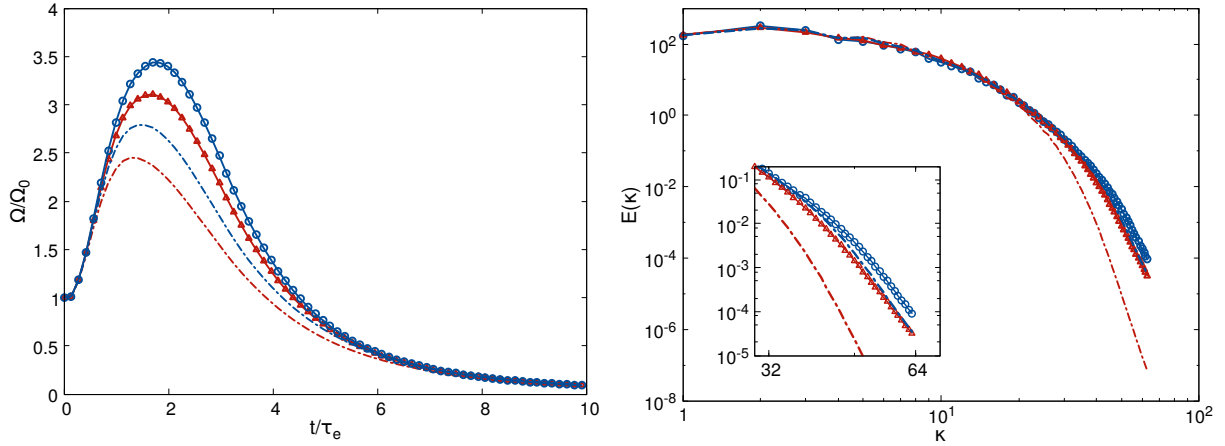


Figure 5.17: Evolution of enstrophy and turbulent kinetic energy spectrum at $t=10\tau_e$ for different types of numerical dissipation. Baseline FE-MUSCL schemes at $M_{t0}=0.5$. 9th-order (matrix): $\text{---}\circ\text{---}$, 5th-order (matrix): $\text{---}\triangle\text{---}$, 9th-order (scalar): $\text{---}\text{---}$, 5th-order (scalar): $\text{---}\cdot\text{---}$.

are shown in Fig. 5.17. The calculation of the enstrophy peak clearly indicates that the use of a matrix (i.e. Roe matrix) dissipation gives better resolvability compared to the more “intrusive” spectral radius-based scalar dissipation. Furthermore, it indicates that a 5th-order scheme with matrix dissipation is superior to a 9th-order scheme with scalar dissipation, but this is only true for the early stages of the HIT decay. The kinetic energy spectrum at $t=10\tau_e$ demonstrates that a 9th-order accurate numerical flux gives a better spatial resolution over sufficient time, where the resolution of smaller structures is involved.

Next, the HIT decay at $M_{t0}=1$ is computed using FE-MUSCL schemes with scalar numerical dissipation, and the dissipation coefficients given above. To evaluate the effect of VC, we are considering three pairs of confinement parameters: $(\mu/\varepsilon, \varepsilon) = \{(0.0, 1.2k_5), (0.2, 1.2k_5), (0.4, 2.4k_5)\}$. As the strong anti-dissipative effects of setting high values of ε with $\mu/\varepsilon = 0$ have already been clearly portrayed in the previous studies, the value of μ/ε is here increased for the $\varepsilon = 2.4k_5$ case, to allow a fair comparison between the cases. The other values are the same as the ones presented in Table 5.1.

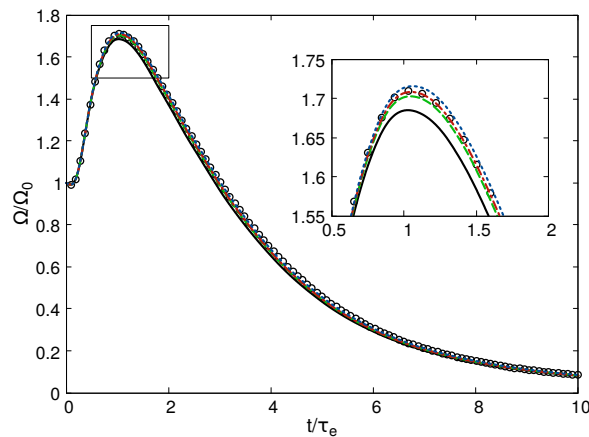


Figure 5.18: Comparison of the time evolution of enstrophy obtained with FE-MUSCL schemes with and without VC at $M_{t0}=1.0$. Reference: \circ , Baseline FE-MUSCL5: --- , $(\mu/\varepsilon, \varepsilon) = (0.0, 1.2k_5)$: $\text{---}\cdot\text{---}$, $(\mu/\varepsilon, \varepsilon) = (0.2, 1.2k_5)$: $\text{---}\text{---}$, $(\mu/\varepsilon, \varepsilon) = (0.4, 2.4k_5)$: $\text{---}\cdot\text{---}$.

Fig. 5.18 shows the time evolution of enstrophy at $M_{t0}=1$. The difference between the baseline 5th-order and 9th-order schemes in the resolution of the enstrophy peak is noticeably smaller with

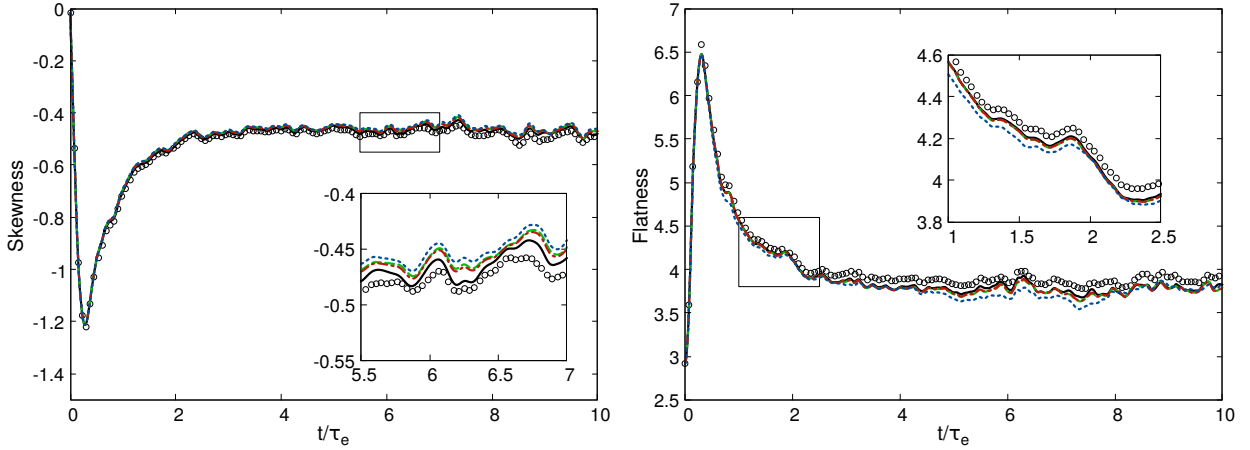


Figure 5.19: Time evolution of the skewness and flatness factor of the fluctuating velocity gradient distribution. FE-MUSCL schemes with and without VC at $M_{t0} = 1.0$. Reference: \circ , Baseline FE-MUSCL5: —, $(\mu/\varepsilon, \varepsilon) = (0.0, 1.2k_5)$: -.-.-, $(\mu/\varepsilon, \varepsilon) = (0.2, 1.2k_5)$: -.-.-, $(\mu/\varepsilon, \varepsilon) = (0.4, 2.4k_5)$:

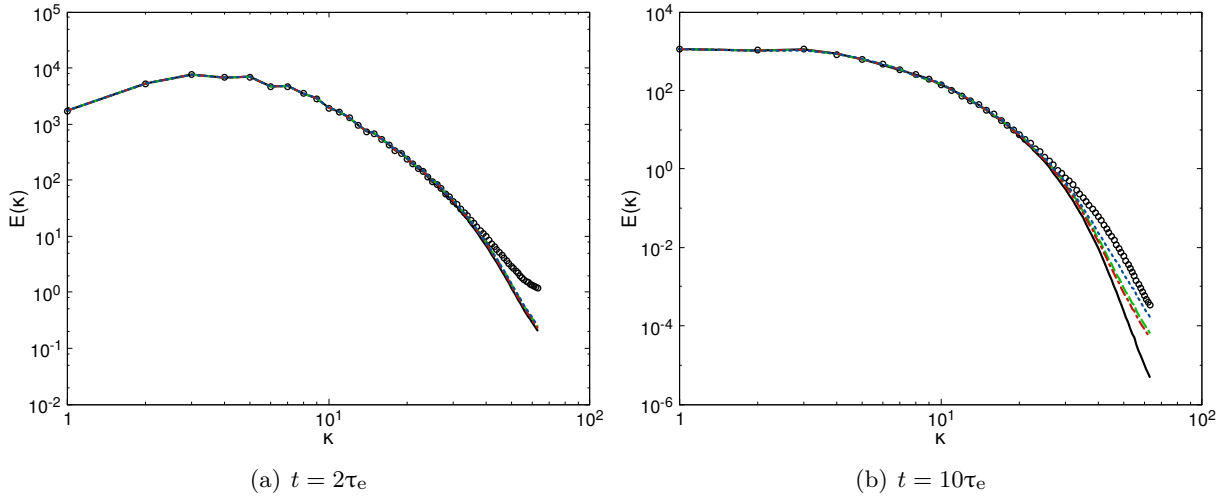


Figure 5.20: Comparison of the turbulent kinetic energy spectrum at different time instants. FE-MUSCL schemes with and without VC at $M_{t0} = 1.0$. Reference: \circ , Baseline FE-MUSCL5: —, $(\mu/\varepsilon, \varepsilon) = (0.0, 1.2k_5)$: -.-.-, $(\mu/\varepsilon, \varepsilon) = (0.2, 1.2k_5)$: -.-.-, $(\mu/\varepsilon, \varepsilon) = (0.4, 2.4k_5)$:

respect to the previous cases. The comparison of Fig. 5.17 at $M_{t0} = 0.5$ indicates that the reduced difference between orders is not related to the use of scalar dissipation itself. It is possible however that at $M_{t0} = 1$, where compressibility effects are significantly increased, the reduced difference between orders is related to the larger influence of the low-order dissipation term of Eq. (4.27). As regards cases with VC, they are again achieving an increased enstrophy peak value, which is comparable to the 9th-order baseline solution.

The effect of the low-order dissipation in these schemes can be mitigated by the introduction of Ducros' sensor (see Section 4.2.1.1). This has however been found to compromise the robustness of the reference 9th-order baseline scheme for the initial condition and dissipation coefficients of the present study. For this reason, computations were not performed using this type of dissipation. High-order VC is not expected to degrade the shock-capturing properties of the scheme in this case, as Ducros' sensor provides a reduction of the effect of the low-order dissipation in vortical regions, whereas VC represents a correction to the high-order dissipation of the scheme. The dissipation near shocks should therefore still be dominated by the lower-order term, although this should be verified in future studies.

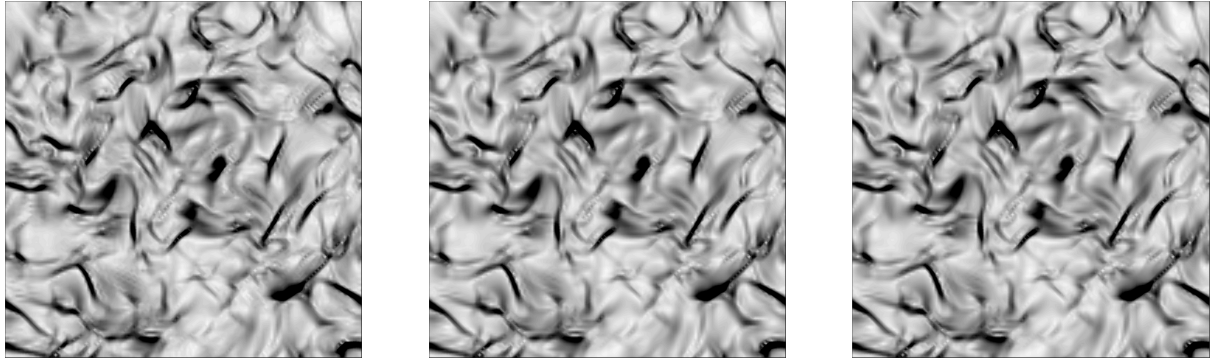
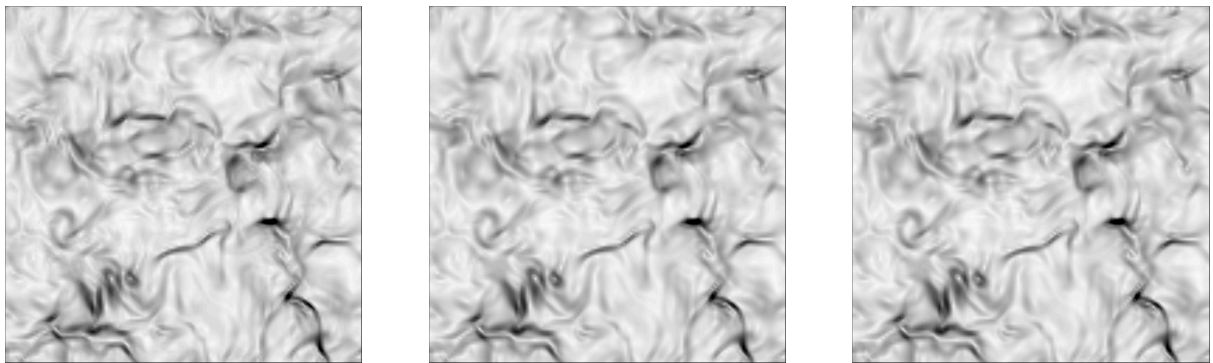
(a) $t = 1\tau_e$ (b) $t = 3\tau_e$

Figure 5.21: Iso-contours of $\|\vec{\nabla}\rho\|$ at $M_{t0}=1$ (51 contour levels from 0 to 7). Darker regions correspond to high compressibility effects. Baseline FE-MUSCL9 (left), baseline FE-MUSCL5 (middle) and FE-MUSCL5 with 5th-order VC using $\mu/\varepsilon=0.0$, $\varepsilon = 1.2k_5$ (right).

The evolution of high-order statistics of the velocity gradient distribution are shown in Fig. 5.19. Due to the higher initial turbulent Mach number, the initial transient phase of the flow is more intense than for the previous cases. This results in increased peak values for the skewness and flatness factor, as well as for thermodynamic quantities. The effect of VC was however found to be small on the evolution of thermodynamic quantities, as for the lower Mach number cases. After the transient phase, both high-order statistical moments eventually converge to similar values as in the previous cases, as these values are dependent on Re_λ rather than M_{t0} . Again, cases with VC do not give results closer to the 9th-order reference, but the difference is small compared to the baseline 5th-order scheme.

The turbulent kinetic energy spectrum at an early stage of the HIT decay and at the final computed time is shown in Fig. 5.20. For the chosen dissipation coefficients, the numerical dissipation of the 9th-order reference is low during the early stages of the flow, which appears as slightly increased energy at the smallest scales of the spectrum. This effect is however balanced over time. Similarly to previous cases, the influence of VC is more important at later time instants, where the effects of dissipation are accumulated for the baseline 5th-order scheme. At time $t=10\tau_e$, all cases with VC display increased resolvability, giving an energy spectrum with an extended dissipation cut-off that is closer to the reference than the baseline case.

Last, Fig. 5.21 shows contours of the density gradient norm in a plane of the cubic domain at different time instants. Regions of high density gradient indicate strong effects of compressibility. Contrary to previous calculations at lower M_{t0} (see Fig. 5.14), these results show almost no observ-

able differences between the different schemes. This is most likely because their accuracy in this compressible case is primarily determined by the low-order part of the dissipation, and this is the same for all schemes. The same is also depicted in the time evolution of enstrophy (see Fig. 5.18). An additional scaling of the low-order dissipation in vortices using Ducros' sensor (see Eq. (4.31)) would probably reveal more representative differences between the schemes. A close inspection of Fig. 5.21 shows that small oscillations may appear near high-compressibility regions for the 9th-order scheme at early times, due to the low values of the baseline dissipation coefficients. Similar oscillations are not however observed for the baseline 5th-order scheme, or for the case with VC. It should however be noted that oscillations may also appear for $\varepsilon = 2.4k_5$ at $\mu/\varepsilon = 0$ due to the strong anti-dissipation that is introduced, but they are removed by augmenting the value of μ/ε . These results thus indicate that the low-order dissipation is not degraded by the high-order anti-dissipation of VC in the vicinity of discontinuities. This would most likely not be the case if a low-order VC was used. Apart from preserving the global order of accuracy, this is an additional advantage of high-order VC alongside schemes with a hybrid low-/high-order numerical dissipation.

5.3 Chapter summary

In this chapter, the developed high-order Vorticity Confinement corrections have been applied to the computation of complex problems, including flows in turbulent regime. The principal objective of these studies was to evaluate the consistency of high-order VC in complex applications, in particular with the dynamics of turbulent flows. For this purpose, the developed schemes have been tested in the case of the Taylor-Green vortex (TGV) and the case of decaying compressible homogeneous isotropic turbulence (HIT). In these studies, a deliberate effort has been made to assess the sensitivity of results to the values of the confinement parameters.

Results on the TGV case have shown that the developed high-order VC corrections give results that are consistent with complex vortical flow dynamics. For reasonable values of the confinement parameter ε , close to the baseline numerical dissipation coefficient, the scheme with high-order VC was found to be overall more accurate than the baseline scheme without VC. This is especially the case during the vortex stretching phase of the flow, where larger flow structures are involved. The upwind dissipative FE-MUSCL baseline schemes considered in this study were also shown to be robust without the internal artificial dissipation of VC. If not set to zero, this dissipation was found to have a moderate influence on the computed results, and even negligible during the treatment of large-scale structures. Furthermore, even on a complex flow, the effectiveness of VC was found to have moderate sensitivity to the velocity gradient calculation scheme. The interpretation of results at the end of the turbulence decay phase of the TGV flow is not however straightforward, as these are heavily dependent on the intermediate computed flow state.

A closer investigation of the treatment of smaller structures has thus been performed for the compressible HIT decay. This case has been computed at three different turbulent Mach number initial conditions, ranging from quasi-incompressible to highly compressible, and using different types of numerical dissipation for the baseline numerical flux. In these studies, high values of the confinement parameter ε were shown to overly reduce numerical dissipation and lead to an accumulation of energy at the smallest scales. This effect can be mitigated by the augmentation of the internal dissipation of the high-order VC correction. Alternatively, it is possible that higher values of ε give better results in an explicit LES simulation approach. It was however demonstrated that consistent results can be obtained by a more prudent choice of the confinement parameter ε , closer to the baseline numerical dissipation coefficient. For such values, schemes with VC were shown to exhibit improved resolvability properties compared to the baseline 5th-order ones considered in this study. Specifically, they were found to extend the resolved turbulent kinetic energy spectrum and improve the resolution of the enstrophy peak during the vortex stretching phase. Albeit not beneficial, the effect of VC was found to be small on the high-order statistics of the turbulent flow, while it was not found to have an important effect on the evolution of thermodynamic quantities. Finally, high-order VC was applied to a high-compressibility HIT decay case alongside a baseline

scheme with hybrid low-/high-order dissipation, similar to schemes commonly applied in aerodynamic problems. The results of this case showed no negative effect of the high-order anti-dissipation of VC on this baseline scheme's shock-capturing properties.

High-order VC corrections were overall found to be consistent with complex vortical flow dynamics without the need of special treatment to accommodate the vortex interaction mechanisms characteristic of turbulent flows. Furthermore, they were found to consistently improve the resolvability of baseline FE-MUSCL schemes for reasonable values of the confinement parameter ε . Last, the dependence of the solution on the internal dissipation of VC was found to be moderate for reasonable values of the ratio μ/ε , and more important in the treatment of smaller scales. Advanced turbulent flow calculations in the research field are generally performed using baseline methods that already exhibit high spectral accuracy. The assessment of this chapter is however important to ensure that high-order VC corrections can provide consistent results in high-fidelity engineering applications involving turbulent flows (wakes, turbulence injection, separation etc.).

Chapter 6

Conclusions and perspectives

Conclusions

The present thesis has consisted in an extension of the capability of the Vorticity Confinement method of J. Steinhoff to high-order discretizations. This development aims at reducing the problem of artificial diffusion of vortices in high-order numerical simulations via the introduction of a nonlinear anti-dissipative term in the discretization, so as to balance the baseline scheme's numerical dissipation in vortical flow regions. Several theoretical and numerical analyses of these corrections have also been carried out to investigate their nonlinear properties and their limitations.

The first part of the investigation has been devoted to the analysis of schemes with scalar confinement corrections for the linear transport equation. A new family of high-order confinement corrections has been developed for decoupled discretizations in space and time. These are based on a similar principle as previous space-time coupled formulations, and have been shown to exhibit the same discrete asymptotic balance. The developed approach has been applied to standard non-compact linear dissipative schemes which achieve the optimal order of accuracy on the given stencil, but is not limited to this case. In principle, the same approach can be applied to other forms of dissipative operators, as long as the same operator is used for the baseline dissipation and the confinement correction.

A detailed analysis of these nonlinear schemes' spectral properties has then been carried out, making use of a numerical quasi-linear method. This analysis showed that confinement corrections affect both the dispersive and dissipative properties of the scheme, although they are originally based on a purely dissipative operator. This effect was found to be beneficial both in terms of dispersion and dissipation. Confinement was thus shown to extend the scheme's resolvability limit at all orders of accuracy, with the improvement being more important up to fifth order. Nonetheless, it was found that schemes with confinement may display a mild instability in the low wavenumber range if the confinement parameter is chosen larger than the baseline artificial dissipation coefficient. At high orders of accuracy, this instability is weaker and therefore should be observed only over very long advection distances. On the other hand, for space-time coupled schemes based on the Lax-Wendroff approach, the instability is damped by the scheme's time-coupled dissipation. For smaller values of the confinement parameter however, the schemes do not exhibit this instability and are always less dissipative than their linear version (i.e. without confinement). More importantly, it has been shown that the anti-dissipation introduced by the confinement correction resembles the form of the dissipation operator on which it is built. In other terms, the anti-dissipation of confinement is transferred towards higher frequencies at higher-orders of accuracy, having a reduced effect on the well-resolved wavenumber range. This demonstrates the importance of building the confinement correction on a high-order dissipative operator. Another interesting property is that this anti-dissipation decreases progressively at high frequencies and does not modify the damping of grid-to-grid oscillations.

Results from the application of the schemes to advection studies support the previous observations. Confinement corrections were shown to balance excess dissipation and to be capable of

propagating thin signals resembling their asymptotic solution over very long distances. In the case of space-time decoupled schemes, the confinement correction is only associated with the space discretization. Therefore, the dissipation of the time integration algorithm may be accumulated and eventually dissipate the signal over a very long distance for calculations at a larger CFL number. In the case of space-time coupled Lax-Wendroff schemes however, confinement corrections are also space-time coupled and thus show decreased sensitivity to the CFL number value. Finally, confinement was found to give improved results in the propagation of mixed-frequency wave packets at all orders, without showing any negative effect on numerical group velocity. This improvement in accuracy is especially interesting as confinement corrections can be integrated at a very small computational cost for linear space-time decoupled schemes.

In a following step, high-order extensions of the Vorticity Confinement method have been developed for the Navier-Stokes equations. These are high-order nonlinear anti-dissipative terms, interpreted as numerical corrections added to the momentum conservation equation to balance the excess numerical dissipation in regions of vortical flow. They have been derived in the continuous framework, based on the Laplacian of the original first-order VC2 formulation of J. Steinhoff. As a result, they are based on high-order even derivatives, in similarity to standard high-order dissipation terms, even though these derivatives are not purely one-dimensional in the case of VC. At the same time, the high-order extensions preserve some important properties of the original VC2 formulation: they remain conservative, rotationally invariant and independent of the baseline scheme. Moreover, it has been demonstrated that both the original VC2 term and its high-order extensions are equivalent to nonlinear anti-dissipative flux corrections explicitly based on vorticity. VC corrections can be thus implemented either as a source term or as a contribution to the numerical flux. The two are equivalent within vortices, except at cells on the vortex boundary due to the different deactivation of the VC correction.

The original VC2 term has been found to degrade the global order of accuracy in vortical regions when applied alongside high-order schemes. The developed high-order VC extensions on the other hand allow to recover the baseline scheme's nominal order of accuracy. Furthermore, the convergence error is similar for primitive variables and entropy. The absolute error with respect to the exact solution depends on the value of the confinement parameters, but the order of accuracy shows little sensitivity to these values. Subsequent calculations have demonstrated that the developed VC schemes can allow the advection of vortices over very long distances with low effects of dissipation, even in a case where the flow is inclined by 45° with respect to the grid. They provide results considerably closer to the exact solution than the linear version of the scheme, both at third- and at fifth-order of accuracy. Last, schemes with high-order VC have been shown to be more accurate in terms of vortex trajectory prediction than with the original VC.

An additional insight has also been obtained into the influence of the confinement parameters on the error of the scheme. The two parameters of the VC correction, μ and ε , correspond to opposite contributions (linear dissipation and nonlinear anti-dissipation respectively). Numerical experiments indicate that a high-value of one parameter can thus be balanced by an increased value of the other, at least in a simple vortex advection case. Although the result may be similar in terms of dissipation, significantly increasing the magnitude of the confinement correction (i.e. the parameter ε) may introduce additional error, particularly in terms of dispersion. Nonetheless, the effect on dispersion has in practice been found to be small for reasonable values of ε , in the order of magnitude of the artificial dissipation coefficient.

The schemes have then been applied to complex vortical flow computations, including flows at a turbulent regime. VC corrections are particularly appropriate for cases characterized by vortex transport over long distances. Nevertheless, the chosen applications were preferred to give an improved insight on the scheme's dissipation and thus on the consistency of the developed corrections.

Results on the Taylor-Green vortex flow have shown that VC corrections can accommodate complex dynamics without the need for special treatment. Schemes with VC have provided consistent results with reduced effects of numerical dissipation compared to the baseline linear version

of the scheme, particularly during the vortex stretching phase. The improvement was found to be especially beneficial in the calculation of enstrophy, even for finer meshes. Finally, the efficiency of high-order VC has been shown to have small dependence on the velocity gradient calculation scheme, with differences between low- and high-precision methods appearing in the treatment of smaller scales.

More detailed analyses of the schemes' small-scale dissipation were performed for the homogeneous isotropic turbulence (HIT) decay at different turbulent Mach number initial conditions. Confinement parameters were intentionally chosen so as to evaluate the limitations of the VC corrections. Excessive augmentation of the nonlinear anti-dissipation of VC was shown to overly reduce numerical dissipation and lead to an accumulation of energy at the smallest scales. Although this can be alleviated by augmenting the VC term's internal dissipation, the magnitude of the VC correction (determined by the parameter ε) should be more prudently chosen instead. However, for ε closer to the value of the underlying artificial dissipation coefficient, schemes with VC have been shown to yield consistent results and be more accurate compared to the baseline 5th-order ones used in this study. More specifically, VC was shown to extend the resolved energy spectrum and to improve the calculation of the enstrophy peak during the vortex stretching phase. The effect of VC was found to be small on high-order statistics of the HIT decay, but not closer to the reference solution than the baseline scheme. Last, VC was found to have a minor effect on thermodynamic quantities.

For reasonable values of the confinement parameters, VC was also found to give consistent results alongside a scheme with hybrid low-/high-order scalar dissipation. The anti-dissipation of high-order VC showed no deterioration of the scheme's shock-capturing properties, as it represents a correction to the high-order part of the baseline dissipation.

In the present study, high-order Vorticity Confinement has been shown capable of consistently balancing the excess dissipation of the scheme in vortical regions and improving the calculation of vorticity in numerical simulations for both simple advection studies and cases involving complex dynamics. Due to its nonlinear formulation, the method is also demonstrated to have an additional effect on the dispersive properties of the numerical scheme, but this effect has been found to be small for the cases investigated in this work, and even beneficial for reasonable values of the confinement parameters. The role of these parameters is also clearer due to the numerical interpretation of the VC method. Specifically, throughout this study, consistent results were obtained for ε in the order of magnitude of the coefficient of the high-order baseline artificial dissipation, although good values may differ for other types of dissipation. Schemes with high-order VC were also shown to be robust even in physically complex cases, without requiring special treatment. In conclusion, high-order VC corrections represent an overall interesting approach for high-order simulations of vortical flows, combining the vorticity-preservation capability of the original 1st-order VC and preserving the accuracy order of the baseline method. They are particularly appropriate for the calculation of wakes and cases dominated by vorticity convection, but have been shown to be advantageous even in turbulent flow simulations.

Perspectives

Following investigations may be performed both for scalar confinement corrections and for VC corrections in the case of the Navier-Stokes equations. Regarding the first case, it is important that the space-time decoupled approach for confinement corrections is also applied to other forms of dissipative operators. These operators can be compact, nonlinear, or also non-compact linear ones with optimized coefficients. Some preliminary results have already been obtained for some schemes of the latter category. A more detailed investigation can also be performed on the nonlinear properties of the confinement correction for values of ε smaller than the artificial dissipation coefficients, where decoupled schemes exhibit no instability but remain less dissipative than the baseline version of the scheme. Moreover, for ε greater than the artificial dissipation coefficient, an analysis of the upper

frequency bound of the mild instability can be interesting with regard to the schemes' asymptotic solution. Last, for application of these schemes to scalar transport equations, the spectral properties of schemes with confinement should be also investigated in multiple space dimensions.

The most prominent continuations of this study however would be in the case of the Navier-Stokes equations. First, a detailed comparative assessment should be performed between the source term and numerical flux implementation of high-order VC corrections. The latter has been only formulated in the present work, but can be important in flows with compressible effects. The two formulations are expected to yield similar results for fine mesh computations. On a coarse grid resolution however, differences are likely to occur due to the core being closer to the vortex boundary, where the two formulations differ. An important advantage of VC is its independence from the baseline method. Its applicability and efficiency should therefore be also carefully evaluated alongside schemes with different types of numerical dissipation than the ones considered in the present study. In this context, further investigations can be performed for baseline schemes with hybrid low-/high-order numerical dissipation (as the ones presented in Section 4.2.1.1). For such schemes, high-order VC represents a corrective term to the high-order part of the dissipation. It is therefore differentiated from the low-order dissipation near shocks, and should in principle be applicable to compressible cases in a hybrid dissipation approach. This includes strategies involving a Ducros-type sensor, which also reduces the low-order part of the dissipation within vortices. Last, its applicability to irregular curvilinear grids can also be assessed alongside k -exact finite volume schemes.

Improvements can also be pursued in terms of numerical implementation. On one part, the accuracy of the calculation of the derivatives of high-order VC can be addressed. Adaptive stencil reconstruction techniques were shown to improve the calculation of the VC term at the vortex boundary, albeit at the price of robustness (see discussion of Appendix A). It is however possible that better-performing alternatives can be devised. The numerical calculation of high-order VC also permits algorithmic improvements and further optimization of computational resources. On this subject, a possible alternative has already been proposed to reduce the number of ghost cell layers required to accurately compute the high-order VC term on zone boundaries.

In terms of applications, it can be interesting to assess the performance of high-order VC in LES using explicit subgrid-scale modeling. Moreover, the numerical calculations presented here have shown the potential of high-order VC corrections in academic test cases, which are physically complex but geometrically simple. Naturally, high-order VC corrections should also be assessed in the calculation of more realistic aeronautic configurations. Examples of such cases are calculations of rotor wakes or wing-tip vortices, where the use of VC is particularly appropriate.

Appendix A

Treatments for the discontinuity of harmonic mean derivatives on the vortex boundary

This chapter discusses some numerical treatments which can be applied to reduce or remove the production of oscillations in the calculation of the VC term on the vortex boundary. These have not been applied for the computations in the main part of the thesis. They are however briefly presented here because they may be found useful for future developments or other applications.

A.1 Description of the problem

Vorticity Confinement corrections for the Euler and Navier-Stokes equations require the calculation of spatial derivatives of the vorticity vector $\vec{\omega} = \vec{\nabla} \times \vec{v}$ and the ‘harmonic mean’ vector \vec{w} . Specifically, the calculation of a p th-order accurate VC term requires p th-order derivatives of these two vectors, as shown in Eqs. (4.42), (4.62) and (4.63). This naturally requires the smoothness of the vector fields $\vec{\omega}$ and \vec{w} . While both are smooth within the region where the VC correction is applied, \vec{w} is locally C^0 near points of zero vorticity.

For the sake of simplicity, in the rest of this chapter we will use the case of a static isentropic vortex in two space dimensions as a reference. This is the test case investigated in Section 4.5.1, which is discretized on a square computational domain $[-5, 5]^2$. In this two dimensional case, the ‘harmonic mean’ vector \vec{w} at the center of a cell Ω_J reduces to:

$$w_J = \text{sgn}(\omega_J) N_c \left(\sum_{\ell=1}^{N_c} \|\omega_\ell\|^{-1} \right)^{-1} \quad (\text{A.1})$$

where the summation is performed for the N_c cells in the complete neighborhood of cell Ω_J . Within vortices, where vorticity does not change sign among the N_c neighboring cells, the above equation is equivalent to:

$$w_J = N_c \left(\sum_{\ell=1}^{N_c} \omega_\ell^{-1} \right)^{-1} \quad (\text{A.2})$$

which is an algebraically smooth form.

Fig. A.1 shows a contour of the Q -criterion and vorticity profiles for the static vortex. It is shown that for a smooth solution, Eq. (A.2) does indeed give a smooth harmonic mean field within the vortex. It is not however the case close to the position of zero vorticity, as vorticity at this position changes sign among the cells N_c . In that case, the harmonic mean calculation of Eq. (A.1) is not smooth. In other words, on a smooth vorticity field, the harmonic mean is of class C^∞ within clearly defined vortical regions, but of class C^0 near points of zero vorticity. As detailed in Section 4.4.3, the VC correction is not applied close to these points. However, for higher-order VC, the stencil is

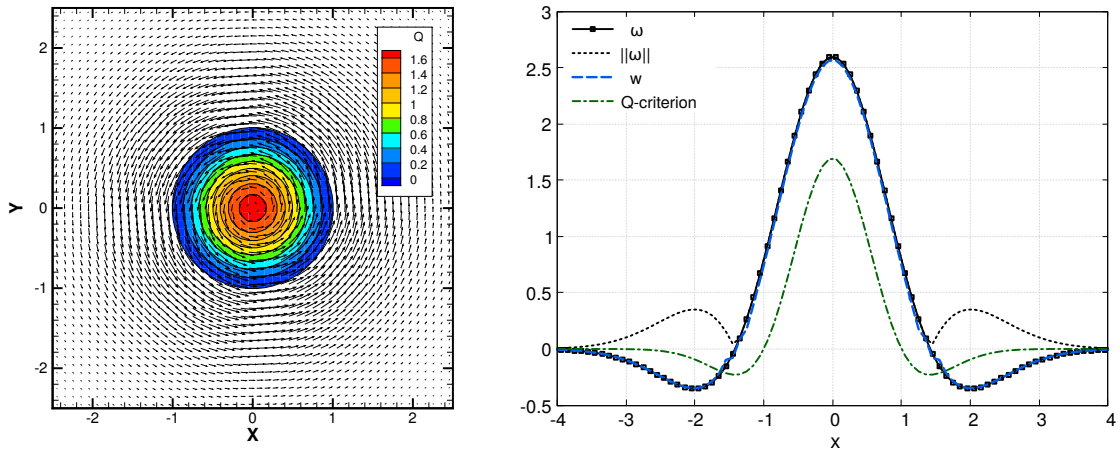


Figure A.1: Contour of the Q -criterion with superimposed velocity vectors (left) and horizontal profile extractions (right). Isolated two-dimensional isentropic vortex case on the 100^2 mesh.

larger and higher-order derivatives are computed. As a result, for points near the vortex boundary, the global stencil of the VC calculation may cross the region of zero vorticity and oscillations may appear in the calculation of the VC term. This is portrayed in the vector representation of the VC source term, shown in Fig. A.2. The anti-dissipation of VC exhibits numerical oscillations near the vortex boundary at higher-orders of accuracy. Note that in these figures, the cut-off of the Q -criterion has been set to $Q_o = 10^{-5}$. These oscillations are rapidly reduced with mesh refinement, as eventually the VC stencil does not cross the region of zero vorticity. For the finer 200^2 and 400^2 meshes of the grid convergence study, such oscillations do not appear on the vortex boundary.

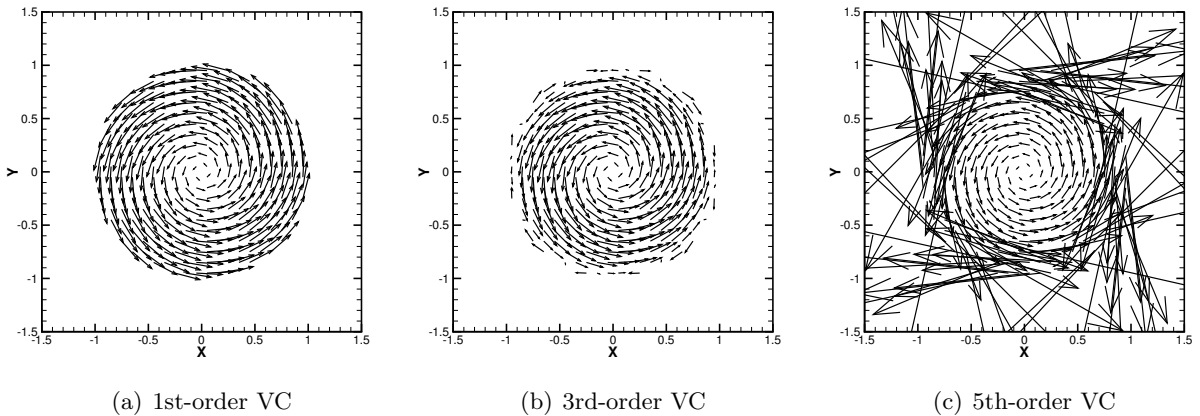


Figure A.2: Vector contribution of the computed VC term on the 100^2 grid. Computed with the 5-point Laplacian scheme and simple arithmetic average reconstruction. The plotted relative vector length is augmented at higher-order VC for visibility, as the term's magnitude is significantly lower.

The importance of using a nonlinear function with a smooth algebraic form in the construction of VC has already been identified by J. Steinhoff [195]. The harmonic mean function is smooth within vortices and therefore is not affected by oscillations at first-order of accuracy of VC. The effect of oscillations appears essentially at 5th-order of accuracy. The non-smoothness around points of zero vorticity can be fixed either by adopting a globally (i.e. even at points where vorticity changes sign) smooth nonlinear function instead of the harmonic mean, or by a regularization of the harmonic mean derivatives. Neither of the two is however straightforward in practice.

On the other hand, the numerical calculation of oscillation-free high-order derivatives in the

neighborhood of a discontinuity is far from a simple task. The same problem exists also for the calculation of baseline numerical dissipation terms near discontinuities. In the case of VC, the discontinuity of harmonic mean derivatives is not aligned with the mesh directions, but an important advantage is that the position of discontinuity is known *a priori*. On this basis, a detailed investigation of strategies to treat this problem has been carried out. Some of these are briefly discussed in the following. They can be separated in two different categories: approaches to detect problematic cells and deactivate the VC correction, and approaches to reduce or remove the appearance of numerical oscillations.

The most obvious way to remove oscillations at the vortex boundary would be to augment the minimum cut-off value of the vortex identification criterion (see Eq. (4.95)). Even for a dimensionless criterion however, it is very likely that a good value of this cut-off is going to be case-dependent. An alternative would then be to deactivate the VC correction in problematic cells, by further restricting the criteria of the cut-off variable β_J . For example, on a smooth vorticity field, the positive dissipation part of the VC term is free from oscillations. A possibility would be therefore to detect problematic cells via the alignment between the high-order gradients of the linear positive dissipation part and those of the nonlinear anti-dissipative part of the VC term. This however requires the calculation of high-order derivatives separately for the two parts of VC, and thus significantly increasing computational cost. Furthermore, high-order derivatives of the harmonic mean function are not necessarily aligned with those of vorticity in general three-dimensional cases. In any case, we have found that more consistent results are obtained when the region of application of the VC correction is not significantly reduced.

A.2 Adaptive stencil reconstruction

Adaptive stencil reconstructions have been investigated in an effort to reduce numerical oscillations without restricting the region of application of the VC correction. In particular, the approach adopted here is that of Essentially Non-Oscillatory (ENO) and Weighted ENO (WENO) schemes. A brief review of these can be found in Section 2.2.4, whereas an extensive presentation of the method's principles and implementation is given by C.-W. Shu [186].

High-order derivatives for the VC correction are again calculated recursively, as described in Section 4.4.1. The idea is to replace the simple average of Eq. (4.78) with an adaptive stencil reconstruction of the cell-face values. In the following, the study will be limited to the case of uniform Cartesian grids.

We suppose a general k th-order accurate polynomial reconstruction of the face value $(\bullet)_{J+\frac{1}{2}}^d$. The reconstruction stencil is composed of r cells on the left and s cells on the right of the cell Ω_J , in mesh direction d . Since it is $r + s + 1 = k$, the stencil points for a given order of accuracy can be uniquely defined by r . The reconstruction can then be written:

$$(\bullet)_{J+\frac{1}{2}}^{(r)} = \sum_{\ell=0}^{k-1} c_{r,\ell} \overline{(\bullet)}_{J-r+\ell} \quad r = 0, \dots, k-1 \quad (\text{A.3})$$

where the superscript d denoting the mesh direction has been omitted for simplicity. Above, $c_{r,\ell}$ are the stencil coefficients and $\overline{(\bullet)}_J$ denotes the volume-averaged value in the cell Ω_J .

ENO schemes select the smoothest out of k candidate stencils based on values of undivided differences. On the other hand, WENO schemes employ a convex combination of all these stencils:

$$(\bullet)_{J+\frac{1}{2}} = \sum_{r=0}^{k-1} \gamma_r (\bullet)_{J+\frac{1}{2}}^{(r)} \quad (\text{A.4})$$

Above, γ_r are nonlinear weights of the candidate stencils, given by:

$$\gamma_r = \frac{\alpha_r}{\sum_{m=0}^{k-1} \alpha_m}, \quad \text{with:} \quad \alpha_r = \frac{d_r}{(\epsilon + \beta_r)^{p_\beta}}, \quad r = 0, \dots, k-1 \quad (\text{A.5})$$

where $\epsilon = 10^{-6}$ and p_β is an integer constant, usually taken $p_\beta = 2$. The real coefficients d_r are the so-called optimal linear weights of the WENO scheme, since for $\gamma_r = d_r$ the reconstruction (A.4) is accurate to $(2k-1)$ th-order. This is achieved on smooth regions of the solution.

A most important part of the WENO scheme are the smoothness indicators β_r in Eq. (A.5). These give a measure of smoothness of the reconstruction on each candidate stencil. For the WENO schemes of G.-S. Jiang and C.-W. Shu [107, 186], β_r are based on the sum of the scaled L^2 -norms of derivatives of the candidate interpolation polynomial over the cell:

$$\beta_r = \sum_{m=1}^{k-1} \int_{x_{J-\frac{1}{2}}}^{x_{J+\frac{1}{2}}} \Delta x^{2m-1} \left(\frac{\partial^m p_r(x)}{\partial x^m} \right)^2 dx \quad (\text{A.6})$$

where $p_r(x)$ is the reconstruction polynomial. Since the WENO method is adopted here for the calculation of high-order derivatives, this definition of smoothness indicators is particularly appropriate.

An important difference with respect to the standard ENO/WENO reconstruction is the upwind-biasing of candidate stencils. For the reconstruction of primitive or characteristic variables, the upwinding direction is defined from the local direction of wave propagation. In the case of VC, the biasing direction should be such that the stencil does not cross the location of discontinuity. The location of the derivative discontinuity is known *a priori*: towards the direction of decreasing vorticity modulus. For the reconstruction of the value $(\bullet)_{J+\frac{1}{2}}^d$, the direction of upwind-biasing can then be easily determined by the difference:

$$(\delta_d \|\vec{\omega}\|)_J = \|\vec{\omega}\|_{J+1}^d - \|\vec{\omega}\|_J \quad (\text{A.7})$$

Depending on the sign of the difference (A.7), the ENO/WENO reconstruction process may be modified symmetrically with respect to the face $x_{J+\frac{1}{2}}^d$.

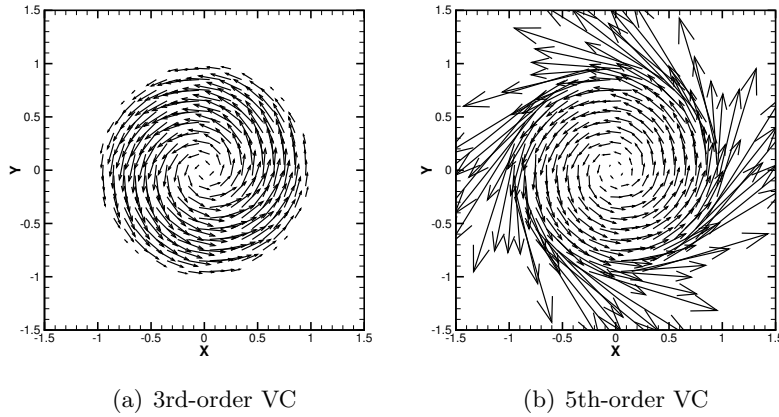


Figure A.3: Vector contribution of the computed VC term on the 100^2 grid. Computed with the 5-point Laplacian scheme and ENO5 reconstruction. $Q_o = 10^{-5}$.

First, ENO reconstructions were investigated up to 7th-order of accuracy. The ideal choice would be a second-order ENO reconstruction ($k=2$), which alternates between the simple average and the 2-point extrapolation:

$$\begin{aligned} (\bullet)_{J+\frac{1}{2}}^{(0)} &= \frac{1}{2} \overline{(\bullet)}_J + \frac{1}{2} \overline{(\bullet)}_{J+1} \\ (\bullet)_{J+\frac{1}{2}}^{(1)} &= -\frac{1}{2} \overline{(\bullet)}_{J-1} + \frac{3}{2} \overline{(\bullet)}_J \end{aligned} \quad (\text{A.8})$$

as the order of the reconstruction itself is not of primary importance in the case of VC. The above reconstruction includes the adaptive stencil choice and at the same time keeps a minimum stencil

size. For a low-order ENO reconstruction however, the degree of undivided differences cannot account for higher-order derivatives. Also, since variations of the field are not monotone in the directions of the mesh within the vortex, the stencil changes also in the vortex interior. These stencil changes result in a discontinuous reconstruction, an effect which is amplified by performing successive derivations.

It has thus been found that the reconstruction must be at least of the order of accuracy of the VC term to give a smooth result in the vortex interior. A good choice is the 5th-order ENO reconstruction (ENO5), both for 3rd- and 5th-order VC. The vector contribution of the VC term in this case is shown in Fig. A.3. The effect of numerical oscillations at the vortex border is effectively reduced, even at fifth-order of accuracy. The magnitude of the VC term is higher on the boundary at 5th-order VC, but these values are rapidly suppressed by a small augmentation of the value of Q_o . In practice however, numerical experiments have shown that the robustness of the VC method is degraded by the discontinuous reconstruction of ENO schemes.

The WENO approach is interesting because the weighting process results in a smoother reconstruction in space. The increased order of accuracy on the same reconstruction stencils as ENO schemes is of secondary importance for the case of VC. These reconstructions were investigated up to 9th-order of accuracy. As for ENO schemes, a sufficiently high reconstruction order is necessary to give a smooth reconstruction of the VC term within the vortex. This is because the indicators (A.6) measure the smoothness up to the $(k - 1)$ th-order derivative, i.e. the highest-order derivative that can be supported on the given stencil. The stencil must be therefore sufficiently large to account for the smoothness of the derivatives which will be calculated for the VC term.

Fig. A.4 shows the vector contribution of the VC term at 5th-order of accuracy for the 9th-order WENO reconstruction ($k = 5$). The parameter p_β in Eq. (A.5) adjusts the penalization of candidate stencils, depending on the value of the smoothness indicators β_r . The influence of the value of p_β is generally more important as the reconstruction order increases, or in the present case as higher-order derivatives are computed. Results show that the standard choice $p_\beta = 2$ is not enough to suppress the oscillations at the vortex boundary. A choice $p_\beta = k$ or even as high as $p_\beta = 2k - 1$ has been found to yield better results. An increased value of p_β ($p_\beta = k$) has been also found necessary to preserve the ENO property for very high-order WENO schemes [79]. Last, we have found that the introduction of Monotonicity-Preserving bounds in the reconstruction [9] did not have an considerable effect in the calculation of high-order VC.

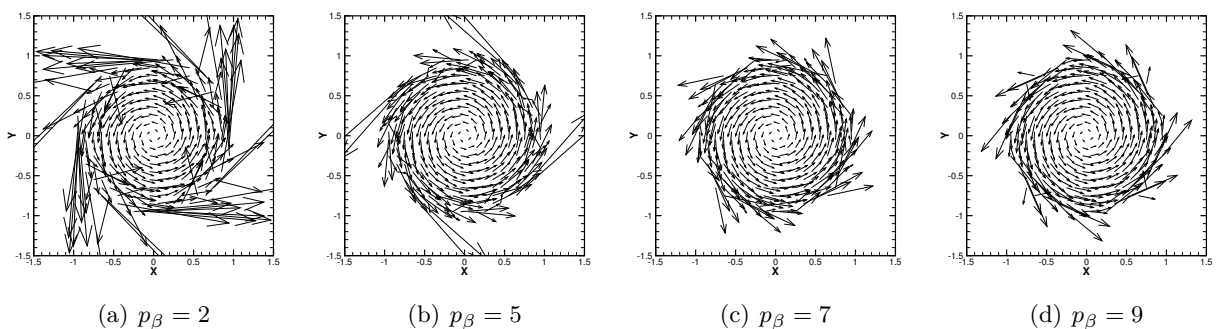


Figure A.4: Vector contribution of the computed 5th-order VC term on the 100^2 grid. Computed with the 5-point Laplacian scheme and WENO9 reconstruction. $Q_o = 10^{-5}$.

A.3 Synthesis and remarks

The use of an adaptive stencil reconstruction in the calculation of gradients has been found to effectively reduce numerical oscillations at the vortex boundary. Not surprisingly, WENO methods have been found to be significantly more robust than the corresponding ENO ones, due to their smoother reconstruction in space. Still, a simple average reconstruction has been found to be more

robust than the adaptive stencil methods in the calculation of complex flows, where stencil changes are more frequent. This is most likely because a smooth reconstruction is particularly important for the calculation of high-order derivatives. Furthermore, VC is not a physical term of the flow equations, but an anti-dissipative correction of the baseline numerical dissipation. It is therefore possible that its efficiency is not very sensitive to the oscillations observed at high-order of accuracy. Even without specific treatment for the reduction of spurious oscillations on the vortex boundary, a simple average reconstruction has been found to be robust and give consistent results for all cases investigated in the main part of this thesis.

Appendix B

Application to an airfoil-vortex interaction

This chapter presents a preliminary validation of a third-order accurate Vorticity Confinement method in a two-dimensional inviscid Blade-Vortex Interaction (BVI) application. The results of this study have been published in [47].

B.1 Description of the test case

The test case investigated here is the experimental study of a parallel blade-vortex interaction carried out by C. Kitaplioglu, F. Caradonna et al. [110, 111]. This was performed in the acoustically treated test section of the NASA Ames 80- by 120-foot wind tunnel, using a rotor blade equipped with a constant NACA0012 airfoil section. For the chosen experimental case, the hover tip Mach number is $M_{\text{tip}} = 0.714$, the rotor advance ratio is $\mu = 0.198$ and the vortex-airfoil separation distance in the rotor plane is $-0.25c$. A schematic representation of the experimental setup is shown in Fig. B.1. Similar configurations are often studied in aeroacoustics since airfoil-vortex interaction is a major source of aerodynamic noise. Within ONERA, this case has been previously studied by M. Costes [43], O. Saunier [178] and by S. Peron et al. [159] in the frame of the ONERA-JAXA cooperation. Similarly to the present thesis, the objective of the aforementioned studies was the evaluation and comparison of numerical methods, rather than the reproduction of the experiment. The blade-vortex interaction occurs when the rotor lies in the wind tunnel axis. The case is therefore simulated in the two-dimensional interaction plane. Specifically, we are considering the plane corresponding to a blade section located at $r/R = 87.6\%$. For the above experimental parameters, the freestream Mach number in the two-dimensional interaction plane is $M_{\text{inf}} = 0.626$.

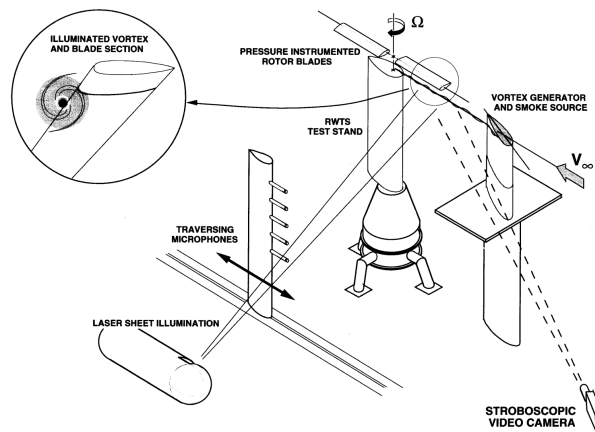


Figure B.1: Sketch of the experimental BVI setup. C. Kitaplioglu et al. [111].

B.2 Meshing and numerical strategy

The meshing strategy consists in the use of a C-type curvilinear mesh for the NACA airfoil and a set of Cartesian background meshes communicating via Chimera interpolation [13]. The meshes were generated using tools of the Cassiopée library [15]. Views of the computational domain are presented in Fig. B.2. The background mesh is divided into four zones of varying density. To minimize mesh size, the vortex path is not covered by a uniform Cartesian region, but the mesh is refined only close to the airfoil so that a reasonable size ratio between the NACA and background mesh is maintained (Fig. B.2(b)). Studies were performed for varying background mesh density $\Delta x_{min} = 0.025/0.0125$ on the coarse and fine grids respectively, where Δx_{min} refers to the thickness of the finest background region. The NACA mesh is composed of 228×10 points for the coarse mesh and 450×18 points for the fine mesh. The cell size ratio is $1/2$ between the two finest background zones, which cover the vortex advection path, and $1/3$ for the other cases. The coarse and fine grids contain a total of 66.147 and 254.057 cells respectively. The approximate number of cells per vortex radius is 3 and 6 during the main part of the advection. A finer mesh of 3.252.720 cells with $\Delta x = 0.00625$ in the vortex advection region and a 914×36 point mesh for the NACA was also generated and studied as a higher-accuracy reference solution. For this case, the finest background region covers the complete vortex path during the interaction, and not only the area close to the airfoil.

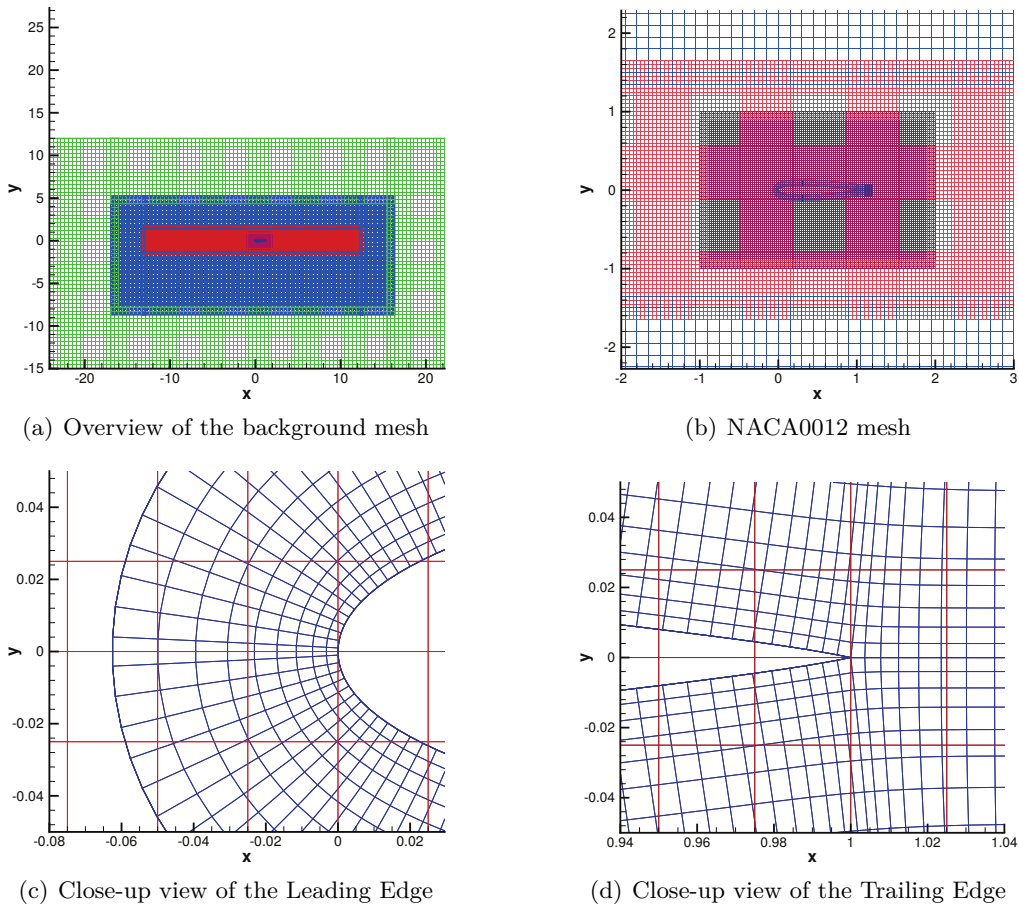


Figure B.2: Overview of the background mesh and details of the NACA0012 curvilinear mesh. The background mesh is divided in four zones of varying density. The meshes correspond to the coarse computational domain ($\Delta x = 0.025$ in the finest Cartesian region).

The airfoil is set at 0° incidence. The initial field is obtained as the result of a steady calculation of the flow at $M_{inf} = 0.626$. For this steady calculation, sufficient iterations are performed so that the L^∞ -norm of the residuals for all equations is reduced by at least 10 orders of magnitude. The

initial condition for the unsteady calculation is obtained by superimposing the clockwise-rotating vortex to the steady field at the position $(x_o, y_o) = (-10c, -0.25c)$. The vortex is initialized using an algebraic model proposed by M. P. Scully [182], with its dimensionless tangential velocity given by:

$$v_\theta(r) = \frac{\Gamma_v}{2\pi} \frac{r}{r^2 + \zeta_v^2} \quad (\text{B.1})$$

where Γ_v is the vortex circulation and ζ_v the vortex core radius. The experimentally estimated vortex characteristics are $\Gamma_v = 0.2536$ and $\zeta_v = 0.162c$.

Presented computations have been performed by solving the compressible Euler equations, using a Cartesian solver presented in [178]. The discretization of the convective part of the physical fluxes is performed with the schemes described in Section 4.2.1.1. The consistent part is approximated with a centered formula and the dissipation is scalar, based on the spectral radius of the inviscid flux Jacobian matrix. The second- and higher-order dissipation coefficients are taken $k_2 = 0$ and $k_{\text{ho}} \approx 1/60$ for all cases. Curvilinear grids are solved in a finite volume approach, whereas Cartesian grids are solved in a finite difference approach. For each case the order of accuracy in the Cartesian and curvilinear regions is the same except for the 5th-order scheme, which is combined with the 3rd-order accurate weighted curvilinear scheme of A. Rezgui et al. [165]. The same curvilinear scheme is used for the 3rd-order scheme. Time discretization is performed using an implicit 2nd-order accurate Gear scheme, solved by a maximum of 10 Newton sub-iterations at each time step. The time step is $\Delta t = 0.01/0.005/0.0025$ for the coarse, fine and reference meshes respectively, so that the maximum CFL number is the same for all cases. Computations were run for non-dimensional time $t = -10$ to $t = 10$ so that interaction occurs approximately at $t = 0$. The Chimera interpolations are 2nd-order accurate for the 2nd-order scheme and 3rd-order accurate for the higher-order schemes. The reference solution is computed using the 5th-order scheme. For cases with VC, the source term is applied in Cartesian regions only and the confinement parameters were set to $\mu/\varepsilon = 0.6$ and $\varepsilon = 0.02$. These calculations were performed with an early version of the VC method, which is at most third-order accurate and implemented for Cartesian grids in a finite difference formulation. The undivided differences for the third-order VC term are thus calculated as in Eq. (4.81). Last, in this version of the method, the VC source term in Eq. (4.41) is also multiplied with density.

B.3 Numerical results

Reference results for the finer mesh with $\Delta x_{\text{min}} = 0.00625$ using the 5th-order baseline scheme are shown in Fig. B.3 and show satisfactory preservation of the vortex shape during the advection phase. Profile extractions, performed horizontally for $x = 0.5$ in both directions from the position of maximum absolute vorticity value, show an amplification of core vorticity by approximately 7%. This is probably related to the initial vortex not being an exact solution of the Euler equations. It will thus need to deform in order to eventually relax towards an exact solution. Figs. B.3(c)-B.3(d) display the time evolution of pressure on the airfoil surface in the upper and lower sides respectively at $x/c = 0.02$. Results are compared with experimental measurements of C. Kitaplioglu, F. Caradonna et al. at the same positions. Computational pressure predictions are different from the experimental measurements, probably as a result of the 3D effects of the experiment that are not accounted for in the computational study. For comparison, the computational curves are displaced so that they match the experimental pressure coefficient at time $t = -7$, as in [159]. Computations produce a good approximation of the pressure evolution close to the moment of interaction, for both sides. A slight miscalculation of the time of interaction is still observed, due to the phase approximation error of the scheme.

Fig. B.4 shows iso-vorticity contours near the moment of interaction for the baseline schemes on the coarse and fine grids. These underline the effect of numerical error in lower-accuracy numerical schemes. The numerical diffusion of the vortex is severe on the coarse mesh, and especially for the lower-order 2nd-order computation. Iso-vorticity contours also show that the vortex shape is

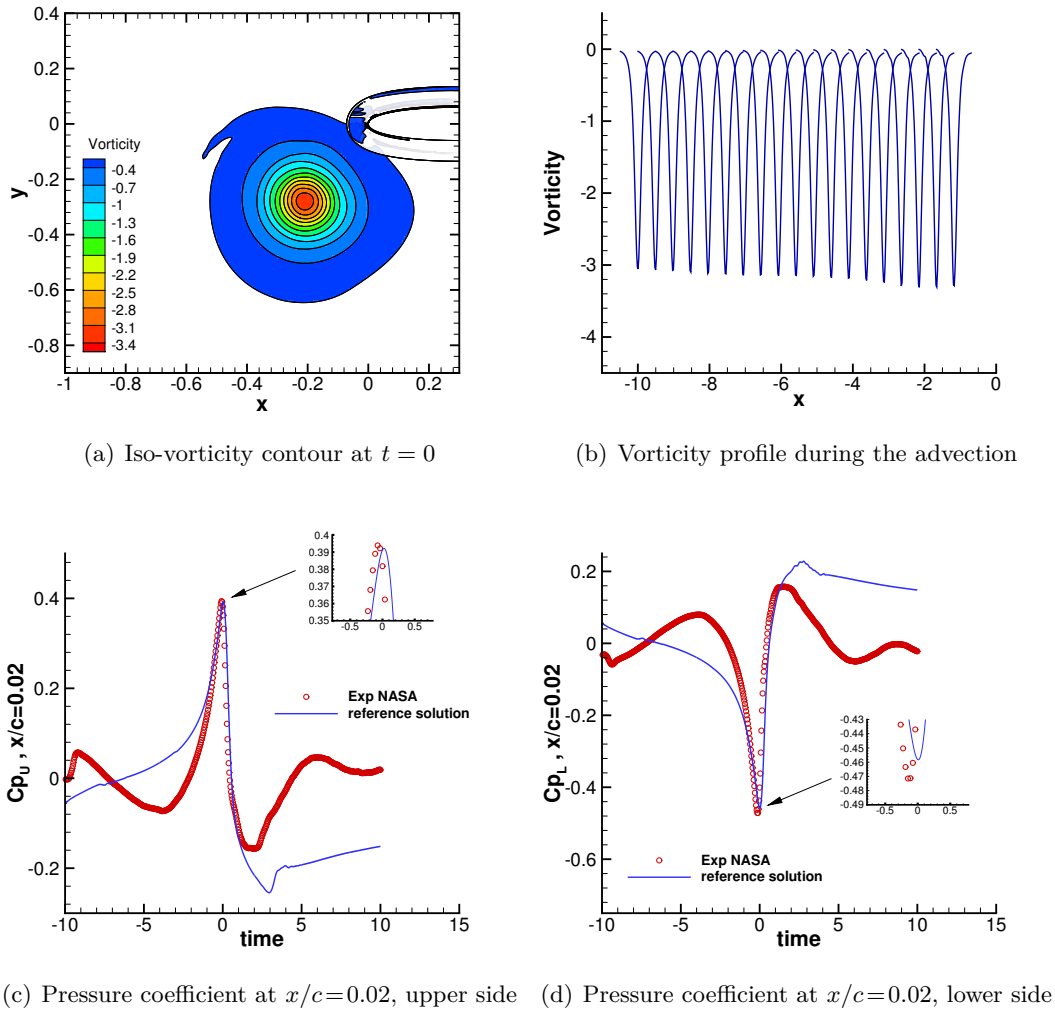


Figure B.3: Results of the reference computation with $\Delta x=0.00625$ during the complete advection distance, 5th-order scheme.

noticeably distorted. The vortex core position at $t = 0$ and the pressure peaks at the moment of interaction are shown in Table B.1. The pressure peaks achieved on the airfoil are shown to be less intense for higher-order of the baseline scheme. This behavior is however related to the improved prediction of the vortex trajectory, rather than their reduced numerical dissipation, as demonstrated from the vortex core position at $t=0$ shown on the same table. The x -position of the vortex is related to the interaction time and the y -position is related to the interaction intensity. For the reference computation, the small vertical displacement of the vortex with regard to the initialization can be attributed either to the airfoil presence in the flow field or to the dispersion error of the 5th-order scheme. For the 2nd-order scheme, the vortex is positioned closer to the airfoil in the y -direction than for the other cases, both for the coarse and fine mesh. This leads to a significant amplification of the interaction, i.e. an increase of the interaction pressure peak on both sides, especially for the 2nd-order scheme on the coarse mesh. For higher order schemes, the vortex is positioned further from the airfoil in the y -direction, so the interaction pressure peaks are reduced even if the intensity of the vortex is better preserved. Last, for the lower-accuracy 2nd-order computation on the coarse mesh, the computed vortex is positioned further from the airfoil in the x -direction, which is fortuitously in agreement with the reference computation.

Fig. B.5 shows that the original first-order VC results in a significant amplification of the vortex core alongside a fifth-order scheme. Naturally, this is more apparent as the mesh is refined. In

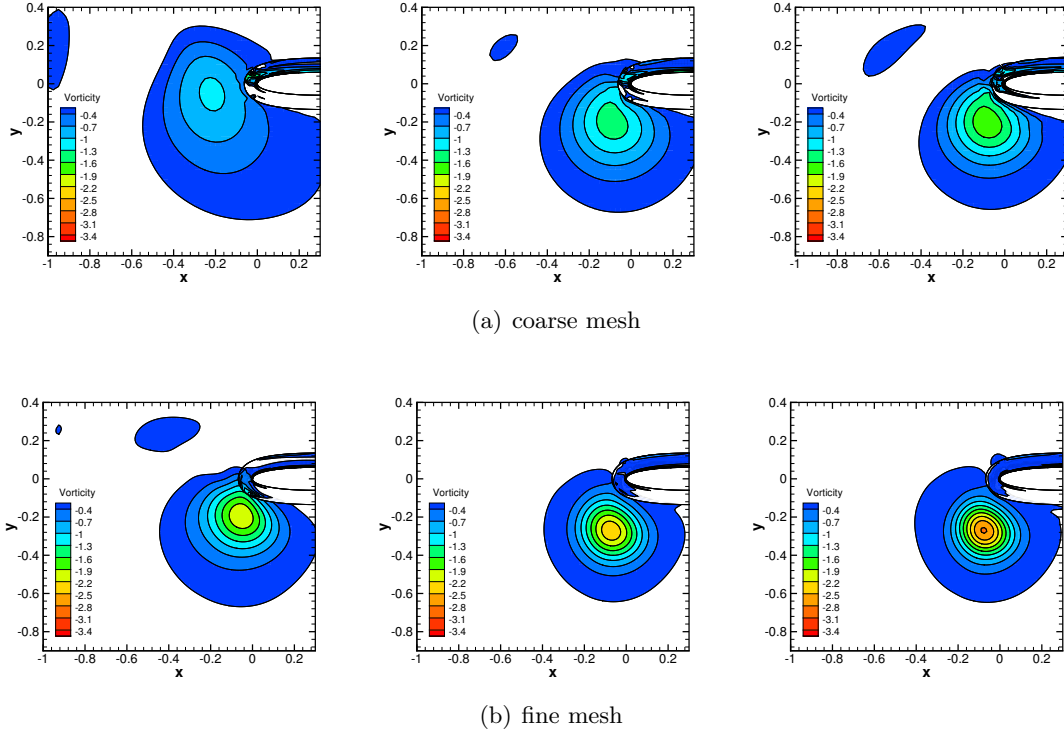


Figure B.4: Iso-vorticity contours at $t = 0$. From left to right, 2nd-order, 3rd-order and 5th-order baseline scheme.

Case	Scheme order	x_{core}	y_{core}	$\max(C_{pU})$	$\min(C_{pL})$
Experiment	-	-	-	0.3939	-0.4715
Reference	5th	-0.2094	-0.2781	0.3921	-0.4583
Coarse mesh	2nd	-0.2125	-0.0375	0.4565	-0.5908
	3rd	-0.0875	-0.1875	0.4445	-0.5530
	5th	-0.0875	-0.1875	0.4334	-0.5468
Fine mesh	2nd	-0.0563	-0.1938	0.4413	-0.5194
	3rd	-0.0688	-0.2688	0.4114	-0.4895
	5th	-0.0813	-0.2688	0.4098	-0.4869

Table B.1: Vortex core position at $t = 0$ and interaction pressure peaks at $x/c = 0.02$ for baseline schemes, without VC.

this case, the numerical dissipation of the fifth-order scheme is reduced and the scheme already gives a fair preservation of the vortex. The magnitude of the original first-order VC however clearly decreases at a lower rate with mesh refinement, which is not consistent with the baseline scheme's order of accuracy. Results show that the third-order VC displays an increased compatibility with the higher-order underlying scheme. This is more clearly seen from profile extractions at different instants of the vortex advection, presented in Fig. B.6. The third-order VC term improves the presentation of vortex intensity without noticeable modification of the vorticity profile. The global order of accuracy is still however degraded to third within the vortex, as the order of the VC term is lower compared to the baseline scheme (see Section 4.5.1). A similar over-amplification of the vortex should thus be observed for 3rd-order VC, given a further refinement of the mesh.

The computed vortex core position and pressure peaks for the fifth-order scheme and VC are shown in Table B.2. Within the computed distance, which is significantly shorter than the ones computed in the study of Section 4.5.2, the VC term introduces small or no modification in vortex trajectory. Specifically, a difference is observed only in the x-direction on the coarse mesh and is the same for both orders of VC. The y-position, which determines the intensity of the interaction,

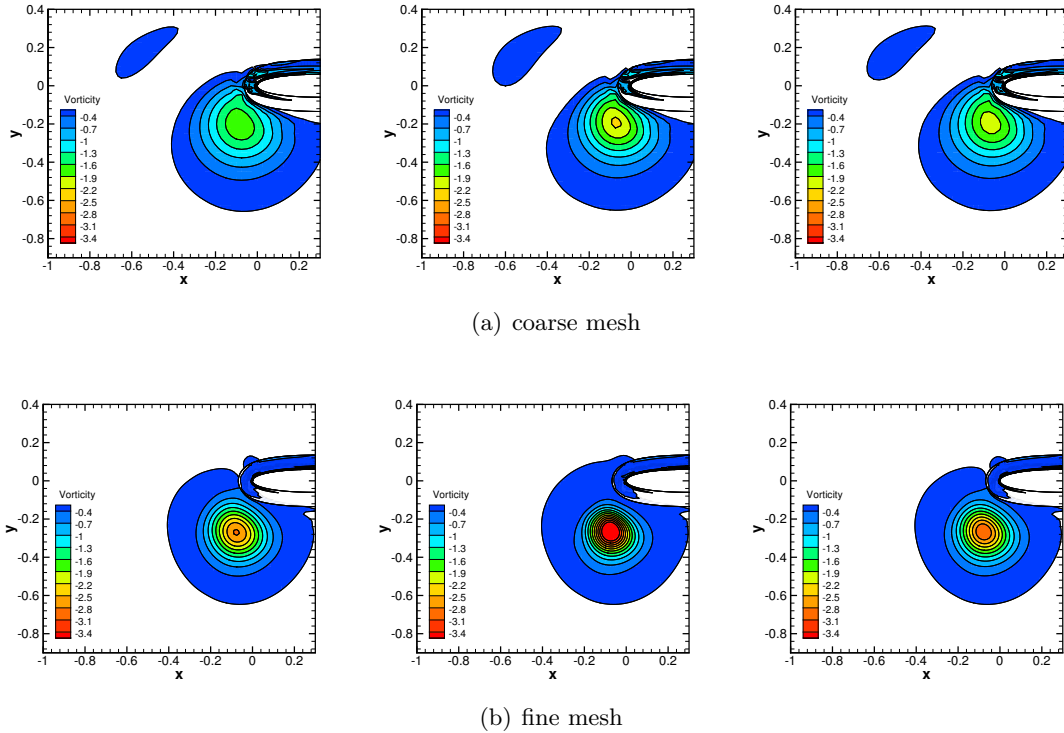


Figure B.5: Iso-vorticity contours at $t=0$ using the 5th-order baseline scheme. From left to right, baseline scheme without VC, with 1st-order VC and with 3rd-order VC, $\mu/\varepsilon = 0.6$ and $\varepsilon = 0.02$.

is not modified. On the fine mesh, confinement does not modify the vortex position at the moment of interaction. The pressure peaks on the upper and lower side of the airfoil are presented in the same table. As expected, absolute values of the interaction pressure increase when confinement is applied, since the computed vortex intensity is stronger. It is important to note that the interest of the present case is to investigate whether confinement is compliant with the physics of the airfoil-vortex interaction, rather than significantly improve the calculation of the peak pressure. In any case, the pressure obtained from the two-dimensional computation itself is not directly comparable to the experiment, which is naturally three-dimensional. Similarly to the baseline schemes without confinement, the absolute peak values of computed pressure are increased compared to the reference case. This is related to the dispersion error of the baseline scheme, in particular concerning the vortex position in the y -direction. Finally, the effect of VC on the interaction physics can be observed by the evolution of the pressure coefficient on the airfoil surface. This is shown in Fig. B.7 for a point positioned at $x/c=0.02$, on the lower side of the airfoil. Apart from the slight increase of the pressure peak, as shown in Table B.2, the use of VC does not introduce any observable modification in the evolution of the pressure, even during the stabilization of the flow after $t=0$.

The inconsistency of first-order VC with higher-order schemes as soon as the mesh is refined is often hindering for its application in realistic problems. Already for the short advection distance and the mesh resolutions considered in this study, a significant improvement has been observed by using a third-order accurate VC method. Nonetheless, the use of a VC term of at least the same order of accuracy as the baseline scheme is always preferable. In the present problem, VC itself does not introduce any considerable improvement in the prediction of surface pressure. This is because this case shows more sensitivity to the prediction of the distance between the vortex and the airfoil, and this is practically unmodified with VC.

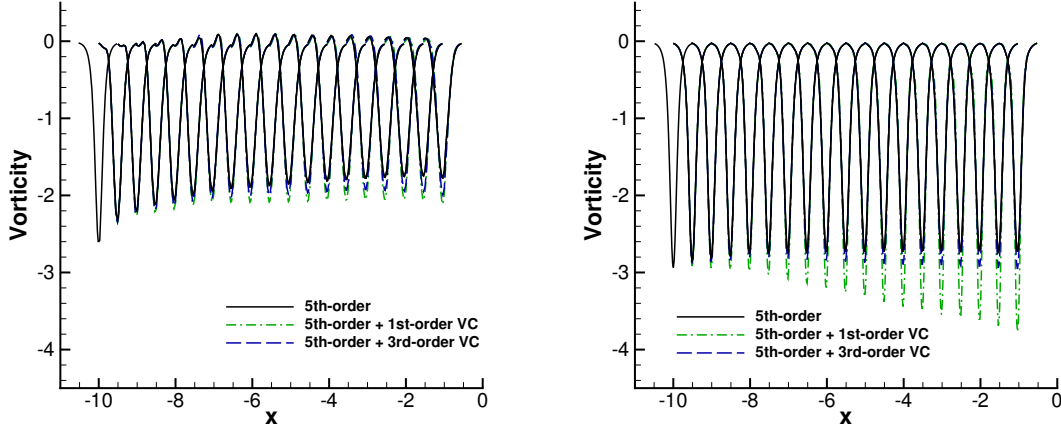


Figure B.6: Vorticity profile over time using the 5th-order scheme and vorticity confinement. Results on the coarse mesh (left) and the fine mesh (right), $\mu/\varepsilon = 0.6$ and $\varepsilon = 0.02$.

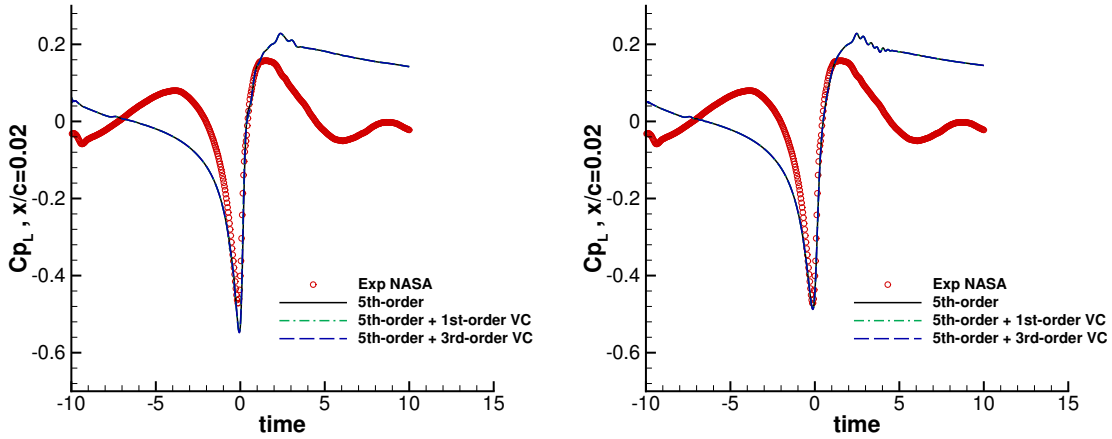


Figure B.7: Time evolution of pressure coefficient on the lower side at $x/c = 0.02$ using the 5th-order scheme and vorticity confinement. Results on the coarse mesh (left) and on the fine mesh (right), $\mu/\varepsilon = 0.6$ and $\varepsilon = 0.02$.

Case	Scheme order	VC order	x_{core}	y_{core}	$\max(C_{pU})$	$\min(C_{pL})$
Experiment	-	-	-	-	0.3939	-0.4715
Reference	5th	-	-0.2094	-0.2781	0.3921	-0.4583
Coarse mesh	5th	-	-0.0875	-0.1875	0.4334	-0.5468
		1st	-0.0625	-0.1875	0.4360	-0.5487
		3rd	-0.0625	-0.1875	0.4346	-0.5479
Fine mesh	5th	-	-0.0813	-0.2688	0.4098	-0.4869
		1st	-0.0813	-0.2688	0.4113	-0.4884
		3rd	-0.0813	-0.2688	0.4105	-0.4877

Table B.2: Vortex core position at $t=0$ and interaction pressure peaks at $x/c=0.02$ with VC.

Appendix C

List of publications

This chapter presents a list of journal publications, participations in international conferences and distinctions related to the work presented in this thesis.

Publications in peer-reviewed journals

- I. Petropoulos, M. Costes, and P. Cinnella. Development and analysis of high-order vorticity confinement schemes. *Computers & Fluids*, 156:602–620, 2017. <http://dx.doi.org/10.1016/j.compfluid.2017.04.011>
- M. Costes, I. Petropoulos, and P. Cinnella. Development of a third-order accurate vorticity confinement scheme. *Computers & Fluids*, 136:132–151, 2016. <https://doi.org/10.1016/j.compfluid.2016.05.025>

Conference and seminar participations

- I. Petropoulos, M. Costes, and P. Cinnella, Vortical flow calculations using a high-order vorticity confinement method. In *23rd AIAA Computational Fluid Dynamics Conference, AIAA Aviation Forum*, Denver, Colorado, 2017, AIAA Paper 2017–3291. <https://doi.org/10.2514/6.2017-3291>
- I. Petropoulos, M. Costes, and P. Cinnella, Development and analysis of high-order vorticity confinement schemes, *9th International Conference of Computational Fluid Dynamics (ICCFD9)*, Istanbul, Turkey, 2016. <https://hal.archives-ouvertes.fr/hal-01371794v1>
- I. Petropoulos, M. Costes, and P. Cinnella, High-order extensions of the vorticity confinement method, *CEA–SMAI/GAMNI Annual seminar on Numerical Fluid Mechanics – Poster session*, Institut Henri Poincaré, Paris, 2016.

Distinction

- ‘Young CFD Investigator Award – In memory of Prof. Kunio Kuwahara’, *9th International Conference of Computational Fluid Dynamics (ICCFD9)*, Istanbul, Turkey, 2016.

Appendix D

Résumé étendu

Introduction

Au cours des dernières décennies, les méthodes numériques prennent progressivement la place des essais en soufflerie ou en vol dans le processus de conception des dispositifs aérodynamiques. Les études expérimentales restent néanmoins indispensables, car elles représentent généralement mieux l'ensemble de la physique des phénomènes complexes. Leur mise en place est cependant coûteuse, ce qui les rend prohibitives pour de vastes études exploratoires, souvent nécessaires dans les premières phases de conception industrielle. En même temps, les progrès significatifs dans les capacités de calcul scientifique ont donné une bonne base pour le développement des méthodes pour la mécanique des fluides numérique (CFD : *Computational Fluid Dynamics*). Compte tenu de la résolution appropriée dans l'espace et le temps, les méthodes CFD modernes sont capables de représenter avec précision les mécanismes d'écoulement à grande et petite échelle dans un large éventail de cas. Cependant, les ressources nécessaires pour résoudre suffisamment finement l'écoulement à la fois en espace et en temps sont prohibitives pour de nombreuses applications, particulièrement en ce qui concerne la résolution des structures turbulentes fines associées à des écoulements à grand nombre de Reynolds. En même temps, l'amélioration de l'efficacité des dispositifs aérodynamiques actuels repose sur la compréhension et la prédiction de phénomènes de plus en plus fins et souvent intrinsèquement instationnaires à la limite de l'enveloppe de vol, souvent liés à des structures turbulentes (vibrations induites par la turbulence, tremblement transsonique, écoulements décollés, etc.). Celles-ci nécessitent l'utilisation d'une modélisation plus avancée, ainsi qu'une résolution spatiale et temporelle nettement plus fine que les méthodes RANS qui sont plus couramment appliquées dans les calculs industriels. En conséquence, la communauté de recherche travaille constamment sur le développement de méthodes numériques précises et efficaces pour la mécanique des fluides numérique.

Un sujet spécifique où la majorité des méthodes CFD standard échouent est de fournir une représentation précise des écoulements contenant des structures tourbillonnaires. Ce problème concerne à la fois le domaine de la recherche et celui de l'industrie, car les tourbillons sont des caractéristiques d'écoulement d'un intérêt majeur en dynamique des fluides et en aérodynamique. Parmi de nombreuses autres applications d'ingénierie, les structures tourbillonnaires sont importantes dans les cas de décollement en condition de décrochage dynamique, car elles produisent une portance accrue mais aussi induisent des vibrations et augmentent considérablement les charges structurales. D'autres simulations aérodynamiques externes complexes concernent la prédiction précise de la génération et de la propagation des sillages générés par les surfaces portantes. Pour les hélicoptères, l'interaction pale-tourbillon est une source majeure de bruit aérodynamique, tandis que l'interaction du sillage du rotor principal avec l'empennage et le fuselage est un facteur important pour la performance aérodynamique et la stabilité du vol. Les sillages présentent également un intérêt particulier pour l'accélération du trafic des aéroports, la perturbation de l'écoulement suite au décollage ou à l'atterrissage d'un avion de transport imposant de fortes restrictions sur la distance de séparation minimale autorisée entre aéronefs.

Les tourbillons sont générés principalement à partir des couches de cisaillement et sont généralement des structures à longue durée de vie dans les écoulements de fluide. En même temps, leur évolution est caractérisée par une dynamique complexe impliquant le transport, l'étirement, la diffusion par la viscosité du fluide et les effets de baroclinicité. La vorticit  est  galement  troitement li e   la g n ration de tra n e et, plus g n ralement, elle est importante pour l' tude et la caract risation des  coulements de fluides, en particulier en r gime turbulent. Les m canismes de dynamique de la vorticit  sont donc d licats et rendent les tourbillons particuli rement sensibles aux erreurs num riques. De telles erreurs peuvent avoir plusieurs origines (voir Section 2.1) mais sont principalement associ es   l'utilisation de sch mas num riques trop dissipatifs dans la discr tisation des  quations. Bien que la dissipation num rique soit elle-m me n cessaire pour des raisons de stabilit , l'introduction d'un exc s de dissipation num rique conduit   une diffusion artificielle rapide des structures tourbillonnaires dans les simulations num riques.

Pour contrer ce probl me, diverses strat gies num riques ont  t  d velopp es pour le calcul des  coulements tourbillonnaires. Les m thodes lagrangiennes sont th oriquement non dissipatives et semblent donc prometteuses de ce point de vue [49]. Elles ont  t  efficacement appliqu es au calcul des sillages depuis plusieurs d cennies, mais sont limit es par le co t de calcul  lev  n cessaire pour le traitement des  coulements complexes ou en pr sence de parois solides en  coulement visqueux. Cette difficult  peut  tre r duite par l'utilisation des m thodes hybrides lagrangiennes-eul riennes [156], qui semblent prometteuses pour les calculs des  coulements tourbillonnaires mais n cessitent une augmentation importante du co t de calcul. Une autre approche couramment adopt e est l'utilisation des m thodes AMR (Raffinement de Maillage Adaptatif) [25, 32, 158], g n ralement appliqu es sur des maillages non structur s ou structur s cart siens. Celles-ci peuvent donner une repr sentation tr s d taill e des sillages, mais   un co t de calcul significativement augment  en raison du nombre tr s  lev  de cellules dans le maillage raffin  et de l'algorithme de raffinement lui-m me. Une approche plus fondamentale est le d veloppement des sch mas num riques pr servant la vorticit  [72, 148], qui sont cependant tr s rarement prioritaires par rapport aux sch mas de capture de choc pour le calcul des  coulements a ronautiques. Une am lioration importante dans le calcul des  coulements tourbillonnaires a  t  r alis e par le d veloppement des m thodes d'ordre  lev  [67, 114, 219, 220], qui fournissent une approximation plus pr cise des  quations de la dynamique des fluides, mais souvent les erreurs restent importantes pour le calcul des structures tourbillonnaires de nombreuses applications a rodynamiques. En cons quence, des techniques de calibration/adaptation de la dissipation num rique des sch mas d'ordre faible ou  lev  existants dans les r gions d' coulement tourbillonnaire sont tr s souvent utilis es pour r soudre le probl me de la diffusion artificielle des tourbillons [64, 138, 162]. Parmi ces approches, il existe la m thode de confinement de la vorticit  (VC) propos e par J. Steinhoff dans les ann es 90 [189, 199]. Cette m thode a  t  d velopp e   l'origine dans le cadre des  coulements incompressibles, en tant que mod le des structures tourbillonnaires fines   grand nombre de Reynolds. L'id e du VC consiste   ajouter un terme source de dissipation n gative non-lin aire dans les  quations de la dynamique des fluides pour  quilibrer la dissipation excessive du sch ma num rique dans les r gions tourbillonnaires. L'efficacit  de cette m thode a  t  d montr e par son application  tendue dans le domaine de l'a ronautique au cours des deux derni res d cennies [41, 48, 149, 150, 194–198]. Elle a permis le calcul des caract ristiques principales des  coulements tourbillonnaires et l'advection des structures tourbillonnaires minces sur de longues distances et sur des maillages grossiers, donc   un co t de calcul tr s r duit par rapport aux m thodes conventionnelles. L'utilisation du VC reste int ressante   c t  des m thodes d'ordre  lev , mais la m thode originale de J. Steinhoff est au plus pr cise au premier ordre. Cela signifie qu'elle entra ne une d gradation de l'ordre de discr tisation global de la m thode dans les r gions tourbillonnaires lorsqu'elle est appliqu e aux simulations num riques d'ordre  lev .

La pr sente th se constitue une  tude des extensions d'ordre  lev  de la m thode de confinement de la vorticit  – et plus sp cifiquement de la formulation VC2 – pour les  quations compressibles d'Euler et de Navier-Stokes, suite au travail de M. Costes et F. Juillet [45] sur l' quation lin aire de transport. De plus, ce travail vise   analyser les propri t s intrins quement non lin aires de ces

schémas et leurs capacités dans le calcul des écoulements tourbillonnaires aérodynamiques.

Analyse des schémas de confinement scalaire pour l'équation linéaire de transport

La première partie du présent travail concerne les schémas de discrétisation de l'équation linéaire de transport, qui est couramment utilisée comme modèle simple pour l'analyse des schémas numériques. Dans ce cadre, la méthode VC sera simplement appelée "confinement" ou "confinement scalaire". Les corrections de confinement d'ordre élevé développées précédemment pour les schémas de Lax-Wendroff et Warming-Beam ont été basées sur des termes dissipatifs d'ordre élevé [45]. Ces développements ont été revus et une nouvelle formulation des corrections de confinement d'ordre élevé a été développée en utilisant une approche similaire, pour les schémas découplés en espace et en temps (voir Section 3.2.3). Les corrections de confinement ont été développées comme corrections anti-dissipatives non-linéaires du flux numérique du schéma de base. Cette formulation a été implémentée à partir de schémas linéaires standards et non-compacts, d'ordre de précision optimal sur le stencil donné. Néanmoins, l'approche développée devrait également s'appliquer à d'autres types de dissipation numérique, à condition que le même opérateur de dissipation soit utilisé à la fois pour la dissipation du schéma de base et pour la correction de confinement.

Les schémas développés avec des corrections de confinement non-linéaires ont ensuite été analysés du point de vue de leur résolvabilité dans l'espace spectral. Une telle analyse permet de quantifier leur résolvabilité et la décomposition de leur erreur numérique en termes de dispersion et de dissipation. Dans un premier temps, une linéarisation de la moyenne harmonique a permis l'application de la théorie de la stabilité linéaire, mais cette analyse ne semble pas représenter fidèlement le mécanisme non linéaire des corrections de confinement. Pour cette raison, les propriétés spectrales des schémas ont été analysées en utilisant une approche numérique quasi-linéaire [160]. Après avoir été validée par rapport aux résultats analytiques pour les schémas linéaires, cette méthode a été appliquée à l'analyse des schémas avec des corrections de confinement allant jusqu'au neuvième ordre de précision.

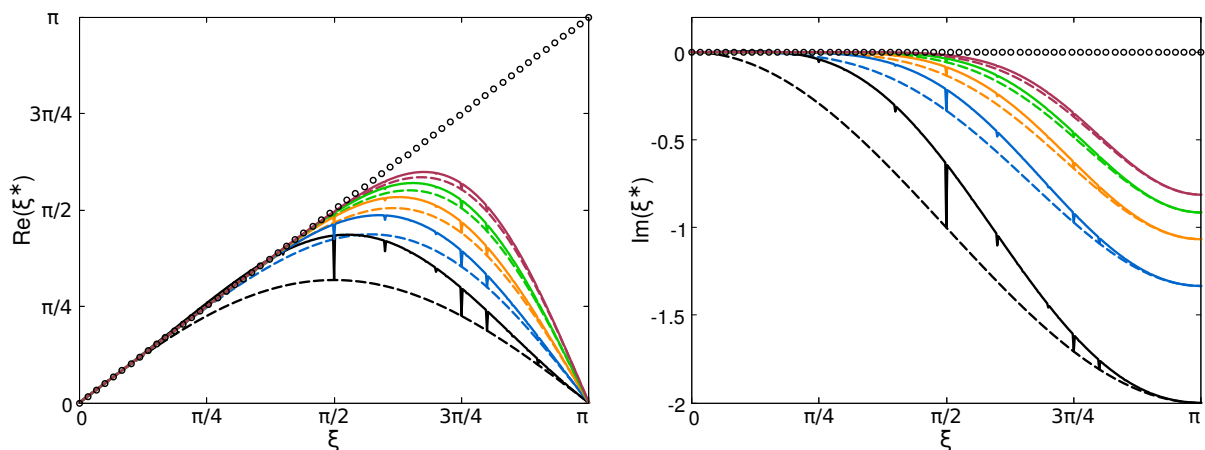


Figure D.1: Approximation de phase et dissipation des schémas FE-MUSCL avec et sans confinement. Résolution spectrale: \circ , 1er ordre: —, 3ème ordre: —, 5ème ordre: —, 7ème ordre: —, 9ème ordre: —. Version de base linéaire des schémas (ligne pointillée) et avec la correction de confinement (ligne continue), $\varepsilon = 1.14 k_p$.

Cette analyse a montré que les schémas avec correction de confinement ont des propriétés dispersives et dissipatives améliorées par rapport à leurs versions linéaires (voir Fig. D.1). L'amélioration en terme de limites de résolvabilité est particulièrement favorable au troisième et au cinquième ordre de précision (voir Section 3.4.4), mais elle est également maintenue aux ordres encore plus élevés.

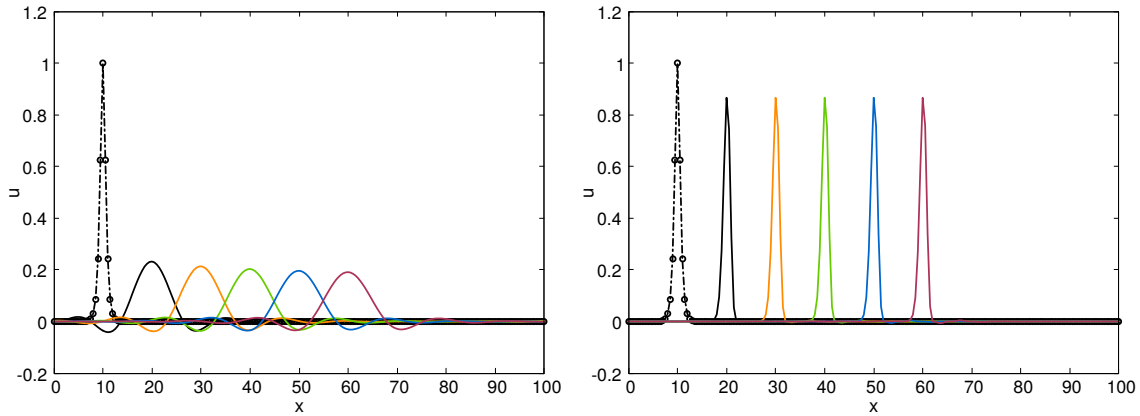


Figure D.2: Perturbation de sécante hyperbolique à des instants différents au cours d’une advection à très longue distance. Schéma FE-MUSCL7 (gauche) et FE-MUSCL7-C avec $\varepsilon = 1.14 k_p$ (droite) en $CFL = 0.02$. Solution exacte: $-\bullet-$, $1.2 \cdot 10^7 \Delta x$: $—$, $2.4 \cdot 10^7 \Delta x$: $—$, $3.6 \cdot 10^7 \Delta x$: $—$, $4.8 \cdot 10^7 \Delta x$: $—$, $6 \cdot 10^7 \Delta x$: $—$. Les courbes successives sont déplacées par $+10$ le long de l’axe x pour visibilité.

Plus important encore, cette analyse a démontré l’intérêt de construire la correction de confinement sur un opérateur de dissipation d’ordre élevé et donc que l’effet positif du confinement n’est pas limité à une discrétisation d’ordre faible. Dans un sens, la correction de confinement hérite de la forme de la fonction de transfert de l’opérateur de dissipation, et a donc une contribution minimale dans la gamme des nombres d’onde bien résolus. Une autre propriété importante est que les corrections anti-dissipatives ne modifient pas l’amortissement des oscillations maille-à-maille. De plus, il a été montré que les schémas avec corrections de confinement sont légèrement instables dans la plage des faibles nombres d’onde. Cette instabilité apparaît au-delà d’un seuil spécifique du paramètre de confinement, lorsqu’il devient supérieur au coefficient de la dissipation numérique de base. Pour les schémas de Lax-Wendroff cependant, cette instabilité est naturellement équilibrée par la partie de la dissipation numérique couplée avec la discrétisation temporelle. En ce qui concerne les schémas standards découplés, cette instabilité est plus petite pour un ordre de précision plus élevé. Aux ordres supérieurs, elle peut donc être observée seulement si une advection de très longue distance est considérée. Enfin, il a été montré que les schémas découplés en espace et en temps peuvent être utilisés avec les méthodes classiques de Runge-Kutta pour l’intégration temporelle, leur région de stabilité montrant une très faible sensibilité au choix du paramètre de confinement.

Les observations ci-dessus ont été confirmées par l’application des schémas aux problèmes d’advection scalaire sur de longues distances. Le premier cas est la propagation d’une perturbation impulsive en forme de sécante hyperbolique, qui correspond à la forme de la solution asymptotique des schémas avec corrections de confinement. La condition initiale correspond à une perturbation à haute fréquence et est donc rapidement diffusée par la dissipation du schéma de base, malgré l’ordre de précision élevé du schéma numérique. Celui-ci conduit à une solution lissée avec un pic réduit qui est ensuite propagé avec moins d’effets de dissipation. D’autre part, la correction de confinement anti-dissipative équilibre efficacement l’excès de dissipation au voisinage de la perturbation, permettant sa propagation avec pratiquement aucun effet de dissipation et avec une vitesse d’advection exacte sur une très longue distance (voir Fig. D.2). Dans le cas des schémas de Lax-Wendroff, la correction de confinement est couplée en espace et en temps, et permet donc de conserver des signaux sur de longues distances, même à grand nombre de CFL. D’un autre côté, les schémas découplés standards sont plus sensibles à la dissipation associée à la discrétisation temporelle, en particulier dans le cas d’une advection à très longue distance. Des résultats similaires ont été obtenus dans la propagation numérique de paquets d’ondes. Dans tous les cas, le confinement améliore la conservation de l’amplitude de la perturbation sur de longues distances, même sur des ordres de précision élevés (voir Fig. D.3). En même temps, les résultats présentés montrent qu’ils n’ont pas d’effet négatif sur la vitesse de groupe numérique, même au-delà des distances d’advection usuelles.

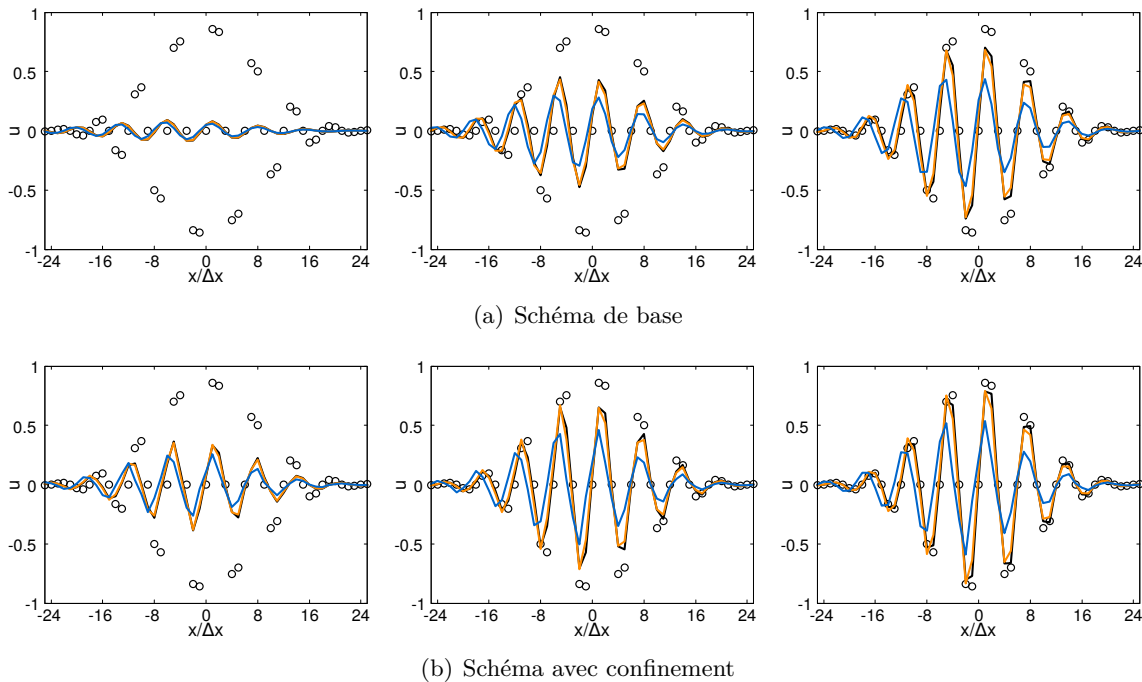


Figure D.3: Résultats pour le Packet II après l'advection à une distance $200 \Delta x$ pour des valeurs différentes du nombre de CFL. Solution exacte: \circ , $\sigma = 0.2$: —, $\sigma = 0.5$: —, $\sigma = 0.8$: —. De gauche à droite, schémas FE-MUSCL de 5ème, 7ème et 9ème ordre de précision ($\varepsilon = 1.14 k_p$).

Ces applications ont montré que les corrections de confinement dans le cas des schémas Lax-Wendroff couplés en espace et en temps sont supérieures à bien des aspects. Elles permettent des calculs précis à longue distance à un nombre de CFL plus grand et ont une dissipation numérique intrinsèquement bien adaptée qui équilibre la légère instabilité des corrections de confinement. D'autre part, la formulation de confinement pour les schémas découplés est plus limitée en raison de la faible instabilité aux faibles nombres d'ondes et de l'accumulation de la dissipation temporelle sur de très longues distances. Cette formulation reste néanmoins intéressante, car les schémas découplés sont plus souvent appliqués dans les solveurs de calcul en raison de la facilité de mise en œuvre et offrent une liberté en termes de choix de schémas de discrétisation en espace ou en temps. D'autant plus que, pour un paramètre de confinement inférieur ou égal au coefficient de la dissipation numérique de base, ces schémas ne présentent aucune instabilité tout en étant toujours moins dissipatifs que le schéma de base. De plus, dans le cas de schémas linéaires découplés, il a été montré que les corrections de confinement peuvent être intégrées à un très faible coût de calcul.

Développement des schémas de confinement de vorticité d'ordre élevé

Sur la base de l'analyse précédente, la partie suivante du travail est consacrée au développement des corrections de confinement de vorticité d'ordre élevé pour les équations d'Euler et Navier-Stokes compressibles. Les développements de ce travail sont basés sur la formulation conservative VC2 de J. Steinhoff [192, 193, 195]. Plusieurs interprétations de la méthode VC existent dans le cadre des écoulements compressibles (voir Section 2.2.7). L'approche adoptée ici suit le travail de M. Costes [41], où le terme source VC2 est interprété comme une correction purement numérique. Cette interprétation a les deux implications suivantes. Premièrement, la contribution du terme de confinement de vorticité n'est incluse que dans l'équation de quantité de mouvement. Deuxièmement, elle doit être consistante avec les équations originales de Navier-Stokes. En d'autres termes, la correction VC doit tendre vers zéro lorsque le maillage est suffisamment raffiné, de manière similaire

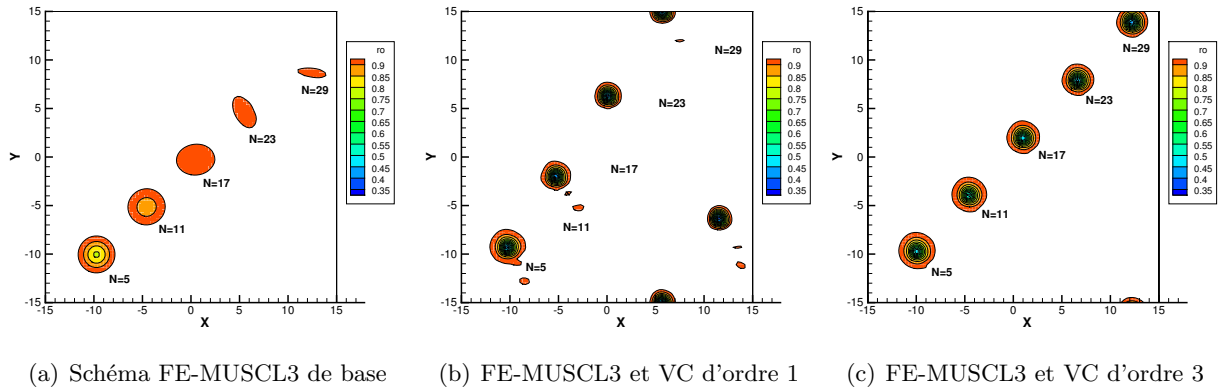


Figure D.4: Instantanés de l'écoulement et contours de densité pendant l'advection diagonale d'un tourbillon isentropique. Solution calculée en utilisant un schéma FE-MUSCL d'ordre trois avec et sans VC dans un maillage 100^2 . Le nombre approximatif des passages dans le domaine de calcul est indiqué à côté du contour correspondant.

aux termes de dissipation artificielle de base. Ceci est obtenu en utilisant des différences non-divisées dans la discrétisation numérique de la correction VC.

La formulation originale VC2 est revue et analysée en détail, en particulier en étudiant son analogie avec les schémas de confinement scalaire de la partie précédente du travail. Des extensions d'ordre élevé de la méthode VC2 sont ensuite dérivées analytiquement, en introduisant des dérivées d'ordre élevé dans le cadre continu. Cette approche est similaire à la construction des termes de dissipation numérique d'ordre élevé de base, et est basée sur le Laplacien du terme original de VC de premier ordre. En conséquence, les extensions d'ordre élevé développées restent invariantes par rotation et indépendantes du schéma de base. De plus, il est montré que le terme source VC2 du premier ordre et ses extensions d'ordre élevé sont analytiquement équivalents aux corrections anti-dissipatives non-linéaires du flux numérique dans les régions d'écoulement tourbillonnaire.

Dans une étape suivante, la discrétisation numérique des schémas développés est discutée en détail, en particulier en ce qui concerne le calcul des dérivées d'ordre élevé. Sur les maillages cartésiens, celles-ci peuvent être calculées en utilisant de longs stencils dans une formulation par différences finies. Sur les maillages plus généraux, les dérivées d'ordre élevé peuvent être calculées récursivement dans une formulation volumes finis. Cette approche est applicable à la fois aux maillages structurés et non-structurés. La mise en œuvre des conditions aux limites et les différents schémas de discrétisation de l'opérateur de Laplace sont également discutés. Enfin, pour éviter l'introduction d'oscillations parasites dans les régions d'écoulement irrotationnelles dues à la correction anti-dissipative, le terme VC est désactivé de manière appropriée à l'extérieur des tourbillons.

Les schémas développés sont ensuite validés par application de la méthode sur une série de cas tests académiques. Tout d'abord, l'ordre de précision des schémas avec VC a été évalué dans le cas d'un tourbillon isentropique statique. Cette étude démontre que la méthode originale du premier ordre dégrade l'ordre de précision dans les régions tourbillonnaires lorsqu'elle est appliquée à des simulations d'ordre élevé. D'autre part, les extensions VC d'ordre élevé conservent une précision élevée et sont donc cohérentes avec les discrétisations de flux d'ordre élevé. Les schémas développés sont ensuite appliqués à des advections de tourbillon sur de longues distances. Ces calculs ont démontré que les schémas avec VC fournissent des résultats considérablement plus proches de la solution exacte que le schéma de base, à la fois au troisième et au cinquième ordre de précision (voir Fig. D.5). Ils sont donc capables de propager des tourbillons sur de très longues distances avec de faibles effets de dissipation, même lorsque la direction de propagation n'est pas alignée avec le maillage de calcul (voir Fig. D.4). En outre, il a été démontré qu'il existe un large éventail de paires de paramètres de confinement produisant une conservation de tourbillon similaire, mais des valeurs trop grandes de ces paramètres tendent à introduire des erreurs dispersives supplémentaires

dans le calcul. En pratique cependant, les erreurs de dispersion restent faibles pour des valeurs des paramètres de confinement de l'ordre de grandeur du coefficient de dissipation artificielle de base. Il est ensuite montré que le coût de calcul de la méthode est raisonnable par rapport aux schémas FE-MUSCL de base utilisés dans cette étude, en particulier pour des problèmes à deux dimensions d'espace. Cependant, une analyse des coûts dépendra toujours de la méthode numérique de base, car le VC est une correction ajoutée au schéma de base et non une méthode numérique complète.

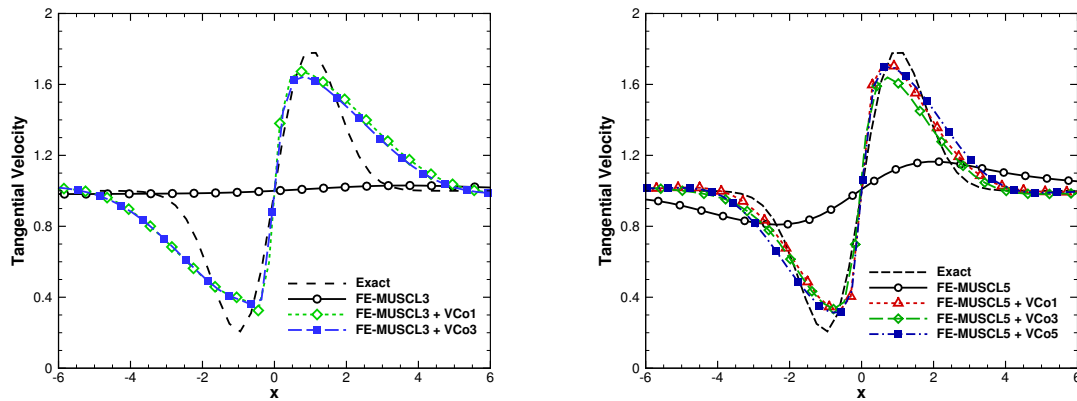


Figure D.5: Comparaison des profils de vitesse tangentielle avec et sans VC. Profils après 30 passages par le domaine de calcul pour le schéma FE-MUSCL3 (gauche) et après 300 passages par le domaine de calcul pour le schéma FE-MUSCL5 (droite), maillage cartésien 100^2 .

Application à la simulation des écoulements tourbillonnaires complexes

La dernière partie de la thèse étudie plus en détail la robustesse et la résolubilité des schémas avec VC d'ordre élevé, par l'application de ces schémas à une série d'écoulements tourbillonnaires complexes. L'objectif de ces applications est d'évaluer la robustesse des corrections VC d'ordre élevé et leur consistance, dans une série de cas géométriquement simples mais physiquement complexes. Dans ces études, un effort délibéré a été fait pour évaluer la sensibilité des résultats aux valeurs des paramètres de confinement. Le premier cas est l'écoulement visqueux du tourbillon de Taylor-Green (TGV), qui implique une dynamique tourbillonnaire multi-échelle et est une référence bien documentée pour l'évaluation des méthodes numériques d'ordre élevé. Une étude plus détaillée de la dissipation des schémas est ensuite effectuée dans le cas de la turbulence homogène isotrope en décroissance (THI). Les calculs d'écoulements turbulents avancés dans le domaine de la recherche sont généralement effectués avec des méthodes de base qui présentent déjà une haute précision spectrale. L'évaluation de cette partie est cependant importante pour s'assurer que les corrections VC d'ordre élevé peuvent fournir des résultats cohérents dans les applications d'ingénierie de haute fidélité impliquant des écoulements turbulents (sillages, injection de turbulence, décollements, etc.).

Les résultats sur le cas du TGV ont montré que les corrections VC d'ordre élevé développées donnent des résultats cohérents avec la dynamique des écoulements tourbillonnaires complexes. Pour des valeurs raisonnables du paramètre de confinement ε , proches du coefficient de dissipation numérique de base, le schéma avec VC d'ordre élevé s'est avéré globalement plus précis que le schéma de base sans VC (voir Fig. D.6). C'est particulièrement le cas lors de la phase d'étirement tourbillonnaire de l'écoulement, où des structures d'écoulement de taille plus importante sont impliquées. Les schémas de base FE-MUSCL dissipatifs utilisés dans cette étude se sont également révélés robustes sans la dissipation artificielle interne de la correction VC. Si elle n'est pas mise à zéro, cette dissipation a une influence modérée sur les résultats calculés, voire négligeable lors du traitement des structures à grande échelle. De plus, même sur un écoulement complexe, l'efficacité

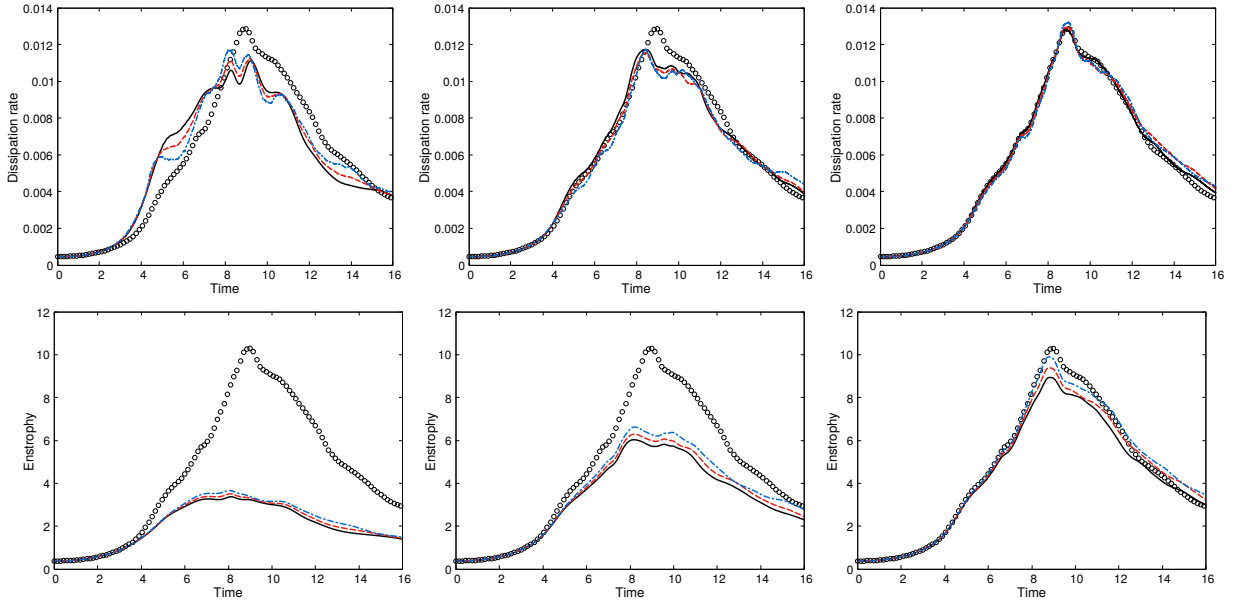


Figure D.6: Influence du VC dans la prédiction de l'évolution du taux de dissipation d'énergie cinétique $-\frac{dK}{dt}$ et l'évolution d'ensrophie pour $\mu/\varepsilon = 0.4$ et différentes valeurs de ε . Solution spectrale de référence – 512^3 : \circ , schéma de base: —, $\varepsilon = 0.02$: - - -, $\varepsilon = 0.04$: - · - · -. De gauche à droite, maillage 64^3 , 128^3 et 256^3 . Schéma FE-MUSCL5 et confinement de vorticit  d'ordre cinq.

de la correction VC s'est av r e avoir une sensibilit  mod r e au sch ma de calcul du gradient de vitesse. L'interpr tation des r sultats   la fin de la phase de d croissance de la turbulence pour le cas du TGV n'est cependant pas  vidente, car ceux-ci d pendent fortement de l'histoire de l' coulement calcul .

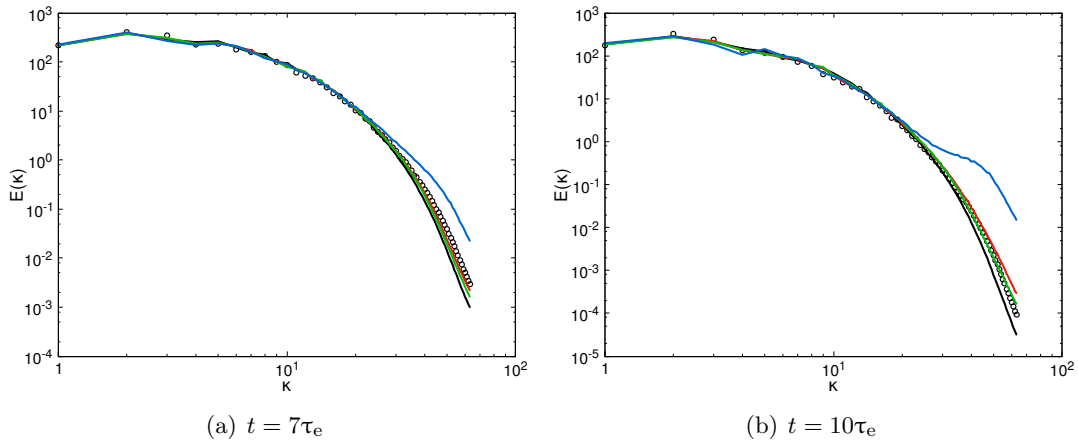


Figure D.7: Comparaison du spectre d' nergie cin tique turbulente   diff rents instants pendant la d croissance de la THI. R f rence FE-MUSCL9: \circ , sch ma FE-MUSCL5 de base: —, $(\mu/\varepsilon, \varepsilon) = (0.0, 1.2k_5)$: —, $(\mu/\varepsilon, \varepsilon) = (0.0, 2.4k_5)$: —. Sch mas FE-MUSCL avec et sans VC pour un nombre de Mach turbulent initial de $M_{t0} = 0.5$.

Une  tude plus approfondie du traitement des structures plus petites a ainsi  t  r alis e pour la d croissance de la THI en compressible. Ce cas a  t  calcul    trois conditions initiales de nombre de Mach turbulent diff rentes, allant de conditions quasi-incompressibles   fortement compressibles, et en utilisant diff rents types de dissipation num rique pour le flux num rique de base. Dans ces  tudes, des valeurs  lev es du param tre de confinement ε r duisent excessivement la dissipation num rique et conduisent   une accumulation d' nergie aux plus petites  chelles (voir Fig. D.7). Cet

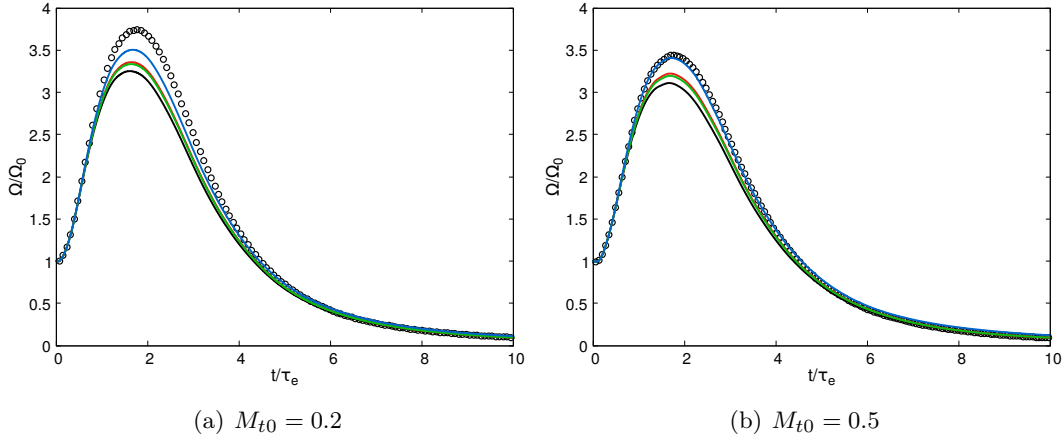


Figure D.8: Comparaison de l'évolution temporelle de l'enstrophie calculée avec des schémas FE-MUSCL avec et sans VC. Référence FE-MUSCL9: \circ , schéma FE-MUSCL5 de base: — , $(\mu/\varepsilon, \varepsilon) = (0.0, 1.2k_5)$: — , $(\mu/\varepsilon, \varepsilon) = (0.2, 1.2k_5)$: — , $(\mu/\varepsilon, \varepsilon) = (0.0, 2.4k_5)$: — .

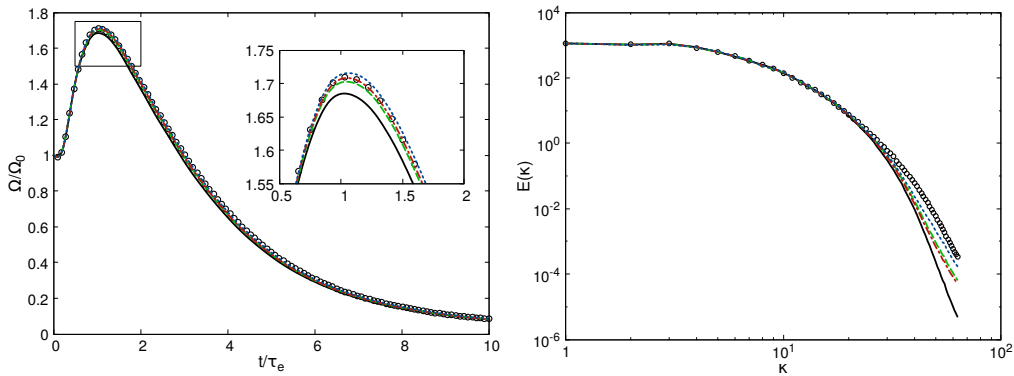


Figure D.9: Comparaison de l'évolution temporelle de l'enstrophie (gauche) et spectre d'énergie cinétique turbulente à $t = 10\tau_e$ (droite) calculé avec des schémas FE-MUSCL avec et sans VC à $M_{t0} = 1.0$. Référence FE-MUSCL9: \circ , schéma FE-MUSCL5 de base: — , $(\mu/\varepsilon, \varepsilon) = (0.0, 1.2k_5)$: $\text{-}\cdot\text{-}\cdot\text{-}$, $(\mu/\varepsilon, \varepsilon) = (0.2, 1.2k_5)$: $\text{-}\cdot\text{-}\cdot\text{-}$, $(\mu/\varepsilon, \varepsilon) = (0.4, 2.4k_5)$: \cdots .

effet peut être atténué par l'augmentation de la dissipation interne de la correction VC d'ordre élevé. Il a cependant été démontré que des résultats cohérents peuvent être obtenus par un choix plus prudent du paramètre de confinement ε , plus proche du coefficient de dissipation numérique de base. Pour de telles valeurs, il a été démontré que les schémas avec VC présentaient des propriétés de résolubilité améliorées par rapport aux schémas de base du 5ème ordre considérés dans cette étude. Spécifiquement, ils permettent d'étendre le spectre d'énergie cinétique turbulente résolu et d'améliorer la résolution du pic d'enstrophie pendant la phase d'étirement tourbillonnaire (voir Fig. D.7-D.8). Bien que non bénéfique, l'effet du VC s'est révélé faible sur les statistiques d'ordre élevé de l'écoulement tourbillonnaire, alors qu'il n'a pas d'effet notable sur l'évolution des quantités thermodynamiques. Enfin, la méthode VC d'ordre élevé a été appliquée à un cas de décroissance de THI à forte compressibilité, à côté d'un schéma de base avec une dissipation hybride d'ordre faible/élevé, similaire aux schémas couramment utilisés dans les problèmes aérodynamiques. Les résultats de ce cas n'ont montré aucun effet négatif de l'anti-dissipation d'ordre élevé du VC sur les propriétés de capture de choc de ce schéma de base (voir Fig. D.9).

Les corrections VC d'ordre élevé se sont globalement révélées consistantes avec la dynamique des écoulements tourbillonnaires complexes sans exiger de traitement spécial pour s'adapter aux mécanismes d'interaction des tourbillons caractéristiques des écoulements turbulents. En outre, ils améliorent de façon cohérente la résolubilité des schémas de base FE-MUSCL pour des valeurs

raisonnables du paramètre de confinement ε . Enfin, la dépendance de la solution vis-à-vis de la dissipation interne du VC s'est révélée modérée pour des valeurs raisonnables du rapport μ/ε , et plus importante dans le traitement des petites échelles.

Conclusions

La présente thèse a consisté en une extension de la méthode de confinement de la vorticit  de J. Steinhoff aux discr tisations d'ordre  lev . Ce d veloppement vise   r duire le probl me de la diffusion artificielle des tourbillons dans les simulations num riques d'ordre  lev  par l'introduction d'un terme anti-dissipatif non-lin aire dans la discr tisation, afin d' quilibrer la dissipation num rique du sch ma de base dans les r gions d' coulement tourbillonnaire. Plusieurs analyses th oriques et num riques de ces corrections ont  galement  t  effectu es pour  tudier leurs propri t s non lin aires et leurs limites.

La premi re partie de l' tude a  t  consacr e   l'analyse des sch mas avec des corrections de confinement scalaire pour l' quation lin aire de transport. Une nouvelle famille de corrections de confinement d'ordre  lev  a  t  d velopp e pour des discr tisations d coupl es en espace et en temps, et a  t  compar e   une approche coupl e espace-temps d j  existante. Une analyse spectrale num rique quasi-lin aire a montr  que les corrections de confinement affectent   la fois les propri t s dispersives et dissipatives du sch ma, bien que ces corrections soient   l'origine bas es sur un op rateur purement dissipatif. Cet effet s'est av r  b n fique   la fois en termes de dispersion et de dissipation,   tous les ordres de pr cision. En outre, il a  t  montr  que l'anti-dissipation du confinement est transf r e vers des fr quences plus  lev es   des ordres de pr cision plus  lev s, ce qui a un effet r duit sur la gamme des nombres d'onde d j  bien r solus par le sch ma de base lin aire. D'autre part, cette anti-dissipation diminue progressivement aux hautes fr quences et ne modifie pas l'amortissement des oscillations maille- -maille. Les r sultats des  tudes d'advection   longue distance ont montr  que les corrections de confinement peuvent  quilibrer l'exc s de dissipation et sont capables de propager des signaux impulsifs sur de tr s longues distances, sans effet n gatif sur la vitesse num rique de groupe.

Dans une  tape suivante, des extensions d'ordre  lev  de la m thode de confinement de vorticit  (VC) ont  t  d velopp es pour les  quations de Navier-Stokes. Ce sont des termes anti-dissipatifs non lin aires d'ordre  lev , interpr t s comme des corrections num riques ajout es   l' quation de conservation de la quantit  de mouvement pour  quilibrer l'exc s de dissipation num rique dans les r gions d' coulement tourbillonnaire. Ils ont  t  d riv s dans le cadre continu,   partir du laplacien du terme VC2 de premier ordre de J. Steinhoff. De plus, il a  t  d montr  que le terme VC2 original et ses extensions d'ordre  lev  sont  quivalents aux corrections de flux anti-dissipatives non-lin aires explicitement bas es sur la vorticit . Des  tudes num riques ont montr  que les extensions VC d'ordre  lev  d velopp es sont capables de pr server l'ordre de pr cision nominal des sch mas de base d'ordre  lev . Des calculs ult rieurs ont d montr  que les sch mas d velopp s avec VC peuvent permettre l'advection des tourbillons sur de tr s longues distances avec de faibles effets de dissipation. Ils ont ainsi donn  des r sultats consid rablement plus proches de la solution exacte que la version lin aire du sch ma, au troisi me et au cinqui me ordre de pr cision, tout en  tant plus pr cis en termes de pr diction de trajectoire du tourbillon que la m thode VC originale.

Des  tudes sur les cas plus complexes de TGV et THI compressibles ont montr  que les corrections VC peuvent s'adapter   des dynamiques complexes sans avoir besoin d'un traitement sp cial. Les sch mas avec VC ont fourni des r sultats coh rents avec des effets r duits de dissipation num rique par rapport   la version lin aire de base du sch ma, en particulier pendant les phases d' tirement tourbillonnaire o  des structures   grande  chelle sont impliqu es. L'am lioration s'est av r e particuli rement b n fique dans le calcul de l'enstrophie, m me pour des maillages plus fins. Pour les valeurs du param tre de confinement ε proches de la valeur du coefficient de dissipation artificielle sous-jacent, il a  t  d montr  que les sch mas avec VC produisent des r sultats coh rents et plus pr cis que ceux des sch mas d'ordre cinq de base utilis s dans cette  tude. Plus sp cifiquement, il a  t  montr  que le VC peut  tendre le spectre d' nergie r solu et am liorer le calcul du

pic d'ensrophie pendant la phase d'étirement tourbillonnaire. L'effet du VC s'est avéré faible sur les statistiques d'ordre élevé de la décroissance de la THI, mais pas plus proches de la solution de référence que le schéma linéaire de base. Enfin, il a été constaté que le VC avait un effet mineur sur les quantités thermodynamiques.

La méthode de confinement de la vorticité d'ordre élevé a été montrée globalement capable d'équilibrer l'excès de dissipation du schéma de base dans les régions tourbillonnaires et d'améliorer le calcul de la vorticité dans les simulations numériques pour les cas d'advection simples et pour des cas impliquant une dynamique complexe. En raison de sa formulation non-linéaire, il a également été démontré que la méthode a un effet supplémentaire sur les propriétés dispersives du schéma numérique, mais cet effet s'est révélé faible pour les cas étudiés dans ce travail, et même bénéfique pour des valeurs raisonnables du paramètre de confinement. En conclusion, les corrections VC d'ordre élevé représentent une approche globale intéressante pour les simulations d'ordre élevé des écoulements tourbillonnaires, combinant la capacité de préservation de vorticité de la méthode VC originale du 1er ordre et préservant l'ordre de précision de la méthode de base. La méthode est particulièrement appropriée pour le calcul des sillages et des cas dominés par la convection des structures tourbillonnaires, et s'est avérée bénéfique même dans les simulations d'écoulements turbulents.

Bibliography

- [1] R. Abgrall. Residual distribution schemes: current status and future trends. *Computers & Fluids*, 35(7):641–669, 2006.
- [2] R. Abgrall. A residual distribution method using discontinuous elements for the computation of possibly non smooth flows. *Adv. Appl. Math. Mech*, 2(1):32–44, 2010.
- [3] R. Abgrall. A review of residual distribution schemes for hyperbolic and parabolic problems: the July 2010 state of the art. *Communications in Computational Physics*, 11(4):1043–1080, 2012.
- [4] R. Abgrall, A. Larat, and M. Ricchiuto. Construction of very high order residual distribution schemes for steady inviscid flow problems on hybrid unstructured meshes. *Journal of Computational Physics*, 230(11):4103–4136, 2011.
- [5] R. Abgrall, Q. Viville, H. Beaugendre, and C. Dobrzynski. Construction of a p-adaptive continuous residual distribution scheme. *Journal of Scientific Computing*, pages 1–37, 2017.
- [6] P. Anusonti-Inthra and M. Floros. Coupled CFD and particle vortex transport method: Wing performance and wake validations. In *38th AIAA Fluid Dynamics Conference and Exhibit*, 2008. AIAA Paper 2008–4177.
- [7] K. Asthana and A. Jameson. High-order flux reconstruction schemes with minimal dispersion and dissipation. *Journal of Scientific Computing*, 62(3):913–944, 2015.
- [8] D. S. Balsara, S. Garain, and C.-W. Shu. An efficient class of WENO schemes with adaptive order. *Journal of Computational Physics*, 326:780–804, 2016.
- [9] D. S. Balsara and C.-W. Shu. Monotonicity preserving weighted essentially non-oscillatory schemes with increasingly high order of accuracy. *Journal of Computational Physics*, 160(2):405–452, 2000.
- [10] T. J. Barth. Recent developments in high order k-exact reconstruction on unstructured meshes. In *31st AIAA Aerospace Sciences Meeting & Exhibit, AIAA Paper 93-0668*, 1993.
- [11] T. J. Barth and P. O. Frederickson. Higher order solution of the Euler equations on unstructured grids using quadratic reconstruction. In *28th AIAA Aerospace Sciences Meeting, AIAA Paper 90-0013*, 1990.
- [12] A. Bauknecht, B. Ewers, C. Wolf, F. Leopold, J. Yin, and M. Raffel. Three-dimensional reconstruction of helicopter blade–tip vortices using a multi-camera BOS system. *Experiments in Fluids*, 56(1):1866, 2015.
- [13] J. Benek, J. Steger, and F. Dougherty. A flexible grid embedding technique with application to the Euler equations. In *Fluid Dynamics and Co-located Conferences*, pages –. American Institute of Aeronautics and Astronautics, July 1983.

-
- [14] C. Benoit and G. Jeanfaivre. Three-dimensional inviscid isolated rotor calculations using chimera and automatic cartesian partitioning methods. *Journal of the American Helicopter Society*, 48(2):128–138, 2003.
- [15] C. Benoit, S. Péron, and S. Landier. Cassiopee: a CFD pre-and post-processing tool. *Aerospace Science and Technology*, 45:272–283, 2015.
URL: <http://elsa.onera.fr/Cassiopee/>.
- [16] M. J. Berger and P. Colella. Local adaptive mesh refinement for shock hydrodynamics. *Journal of Computational Physics*, 82(1):64 – 84, 1989.
- [17] M. J. Berger and A. Jameson. Automatic adaptive grid refinement for the euler equations. *AIAA Journal*, 23(4):561–568, Apr. 1985.
- [18] M. J. Berger and J. Olinger. Adaptive mesh refinement for hyperbolic partial differential equations. *Journal of Computational Physics*, 53(3):484 – 512, 1984.
- [19] M. Biava and L. Vigevano. Assessment of the vorticity confinement technique applied to rotorcraft flows. In *21st AIAA Applied Aerodynamics Conference, AIAA Paper 2003-3524*. American Institute of Aeronautics and Astronautics, 2003.
- [20] C. Bogey and C. Bailly. A family of low dispersive and low dissipative explicit schemes for flow and noise computations. *Journal of Computational Physics*, 194(1):194–214, 2004.
- [21] C. Bogey and C. Bailly. Turbulence and energy budget in a self-preserving round jet: direct evaluation using large eddy simulation. *Journal of Fluid Mechanics*, 627:129–160, 2009.
- [22] C. Bogey, N. De Cacqueray, and C. Bailly. A shock-capturing methodology based on adaptive spatial filtering for high-order non-linear computations. *Journal of Computational Physics*, 228(5):1447–1465, 2009.
- [23] R. Borges, M. Carmona, B. Costa, and W. S. Don. An improved weighted essentially non-oscillatory scheme for hyperbolic conservation laws. *Journal of Computational Physics*, 227(6):3191–3211, 2008.
- [24] J. R. Bull and A. Jameson. Simulation of the Taylor–Green vortex using high-order flux reconstruction schemes. *AIAA Journal*, 53(9):2750–2761, 2015.
- [25] P. G. Buning and T. H. Pulliam. Cartesian off-body grid adaption for viscous time-accurate flow simulations. In *20th AIAA Computational Fluid Dynamics Conference*, 2011. AIAA Paper 2011-3693.
- [26] P. G. Buning and T. H. Pulliam. Near-body grid adaption for overset grids. In *46th AIAA Fluid Dynamics Conference*, 2016. AIAA Paper 2016-3326.
- [27] N. Butsumtorn and A. Jameson. Time spectral method for rotorcraft flow. In *46th AIAA Aerospace Sciences Meeting and Exhibit, AIAA Paper 2008-0403*. American Institute of Aeronautics and Astronautics, 2008.
- [28] D. Caraeni and L. Fuchs. Compact third-order multidimensional upwind discretization for steady and unsteady flow simulations. *Computers & fluids*, 34(4):419–441, 2005.
- [29] D. Caraeni and D. C. Hill. Efficient 3rd-order finite-volume discretization using iterative quadratic data reconstruction on unstructured grids. In *47th AIAA Aerospace Sciences Meeting including The New Horizons Forum and Aerospace Exposition, AIAA Paper 2009-1332*, 2009.

- [30] C. Carton de Wiart, K. Hillewaert, M. Duponcheel, and G. Winckelmans. Assessment of a discontinuous Galerkin method for the simulation of vortical flows at high Reynolds number. *International Journal for Numerical Methods in Fluids*, 74(7):469–493, 2014.
- [31] N. M. Chaderjian. Advances in rotor performance and turbulent wake simulation using DES and adaptive mesh refinement. In *7th International Conference on Computational Fluid Dynamics, Big Island, Hawaii*, 2012.
- [32] N. M. Chaderjian. Navier–Stokes simulation of UH–60A rotor/wake interaction using adaptive mesh refinement. In *Proceedings of the 73rd Annual Forum of the American Helicopter Society, Forth Worth, TX*, 2017.
- [33] J.-B. Chapelier, M. De La Llave Plata, F. Renac, and E. Lamballais. Evaluation of a high-order discontinuous Galerkin method for the DNS of turbulent flows. *Computers & Fluids*, 95:210–226, 2014.
- [34] P. Chatelain, A. Curioni, M. Bergdorf, D. Rossinelli, W. Andreoni, and P. Koumoutsakos. Billion vortex particle direct numerical simulations of aircraft wakes. *Computer Methods in Applied Mechanics and Engineering*, 197(13):1296–1304, 2008.
- [35] A. J. Chorin. Numerical study of slightly viscous flow. *Journal of Fluid Mechanics*, 57(4):785–796, 1973.
- [36] P. Cinnella and C. Content. High-order implicit residual smoothing time scheme for direct and large eddy simulations of compressible flows. *Journal of Computational Physics*, 326:1 – 29, 2016.
- [37] B. Cockburn, G. E. Karniadakis, and C.-W. Shu. The development of discontinuous Galerkin methods. In *Discontinuous Galerkin Methods*, pages 3–50. Springer, 2000.
- [38] P. Colella and P. R. Woodward. The piecewise parabolic method (PPM) for gas-dynamical simulations. *Journal of Computational Physics*, 54(1):174–201, 1984.
- [39] C. Corre, F. Falissard, and A. Lerat. High-order residual-based compact schemes for compressible inviscid flows. *Computers & Fluids*, 36(10):1567–1582, 2007.
- [40] C. Corre and A. Lerat. High-order residual-based compact schemes for advection–diffusion problems. *Computers & Fluids*, 37(5):505–519, 2008.
- [41] M. Costes. *Étude de méthodes de confinement pour le calcul numérique des écoulements tourbillonnaires en compressible*. PhD thesis, Université d’Orleans, 2006.
- [42] M. Costes. Analysis of the second vorticity confinement scheme. *Aerospace Science and Technology*, 12(3):203 – 213, 2008.
- [43] M. Costes. Development of a 3rd-order vorticity confinement scheme for rotor wakes simulations. In *38th European Rotorcraft Forum*, Amsterdam, The Netherlands, September 2012.
- [44] M. Costes. Stability analysis of the VC2 confinement scheme for the linear transport equation. *Computers & Fluids*, 86(0):537 – 557, 2013.
- [45] M. Costes and F. Juillet. Analysis and higher-order extension of the VC2 confinement scheme. *Computers & Fluids*, 56(0):102 – 117, 2012.
- [46] M. Costes and G. Kowani. An automatic anti-diffusion method for vortical flows based on vorticity confinement. *Aerospace Science and Technology*, 7(1):11 – 21, 2003.
- [47] M. Costes, I. Petropoulos, and P. Cinnella. Development of a third-order accurate vorticity confinement scheme. *Computers & Fluids*, 136:132–151, 2016.

- [48] M. Costes, T. Renaud, B. Rodriguez, and G. Reboul. Application of vorticity confinement to rotor wake simulations. *Int. J. of Engineering Systems Modelling and Simulation*, 2012 Vol.4, No.1/2, pp.102 - 112, 4(1/2):102–112, 2012.
- [49] G.-H. Cottet and P. D. Koumoutsakos. *Vortex methods: theory and practice*. Cambridge University Press, 2000.
- [50] G. Cunha and S. Redonnet. On the effective accuracy of spectral-like optimized finite-difference schemes for computational aeroacoustics. *Journal of Computational Physics*, 263:222–232, 2014.
- [51] J. Dacles-Mariani, G. G. Zilliac, J. S. Chow, and P. Bradshaw. Numerical/experimental study of a wingtip vortex in the near field. *AIAA Journal*, 33(9):1561–1568, 1995.
- [52] A. Dadone, G. Hu, and B. Grossman. Towards a better understanding of vorticity confinement methods in compressible flow. In *15th AIAA Computational Fluid Dynamics Conference, AIAA Paper 2001-2639*. American Institute of Aeronautics and Astronautics, 2001.
- [53] V. Daru and X. Gloerfelt. Aeroacoustic computations using a high-order shock-capturing scheme. *AIAA Journal*, 45(10):2474–2486, Oct. 2007.
- [54] V. Daru and C. Tenaud. High order one-step monotonicity-preserving schemes for unsteady compressible flow calculations. *Journal of Computational Physics*, 193(2):563–594, 2004.
- [55] L. Davidson. Fluid mechanics, turbulent flow and turbulence modeling. Lecture Notes, Division of Fluid Dynamics, Department of Applied Mechanics, Chalmers University of Technology, August 2017.
- [56] M. de la Llave Plata, V. Couaillier, M.-C. Le Pape, C. Marmignon, and M. Gazaix. elsA-Hybrid: an all-in-one structured/unstructured solver for the simulation of internal and external flows. Application to turbomachinery. *EUCASS Proceedings Series, Progress in Propulsion Physics*, 4:417–444, 2013.
- [57] M. de la Llave Plata, V. Couaillier, C. Marmignon, M.-C. Le Pape, M. Gazaix, and B. Cantaloube. Further developments in the multiblock hybrid CFD solver elsA-H. In *50th AIAA Aerospace Sciences Meeting, AIAA Paper 2012-1112*, 2012.
- [58] H. Deconinck and M. Ricchiuto. Residual distribution schemes: Foundations and analysis. In *Encyclopedia of Computational Mechanics*. John Wiley & Sons, Ltd, 2007.
- [59] P. Degond and S. Mas-Gallic. The weighted particle method for convection-diffusion equations. I. the case of an isotropic viscosity. *Mathematics of Computation*, 53(188):485–507, 1989.
- [60] J. M. Délery. Robert Legendre and Henri Werlé: Toward the elucidation of three-dimensional separation. *Annual Review of Fluid Mechanics*, 33(1):129–154, 2001.
- [61] B. Després and F. Lagoutière. Contact discontinuity capturing schemes for linear advection and compressible gas dynamics. *Journal of Scientific Computing*, 16(4):479–524, 2001.
- [62] J. Desse and F. Olchewsky. Digital holographic interferometry for analysing high-density gradients in fluid mechanics. In I. Naydenova, D. Nazarova, and T. Babeva, editors, *Holographic Materials and Optical Systems*, chapter 13. InTech, Rijeka, 2017.
- [63] X. Du, C. Corre, and A. Lerat. A third-order finite-volume residual-based scheme for the 2D Euler equations on unstructured grids. *Journal of Computational Physics*, 230(11):4201–4215, 2011.

-
- [64] F. Ducros, V. Ferrand, F. Nicoud, C. Weber, D. Darracq, C. Gacherieu, and T. Poinso. Large-eddy simulation of the shock/turbulence interaction. *Journal of Computational Physics*, 152(2):517–549, 1999.
- [65] E. P. Duque, C. P. Stone, C. C. Hennes, and A. Gharakhani. A hybrid vortex-particle method for rotorcraft applications. In *30th AIAA Applied Aerodynamics Conference*, page 2912, 2012. AIAA Paper 2012-2912.
- [66] J. R. Edwards and M.-S. Liou. Low-diffusion flux-splitting methods for flows at all speeds. *AIAA Journal*, 36(9):1610–1617, 1998.
- [67] J. A. Ekaterinaris. High-order accurate, low numerical diffusion methods for aerodynamics. *Progress in Aerospace Sciences*, 41(3):192–300, 2005.
- [68] J. D. Eldredge, T. Colonius, and A. Leonard. A vortex particle method for two-dimensional compressible flow. *Journal of Computational Physics*, 179(2):371–399, 2002.
- [69] F. Falissard. *Schémas numériques préservant la vorticit  en a rodynamique compressible*. PhD thesis,  cole Nationale Sup rieure d’Arts et M tiers (ENSAM), Paris, 2006.
- [70] F. Falissard. Genuinely multi-dimensional explicit and implicit generalized shapiro filters for weather forecasting, computational fluid dynamics and aeroacoustics. *Journal of Computational Physics*, 253:344–367, 2013.
- [71] F. Falissard. Explicit filters with spectral-like accuracy: review of design criteria and latest developments. In *23rd AIAA/CEAS Aeroacoustics Conference, AIAA Paper 2017-4182*, 2017.
- [72] F. Falissard, A. Lerat, and J. Sid s. Computation of airfoil-vortex interaction using a vorticity-preserving scheme. *AIAA Journal*, 46(7):1614–1623, 2008.
- [73] R. Fedkiw, J. Stam, and H. W. Jensen. Visual simulation of smoke. In *Proceedings of the 28th Annual Conference on Computer Graphics and Interactive Techniques*, pages 15–22. ACM SIGGRAPH, 2001.
- [74] K. J. Fidkowski and P. L. Roe. An entropy adjoint approach to mesh refinement. *SIAM Journal on Scientific Computing*, 32(3):1261–1287, 2010.
- [75] U. S. Fjordholm and S. Mishra. Vorticity preserving finite volume schemes for the shallow water equations. *SIAM Journal on Scientific Computing*, 33(2):588–611, 2011.
- [76] P.-J. Frey and F. Alauzet. Anisotropic mesh adaptation for CFD computations. *Computer Methods in Applied Mechanics and Engineering*, 194(48):5068–5082, 2005.
- [77] E. Garnier, M. Mossi, P. Sagaut, P. Comte, and M. Deville. On the use of shock-capturing schemes for large-eddy simulation. *Journal of Computational Physics*, 153(2):273–311, 1999.
- [78] G. J. Gassner and A. D. Beck. On the accuracy of high-order discretizations for underresolved turbulence simulations. *Theoretical and Computational Fluid Dynamics*, pages 1–17, 2013.
- [79] G. Gerolymos, D. S n chal, and I. Vallet. Very-high-order WENO schemes. *Journal of Computational Physics*, 228(23):8481–8524, 2009.
- [80] S. K. Godunov. A difference method for numerical calculation of discontinuous solutions of the equations of hydrodynamics. *Matematicheskii Sbornik*, 89(3):271–306, 1959. [In Russian: translated as JPRS 7226 (U.S. Joint Publishing Research Service, 1969)].
- [81] B. Govindarajan and J. Leishman. Curvature corrections to improve the accuracy of free-vortex methods. *Journal of Aircraft*, 53(2):378–386, 2015.

- [82] L. Greengard and V. Rokhlin. A fast algorithm for particle simulations. *Journal of Computational Physics*, 73(2):325 – 348, 1987.
- [83] K. Grimich, P. Cinnella, and A. Lerat. Spectral properties of high-order residual-based compact schemes for unsteady compressible flows. *Journal of Computational Physics*, 252:142–162, 2013.
- [84] K. Grimich, B. Michel, P. Cinnella, and A. Lerat. An accurate finite-volume formulation of a Residual-Based Compact scheme for unsteady compressible flows. *Computers & Fluids*, 92:93 – 112, 2014.
- [85] J.-L. Guermond, S. Huberson, and W.-Z. Shen. Simulation of 2D external viscous flows by means of a domain decomposition method. *Journal of Computational Physics*, 108(2):343–352, 1993.
- [86] S. Hahn and G. Iaccarino. Towards adaptive vorticity confinement. In *47th AIAA Aerospace Sciences Meeting Including The New Horizons Forum and Aerospace Exposition, AIAA Paper 2009-1613*. American Institute of Aeronautics and Astronautics, 2009.
- [87] F. Haider. *Discrétisation en maillage non structuré général et applications LES*. PhD thesis, Université Pierre et Marie Curie - Paris VI, 2009.
- [88] G. Haller. An objective definition of a vortex. *Journal of Fluid Mechanics*, 525:1–26, 2005.
- [89] R. Harris, Z. J. Wang, and Y. Liu. Efficient quadrature-free high-order spectral volume method on unstructured grids: Theory and 2D implementation. *Journal of Computational Physics*, 227(3):1620–1642, 2008.
- [90] A. Harten, B. Engquist, S. Osher, and S. R. Chakravarthy. Uniformly high order accurate essentially non-oscillatory schemes, III. *Journal of Computational Physics*, 71:231–303, 1987.
- [91] A. K. Henrick, T. D. Aslam, and J. M. Powers. Mapped weighted essentially non-oscillatory schemes: achieving optimal order near critical points. *Journal of Computational Physics*, 207(2):542–567, 2005.
- [92] W. D. Henshaw and D. W. Schwendeman. Parallel computation of three-dimensional flows using overlapping grids with adaptive mesh refinement. *Journal of Computational Physics*, 227(16):7469–7502, 2008.
- [93] C. Hirsch. *Numerical Computation of Internal and External Flows: The Fundamentals of Computational Fluid Dynamics*. Butterworth-Heinemann, 2007.
- [94] F. Q. Hu, M. Y. Hussaini, and J. L. Manthey. Low-dissipation and low-dispersion Runge–Kutta schemes for computational acoustics. *Journal of Computational Physics*, 124(1):177–191, 1996.
- [95] G. Hu and B. Grossman. The computation of massively separated flows using compressible vorticity confinement methods. *Computers & fluids*, 35(7):781–789, 2006.
- [96] G. Hu, B. Grossman, and J. Steinhoff. Numerical method for vorticity confinement in compressible flow. *AIAA Journal*, 40(10):1945–1953, 2002.
- [97] M. Hubbard. Discontinuous fluctuation distribution. *Journal of Computational Physics*, 227(24):10125–10147, 2008.
- [98] J. C. R. Hunt, A. A. Wray, and P. Moin. Eddies, streams, and convergence zones in turbulent flows. In *CTR – Proceedings of the 1988 Summer Program*, pages 193–208, 1988.

- [99] H. T. Huynh. A flux reconstruction approach to high-order schemes including discontinuous Galerkin methods. In *18th AIAA Computational Fluid Dynamics Conference*. American Institute of Aeronautics and Astronautics, 2007. AIAA Paper 2007-4079.
- [100] H. T. Huynh. A reconstruction approach to high-order schemes including discontinuous Galerkin for diffusion. In *47th AIAA Aerospace Sciences Meeting Including The New Horizons Forum and Aerospace Exposition*. American Institute of Aeronautics and Astronautics, 2009. AIAA Paper 2009-0403.
- [101] H. T. Huynh, Z. J. Wang, and P. E. Vincent. High-order methods for computational fluid dynamics: a brief review of compact differential formulations on unstructured grids. *Computers & Fluids*, 98:209–220, 2014.
- [102] F. Ismail and P. Roe. Towards a vorticity preserving second order finite volume scheme solving the Euler equations. In *17th AIAA Computational Fluid Dynamics Conference*. American Institute of Aeronautics and Astronautics, 2005. AIAA Paper 2005-5235.
- [103] L. Ivan and C. P. Groth. High-order solution-adaptive central essentially non-oscillatory (CENO) method for viscous flows. *Journal of Computational Physics*, 257:830–862, 2014.
- [104] A. Jameson, W. Schmidt, and E. Turkel. Numerical solutions of the Euler equations by finite volume methods using Runge-Kutta time-stepping schemes. In *14th AIAA Fluid and Plasma Dynamics Conference*. American Institute of Aeronautics and Astronautics, 1981.
- [105] R. Jeltsch and M. Torrilhon. On curl-preserving finite volume discretizations for shallow water equations. *BIT Numerical Mathematics*, 46(1):35–53, 2006.
- [106] J. Jeong and F. Hussain. On the identification of a vortex. *Journal of Fluid Mechanics*, 285:69–94, 1995.
- [107] G.-S. Jiang and C.-W. Shu. Efficient implementation of weighted ENO schemes. *Journal of Computational Physics*, 126(1):202 – 228, 1996.
- [108] S. Kamkar, A. M. Wissink, V. Sankaran, and A. Jameson. Feature-driven cartesian adaptive mesh refinement for vortex-dominated flows. *Journal of Computational Physics*, 230(16):6271–6298, 2011.
- [109] J. W. Kim and D. J. Lee. Adaptive nonlinear artificial dissipation model for computational aeroacoustics. *AIAA Journal*, 39(5):810–818, 2001.
- [110] C. Kitaplioglu, F. X. Caradonna, and C. L. Burley. Parallel blade-vortex interactions: an experimental study and comparison with computations. *Journal of the American Helicopter Society*, 42(3):272–281, July 1997.
- [111] C. Kitaplioglu, F. X. Caradonna, and M. McCluer. An experimental study of parallel blade-vortex interaction aerodynamics and acoustics utilizing an independently generated vortex. Technical Report NASA/TM-1999-208790, NASA Ames Research Center, July 1999.
- [112] P. Koumoutsakos. Multiscale flow simulations using particles. *Annu. Rev. Fluid Mech.*, 37:457–487, 2005.
- [113] P. Koumoutsakos and A. Leonard. High-resolution simulations of the flow around an impulsively started cylinder using vortex methods. *Journal of Fluid Mechanics*, 296:1–38, 1995.
- [114] N. Kroll, C. Hirsch, F. Bassi, C. Johnston, and K. Hillewaert, editors. *IDIHOM: Industrialization of High-Order Methods-A Top-Down Approach. Results of a Collaborative Research Project Funded by the European Union, 2010-2014*, volume 128 of *Notes on Numerical Fluid Mechanics and Multidisciplinary Design*. Springer, 2015.

-
- [115] D. Küchemann. Report on the I.U.T.A.M. symposium on concentrated vortex motions in fluids. *Journal of Fluid Mechanics*, 21(1):1–20, 1965.
- [116] P. Lax and B. Wendroff. Systems of conservation laws. *Communications on Pure and Applied Mathematics*, 13(2):217–237, 1960.
- [117] J. Leishman, M. Bhagwat, and A. Bagai. Free-vortex filament methods for the analysis of helicopter rotor wakes. *Journal of aircraft*, 39(5):759–775, 2002.
- [118] S. K. Lele. Compact finite difference schemes with spectral-like resolution. *Journal of Computational Physics*, 103(1):16–42, 1992.
- [119] A. Leonard. Vortex methods for flow simulation. *Journal of Computational Physics*, 37(3):289–335, 1980.
- [120] A. Lerat. Steady discrete shocks of 5th and 7th-order RBC schemes and shock profiles of their equivalent differential equations. *Journal of Computational Physics*, 272:629–643, 2014.
- [121] A. Lerat. A high-order time formulation of the RBC schemes for unsteady compressible Euler equations. *Journal of Computational Physics*, 303:251–268, 2015.
- [122] A. Lerat. An efficient high-order compact scheme for the unsteady compressible Euler and Navier–Stokes equations. *Journal of Computational Physics*, 322:365–386, 2016.
- [123] A. Lerat, P. Cinnella, B. Michel, and F. Falissard. High-order residual-based compact schemes for aerodynamics and aeroacoustics. *Computers & Fluids*, 61:31–38, 2012.
- [124] A. Lerat and C. Corre. A residual-based compact scheme for the compressible Navier–Stokes equations. *Journal of Computational Physics*, 170(2):642–675, 2001.
- [125] A. Lerat and C. Corre. Residual-based compact schemes for multidimensional hyperbolic systems of conservation laws. *Computers & Fluids*, 31(4):639–661, 2002.
- [126] A. Lerat and C. Corre. *High-order residual-based compact schemes on structured grids*, In: *CFD–Higher order discretization methods*. VKI Lecture Series 2006–01. Von Karman Institute for Fluid Dynamics, November 2005.
- [127] A. Lerat, F. Falissard, and J. Sidès. Vorticity-preserving schemes for the compressible Euler equations. *Journal of Computational Physics*, 225(1):635 – 651, 2007.
- [128] A. Lerat, K. Grimich, and P. Cinnella. On the design of high order residual-based dissipation for unsteady compressible flows. *Journal of Computational Physics*, 235:32–51, 2013.
- [129] K. Lindsay and R. Krasny. A particle method and adaptive treecode for vortex sheet motion in three-dimensional flow. *Journal of Computational Physics*, 172(2):879–907, 2001.
- [130] M.-S. Liou. A sequel to AUSM: AUSM+. *Journal of Computational Physics*, 129(2):364–382, 1996.
- [131] M.-S. Liou and C. J. Steffen. A new flux splitting scheme. *Journal of Computational Physics*, 107(1):23–39, 1993.
- [132] X.-D. Liu, S. Osher, and T. Chan. Weighted essentially non-oscillatory schemes. *Journal of Computational Physics*, 115(1):200–212, 1994.
- [133] Y. Liu, M. Vinokur, and Z. J. Wang. Spectral difference method for unstructured grids I: Basic formulation. *Journal of Computational Physics*, 216(2):780–801, 2006.

- [134] Y. Liu, M. Vinokur, and Z. J. Wang. Spectral (finite) volume method for conservation laws on unstructured grids V: Extension to three-dimensional systems. *Journal of Computational Physics*, 212(2):454–472, 2006.
- [135] R. Löhner. On limiters for minimal vorticity dissipation. In *47th AIAA Aerospace Sciences Meeting Including the New Horizons Forum and Aerospace Exhibition, AIAA Paper 2009-0135*. American Institute of Aeronautics and Astronautics, 2009.
- [136] R. Löhner, C. Yang, and R. Roger. Tracking vortices over large distances using vorticity confinement. In *24th Symposium on Naval Hydrodynamics, Fukuoka, Japan, July 2002*.
- [137] S. Markvorsen. The classical version of Stokes’ theorem revisited. *International Journal of Mathematical Education in Science and Technology*, 39(7):879–888, 2008.
- [138] I. Mary and P. Sagaut. Large eddy simulation of flow around an airfoil near stall. *AIAA Journal*, 40(6):1139–1145, 2002.
- [139] I. Mary, P. Sagaut, and M. Deville. An algorithm for unsteady viscous flows at all speeds. *International Journal for Numerical Methods in Fluids*, 34(5):371–401, 2000.
- [140] B. Maugars. *Méthodes de volumes finis d’ordre élevé en maillages non coïncident pour les écoulements dans les turbomachines*. PhD thesis, Arts et Métiers ParisTech, 2016.
- [141] D. J. Mavriplis. Revisiting the least-squares procedure for gradient reconstruction on unstructured meshes. Technical Report NASA/CR-2003-212683, NIA Report No. 2003-06, NASA Langley Research Center, December 2003.
- [142] B. Michel, P. Cinnella, and A. Lerat. Multiblock residual-based compact schemes for the computation of complex turbomachinery flows. *International Journal of Engineering Systems Modelling and Simulation*, 3(1-2):2–15, 2011.
- [143] S. Mishra and E. Tadmor. Constraint preserving schemes using potential-based fluxes. II. Genuinely multidimensional systems of conservation laws. *SIAM Journal on Numerical Analysis*, 49(3):1023–1045, 2011.
- [144] S. Mishra and E. Tadmor. Constraint preserving schemes using potential-based fluxes. III. Genuinely multi-dimensional schemes for MHD equations. *ESAIM: Mathematical Modelling and Numerical Analysis*, 46(3):661–680, 2012.
- [145] K. Mohamed, S. Nadarajah, and M. Paraschivoiu. Eddy-preserving limiter for unsteady subsonic flows. *AIAA Journal*, 50(2):429–446, 2012.
- [146] J. J. Monaghan. Smoothed particle hydrodynamics. *Reports on Progress in Physics*, 68(8):1703, 2005.
- [147] J. J. Monaghan. Smoothed particle hydrodynamics and its diverse applications. *Annual Review of Fluid Mechanics*, 44(1):323–346, 2012.
- [148] K. Morton and P. L. Roe. Vorticity-preserving Lax–Wendroff-type schemes for the system wave equation. *SIAM Journal on Scientific Computing*, 23(1):170–192, 2001.
- [149] R. Morvant, K. J. Badcock, G. N. Barakos, and B. E. Richards. Airfoil-vortex interaction using the compressible vorticity confinement method. *AIAA Journal*, 43(1):63–75, 2005.
- [150] M. Murayama, K. Nakahashi, and S. Obayashi. Numerical simulation of vortical flows using vorticity confinement coupled with unstructured grid. In *39th AIAA Aerospace Sciences Meeting & Exhibit, AIAA Paper 2001-0606*. American Institute of Aeronautics and Astronautics, 2001.

- [151] R.-H. Ni. A multiple-grid scheme for solving the Euler equations. *AIAA Journal*, 20(11):1565–1571, Nov. 1982.
- [152] M. Nitsche and J. H. Strickland. Extension of the gridless vortex method into the compressible flow regime*. *Journal of Turbulence*, 3:40–40, 2002.
- [153] C. Ollivier-Gooch and M. Van Altena. A high-order-accurate unstructured mesh finite-volume scheme for the advection–diffusion equation. *Journal of Computational Physics*, 181(2):729–752, 2002.
- [154] P.-Y. Outtier, C. Content, P. Cinnella, and B. Michel. The high-order dynamic computational laboratory for CFD research and applications. In *Fluid Dynamics and Co-located Conferences*, pages –. American Institute of Aeronautics and Astronautics, June 2013.
- [155] G. S. Oxley. *A 2-D Hybrid Euler-Compressible Vortex Particle Method For Transonic Rotorcraft Flows*. PhD thesis, Carleton University Ottawa, 2009.
- [156] G. Papadakis. *Development of a hybrid compressible vortex particle method and application to external problems including helicopter flows*. PhD thesis, National Technical University of Athens, Greece, 2014.
- [157] G. Papadakis and S. G. Voutsinas. In view of accelerating CFD simulations through coupling with vortex particle approximations. In *Journal of Physics: Conference Series*, volume 524, page 012126. IOP Publishing, 2014.
- [158] S. Peron and C. Benoit. Automatic off-body overset adaptive Cartesian mesh method based on an octree approach. *Journal of Computational Physics*, 232(1):153–173, 2013.
- [159] S. Peron, C. Benoit, T. Renaud, J. Sidès, Y. Tanabe, S. Saito, C. Yang, and T. Aoyama. ONERA/JAXA common investigations on CFD tools for an accurate prediction of BVI. In *AHS Specialists Meeting, Seoul, Korea*, AHS Specialists Meeting, Seoul, Korea, October 2007.
- [160] S. Pirozzoli. On the spectral properties of shock-capturing schemes. *Journal of Computational Physics*, 219(2):489 – 497, 2006.
- [161] P. Ploumhans, G. Winckelmans, J. Salmon, A. Leonard, and M. Warren. Vortex methods for direct numerical simulation of three-dimensional bluff body flows: Application to the sphere at $Re=300, 500, \text{ and } 1000$. *Journal of Computational Physics*, 178(2):427 – 463, 2002.
- [162] G. Pont, P. Brenner, P. Cinnella, B. Maugars, and J.-C. Robinet. Multiple-correction hybrid k-exact schemes for high-order compressible RANS-LES simulations on fully unstructured grids. *Journal of Computational Physics*, 350:45 – 83, 2017.
- [163] W. H. Reed and T. R. Hill. Triangular mesh methods for the neutron transport equation. Technical Report LA-UR-73-479, Los Alamos Scientific Lab., N. Mex.(USA), 1973.
- [164] N. Renard and S. Deck. Improvements in Zonal Detached Eddy Simulation for Wall Modeled Large Eddy Simulation. *AIAA Journal*, 53:3499–3504, 2015.
- [165] A. Rezgui, P. Cinnella, and A. Lerat. Third-order accurate finite volume schemes for Euler computations on curvilinear meshes. *Computers & Fluids*, 30(7–8):875 – 901, 2001.
- [166] M. Ricchiuto. Contributions to the development of residual discretizations for hyperbolic conservation laws with application to shallow water flows. Habilitation à Diriger des Recherches (HDR), Université de Bordeaux I, 2011.
- [167] M. A. Robinson. Application of vorticity confinement to inviscid missile force and moment prediction. In *42nd AIAA Aerospace Sciences Meeting and Exhibit, AIAA Paper 2004-0717*. American Institute of Aeronautics and Astronautics, 2004.

- [168] S. K. Robinson. Coherent motions in the turbulent boundary layer. *Annual Review of Fluid Mechanics*, 23(1):601–639, 1991.
- [169] P. L. Roe. Approximate Riemann solvers, parameter vectors, and difference schemes. *Journal of Computational Physics*, 43(2):357–372, 1981.
- [170] P. L. Roe. Vorticity capturing. In *15th AIAA Computational Fluid Dynamics Conference, AIAA Paper 01-2523*, Anaheim, California, June 2001.
- [171] P. L. Roe. "Optimum" upwind advection on a triangular mesh. Technical report, NASA Langley Research Center, October 1990. ICASE Report No. 90-75.
- [172] J. Romero, K. Asthana, and A. Jameson. A simplified formulation of the flux reconstruction method. *Journal of Scientific Computing*, 67(1):351–374, 2016.
- [173] M. Sadri, K. Hejranfar, and M. Ebrahimi. On application of high-order compact finite-difference schemes to compressible vorticity confinement method. *Aerospace Science and Technology*, 46:398–411, 2015.
- [174] P. Sagaut and C. Cambon. *Homogeneous Turbulence Dynamics*. Cambridge University Press, 2008.
- [175] P. Sagaut, S. Deck, and M. Terracol. *Multiscale and Multiresolution Approaches in Turbulence*. Imperial College Press, Second edition, 2013.
- [176] R. Samtaney, D. I. Pullin, and B. Kosović. Direct numerical simulation of decaying compressible turbulence and shocklet statistics. *Physics of Fluids*, 13(5):1415–1430, 2001.
- [177] V. Sankaran, A. Wissink, A. Datta, J. Sitaraman, M. Potsdam, B. Jayaraman, A. Katz, S. Kamkar, B. Roget, D. Mavriplis, H. Saberi, W.-B. Chen, W. Johnson, and R. Strawn. Overview of the Helios version 2.0 computational platform for rotorcraft simulations. In *Aerospace Sciences Meetings*, pages –. American Institute of Aeronautics and Astronautics, Jan. 2011.
- [178] O. Saunier. *Méthode d'adaptation de maillages cartésiens basée sur des schémas d'ordre élevé pour les équations d'Euler d'un fluide compressible. Application aux pales de rotor d'hélicoptère*. PhD thesis, École Nationale Supérieure d'Arts et Métiers (ENSAM), Paris, 2008.
- [179] O. Saunier, C. Benoit, G. Jeanfaivre, and A. Lerat. Third-order cartesian overset mesh adaptation method for solving steady compressible flows. *International Journal for Numerical Methods in Fluids*, 57(7):811–838, 2008.
- [180] I. Sbalzarini, J. Walther, M. Bergdorf, S. Hieber, E. Kotsalis, and P. Koumoutsakos. PPM – A highly efficient parallel particle–mesh library for the simulation of continuum systems. *Journal of Computational Physics*, 215(2):566 – 588, 2006.
- [181] L. Sciacovelli, P. Cinnella, and F. Grasso. Dense gas effects in inviscid homogeneous isotropic turbulence. *Journal of Fluid Mechanics*, 800:140–179, 2016.
- [182] M. P. Scully. *Computation of helicopter rotor wake geometry and its influence on rotor harmonic airloads*. PhD thesis, Massachusetts Institute of Technology, 1975.
- [183] S. E. Sherer and J. N. Scott. High-order compact finite-difference methods on general overset grids. *Journal of Computational Physics*, 210(2):459 – 496, 2005.
- [184] E. Shima, K. Kitamura, and T. Haga. Green–Gauss/weighted-least-squares hybrid gradient reconstruction for arbitrary polyhedra unstructured grids. *AIAA Journal*, 51(11):2740–2747, 2013.

- [185] C.-W. Shu. High order weighted essentially nonoscillatory schemes for convection dominated problems. *SIAM review*, 51(1):82–126, 2009.
- [186] C.-W. Shu. Essentially non-oscillatory and weighted essentially non-oscillatory schemes for hyperbolic conservation laws. Technical Report NASA/CR-97-206253, ICASE Report No. 97-65, Langley Research Center, November 1997.
- [187] J. Slotnick, A. Khodadoust, J. Alonso, D. Darmofal, W. Gropp, E. Lurie, and D. Mavriplis. CFD vision 2030 study: A path to revolutionary computational aerosciences. Technical Report NASA/CR-2014-218178, NASA, Langley Research Center, March 2014.
- [188] P. R. Spalart and M. L. Shur. On the sensitization of turbulence models to rotation and curvature. *Aerospace Science and Technology*, 1(5):297–302, 1997.
- [189] J. Steinhoff. Vorticity confinement: A new technique for computing vortex dominated flows. In D. A. Caughey and M. M. Hafez, editors, *Frontiers of Computational Fluid Dynamics*, pages 235–264. John Wiley & Sons, 1994.
- [190] J. Steinhoff and S. Chitta. Long distance wave computation using nonlinear solitary waves. *Journal of Computational and Applied Mathematics*, 234(6):1826–1833, 2010.
- [191] J. Steinhoff and S. Chitta. Solution of the scalar wave equation over very long distances using nonlinear solitary waves: Relation to finite difference methods. *Journal of Computational Physics*, 231(19):6306–6322, 2012.
- [192] J. Steinhoff, W. Dietz, S. Haas, M. Xiao, N. Lynn, and M. Fan. Simulating small scale features in fluid dynamics and acoustics as nonlinear solitary waves. In *41st AIAA Aerospace Sciences Meeting and Exhibit, AIAA Paper 2003-078*. American Institute of Aeronautics and Astronautics, 2003.
- [193] J. Steinhoff, M. Fan, L. Wang, and W. Dietz. Convection of concentrated vortices and passive scalars as solitary waves. *Journal of Scientific Computing*, 19(1):457–478, 2003.
- [194] J. Steinhoff and N. Lynn. Treatment of vortical flow using vorticity confinement. In D. A. Caughey and M. M. Hafez, editors, *Frontiers of Computational Fluid Dynamics*, pages 199–237. World Scientific, 2006.
- [195] J. Steinhoff, N. Lynn, and L. Wang. Vorticity confinement. In F. F. Grinstein, L. G. Margolin, and W. J. Rider, editors, *Implicit Large Eddy Simulation: Computing Turbulent Flow Dynamics*, pages 168–194. Cambridge University Press, 2007.
- [196] J. Steinhoff, N. Lynn, Y. Wenren, M. Fan, L. Wang, and B. Dietz. Turbulent flow simulations using vorticity confinement. In F. F. Grinstein, L. G. Margolin, and W. J. Rider, editors, *Implicit Large Eddy Simulation: Computing Turbulent Flow Dynamics*, pages 370–391. Cambridge University Press, 2007.
- [197] J. Steinhoff, E. Puskas, S. Babu, Y. Wenren, and D. Underhill. Computation of thin features over long distances using solitary waves. In *13th AIAA Computational Fluid Dynamics Conference, AIAA Paper 97-1976*. American Institute of Aeronautics and Astronautics, 1997.
- [198] J. Steinhoff and D. Underhill. Modification of the Euler equations for “vorticity confinement”: Application to the computation of interacting vortex rings. *Physics of Fluids*, 6(8):2738–2744, 1994.
- [199] J. Steinhoff, Y. Wenren, T. Mersch, and H. Senge. Computational vorticity capturing: Application to helicopter rotor flow. In *30th AIAA Aerospace Sciences Meeting and Exhibit, AIAA Paper 1992-0056*. American Institute of Aeronautics and Astronautics, 1992.

- [200] C. Stone, E. Duque, C. Hennes, and A. Gharakhani. Rotor wake modeling with a coupled Eulerian and vortex particle method. In *48th AIAA Aerospace Sciences Meeting*, 2010. AIAA Paper 2010-0312.
- [201] X. Su. Accurate and robust adaptive mesh refinement for aerodynamic simulation with multi-block structured curvilinear mesh. *International Journal for Numerical Methods in Fluids*, 77(12):747–766, 2015.
- [202] Y. Sun, Z. J. Wang, and Y. Liu. Spectral (finite) volume method for conservation laws on unstructured grids VI: Extension to viscous flow. *Journal of Computational Physics*, 215(1):41–58, 2006.
- [203] C. K. W. Tam and J. C. Webb. Dispersion-relation-preserving finite difference schemes for computational acoustics. *Journal of Computational Physics*, 107(2):262–281, 1993.
- [204] G. I. Taylor and A. E. Green. Mechanism of the production of small eddies from large ones. *Proceedings of the Royal Society of London A: Mathematical, Physical and Engineering Sciences*, 158(895):499–521, 1937.
- [205] M. Torrilhon and M. Fey. Constraint-preserving upwind methods for multidimensional advection equations. *SIAM Journal on Numerical Analysis*, 42(4):1694–1728, 2004.
- [206] A. Travin, M. Shur, M. Strelets, and P. R. Spalart. Physical and numerical upgrades in the detached-eddy simulation of complex turbulent flows. In R. Friedrich and W. Rodi, editors, *Advances in LES of Complex Flows: Proceedings of the Euromech Colloquium 412, held in Munich, Germany 4–6 October 2000*, pages 239–254, Dordrecht, 2002. Springer Netherlands.
- [207] S. van der Walt, S. C. Colbert, and G. Varoquaux. The NumPy array: a structure for efficient numerical computation. *Computing in Science & Engineering*, 13(2):22–30, 2011.
- [208] B. Van Leer. Towards the ultimate conservative difference scheme. V. A second-order sequel to Godunov’s method. *Journal of Computational Physics*, 32(1):101–136, 1979.
- [209] W. M. Van Rees, A. Leonard, D. Pullin, and P. Koumoutsakos. A comparison of vortex and pseudo-spectral methods for the simulation of periodic vortical flows at high reynolds numbers. *Journal of Computational Physics*, 230(8):2794–2805, 2011.
- [210] D. A. Venditti and D. L. Darmofal. Grid adaptation for functional outputs: Application to two-dimensional inviscid flows. *Journal of Computational Physics*, 176(1):40–69, 2002.
- [211] R. Vichnevetsky and J. Bowles. *Fourier Analysis of Numerical Approximations of Hyperbolic Equations*. Society for Industrial and Applied Mathematics, 1982.
- [212] P. E. Vincent, P. Castonguay, and A. Jameson. A new class of high-order energy stable flux reconstruction schemes. *Journal of Scientific Computing*, 47(1):50–72, 2011.
- [213] M. Visbal and D. Gaitonde. On the use of higher-order finite-difference schemes on curvilinear and deforming meshes. *Journal of Computational Physics*, 181(1):155–185, 2002.
- [214] M. R. Visbal and D. P. Rizzetta. Large-eddy simulation on curvilinear grids using compact differencing and filtering schemes. *ASME. J. Fluids Eng.*, 124:836–847, 2002.
- [215] J. Von Neumann and R. D. Richtmyer. A method for the numerical calculation of hydrodynamic shocks. *Journal of Applied Physics*, 21(3):232–237, 1950.
- [216] S. G. Voutsinas. Vortex methods in aeronautics: how to make things work. *International Journal of Computational Fluid Dynamics*, 20(1):3–18, 2006.

- [217] Z. Wang, Y. Liu, G. May, and A. Jameson. Spectral difference method for unstructured grids II: extension to the Euler equations. *Journal of Scientific Computing*, 32(1):45–71, 2007.
- [218] Z. J. Wang. Spectral (finite) volume method for conservation laws on unstructured grids: Basic formulation. *Journal of Computational Physics*, 178(1):210–251, 2002.
- [219] Z. J. Wang. High-order methods for the Euler and Navier–Stokes equations on unstructured grids. *Progress in Aerospace Sciences*, 43(1):1–41, 2007.
- [220] Z. J. Wang, K. Fidkowski, R. Abgrall, F. Bassi, D. Caraeni, A. Cary, H. Deconinck, R. Hartmann, K. Hillewaert, H. Huynh, N. Kroll, G. May, P.-O. Persson, B. van Leer, and M. Visbal. High-order CFD methods: current status and perspective. *International Journal for Numerical Methods in Fluids*, 72(8):811–845, 2013.
- [221] Z. J. Wang, Y. Liu, C. Lacor, and J. L. F. Azevedo. Spectral volume and spectral difference methods. *Handbook of Numerical Analysis*, 17:199–226, 2016.
- [222] R. F. Warming and R. M. Beam. Upwind second-order difference schemes and applications in aerodynamic flows. *AIAA Journal*, 14(9):1241–1249, 1976.
- [223] Y. Wenren, M. Fan, W. Dietz, G. Hu, C. Braun, J. Steinhoff, and B. Grossman. Efficient Eulerian computation of realistic rotorcraft flows using vorticity confinement – A survey of recent results. In *39th AIAA Aerospace Sciences Meeting and Exhibit, AIAA Paper 2001-0996*. American Institute of Aeronautics and Astronautics, 2001.
- [224] Y. Wenren, M. Fan, L. Wang, M. Xiao, and J. Steinhoff. Application of vorticity confinement to prediction of the flow over complex bodies. *AIAA Journal*, 41(5):809–816, 2003.
- [225] H. Werlé. Courants et Couleurs. ONERA Cinema Film No. 777, 1974.
- [226] G. Winckelmans, R. Cocle, L. Dufresne, and R. Capart. Vortex methods and their application to trailing wake vortex simulations. *Comptes Rendus Physique*, 6(4–5):467 – 486, 2005. Aircraft trailing vortices.
- [227] A. Wissink, M. Potsdam, V. Sankaran, J. Sitaraman, Z. Yang, and D. Mavriplis. A coupled unstructured-adaptive Cartesian CFD approach for hover prediction. In *66th Annual Forum of the American Helicopter Society*, pages 1300–1317, 2010.
- [228] A. M. Wissink, J. Sitaraman, V. Sankaran, D. Mavriplis, and T. H. Pulliam. A multi-code python-based infrastructure for overset CFD with adaptive cartesian grids. *46th AIAA Aerospace Sciences Meeting and Exhibit*, 2008. AIAA Paper 2008-0927.
- [229] F. D. Witherden, A. M. Farrington, and P. E. Vincent. PyFR: An open source framework for solving advection–diffusion type problems on streaming architectures using the flux reconstruction approach. *Computer Physics Communications*, 185(11):3028–3040, 2014.
- [230] Z.-N. Wu. Steady and unsteady shock waves on overlapping grids. *SIAM Journal on Scientific Computing*, 20(5):1851–1874, 1999.
- [231] Z. Xu and C.-W. Shu. Anti-diffusive flux corrections for high order finite difference WENO schemes. *Journal of Computational Physics*, 205(2):458–485, 2005.
- [232] H. Yang, Z. Chen, A. Przekwas, and J. Dudley. A high-order CFD method using successive differentiation. *Journal of Computational Physics*, 281:690–707, 2015.
- [233] H. Yang, D. Nuernberger, and H.-P. Kersken. Toward excellence in turbomachinery computational fluid dynamics: A hybrid structured-unstructured Reynolds-Averaged Navier-Stokes solver. *Journal of Turbomachinery*, 128(2):390–402, 2006.

-
- [234] H. C. Yee, M. Vinokur, and M. J. Djomehri. Entropy splitting and numerical dissipation. *Journal of Computational Physics*, 162(1):33 – 81, 2000.

ONERA - The French Aerospace Lab
Centre de Meudon
8 rue des Vertugadins, 92190 Meudon, France
Tél. : +33 1 46 23 50 50 - Fax +33 1 46 23 50 80
<http://www.onera.fr>

ÉTUDE DE SCHÉMAS DE CONFINEMENT D'ORDRE ÉLEVÉ

RESUME : Les tourbillons sont des structures importantes pour une large gamme d'écoulements de fluides, notamment les sillages, l'interaction fluide-structure, les décollements de couche limite et la turbulence. Cependant, les méthodes numériques classiques n'arrivent généralement pas à donner une représentation précise des tourbillons. Ceci est principalement lié à la dissipation numérique des schémas qui, si elle n'est pas spécifiquement calibrée pour le calcul des écoulements tourbillonnaires, conduit à une diffusion artificielle très rapide des tourbillons dans les calculs. Parmi d'autres approches, la méthode "Vorticity Confinement" (VC) de J. Steinhoff permet de compenser la dissipation des schémas au sein des tourbillons en introduisant une anti-dissipation non-linéaire, mais elle n'est précise qu'au premier ordre. D'autre part, des progrès significatifs ont récemment été accomplis dans le développement de méthodes numériques d'ordre élevé. Celles-ci permettent de réduire ce problème de dissipation excessive, mais la diffusion des tourbillons reste importante pour de nombreuses applications. La présente étude vise à développer des extensions d'ordre élevé de la méthode VC pour réduire cette dissipation excessive des tourbillons, tout en préservant la précision d'ordre élevé des schémas. Tout d'abord, les schémas de confinement sont analysés dans le cas de l'équation de transport linéaire, à partir de discrétisations couplées et découplées en espace et en temps. Une analyse spectrale de ces schémas est effectuée analytiquement et numériquement en raison de leur caractère non linéaire. Elle montre des propriétés dispersives et dissipatives améliorées par rapport aux schémas linéaires de base à tous les ordres de précision. Dans un second temps, des schémas VC précis au troisième et cinquième ordre sont développés pour les équations de Navier-Stokes compressibles. Les termes correctifs restent conservatifs, invariants par rotation et indépendants du schéma de base, comme la formulation originale VC2. Les tests numériques valident l'ordre de précision et la capacité des extensions VC d'ordre élevé à réduire la dissipation dans les tourbillons. Enfin, les schémas avec VC sont appliqués au calcul des écoulements turbulents, dans une approche de simulation de grandes échelles implicite (ILES). Les schémas numériques avec VC présentent une résolubilité améliorée par rapport à leur version linéaire de base, et montrent leur capacité à décrire de façon cohérente ces écoulements tourbillonnaires complexes.

Mots clés : mécanique des fluides numérique, confinement tourbillonnaire, ordre élevé, schémas numériques, vorticités, corrections anti-dissipatives.

STUDY OF HIGH-ORDER VORTICITY CONFINEMENT SCHEMES

ABSTRACT : Vortices are flow structures of primary interest in a wide range of fluid dynamics applications including wakes, fluid-structure interaction, flow separation and turbulence. Albeit their importance, standard Computational Fluid Dynamics (CFD) methods very often fail to provide an accurate representation of vortices. This is primarily related to the schemes' numerical dissipation which, if inadequately tuned for the calculation of vortical flows, results in the artificial spreading and diffusion of vortices in numerical simulations. Among other approaches, the Vorticity Confinement (VC) method of J. Steinhoff allows balancing the baseline dissipation within vortices by introducing non-linear anti-dissipation in the discretization of the flow equations, but remains at most first-order accurate. At the same time, remarkable progress has recently been made on the development of high-order numerical methods. These allow reducing the problem of excess dissipation, but the diffusion of vortices remains important for many applications. The present study aims at developing high-order extensions of the VC method to reduce the excess dissipation of vortices, while preserving the accuracy of high-order methods. First, the schemes are analyzed in the case of the linear transport equation, based on time-space coupled and uncoupled formulations. A spectral analysis of nonlinear schemes with VC is performed analytically and numerically, due to their nonlinear character. These schemes exhibit improved dispersive and dissipative properties compared to their linear counterparts at all orders of accuracy. In a second step, third- and fifth-order accurate VC schemes are developed for the compressible Navier-Stokes equations. These remain conservative, rotationally invariant and independent of the baseline scheme, as the original VC2 formulation. Numerical tests validate the increased order of accuracy and the capability of high-order VC extensions to balance dissipation within vortices. Finally, schemes with VC are applied to the calculation of turbulent flows, in an implicit Large Eddy Simulation (ILES) approach. In these applications, numerical schemes with VC exhibit improved resolvability compared to their baseline linear version, while they are capable of producing consistent results even in complex vortical flows

Keywords : computational fluid dynamics, vorticity confinement, high-order, numerical schemes, vorticity, anti-dissipative corrections.

